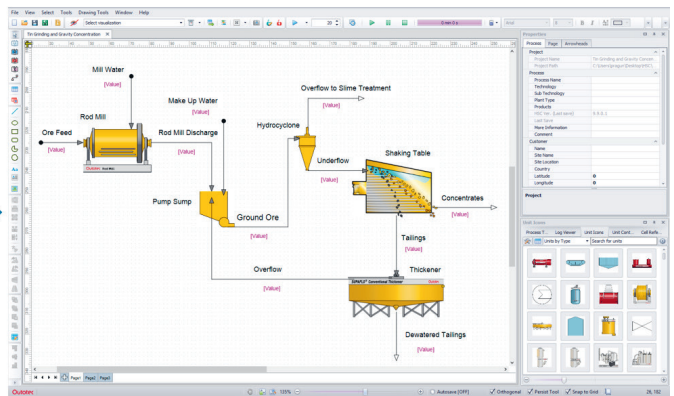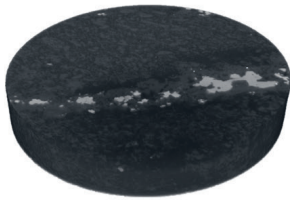# X-ray Microcomputed Tomography (µCT) as a Potential Tool in Geometallurgy

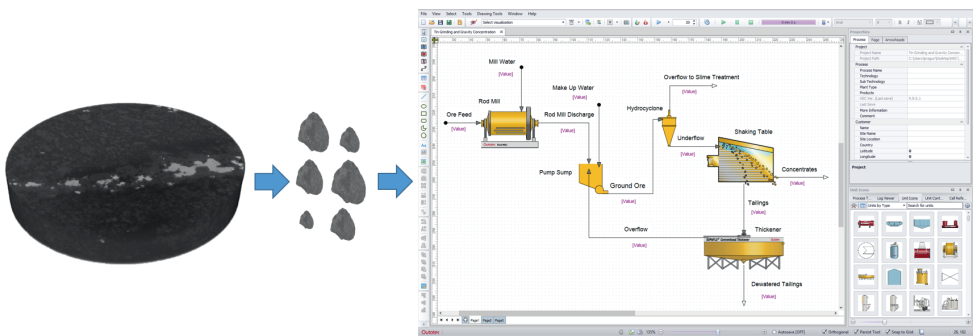Pratama Istiadi Guntoro

Mineral Processing

LULEÅ
UNIVERSITY
OF TECHNOLOGY

X-ray Microcomputed Tomography (μCT) as a Potential Tool in Geometallurgy

Pratama Istiadi Guntoro

Division of Minerals and Metallurgical Engineering
Department of Civil, Environmental, and Natural Resources Engineering
Luleå University of Technology
Luleå, Sweden

Supervisors:

Yousef Ghorbani
Jan Rosenkranz
Cecilia Lund

Untuk Tuhan, Bangsa, dan Almamater..

ABSTRACT

In recent years, automated mineralogy has become an essential tool in geometallurgy. Automated mineralogical tools allow the acquisition of mineralogical and liberation data of ore particles in a sample. These particle data can then be used further for particle-based mineral processing simulation in the context of geometallurgy. However, most automated mineralogical tools currently in application are based on two-dimensional (2D) microscopy analysis, which are subject to stereological error when analyzing three-dimensional (3D) object such as ore particles. Recent advancements in X-ray microcomputed tomography (μCT) have indicated great potential of such system to be the next automated mineralogical tool. μCT's main advantage lies in its ability in monitoring 3D internal structure of the ore at resolutions down to few microns, eliminating stereological error obtained from 2D analysis. Aided with the continuous developments of computing capability of 3D data, it is only the question of time that μCT system becomes an interesting alternative in automated mineralogy system.

This study aims to evaluate the potential of implementing μCT as an automated mineralogical tool in the context of geometallurgy. First, a brief introduction about the role of automated mineralogy in geometallurgy is presented. Then, the development of μCT system to become an automated mineralogical tool in the context of geometallurgy and process mineralogy is discussed (Paper 1). The discussion also reviews the available data analysis methods in extracting ore properties (size, mineralogy, texture) from the 3D μCT image and how these properties relate to processing behaviour (Paper 2). Based on the review, it was found that the main challenge in performing μCT analysis of ore samples is the difficulties associated to the segmentation of mineral phases in the dataset. This challenge is adressed through the implementation of machine learning techniques using Scanning Electron Microscope (SEM) data as a reference to differentiate the mineral phases in the μCT dataset (Paper 3).

LIST OF PAPERS

The licentiate thesis is based on the following papers:

1. Guntoro, P.I., Ghorbani, Y., Rosenkranz, J., 2019. Use of X-ray Micro-computed Tomography (μCT) for 3-D Ore Characterization: A Turning Point in Process Mineralogy, in: Proceedings of the 26th International Mining Congress and Exhibition (IMCET 2019). Antalya, pp. 1044–1054.

2. Guntoro, P.I., Ghorbani, Y., Koch, P.-H., Rosenkranz, J., 2019. X-ray Microcomputed Tomography (μCT) for Mineral Characterization: A Review of Data Analysis Methods. Minerals 9, 183. `https://doi.org/10.3390/min9030183`

3. Guntoro, P.I., Tiu, G., Ghorbani, Y., Lund, C., Rosenkranz, J., 2019. Application of machine learning techniques in mineral phase segmentation for X-ray microcomputed tomography (μCT) data. Miner. Eng. 142, 105882. `https://doi.org/10.1016/j.mineng.2019.105882`

Beside these papers, some tools were also developed during this work:

1. Matlab code for uneven illumination correction of μCT images.

2. Matlab code for registration of Back-Scattered Electron (BSE) images to the corresponding μCT slice for the purpose of creating training data for machine-learning classifications.

3. As a part of the secondment work with Outotec, a new module in Outotec HSC™ Chemistry Software called Particle Tracking (PTr) has also been developed. The module is based on the algorithm developed by Lamberg and Vianna (2007) which allows user to perform mass balancing of a mineral processing circuit down to the particle liberation level.

CONTENTS

Acknowledgments

Part I

CHAPTER 1

Introduction

In this chapter, a brief introduction to the concept of geometallurgy, and how automated mineralogy fits in the framework of geometallurgy is discussed. Based on this discussion, a problem statement is formulated as a basis of this work. The problem statement is then developed into the research questions as well as the approaches and limitations to address the questions.

1.1   Geometallurgy

Geometallurgy is a multi-disciplinary approach that combines geology, mineralogy, ore properties, as well as mineral processing and metallurgy (Lund and Lamberg, 2014; Lamberg, 2011). Such approach aims to maximize economical value, reduce risk, optimize production planning, guide the managerial decision-making process, as well as keeping the project sustainable through efficient resource management (Dominy et al., 2018; Lishchuk et al., 2020). A geometallurgical program is an implementation of geometallurgy in a mining operation. The implementation is mainly done by creating a spatial model of the orebody that preditcs how each ore block behaves in the mineral processing circuit (Lund et al., 2013; Aasly and Ellefmo, 2014; Koch, 2017). By that definition, a geometallurgical program would require two components:

- Spatial model, which includes a 3D block model of the orebody that contain various geometallurgical data.

- Process model, which includes a set of mathematical equations that is able to describe the mineral processing operations. These equations would take the geometallurgical data in the spatial model as the input and predict the mineral processing

performance as the output. The performance can be described through various parameters such as recovery, grade, particle size distribution, energy consumption, and profitability.

An implementation of geometallurgical program can vary depending on the level of details, but can be roughly divided into three types (Lishchuk et al., 2015):

- Traditional approach, which is based on elemental assays obtained from analysis of drill core samples from each block in the orebody. These elemental assays are then used to predict the recovery of the mineral processing circuit using simple recovery functions.

- Proxies approach, which incorporates lab-scale tests to characterize metallurgical behaviour the ores.

- Mineralogical approach, which includes the use of quantitative mineralogical assays of the ore samples in both the spatial and process models. This approach can be further classified by the level of informations needed:

  - One-dimensional (1D), requires chemical and mineralogical composition of the ores.
  - Two-dimensional (2D), same as 1D but requires particle size classes. This allows the definition of chemical and mineralogical composition for each size class.
  - Three-dimensional (3D), same as 2D but requires liberation classes for each size class. This then add a new dimension to the data, in which composition can be defined for each size class and each liberation class.

Lamberg, 2011 has created a geometallurgical concept called "particle-based geometallurgy", in which particles are used to transfer the information from the spatial model to the process model. The particles would inherit the ore properties (mineralogy, chemical composition, size, and texture) of each ore block through the use of breakage models, and used as an input for the process models to forecast production. Then, the output of the process models in the form of performance indicators (recovery, grade, profitability, etc.) is stored back in the spatial model. The whole chain of the particle-based geometallurgy is shown in Figure 1.1.

1.2   Automated mineralogy in geometallurgy

In recent years, automated mineralogy has been widely used in the mining industries, with around two hundreds systems installed worldwide (Gu et al., 2014). Automated
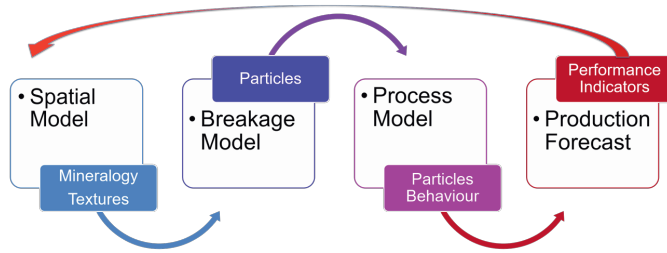
Figure 1.1: Particle based geometallurgy, after Lamberg (2011)

mineralogical tools such as Quantitative Evaluation of Minerals by Scanning Electron Microscopy (QEMSCAN) (Gottlieb et al., 2000) and Mineral Liberation Analyzer (MLA) (Fandrich et al., 2007) have been rapidly widespread in the industry. These tools are usually a complimentary tool together with the Scanning Electron Microscopy and Energy Dispersive X-ray Spectroscopy (SEM-EDS) analysis. These set of tools allow automated measurement of mineralogy and mineral liberation (Fandrich et al., 2007), particle size and shape (Leroy et al., 2011; Sutherland, 2007), as well as stationary textures (Pérez-Barnuevo et al., 2018, 2013) of ore samples.

Traditionally, the development automated mineralogy was considered a breakthrough in the field of process mineralogy in what now known as Modern Process Mineralogy (Lotter et al., 2018b). Process mineralogy itself is a discipline that is closely related to geometallurgy, as it is described as the practical study of mineral characteristics and properties with relation to their beneficiation process (Lotter et al., 2018b; Henley, 1983). The thinking behind process mineralogy is simple: mineral characteristics are thought to be critical in relation to the mineral processing performances, therefore, the evaluation of mineral processing shall not only consider process parameters but also the mineralogy and ore characteristics. In essence, it basically aims to push mineralogical knowledge to mineral processing operations, therefore breaking the separation between mineralogy and mineral processing (Dominy et al., 2018). Many case studies (Lotter, 2011; Gu et al., 2014; Lotter et al., 2018b) have demonstrated the value of ore mineralogical and textural information for optimization of process performances such as flotation (Alves dos Santos and Galery, 2018; Alves dos Santos, 2018; Tungpalan et al., 2015), comminution (Little et al., 2017, 2016; Tøgersen et al., 2018; Jardine et al., 2018), and leaching (Ghorbani et al., 2011; Fagan-Endres et al., 2017).

In relation to geometallurgy, process mineralogy can be considered as a part of geometallurgy in Figure 1.1 by serving as a connection between mineralogy and texture to particles behaviour. Similar to geomatallurgy, process mineralogy also pushes the developments to move away from the traditional qualitative description of mineralogy and texture to quantitative numbers that can be used in process models to predict the ore behaviour in

the beneficiation process (Yildirim et al., 2014; Jardine et al., 2018; Donskoi et al., 2016; Whiteman et al., 2016).

However, in contrast to geometallurgy, process mineralogy does not consider spatial models and orebody variability, therefore only considering the mineralogy and mineral processing part while ignoring the geology part. Additionally, geometallurgy goes beyond process mineralogy; it evaluates the whole mining value chain which then also includes mining and environmental management (Lishchuk et al., 2020). In fact, Lishchuk et al. (2020) further argued that the notion of geometallurgy as a "bridge" between geology and mineral processing is often confused with process mineralogy. Both Dominy et al. (2018) and Lishchuk et al. (2020) highlighted that the orebody variability (spatial or block models) and the subsequent prediction of variations in the process responses, is the main feature of geometallurgy. The management of orebody variability and its effect on a mining project as a whole would ultimately help in production planning in order to reduce risk and maximize profit; which is the main reason why geometallurgy is invented.

With that being said, it is logical that process mineralogy is also an important link in geometallurgy. Therefore the automated mineralogy's role in geometallurgy is also important. In Figure 1.1, automated mineralogy comes to play in the first step, in which it is used to acquire mineralogical and texture information of the orebody to be transferred to the breakage model. This transfer of information relies heavily on accurate and representative sampling techniques; something which has been considered as well in process mineralogy (Lotter et al., 2018a).

In Figure 1.1, it is shown that the mineralogical and textural information are used in the breakage model to generate the particles, in which the particles is then fed to process models. However, a more experimental based approach can also be used, namely by performing experimental breakage (comminution) on the samples from the ore blocks to generate the particles, as illustrated in Figure 1.2. Such experimental approach can be considered as the midway between proxy-based geometallurgy (Lishchuk et al., 2015) and particle-based geometallurgy. In this approach, the particles are generated directly from comminution tests and analyzed using automated mineralogy to get their mineralogical and textural information. This information is used in process simulation to obtain the particles behavior information. Similar to Figure 1.1, the particles behavior information can be used for production forecasting and inputted back to the spatial model (Lamberg, 2011).

Upon examination of both Figure 1.1 and Figure 1.2, several differences become clear:

- The particle based approach requires a representative mineralogy and texture measurement of the ore blocks from the spatial model. In experimental particle based approach, the focus is shifted to the particle; an accurate representation of the particles is required. This means shifting the role of automated mineralogy from the analysis of ore blocks (often sampled in the form of drill cores) to the analysis of
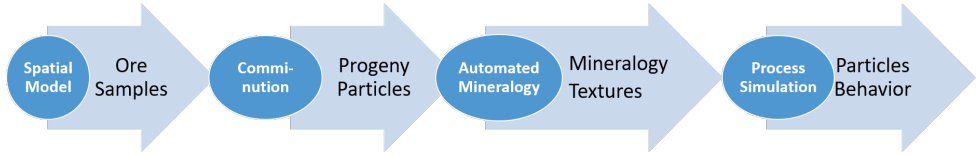
Figure 1.2: Experimental particle based geometallurgy

comminution products (particles). In any case, both approaches require proper and accurate sampling as the ore characteristics are determined by the sample analyzed / tested.

- The particle based approach relies on an accurate breakage model that can forecast liberation distribution of the progeny particles based on mineralogy and texture information of the ore block. In experimental particle based approach, the breakage model is replaced with actual comminution tests to generate the particles. The focus of the comminution tests should be on the generation of the particles instead of measuring rock properties such as grindability. This means shifting the challenge from selecting the suitable breakage model to selecting the suitable comminution test method.

Nevertheless, an accurate breakage model would often require calibration and validation with experimental comminution tests. Conversely, with the analysis of progeny particles from the comminution tests, a breakage model for that ore type can be constructed. Therefore the experimental particle based approach shown in Figure 1.2 should rather be seen as a compliment instead of substitute to the particle based geometallurgy in Figure 1.1.

1.3 The problem of stereology

While automated mineralogy offer a rapid and automated data acquisition and processing of ore samples, it possesses an obvious weakness due to loss of dimensionality. Particles are three-dimensional (3D) objects, while current automated mineralogical tools only produce a two-dimensional (2D) cross section analysis of the ore samples. This loss of dimensionality can lead to overestimation of the mineral liberation, as the cross section of the sample might not represent the actual state of the particles (Lätti and Adair, 2001). This phenomenon is known as stereological error / bias, and illustrated in Figure 1.3.
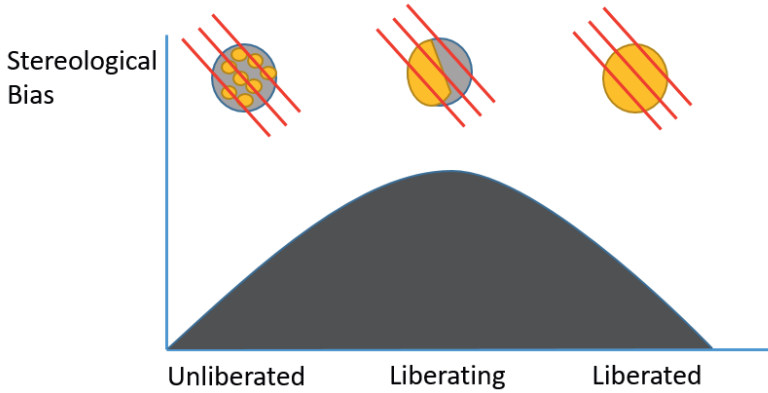
Figure 1.3: The effect of stereological bias on different particles with varying degree of liberation (Spencer and Sutherland, 2000). The possible cross sections analyzed are indicated by the red lines crossing the particles

In order to address this issue, many studies (Ueda et al., 2018a,b, 2017; Lätti and Adair, 2001; Fandrichi et al., 1998; Miller and Lin, 1988; Spencer and Sutherland, 2000; Gay and Morrison, 2006; King and Schneider, 1998) have been devoted to make use the 2D liberation data more accurately, i.e. to estimate the actual 3D liberation data based on the obtained cross-sectional 2D liberation. This estimation is often called stereological correction. However, these correction methods are barely applied in practice and their applicability to various types of particles have not yet been studied extensively(Ueda et al., 2018b). This is quite understandable as it can be seen in 1.3, stereological bias is highly dependent on the internal structure of the minerals in the particles. The bias is large when the particles contain large mineral grains (the middle particle in Figure 1.3) while on the other hand the bias is small when the particle contain small dispersed grains (the left particle in Figure 1.3). Nevertheless, as Figure 1.3 would suggest, the quantification of stereological bias in the Y-axis is merely conceptual. It is unclear what parameters should be taken into account in estimating and quantifying the sterological bias (Ueda et al., 2018a).

It is also worth mentioning that in 2D liberation analysis, a certain number of particles must be analyzed for statistically sound liberation measurement (Mwanga et al., 2014). This is largely due to the stereological effect; by having multiple cross sections of the particle, the stereological bias could be minimized, and therefore more statistically reliable result can be obtained. Ueda et al. (2016) have discussed the issue about statistical variability of the liberation measurement as a function of the number of particles, in which they proposed a model to determine the minimum amount of particles needed to obtain statistically reliable liberation analysis both in 2D and 3D (through stereological correction). This model was then validated through a number of numerical simulations,

in which it aims so that the liberation measurement satisfies the designated confidence level (Ueda et al., 2018c, 2016).

1.4 X-ray microcomputed tomography - a 3D mineral analysis tool

The inherent stereological bias within the 2D automated mineralogical tools paved the way for the more sophisticated instruments that are capable of acquiring 3D data from ore samples. Over the last decades, the development of X-ray microcomputed tomography (μCT) in geosciences have received wide attentions. The main advantage of μCT lies on its ability to non-destructively analyze the 3D interior of an object. Many studies have been done to evaluate the potential applicability of μCT system in mineral processing and ore characterization (Miller et al., 1990; Kyle and Ketcham, 2015; Lin and Miller, 1996) as well as geoscience in general (Cnudde and Boone, 2013; Mees et al., 2003).

The μCT system has been demonstrated to be capable of extracting ore properties in 3D, including porosity (Lin and Miller, 2005; Peng et al., 2011; Yang et al., 2017; Zandomeneghi et al., 2010), mineralogy and mineral liberation (Ghorbani et al., 2011; Lin and Miller, 1996; Reyes et al., 2017, 2018; Tiu, 2017), size and shape (Wightman et al., 2015; Lin and Miller, 2005), and to some extent stationary textures (Jardine et al., 2018). Additionally, the μCT system also offers new information that would not have been available using traditional 2D analysis, such as information about depth and mineral surface exposure (Miller et al., 2003; Reyes et al., 2018; Wang et al., 2017). This new depth of information has been demonstrated to be useful for evaluating process that are dependent on surface properties such as leaching (Fagan-Endres et al., 2017; Lin et al., 2016a) and flotation (Miller and Lin, 2016, 2018; Reyes et al., 2019). Furthermore the development of μCT systems have also contributed for evaluating statistical reliability of liberation measurement and stereological correction models; Ueda (2019) have recently performed experimental validation of their model (Ueda et al., 2016) with the use of 3D liberation analysis using μCT systems.

However, the implementation of μCT system as an automated mineralogical tool is not without challenge. While the μCT system's effectiveness in measuring structural properties such as size, shape, and porosity has been well demonstrated, its effectiveness in differentiating mineral phases in the sample is lagging behind due to lack of contrasts between mineral phases (similar attenuations between some minerals), limited resolution, and lack of automated mineralogical analysis software. These challenges have been addressed by several researchers through optimization of scanning parameters (Reyes et al., 2017; Kyle et al., 2008; Bam et al., 2019), calibration with pure minerals (Ghorbani et al., 2011), and using another 2D automated mineralogy data as a reference (Reyes et al., 2017).

1.5   Problem statement and scope of work

Geometallurgy relies on accurate mineralogical and textural information of the ore blocks in which such information are then used as a basis for the predictive modelling and production forecasting. These information are currently obtained through 2D automated mineralogy system, which entails dimensionality loss and stereological error. μCT offers a non-destructive 3D analysis of ore samples, but challenges and hurdles prevail in the process of establishing μCT system as an alternative automated mineralogy tool. These challenges and hurdles in using μCT system for ore characterization are the main issue that this work tries to tackle.

This work aims to evaluate and explore the current state and potentials of μCT application as an automated mineralogical tool in the context of geometallurgy. The main hypothesis that serves as the backbone of this work is that there exist significant differences between the 3D and 2D ore properties, which then necessitates the use of μCT for ore characterization. In particular, this work addresses the following questions:

1. How can ore properties such as mineralogy and texture be extracted accurately using μCT systems?
   This question can be broken down into two parts of the ore properties: mineralogy and texture. By defining what constitutes a "texture", the latter part could be broken down further. In this study, texture is defined as three categories, namely structural textures, stationary textures, and surface textures. Structural texture refer to grain and particles morphology (size, shape, orientation), while stationary textures refer to the spatial relationship between the grains in the ore (Lobos et al., 2016). Surface texture, which is unique to 3D, is defined as the topology (surface properties) such as roughness, roundness, and mineral exposure.

2. How to use the extracted (3D) ore properties from the μCT data in a geometallurgical program? This question is focused more to the utilization of 3D ore properties in the context of particle-based geometallurgy (Figure 1.1).

In order to address these questions, the following approaches are used. These approaches are illustrated further in Figure 1.4.

- Literature review. The possible μCT data processing methods for extracting mineralogy and texture of ore samples are systematically reviewed in Chapter 2 (Paper 1 and Paper 2). The review focuses more on current methods and examples applied on ore samples as well as the implications for mineral processing. Other methods applied for other type of samples such as rocks and aggregates are briefly discussed. The review also serves to establish a step-by-step working pipeline in processing μCT data, in which various alternatives of data analysis methods are presented for

each step. In the end of the chapter, a library of applicable data analysis methods for different purposes of ore characterization is presented.

- Method development. After systematically reviewing the current state of μCT data analysis methods for ore characterization, the gaps for future developments are then identified. Chapter 3 (Paper 3) then addresses exactly this; a new data analysis method for 3D μCT data is developed. The performance of this method is benchmarked against traditional automated mineralogical techniques.

- Process modelling and simulation. In order to address the second research question, the data extracted using potential techniques reviewed and developed in Chapter 2 and 3 respectively would be used in a process simulation. Similarly, the result of the simulation can be benchmarked against the the same simulation but using 2D mineralogy and texture data. This approach however is not yet discussed in this licentiate thesis, but it is included in the whole framework of the PhD thesis.
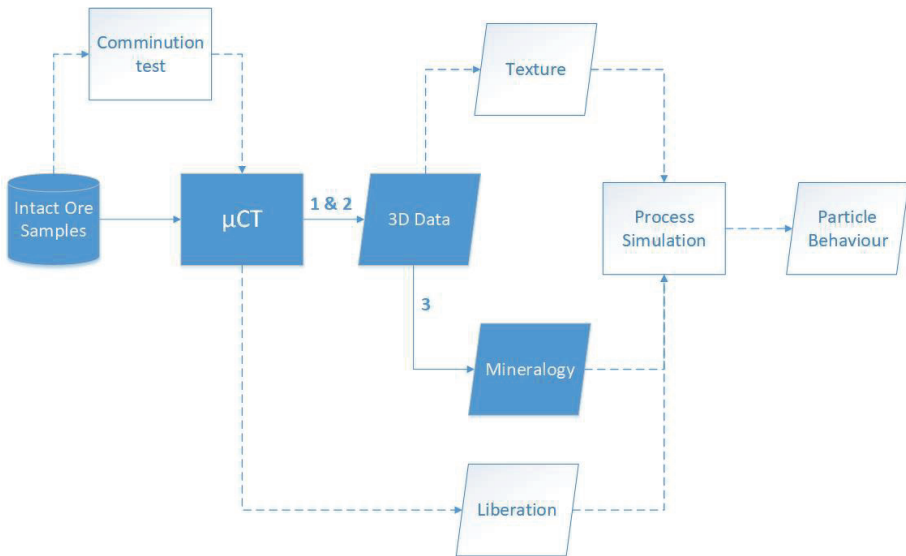
Figure 1.4: General workflow of this thesis. Solid lines and blue boxes refer to the work done in the licentiate, while dashed line and white boxes are planned in the scope of the whole PhD work. §The numbers denote the papers published as a result of this work.

The author is aware that the possibility of using μCT in the context of geometallurgy is potentially huge. Therefore there is a need to define the limit of the work, which is illustrated in Figure 1.5. The term "ore properties" in this context is limited to the mineralogy and texture properties of the ores, as explained earlier in the first research

question. The relevance of these ore properties to the processing behaviour is established through the literature review and benchmark studies. Regarding the tool (µCT), more focus would be placed on the use of conventional laboratory-µCT systems, as they are more prevalent compared to synchrotron systems.
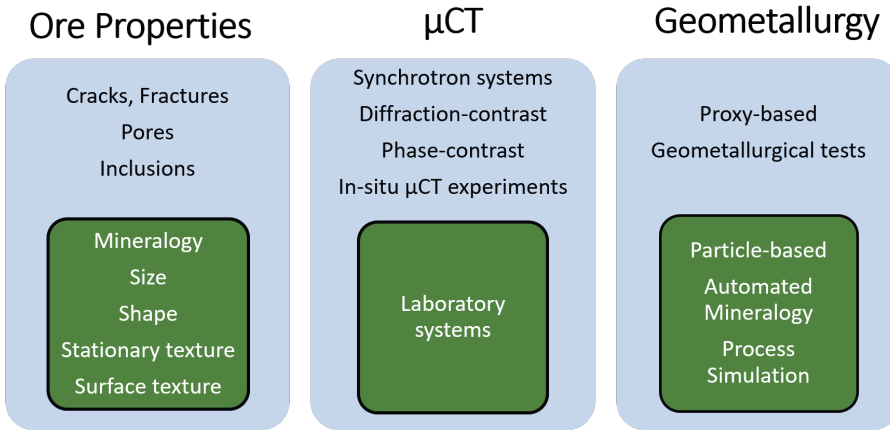
Figure 1.5: The limitation and scope of this work, divided into three main components of the work, which are the material (ore), the method (µCT), and the application (geometallurgy). The main focus of the work are the ones inside the green squares

In terms of the relationship with geometallurgy, the work is limited in applying the tool (µCT) as an automated mineralogy system in the context of geometallurgy shown in Figure 1.2. The working pipeline from (2D) automated mineralogy data to the particle-based process simulation has been established by Lamberg and Vianna (2007), and has been evaluated in the modelling of wet low intensity magnetic separation (WLIMS) operations by Parian et al. (2016). This work would simply test the established working pipeline but using 3D µCT data as an input.

Other potentials of applying µCT systems in geometallurgy may include the use of in-situ experiments such as breakage (Alikarami et al., 2015) and leaching (Dobson et al., 2017) which is potentially useful for the proxy-based geometallurgy. In-situ breakage experiments could give some information on how crack and fracture propagates in the ore, which in turn could be very valuable in establishing a breakage model in the context of particle-based geometallurgy (Figure 1.1). The possibility of using more powerful synchrotron CT systems that enable phase-contrast tomography (PCT) and diffraction-contrast tomography (DCT) is also of an interest as it may increase the capability of µCT systems in differentiating phases in the samples. While these potentials are out of scope of this work, they will be succinctly discussed.

CHAPTER 2

Mineral characterization with μCT

In this chapter, the current state and potential applications of μCT systems for mineral characterization are discussed. The term "mineral characterization" is defined more as extraction of mineralogical and textural information from an ore sample, whether it be particulate or intact (drill core) samples.

2.1 Principles of μCT analysis

A configuration of μCT system is shown in Figure 2.1. During acquisition, the sample is exposed to the incident X-ray beam and rotated through 180° to obtain a number of projections (typically between 600 - 3600 projections). These projections are then reconstructed to create 2D slices (projection images) of the measured volume. The pixels in the 2D slices retain spatial information regarding the originating volume elements (voxels), so that the slices could be stacked and rendered to visualize the 3D volume of the sample. These 2D slices are usually considered the "raw data" in which it is subjected to various image processing procedures aiming to obtain information about the sample.

The principle of μCT measurement is that it records the differences in X-ray attenuation of the object. Attenuation is described as the proportion of the X-ray that interacts with the material and represented by the gray intensities in the reconstructed slice images. The interaction between material and the X-ray beam decrease the intensity of the X-ray as it passes through the object. This decrease of intensity can be described by Lambert-Beer law (Equation 2.1), in which $I(x)$ is the intensity measured at the detector (units: mas time^{-3}), I^0 is the intensity of the original incident beam from the X-ray source, x is the length of X-ray path within the material, and μ is the attenuation coefficient of the
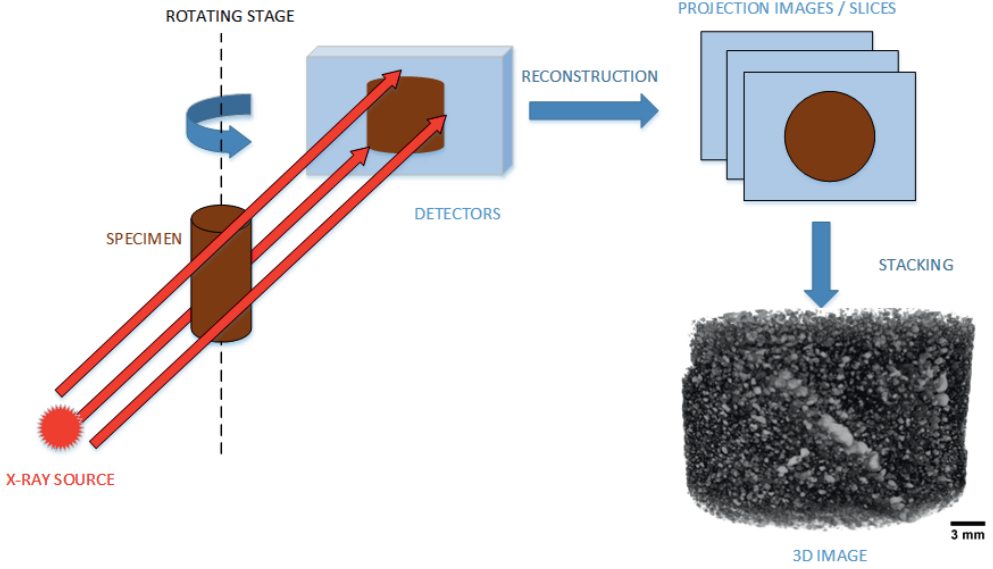
Figure 2.1: Measurement and data acquisition using μCT. The X-ray source originates form a small focal spot and illuminates a planar detector. This configuration resembles the most widely used modern laboratory cone beam scanning configuration

material (units: length^{-1}), which depends on the material atomic number and density.

$$I(x) = I^0 e^{-\mu x} \tag{2.1}$$

Due to stage rotation, the beam angle (α) is varied, which in turn affects the attenuation coefficient. Deriving from Equation 2.1, the correlation between beam angle and the attenuation coefficient for a given length of X-ray path (L) is given in Equation 2.2.

$$\ln(\frac{I(L,x)}{I^0(\alpha)}) = -\int_0^L \mu(x,\alpha)dx \tag{2.2}$$

The attenuation coefficient is then related to the theoretical coefficient values for different ore minerals (μ_c). These theoretical values can be calculated as a function of the X-ray energy (ϵ, units: mass length^2 time^{-2}), and mineral density (ρ, units: mass length^{-3}). Such calculation is given in Equation 2.3, in which μ_{mass} refers to the mass attenuation coefficient that depends on the X-ray energy used in the measurement. The dependency of μ_{mass} on energy can be described in Equation 2.4, in which a and b are the energy-dependent coefficients, and Z is the bulk atomic number of the material.

$$\mu_c(\epsilon) = \rho\mu_{mass}(\epsilon) \tag{2.3}$$

$$\mu_{mass} = a + b\frac{Z^{3.8}}{\epsilon^{3.2}} \tag{2.4}$$

Depending on the energy spectrum, different attenuation mechanism prevails. In the lower energy spectra (50-100 keV), photoelectric absorption predominates, in which the incoming X-ray photon ejects the inner electron by occupying the inner shell of the atom. This imbalance causes the electron from the outer shell to jump to the inner shell. The resulting attenuation coefficient (μ) based on this mechanism is proportional to Z^{4-5}. In the higher energy range (up to 5-10 MeV), Compton scattering is more prevalent, in which the incoming photon only interacts with outer electron and deflects it to a different direction. With this mechanism, the attenuation coefficient (μ) will be proportional to Z. The relation between Z and μ would suggest that in Compton scattering, the attenuation coefficient is less dependent on the material atomic number as opposed to that in photoelectric absorption. Instead, in Compton scattering, the attenuation would be more affected by the material density (atomic number per unit mass). Both photoelectric absorption and Compton scattering are shown in Figure 2.2.
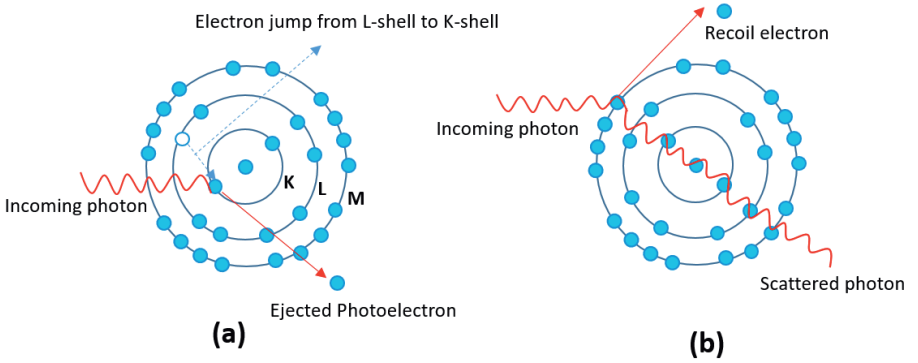
Figure 2.2: Interaction of X-ray photons to the subjected atom, showing (a) photoelectric absorption, and (b) Compton scattering

Keeping these different mechanisms in mind, observe also that in laboratory µCT systems, the X-ray beam generated by the source is polychromatic. This means that the beam consists of a spectrum of different energies as opposed to single energy (monochromatic) beams used in synchrotron µCT. Polychromatic beam is subject to a commonly

known phenomena called beam hardening. This phenomena happens due to the preferential absorption of lower energy beams, leaving behind the higher energy beams, hence the name "beam hardening" (Cantatore and Müller, 2011). The longer the X-ray beam travels through the object, the more lower energy beams are absorbed, increasing the beam energy penetrative capability while decreasing its attenuation. If this is not corrected, the grayscale values of the reconstructed image of an uniform object would appear more attenuated near the edges (Bam et al., 2016). The reconstructed image now possess artifacts, i.e. the property in the image that does not reflect the physical feature of the sample (Cantatore and Müller, 2011).

In order to address the beam hardening effect, several measures can be taken: (a) External (pre-hardening) filters; (b) Reducing sample size; (c) correction during image reconstruction. External filters are usually made from materials such as aluminum, copper, or brass (Cantatore and Müller, 2011), which aim to pre-absorb the lower energy spectra, or in other words "filter out" the the lower energy beams (hence the name "pre-hardening"). Using smaller sample size has also been shown to minimize the beam hardening effect, as the longer the X-ray path, the more pronounced the beam hardening effect is. Lastly, correction can also be done during the reconstruction process, typically by correcting the attenuation coefficient so that it is linearly varied depending on sample thickness. Other correction methods also exist and discussed elsewhere (Ketcham and Hanna, 2014; Bam et al., 2019).

2.1.1   Limitations for mineral characterization

Understanding the attenuation mechanisms and their relation to the attenuation coefficient is the key in understanding how can μCT be used to differentiate minerals in the sample. Higher energy means better penetrative capability of the beam, producing better signal-to-noise ratio. However, the attenuation differences become less, which make mineral segmentation more difficult. Using lower energy will alleviate this issue, but then it reduces the penetrative capability of the X-ray which makes exposure time longer to achieve a good signal-to-noise ratio. This trade-off can be explained due to the fact that in lower energy spectra, the attenuation is highly dependent on the atomic number (μ is proportional to Z^{3-4}) so that differences in atomic number is exemplified in the attenuation coefficient. On the other hand in the high energy spectra, the attenuation is less dependent on atomic number (proportional to Z), and more dependent by density of the material. This create a rather challenging situation for mineral segmentation, as many minerals have similar densities. This dependency of attenuation coefficient of different minerals to the X-ray energy is available some database such as XCOM by National Institute of Science and Technology (NIST) (Berger, 2010).

The issue of finding an "optimum" X-ray energy where sufficient contrast between the minerals can be achieved in a reasonable amount of acquisition time has been investigated by several researchers. Reyes et al. (2017) have found that copper sulphide minerals were

able to be distinguished from at 50 kV X-ray energy. The differentiation was also made possible by using SEM-EDS data as reference. Nevertheless, the differentiation between different copper sulphide minerals (e.g. chalcopyrite, bornite) was not possible at that energy level. Reducing sample size is also one of the measure that can be taken to reduce long exposure time (Kyle and Ketcham, 2015; Bam et al., 2019). Kyle et al. (2008) has demonstrated that differentiation between chalcopyrite and bornite at 180 keV is possible using cores with diameter less than 22 mm.

Other measure that can be taken to help differentiating between minerals is by calibrating the µCT with pure minerals of known density so that the correlation of attenuation coefficient with material density can be obtained. Alternatively, dual-energy scanning (scanning at two different energy levels) can be performed so that the density of the material could be obtained directly by correlating the attenuation coefficients in the two energy levels (Ghorbani et al., 2011; Van Geet et al., 2000). However, dual-energy scanning has been reported to be sensitive to noise (Van Geet et al., 2005).

The ability of µCT to distinguish minerals is also limited by the spatial resolution. Spatial resolution defines how the volume is discretized, i.e. the volume over which Equation 2.2 is integrated. This then means that objects smaller than the spatial resolution could not be detected. A typical µCT scanner has spatial resolution ranging from 10 - 50 µm (Ducheyne et al., 2017). Some newer µCT systems can go below 1 µm (sub-µCT) or even at nano scale (nano-CT) (Kastner et al., 2010). Similarly, spatial resolution is also connected with the acquisition time; longer acquisition time is required when using high spatial resolution as higher number of projections is required.

It is also worth noting that some of the problems associated with mineral differentiation with µCT system can be alleviated by the use of monochromatic (synchrotron) X-ray sources instead of polychromatic sources that are commonly employed in lab-µCT systems. The use of synchrotron sources allows the use of diffraction-contrast tomography (DCT) and phase-contrast tomography (PCT). These contrast modes are useful when differentiating minerals, as it allows high contrast between different phases and crystals (Sun et al., 2018; Kikuchi et al., 2017; Toda et al., 2017; Herbig et al., 2011). Synchrotron systems also allow the use of complimentary tomography methods such as X-ray diffraction tomography (XRD-CT) and X-ray fluorescence tomography (XRF-CT). XRD-CT has found applications mostly for crystalline materials (Artioli et al., 2010; Takahashi and Sugiyama, 2019), while XRF-CT is mostly used for evaluation of inclusions in geological samples (Laforce et al., 2017; Suuronen and Sayab, 2018). Nevertheless, these synchrotron sources are less widely available than conventional laboratory µCT systems mainly due to high operating costs (Cnudde and Boone, 2013). The current technology of laboratory µCT systems has not met the level of synchrotron sources yet (Bam et al., 2019), but recent developments have extended their capabilities further. For example, some works have shown that phase- and diffraction-contrast tomography are possible for laboratory µCT systems (King et al., 2014; Olivo and Castelli, 2014; Viermetz et al., 2018).

2.2   Processing of μCT data

In principle, the processing techniques applied for μCT data would be based on various digital image processing techniques. Although many conventional image processing techniques that are commonly applied on 2D images can be extended to 3D images, adjustment is often needed to reduce the computational cost. Currently, there are several available softwares (both commercial and open-source) that are able to process and visualize (render) 3D images such as Avizo (`http://www.vsg3d.com/`), Fiji/ImageJ (Schindelin et al., 2012), Dragonfly (`https://www.theobjects.com/dragonfly/`), Dristhi (Limaye, 2012), Morpho+ / Octopus (Vlassenbroeck et al., 2007; Brabant et al., 2011), and many more.

A typical workflow of processing μCT data for mineral characterization is given in Figure 2.3. The 2D μCT data slices are stacked into a 3D image. This 3D image is then pre-processed prior to segmentation. Segmentation and classification of the phases in the data are then performed to get the volume of interests (VOI), which usually represents different mineral phases in the sample. The features from that VOI are then extracted. Volume rendering here is done to produce a 3D view on a 2D display screen.

2.2.1   Pre-processing

Pre-processing step is required before segmentation to clear out noises and artifacts in the data. Artifacts are part of the μCT slices that were not found in the original sample. Artifacts could originate from the physical interaction between the materials and the X-ray beam, or from the detectors. Pre-processing step could also be necessary to prepare the data for the subsequent segmentation, for example by enhancing contrasts between the pixels.

Filter is one of the most common pre-processing technique that is used in image processing. Filters are a set of mathematical equation that is implemented in a pixel and its neighbors. The simplest filter is a kernel (matrix) containing a set of values to be convoluted with the image. Depending on the kernel values, various tasks can be performed on the image, which include:

1. Denoising and blurring. This filter mainly aims to clear out noises in the image by smoothing (averaging) the pixels. The drawback of such filter is it blurs the details in the image, such as phase boundaries that are critical for the segmentation process. Example of such filters are Gaussian and mean filters.

2. Edge-preserving filters. Similar to the denoising and blurring filters, it aims to clear out noises in the image, but by also preserving the edges (phase boundaries). Example of these filters are median, non-local mean, and bilateral filters. Variation
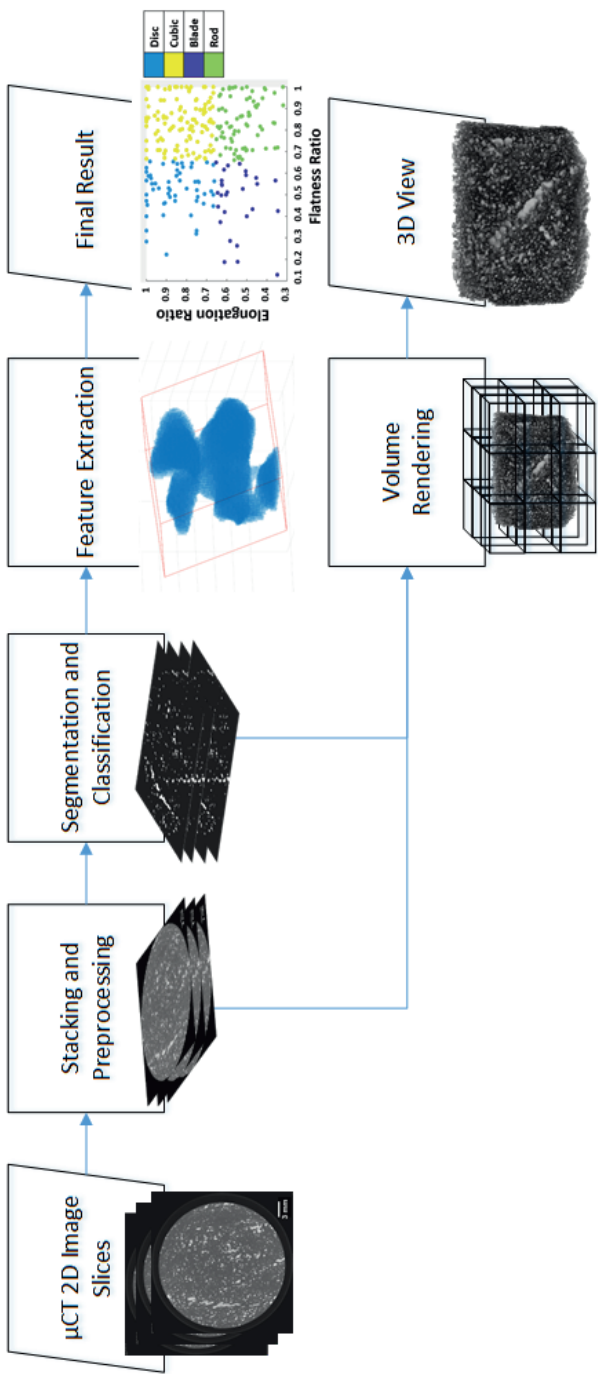
Figure 2.3: Typical data processing workflow involved in mineral characterization with µCT system. Here sulphide grains in the sample are segmented and their shape information extracted

of these filters have been applied in several cases of μCT rock analysis (Müter et al., 2012; Brabant et al., 2011)

3. Sharpening and edge detecting filters. These filters increase the contrast between phase boundary, hence the name "edge detecting". These filters are especially useful in detecting crack and pores in rock samples (Peng et al., 2011; Chun and Xiaoyue, 2009) as well as phase boundary enhancement for segmentation (Schlüter et al., 2014). Example of these filters include Laplacian, Sobel (Sobel, 2014), Canny (Canny, 1986), and Prewitt (Prewitt, 1970) filters.

2.2.2 Mineral Segmentation

Segmentation of μCT data refers to the identification and isolation of voxels that have the same features into a single category (Martínez-Martínez et al., 2007). In most cases the feature that is evaluated is then the voxels' grayscale, which corresponds to the attenuation coefficient (and therefore the material's density and atomic number). In the case of μCT mineral characterization, segmentation mostly refers to the classification of the voxels to different mineral phases in the data. The amount of voxels in each mineral phase corresponds to the proportion of each mineral phase in the sample. Therefore, segmentation is useful to deduce mineralogical composition of the ores, which can also provide some information about the liberation of particulate samples.

Several methods have gain popularity in terms of mineral segmentation for μCT ore characterization. The relevant methods are discussed in this subsection.

2.2.2.1 Thresholding

Tresholding introduces a threshold / limit value on an image, thereby segmenting the voxels with grayscale value lower than the threshold. There are basically two major types of thresholding algorithms:

- Global thresholding. The threshold value is determined from all the grayscale values in the image.

- Local thresholding. The threshold value is determined "locally", i.e. only considering a certain part of the image instead of the whole image.

In general the main problem that many different algorithms try to address is that the determination of optimum threshold value.

One of most popular thresholding algorithm is the Otsu thresholding (Otsu, 1979). Otsu thresholding is widely used in the context of μCT ore characterization, especially in the
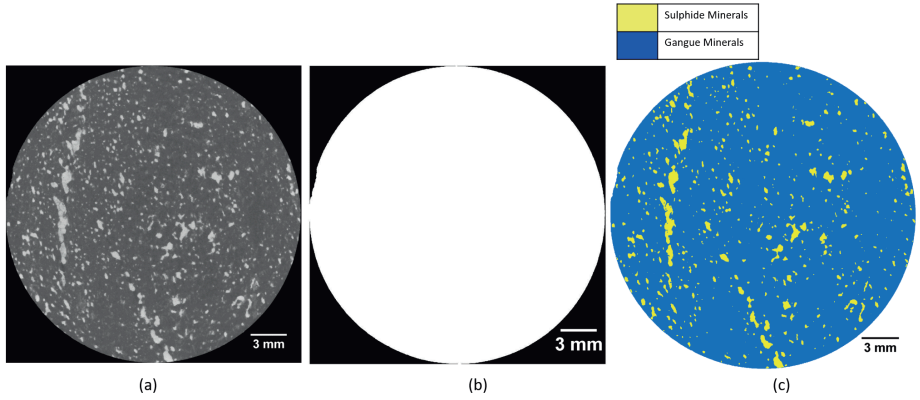
*Figure 2.4: Otsu thresholding for segmentation, showing: (**a**) original slice of drill core stack from* µCT*; (**b**) global thresholding with Otsu; and (**c**) multi-level thresholding with Otsu. It can be seen that directly using global thresholding will only segment the drill core from the background; multi-level thresholding is needed to extract the mineral grains from the drill core*

initial segmentation between the air/pores and the rock matrix (Yang et al., 2017; Reyes et al., 2017; Andrä et al., 2013; Lin et al., 2016a, 2015). While Otsu thresholding is generally effective in such cases, it may not work perfectly when the sample is heterogenous and the VOI (Volume of Interest) is large. If the VOI is large, it should be sub-sampled to produce smaller VOIs, in which the threshold value is determined from these smaller VOIs (Yang et al., 2017). Such approach can be then classified as local thresholding, as the threshold value is determined locally in the smaller VOIs. Furthermore, Otsu thresholding may not work properly in cases where boundaries between high and low grayscale value voxels exist. This is due to boundaries would potentially not be properly segmented due to partial volume effect (Wang et al., 2015).

Otsu thresholding could also be extended to obtain multiple threshold values so that more than two phases can be segmented, as illustrated in Figure 2.4.

Another commonly used thresholding algorithm is the maximum entropy algorithm (Kapur et al., 1985). Such algorithm has found applications in segmenting between the mineral grains and the gangue matrix (Lin et al., 2015, 2016a). In studies by Lin et al. (2015), Otsu algorithm was used for the initial segmentation between the ore particles and the air, while maximum entropy algorithm was used to identify the metal sulphide grains within the mineral matrix. The reasoning behind this was that the occurrences of metal sulphide in the matrix is minimum, so that the sulphide peaks could not be clearly identified in the histogram.

Local thresholding is considered as a refinement of the global thresholding based on local spatial information (Iassonov et al., 2009). Such thresholding technique is used for

example in distinguhing between pores and cracks in rocks in a μCT data (Deng et al., 2016). In general this thresholding technique is useful for small features like cracks, pores, fluid inclusions, and small grains. Other algorithm that can be used to segment small inclusions in a grain is gradient-based segmentation (Godel, 2013). In such algorithm a gradient line is placed in the grain, and the gradient of the grayscale value intercepted by the line is computed. The threshold value is obtained in the points where the gradients are high, indicating phase boundaries. Such technique while effective for small features such as inclusions, it require user manually determine the locations of the lines to get the intercepts.

2.2.2.2   Watershed segmentation

Watershed segmentation is another popular segmentation technique useful for mineral segmentation. Watershed itself refers to a ridge that divide areas drained by different river systems; it separate different catchment basins. As the name suggest, watershed segmentation treats the image as a topographic surface, in which the depth / height of the catchment basin is defined as the grayscale values of the image. Then, each catchment basin is considered as a distinct object in an image. In case of mineral segmentation, each catchment basin can be considered as an individual grain or particle in the sample.

Intuitively, a problem remains when using watershed segmentation which is how to exactly determine that a catchment basin corresponds to an individual grain/particle. It can be that one catchment basin represents multiple grains (under-segmentation), or vice versa, two catchment basins represent one single grain (over-segmentation). Avoiding this problem requires some modifications in the watershed algorithm. One example of such modification is by introducing markers to the grains. These markers can be based on the depth of the basin, i.e. by defining that basins that have depth less than a certain value (shallow basins) would not be treated as a unique basin. In the image, this is done by eliminating areas which gradients are less than the limiting value. Marker-controlled segmentation is illustrated in Figure 2.5

Several researchers have applied marker-controlled watershed segmentation for segmenting different phases in the μCT image (Wang et al., 2015; Lin et al., 2010; Lin and Miller, 2010). Wang et al. (2015) found that watershed segmentation works best for mineral particles greater than the scale parameter of 30. Scale parameter is defined as the ratio of between particle size and voxel size. In Wang's case, the watershed segmentation is modified by introducing markers to the grains, so that each marked grain is preserved.

Additionally, by filtering out basins that are less than a certain depth, it is assumed that the grain size in the ore is not extremely heterogeneous. If the grain size is highly varied, it would be difficult to obtain a threshold value that would balance the two sides: removing unwanted basins while retaining the basins of interest (Kong and Fonseca, 2017). In this case, alternative ways of introducing markers do exist. For example, by taking the topography of the basin, and the threshold value is set as a fraction of the zone
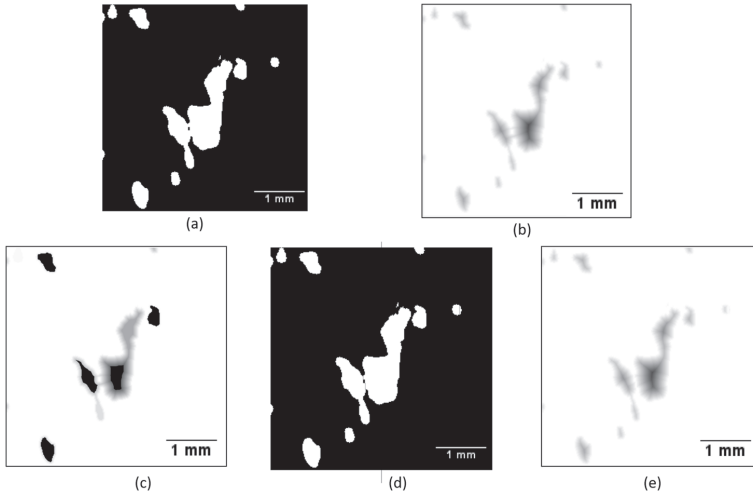
*Figure 2.5: Marker-controlled watershed segmentation for separating touching grains, showing: (**a**) binary image showing touching grains; (**b**) distance transformation of (**a**), indicating that the two grains are connected; (**c**) markers are introduced to define which objects shall constitute as the basins; (**d**) watershed of (**c**), showing a thin ridge is now formed between two grains; and (**e**) the distance transform of (**d**) showing the grains are now separated*

around the basin (Shi and Yan, 2015). The zone corresponding to the fraction is then flattened down, so that the flattened zone would be considered as part of adjacent basin, therefore merging both basins. Again, Kong and Fonseca (2017) have demonstrated that while such algorithm is less affected by highly varied grain size, it does affected by varying grain shape , which is representative of the basin's topography. Kong and Fonseca (2017) offered an iterative technique that perform watershed segmentation in each basin zone to identify potential new basins within the zone. Such methods have been demonstrated to be effective in segmenting grains with varying shape and size.

2.2.2.3 Unsupervised classification

Classification in terms of image processing is considered as clustering the pixels into several clusters based on their similarity (Baklanova and Baklanov, 2016). Usually, pixels with similar grayscale values are grouped together. Unsupervised classification then means the algorithm decides for itself the optimum classification (which pixel shall belong to which cluster). This can be done for example by minimizing the variance within the cluster or maximizing the variance between different clusters.

K-means classification is one the most popular unsupervised classification technique. As the name suggest, it classify the pixels in the image into K numbers of clusters (Duran

and Odell, 2013). The user initiates the algorithm by setting the number of clusters (K) as well as the initial guess of the cluster centroids (c_k). Then the squared euclidean distance between the pixel to the each cluster centroid is calculated as in Equation 2.5. $d_{k-means}$ refers to the distance and $p_{x,y}$ refers to the pixel in xy coordinate. This can be extended to 3D dimension or xyz coordinate. Each pixel is classified to clusters that corresponds to the shortest distance. After all pixels are classified to the clusters, new cluster centroid is calculated by averaging the grayscale values of all pixels in the cluster. This process is reiterated until the cluster centroids are stable around a certain value.

$$d_{k-means} = \|p_{x,y} - c_k\|^2 \tag{2.5}$$

The initial selection of the centroids could be done arbitrarily, or by using available algorithms such as one developed by Arthur and Vassilvitskii (2007). The centroids are selected using a weighted probability distribution, in which the probability is proportional to the distance between the newly selected centroids and previously selected centroids. This means that the algorithm by Arthur and Vassilvitskii (2007) tries to avoid selection of two similar centroids. Example of mineral segmentation using K-means algorithm is shown in Figure 2.6
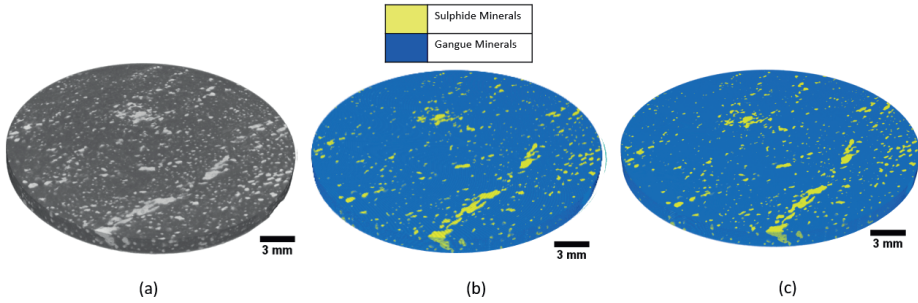
*Figure 2.6: (**a**) Drill core volume acquired from μCT; (**b**) multilevel Otsu thresholding, showing around 10% sulphide content; and (**c**) K-means segmentation, showing around 6% sulphide content. Observe the similarity of both images yet quite different sulphide content*

Another alternative in unsupervised classification is Fuzzy C-means clustering (FCM). The term fuzzy refers to classification technique where the clusters have no distinctive boundary (Zaitoun and Aqel, 2015). A pixel in FCM can be a member of multiple clusters, depending on the fuzzifier constant (m). The constant affects the distance calculation (d_{FCM}), which in turns affect how a pixel is classified to a cluster centroid, as shown in Equation 2.6.

$$d_{FCM} = w_k^m . d_{k-means}; \quad \frac{1}{w_k} = \sum_{j=1}^{c} \left(\frac{\|p_{x,y} - c_k\|}{\|p_{x,y} - c_j\|} \right)^{\frac{2}{m-1}} \tag{2.6}$$

In which $j = 1, ..., c$ with c as the number of clusters, $m \in \mathbb{R}$ with $m \geq 1$ and w_k is the weight of the membership function. As it can be seen in Equation 2.6 that large fuzzifier constant leads to smaller weight, or in other words decreases the weight assigned to clusters that are close to the pixel. In the lower limit of $m = 1$, the weight increases for clusters that are close to the pixel, indicating less fuzzy classification similar to the K-means. Typically the fuzzifier constant is set to 2 (Siddique et al., 2018), unlesss some information is known about the data.

Both techniques (K-means and FCM) have been applied in Chauhan et al. (2016b,a) for segmentation of pores in rock samples. The performance of both classification techniques are compared and benchmarked against experimental porosity measurements using pycnometer.

When comparing performance between classifiers, several measures can be used. First and foremost, the computational speed can be compared, as the fastest algorithm would be preferable. In terms of accuracy, several metrics such as entropy and purity can be used. Entropy refers to class distribution across the clusters, i.e. how likely a member of class i belongs to cluster j. Purity then refers to the most common class in a cluster, with values ranging between 0 and 1. If a cluster contain all pixels that belongs to the same class, then such cluster is considered pure with purity value of 1.

Nevertheless, these metrics can only be calculated if the ground truth is available, i.e. the actual information about the classes (mineral phases) of the pixels.That is why these metrics are considered as an "external validation" in which the validation requires external data as the ground truth. If such data is not available, then internal validation can be done by using sum of squared error (SSE). The error is the distance metrics, so that the SSE is the summation of Equation 2.5 and 2.6 for all pixels in each cluster.

Further applications of both classification tehcniques for mineral segmentation of μCT data is also subject to the third paper (Guntoro et al., 2019) and are discussed further in Chapter 3.

2.2.2.4 Supervised Classification

Supervised classification refers to classification algorithms in which the user trains the classifiers using a training data or ground truth. Supervised classifications have been used for mineral and pores segmentation in of μCT data of ore and rock samples (Guntoro et al., 2019; Wang et al., 2015; Chauhan et al., 2016b,a). Some relevant algorithms are discussed here. A comparison of supervised classification with unsupervised classification

in terms of mineral segmentation is illustrated in Figure 2.7.
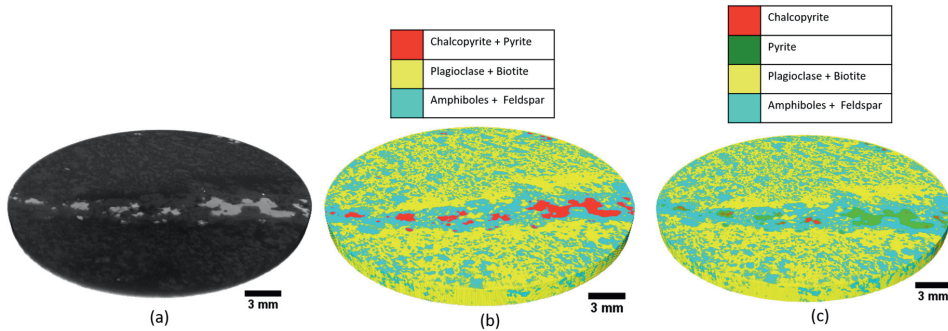
*Figure 2.7: (**a**) 3D image of a drill core sample; (**b**) unsupervised classification performed on the data; and (**c**) supervised classification performed on the data. Observe that in (**b**), pyrite and chalcopyrite is regarded as one phase, while (**c**) both minerals can be separated*

Classification tree is a decision tree with a binary test in each branch, illustrated in Figure 2.8. Decision tree is built by examining all possible binary splits on the data, in which optimum split is obtained when the resulting branches have the most purity. Random forest (Breiman, 2001) is then a technique where multiple classification trees are built by repeatedly by sampling the training data uniformly and with replacement (bagging). This creates multiple classification trees that are built based on different parts of the training data. The pixels are then classified by majority voting of the classification trees. Such method aims to reduce overfitting of the trees to the training data. Building more trees would lead to better performance and lower error at the expense of computational cost.

Another similar classification technique is k-nearest neighbors, or kNN. kNN is often termed as lazy learning, as it has no prior hypothesis about the training data but rather directly learn from the training data (Russell and Norvig, 2016). In comparison to random forest where a classifier (forest of decision trees) is build based on the training data, kNN directly classify pixels by comparing similar pixels in the training data. This is done by calculating the distance between the pixel to the similar (neighbor) pixels in the training data, and by looking on the class majority of the k amount of closest pixels in the training data. In layman's term, kNN classify a pixel into a class by looking the class of similar pixels in the training data. This is illustrated in Figure 2.9

Other classification algorithms that have been applied for μCT data for ore and rock samples include Support Vector Machines (SVM) (Vapnik et al., 1995) and Artificial Neural Network (ANN)(Hepner et al., 1990). Both techniques have been applied by Chauhan et al. (2016b,a) in segmentation of different phases (rock, mineral matrix, and
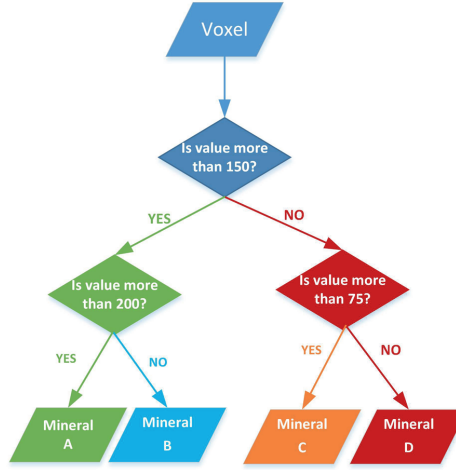
Figure 2.8: Example of a classification tree. Binary decisions are placed in each branch, querying the voxel's value in order to classify the voxel
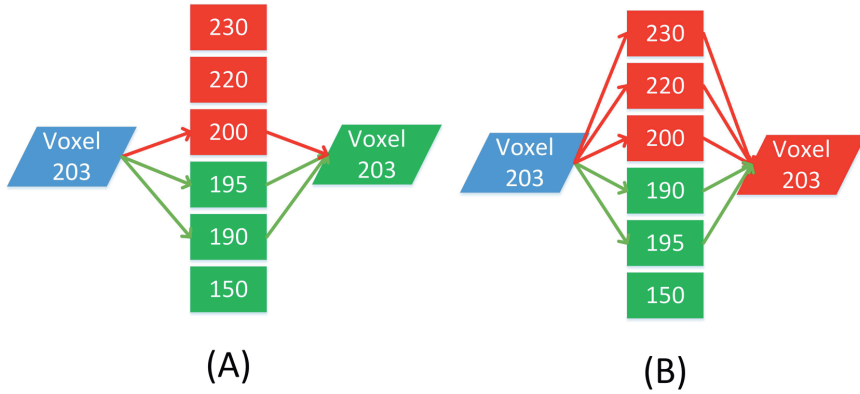
Figure 2.9: kNN classification with k = 3 (A) and k = 5 (B). Different k will affect how a voxel is classified; in (A) the majority of the three closest neighbors are green, therefore the voxel would be classified as green. In (B), the majority of the five closest neighbors are red, threfore the voxel is classified as red

pores) in the µCT image. ANN has been also applied by Cortina-Januchs et al. (2011) to classify pores in a µCT image of soil sample. Random forest classification is used by Wang et al. (2015) to classify ore particles from the background, as it has been previously stated that the marker-controlled watershed segmentation did not perform well for fine and low density particles; around 10-15% decrease in error was obtaiuned when supervised classification was used instead of the watershed segmentation.

The application of these supervised classification techniques is also subject to the third paper (Guntoro et al., 2019) and further discussed in Chapter 3

2.2.3   Extraction of textural features

The term feature in the context of mineral characterization would mostly refer to the textural information of the minerals in the sample. Feature extraction is then the extraction of textural information from the mineral sample. In μCT mineral characterization, usually feature extraction is done after mineral segmentation, so that the features of each mineral in the sample can be obtained. It would then logically follow that the accuracy of the features extracted is very much dependent on the previous mineral segmentation.

Texture, in terms of mineral characterization and ore geology, is defined as the relative size, shape, and spatial interrelationship between the mineral grains in the ore. Size, shape, and orientation of the grains are considered as structural texture, while the spatial relationship between the grains is considered as stationary texture (Lobos et al., 2016). The advantage of 3D data obtained from μCT for evaluating textures is quite clear; features such as size and shape could be more accurately quantified as there is no loss of dimensionality.

On the other hand, stationary textures have traditionally been extracted qualitatively, as it is quite challenging to describe the spatial distribution of mineral grains in an ore using a single number. These textures have usually been described using experiences and textural archetypes. There are several studies and researches devoted to quantitatively analyze stationary textures of ore samples, mainly using 2D computer vision and image processing techniques (Lobos et al., 2016; Koch et al., 2019; Parian et al., 2018; Pérez-Barnuevo et al., 2018; Zhang and Subasinghe, 2012). Some recent studies have further extended the dimensionality of stationary texture quantification to 3D with the use of μCT system (Jardine et al., 2018; Fatima et al., 2019; Voigt et al., 2019). The advancement of μCT system and its data processing routines would certainly open up a new depth of information, as more accurate description of textures can be achieved from 3D data.

2.2.3.1   Size features

Extracting size information from particulate ore samples is relatively straightforward; many experimental techniques are available such as sieving and laser diffraction. However, extracting grain size information from intact ore samples (such as drill cores) requires computer visions such as microscopy (both optical and electron). Furthermore, with optical microscopy alone, the grain size is often described qualitatively as fine-grained or coarse-grained. With the use of μCT systems, it would be a missed opportunity if sizes are still described qualitatively. In this subsection some of the relevant

methods for quantification of size features from μCT 3D image are discussed.

The most common method for extracting size distribution from images is using the concept of mathematical morphology (Serra, 1983; Serra and Soille, 2012). The method takes binary image as an input and make uses of a structuring element to extract morphological features of the binary image. The structuring element can be thought as a moving sieve with predetermined size and shape, in which if grain image fits to the structuring element, then the shape and size of the grain can be inferred. Morphological image analysis has been used in various application for μCT images especially for quantifying size and structures of pores, grains, and particles in ore and rock samples (Pierret et al., 2002; Tiu, 2017; Wu et al., 2007).

Morphological opening is an operation that removes any pixels in the image that is smaller than the size of the structuring element. This method is analogous to sieving, where particles smaller than the sieve size is passed through the sieve, i.e. not retained in the sieve. By performing morphological opening repeatedly with incrementally increasing structuring element size, the size distribution can be extracted. This sequence of operations is often termed as granulometry by opening, as shown in Figure 2.10
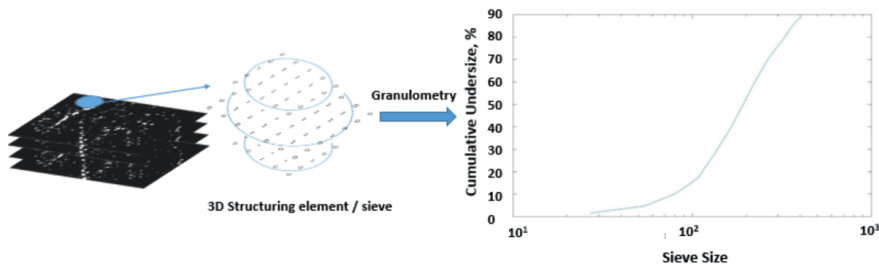
Figure 2.10: Granulometry by opening. A structuring element / sieve is operated on a 3D binary image, in which it represents the mineral grains. The sieve size is incrementally increased in which the percentage of pixels remained in each sieve size is used to calculate the size distribution

Some limitations exist in granulometry. As it has been suggested, granulometry requires repeated opening operation on the whole image, which logically would be computationally expensive. Moreover, as the size of the structuring element increase, the operation also becomes more computationally expensive as more pixels are now included in the operation. For example by using spherical structuring elements, by increasing its radius, the total amount of voxels processed is increased to the power of three of the incremental radius (Pierret et al., 2002). A 32-faced polyhedron could be used instead to alleviate some of the computational costs (Pierret et al., 2002).

2.2.3.2   Shape features

While the role of particle size on various mineral processing operations is relatively well established, the same cannot be said for particle shape. For example in flotation, when bubbles are attached to the particles' surface, the shape of the surface would theoretically affect how can the bubbles be attached to the surface. Particles with rough surface and sharp edges would have effects on rupturing of the bubbles, which in turns affect the effectiveness of bubble attachment to the particles (Koh et al., 2009). If the particles are not properly attached to the bubble, they would not be recovered in the flotation.

Particle shape was found to be correlated to the flotation rate of coal particles, in which more round (higher roundness) particles floated slower as opposed to less round particles (Wen and Xia, 2017). Other studies also found similar result for coal flotation, in which particles with more elongated shape have a higher flotation recovery (Ma et al., 2018). Particle shapes are also found to have a role in floatability of recycled materials such as plastics and glass fragments (Xia et al., 2018; Pita and Castilho, 2017). Other examples include the faster flotation rate of plate-like molybdenite particles in comparison to more ground-shaped particles (Triffett and Bradshaw, 2008). However in other study of flotation of chalcopyrite ores, particle shape was not found to contribute significantly to the flotation rate (Vizcarra et al., 2011). Similarly in the case of UG2 ores flotation, the flotation rate was unlikely to be affected by particle shape (Little et al., 2017)

It is also quite understood that breakage mechanism (i.e. selection of mill types) would produce different particle shapes (Little et al., 2017, 2016; Kaya et al., 2002). Nevertheless, the Little et al. (2017) have stated that the effect of different milling types is disproportionate on top size fraction of the particles; in the top size fraction, increasing grinding time led to more elongated products while in finer size fraction such phenomena was not observed. If breakage mechanism affects the progeny particles' shape which in turn affect the flotation process, interesting process mineralogical question may be raised about whether the ground ore particle shape can be selectively controlled by using specific milling type and operating conditions so that it is more favorable for the flotation process (Guven and Çelik, 2016).

Vizcarra et al. (2011) have stated that one of the main challenge in assessing the effect of particle shape on mineral processing operations is the characterization of the shape itself. As particles are irregular objects, defining and quantifying shape on such objects are not so straightforward. Many shape parameters exist such as roundness, aspect ratio, sphericity, in which all of these could contribute differently on the mineral processing behaviour. These parameters are generally obtained by measuring the dimensions of the 2D cross-sections of the particles obtained from microscopy. With the use of μCT systems, 3D representations of the particles could be obtained so that particle shapes can be more accurately described.

As it has been discussed, particles and grains of ore samples are often irregular. Never-

theless, the shape of such particles can be approximated using a set of defined geometrical objects such as polygons. This is the key concept in computational geometry techniques such as convex hull, Voronoi diagram, and Delaunay triangulation (De Berg et al., 2000). These techniques attempt to use convex polygons to represent an irregular object, i.e. the object is tessellated into a set of convex polygons so that the properties of the object can be estimated from the properties of the polygons. These methods naturally have weaknesses for non-convex particles, but nevertheless the error of using these methods can be easily quantified by comparing the actual volume of the object to its convex volume, also known as solidity. Other measures that can be measured using convex hull is convex surface area of the object.

Other technique include the use of a bounding object, i.e. an object that would bound the particle inside it. The dimensions of the bounding object can be taken as an approximation of the particle's dimension. The bounding object's volume can be minimized until it tightly fits the particle so that the particle could be better represented. The bounding object could take form of either sphere or box. If box is used, shape parameters such as aspect ratio, elongation index, and flatness index can be extracted from the major, minor, and intermediate dimensions of the box (Zhao et al., 2015). Convex hull and bounding box of a particle is illustrated in Figure 2.11
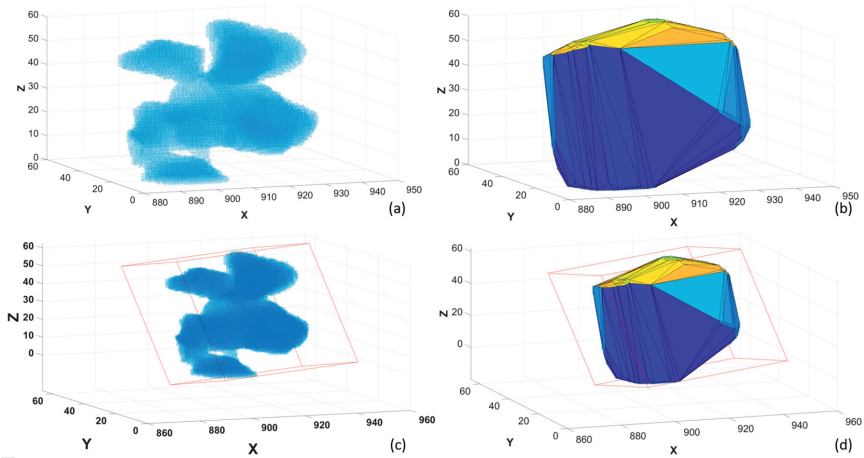
*Figure 2.11: Computational geometry to extract shape features from a particle. (**a**) Scatter plots representing the particle; (**b**) convex hull of the particle; (**c**) minimum volume bounding box of the particle, which is the same as the minimum bounding box of the convex hull*

Few studies have extended the concept of computational geometry for 3D image analysis of μCT data, especially for rock and ore samples (Vecchio et al., 2012; Zhao et al., 2015; Pamukcu et al., 2013). In the study by Pamukcu et al. (2013), it was stated that the

limitation of convex hulls is that it could not evaluate non-convex glass inclusions in the volcanic rock samples. This limitation is even illustrated in Figure 2.11, in which due to the non-convex shape of the particle, the convex hull of the particle differs significantly from the original particle.

Besides using polygons, spheres have also been used to approximate particle shape. The maximum inscribed sphere has been used by Van Dalen et al. (2012) to measure the local thickness of particles. The local thickness of a point inside the particle can be defined as the diameter of maximum inscribed sphere on that point. The maximum inscribed sphere applied together with 3D distance transformation has been used to generate a new shape descriptor for particles termed as the bluntness index (Pirard et al., 2009). Such index has been demonstrated to be able to distinguish blunt particles from sharp particle at a resolution as low as 5000 voxels per particle.

Other method of evaluating particle shape include mathematical functions such as spherical harmonic analysis (Garboczi and Bullard, 2017; Garboczi, 2002). If the previous methods of convex hulls cannot describe properly non-convex particles, spherical harmonics overcome this limitation under one condition: the non-convex particles should be star-shaped. Many natural particles from the ground and inorganic particles in grinding processes are considered star-shaped but not necessarily convex (Garboczi and Bullard, 2017; Bullard and Garboczi, 2013). The definition of both convex and star shaped are as follows, and example illustration is given in Figure 2.12.

- A region is considered as convex if for every pair of points within the region, all points the on the straight line that connects the pairs is also within the region.

- A region is considered as star-shaped, if there is a fixed point in the region for which a straight line drawn from that fixed point to any other point inside the region lies entirely within the region.

- If both conditions are not fulfilled, then the particle is neiher convex nor star-shaped. This is typically for particles with overhangs (crescent shape) and voids (annulus or donut-shaped).

Spherical harmonics, as the name suggest, attempts to describe a particle as a spherical function of $r(\theta, \phi) = R$, in which θ and ϕ are the azimuthal and polar angles respectively as well as r as the distance from the origin in the direction specified by both angles. Spherical harmonics gives an analytical mathematical equation that describe the surface of the particle (Garboczi, 2002). The advantage of spherical harmonics in shape analyis, besides its ability to adress non-convex star particles, is that after the spherical harmonics of a particle is constructed, geometric quantities such as the major, minor, and intermediate dimensions of the particle can be determined. Furthermore, due to its analytical nature, integrals of the function can be calculated as well to obtain the volume
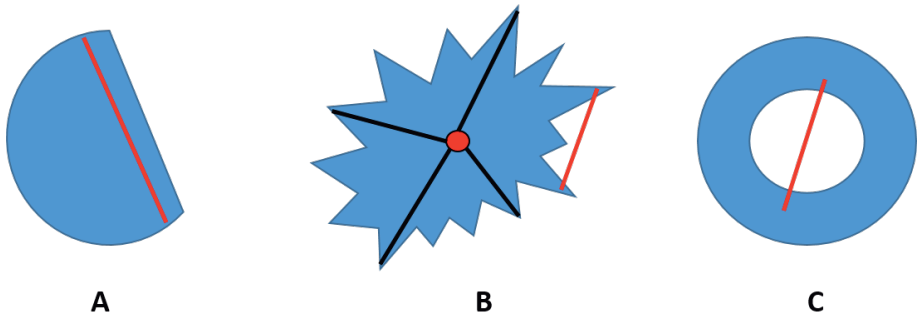
*Figure 2.12: (**A**) Convex particle, in which every lines in the region lies entirely within the region. (**B**) Non-convex particle, as pointed out by the red line in which portion of the line is located outside the region. The particle is however star-shaped, as all lines drawn from the fixed red point in the center lie entirely within the region. (**C**) Non-convex and non-star particle. Both conditions are not fulfilled*

and surface area of the particle (Bullard and Garboczi, 2013). From the dimensions, volume, and surface area, Wadell shape descriptors (Wadell, 1932) such as roundness and sphericity indexes can be calculated. Spherical harmonics have been applied mostly for 3D analysis of sand and aggregate particles (Garboczi and Bullard, 2017; Garboczi, 2002; Cepuritis et al., 2017; Bullard and Garboczi, 2013; Masad et al., 2005), as it is believed that sand particles' morphology affects the performance of concretes (Cepuritis et al., 2016).

Perhaps one of the most potential geometallurgical use of 3D particle shape is to evaluate breakage mechanism and modelling, as it can give an idea whether the breakage is random or non random. In random breakage, the particle properties such as particle shape, exposed grain surface area, interfacial area of the mineral, and mineral grade do not vary with particle size (Barbery, 1991; Little et al., 2016). Each mineral would have the same possibility to report to each size fraction, thereby the use of the term "random". Little et al. (2017) have shown that by evaluating the conservation and variation of shapes in each size fraction of the progeny particles, the prevalence of phase boundary breakage can be inferred. Phase boundary breakage itself is defined as the breakage mechanism along grain boundaries, in which such mechanism would improve mineral liberation (Xu et al., 2013). As the breakage mechanism is dependent on the grinding action (compression, impact, or shear) and subsequently mill types, the question raised earlier on how to selectively controlling particle shape for favorable liberation and downstream processing can potentially be answered by evaluating the shapes of the progeny particles. Furthermore, as it has been stated by Little et al. (2016), with the availability of 3D data from µCT as well as in-situ µCT compression tests (Garcia et al., 2009; Xu et al., 2013), such research topic could potentially become more attractive.

2.2.3.3   Stationary textures

Stationary texture is also one of the important features of ores that have been mostly described qualitatively. Textural attributes of rocks are one of the important aspect during core logging as it may relates to the ore lithology, alteration, and even some idea about formation of the deposit. The importance of ore texture in mineral processing has also been recognized, but it is quite challenging to integrate texture information into a process models. In fact, in relation to geometallurgy, the quantification and integration of rock textures to be used in process simulation have been investigated by several researchers (Koch, 2017; Pérez-Barnuevo et al., 2018).

The quantification of textures have been done mostly by the use of computer vision and digital image processing. With the use of such system, different ore types can be classified accordingly depending on its textures (Koch et al., 2019; Pérez-Barnuevo et al., 2018). Ores that belongs to the same texture category can be predicted to behave similarly in a mineral processing circuit. Nevertheless, such texture classification should be automated and rapid, which means that a proper texture descriptor (quantifier) is needed as a basis for the classification. Some relevant methods to extract these textural descriptors that have been applied in 3D image are discussed here.

As stationary texture is defined as the spatial interrelationship between mineral grains in the ore volume, pixel neighborhood information in the image can be utilized as quantification tool. Local Binary Pattern (LBP) (Ojala et al., 1996), is one such common tool. In the algorithm, the grayscale value of the pixel is compared with the neighboring 3x3 pixels. If the neighboring pixels are greater than the centre then a value of 1 is assigned to the pixel, otherwise 0 is assigned. These binary values are combined to form an 8-bit binary string, in which it stores both the binary value and the location of the pixel in the neighborhood. The advantage of this technique is its computational simplicity. LBP has been applied by Rahimov et al. (2017) for classification of different textures of carbonate rocks 3D image acquired by μCT systems. In Rahimov's work, the textural classificatioon is based on the spatial correlation of the pores with the solid phases, as the study is more focused towards reservoir properties for oil recovery.

Other alternative is by using graylevel Co-occurence Matrices (GLCM) (Haralick and Shanmugam, 1973), with the same concept of comparing grayscale value of the neighboring pixels. The GLCM is composed of an nxn matrix in which n is the number of possible grayscale values in an image, i.e. 256 for an 8-bit image. GLCM shows the frequency of a pair of grayscale values co-exist in a pixel neighborhood, as well as the directional adjacency of such pairs. In a 3D volume, this neighborhood is illustrated in Figure 2.13, while example of GLCM texture analysis is illustrated in Figure 2.14

Another advantage of the GLCM is that it also gives some statistical parameters based on the matrix. Four of these parameters are related to stationary textures, such as energy, correlation, contrast, and homogeneity. GLCM has been applied to 3D μCT drill
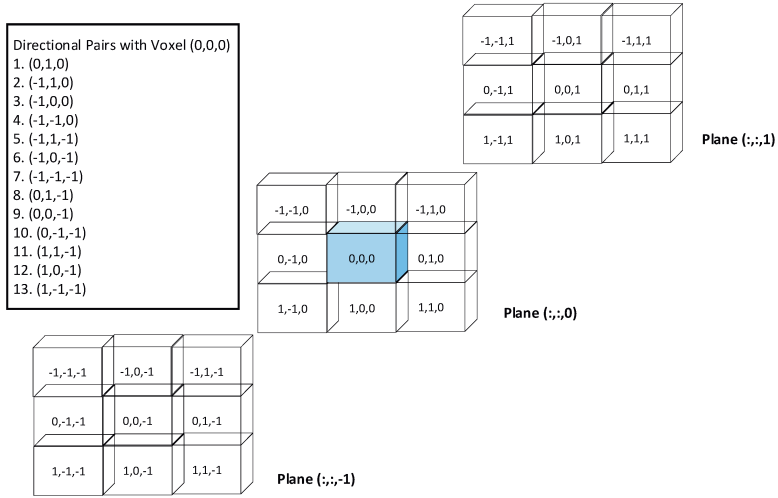
Figure 2.13: Neighborhood and directional voxel pairs in relation to GLCM analysis, adapted from Jardine et al. (2018). All three planes are in a 26-connected neighborhood of voxels, in which there exist 13 unique directional pairs with the origin voxel (0, 0, 0). Keep in mind that mirrored direction does not count as a unique direction, e.g., direction (0, 1, 0) has the same direction with (0, -1, 0), direction (0, 0, -1) has the same as (0, 0, 1), and so on
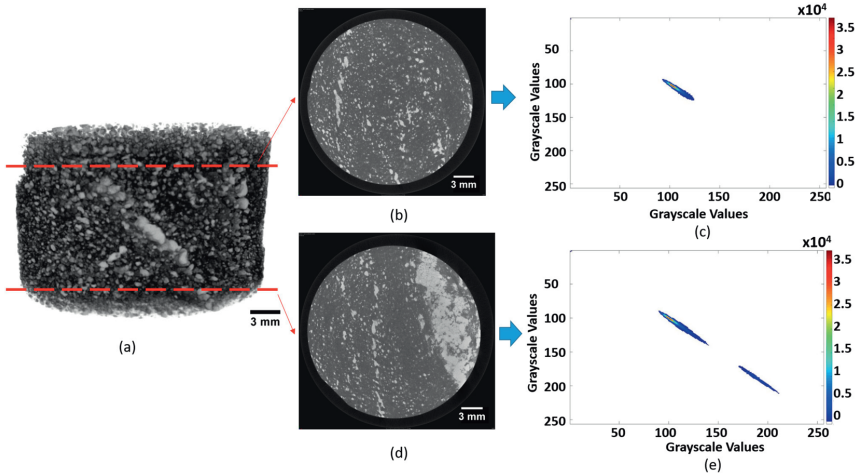
Figure 2.14: GLCM matrix on direction (0,1,0) extracted from a drill core image. (a) Drill core volume showing horizontal slices (b) and (d), and their GLCM heat map (c) and (e) respectively. The results clearly show difference in the GLCM as slice (d) has more sulphide mineralization as compared to slice (b). This can be seen as the higher correlation frequency between the brighter phases, which usually indicates the sulphide minerals

core images by Jardine et al. (2018), in which it was shown that there exist some correlations between various textures and their GLCM statistics. Nevertheless, such statistics captured only the bulk mineralogy (relations between phases), while grain textures (fine versus coarse) were not observed to be correlated with the statistics. Such technique is also very dependent on the voxel pair direction chosen when calculating the GLCM, especially for anisotropic textures. In such textures, several directions of GLCM might be needed to adequately quantify the textural characteristic of the sample, thereby increasing the computational cost.

The orientation of the phases and grains in an ore could also be used as a textural descriptor. In the case of volcanic rocks, the orientation of vesicles in the rock can be attributed to the magma nature and dynamics (Zandomeneghi et al., 2010). In case of ores, the orientation of mineral grains could reveal some idea about the isotropic nature of the ore. Texture orientation could be determined in 3D by using Mean Intercept Length (MIL), in which several parallel lines are generated in a certain direction. The number of intercepts between the lines with the grains can be used for estimating the overal orientation of the grains. As it has been mentioned earlier, this technique has found applications for evaluating the vesicle orientation in volcanic rocks (Zandomeneghi et al., 2010).

2.2.3.4   Surface texture

μCT systems also offers a new information about depth and surface. In 2D images, the notion of stationary texture refers to the correlation between phases in an xy dimension, while in 3D a new dimension z is introduced. As many metallurgical processes such as flotation and leaching are dependent on ore surfaces, this new depth of information becomes critical. With μCT, the "surface exposure" of the grains can be identified, which can be useful to deduce leaching and flotation kinetics, or to deduce the breakage mechanism that is able to produce such particles.

The concept of surface exposure has been evaluated by several researchers (Miller et al., 2003; Garcia et al., 2009; Wang et al., 2017; Reyes et al., 2019), in which its significance for flotation, leaching, and particle breakage was evaluated. In order to get an estimation of the surface properties, marching cube algorithm (Lewiner et al., 2003) is used. Such algorithm is similar in principle to the computational geometry, in which a set of cubes are used to estimate the topography of the particle. In Wang et al. (2017), the marching cube was performed on two different volume of interest which represent the whole particle and the valuable mineral grains. After the marching cube algorithm is performed, the vertices of the two marching cube volumes were matched (superimposed) so that the portion of the grains that are exposed on the particle surface can be identified.

Wang et al. (2017) reported that there exist correlation between the proportion of the exposed mineral grains the particle's floatability, in which a particles should have sufficient area of exposed surface grains in order to be recovered in flotation. This surface area is

in turn affected by the proportion of the grain on the surface, as well particle size (larger particle would have larger surface area). The results also revealed some idea about the size of the exposed grain; for the same proportion of surface exposure, particles with fine and disseminated grain surface would not be recovered in contrast to particles with one or more large exposed grain. The results clearly opened up new understanding about texture and size effect on flotation process.

The mineral exposure analysis is also useful to deduce some idea about the possible breakage mechanisms. As it has been previously stated, random breakage is where the conservation of interfacial area is observed throughout different particle sizes. In principle a liberation process aims to reduce grain interfacial area, in which complete liberation is achieved when interfacial area is zero. This means there are no area in which two different grains (phases) are in contact; all grains are liberated. Calculation of interfacial area requires the information about particle surface area, grain exposed surface area, gangue surface area, and area of internal grains Garcia et al. (2009). All of this parameters would require a 3D data on the particle, and that is where µCT comes to play. Garcia et al. (2009) used µCT systems to quantify the interfacial area of particles before and after comminution and inferred that if the interfacial area is reduced after the breakage, it means that some preferential breakage occurred within the grain boundaries. Correlating this with different breakage energy would gives some idea of suitable breakage mechanism in which significant reduction of interfacial area can be obtained.

In terms of leaching, Miller et al. (2003) have reported some results on the use of mineral exposure analysis. Such analysis could be coupled by particle size analysis to infer which size class where most of the mineral surfaces are exposed (more liberated). Miller et al. (2003) have shown that ultimate heap leaching recovery can be predicted for a specific particle size distribution if the exposure analysis is done so that a correlation between particle size and grain exposure is established. As such parameter of exposure requires information about depth in 3D, it was therefore necessary to use µCT systems to evaluate the surface exposure. The predicted recovery can then be compared to actual recovery from leaching column tests.

Furthermore, the information about mineral grain's location within the particle (whether it is exposed or locked) can be coupled with leaching kinetics, so that the spatial variability of leaching kinetics can be evaluated. The grain's location within a particle can be extracted using distance transformation, in which it transform a binary image into a function of distance of each pixel to the nearest zero pixels. In essence, each voxel in the particle volume is transformed into a value that represent the nearest distance of that voxel to the particle surface. As leaching is mostly modelled after the shrinking core model (Liddell, 2005), it is expected that grains nearer to the surface would be leached faster than the internal grains. The 3D spatial variability of leaching kinetics and recovery have been evaluated using µCT systems have been evaluated by Lin et al. (2016b) and Fagan-Endres et al. (2017), in which both reached similar conclusion that grains that are located further from the surface exhibited lower recovery and leaching rates.

2.3   Summary

In this section, some methods that have been used for different applications for µCT mineral characterization are summarized. This summary is illustrated in Figure 2.15 and Table 2.1 for mineral segmentation.
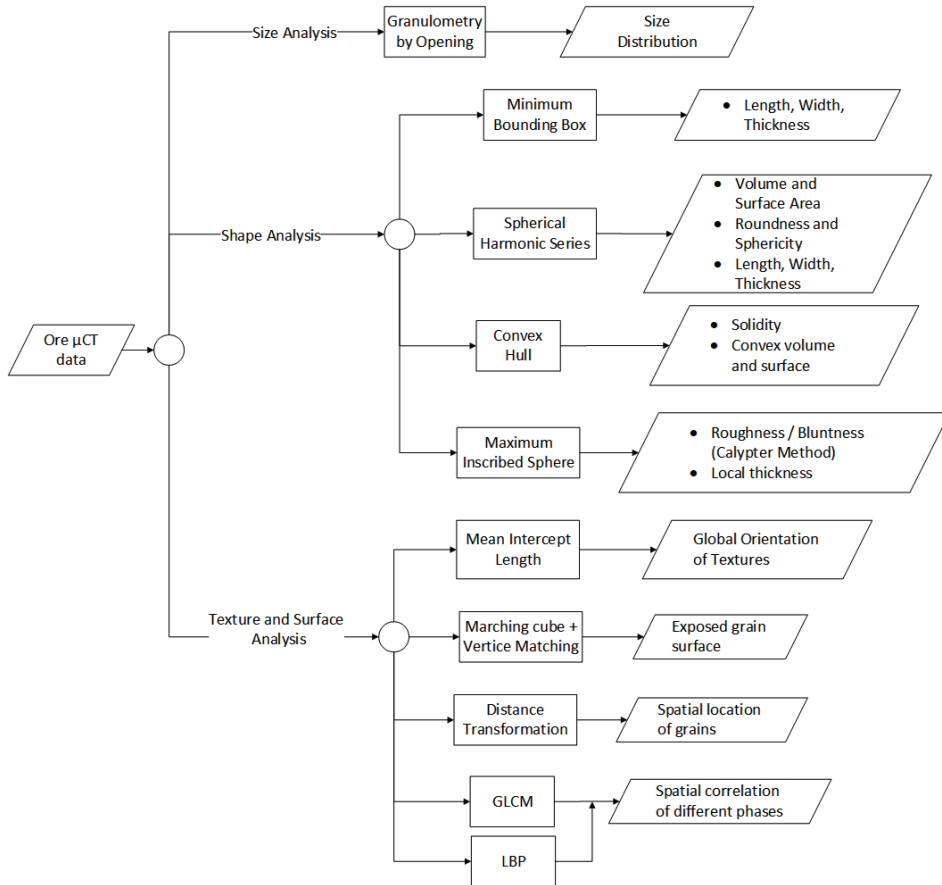
Figure 2.15: A workflow showing different features that can be extracted from 3D µCT ore data as well as the methods applicable to extract said features. Most of these methods have been applied for geological materials such as ores, sands and aggregates, as well as different types of rock

Connecting to geometallurgy, the relevance of these features to mineral processing and metallurgical operating principles are summarized as follows:

Table 2.1: Summary of methods applicable for mineral segmentation of 3D data

Case	Methods	Applicability
Segmentation between air and solid materials (e.g. particles)	1. Otsu global thresholding (Yang et al., 2017; Lin et al., 2015, 2016a) 2. Marker-controlled watershed (Wang et al., 2015; Lin et al., 2010) 3. Adaptive watershed (Kong and Fonseca, 2017; Shi and Yan, 2015) 4. Removal of boundary regions (Wang et al., 2017) 5. Feature-based random forest classification (Wang et al., 2015)	1. Implemented in most simple cases 2. Used to address touching particles 3. Same with no 2, but better suited for highly varying particle morphology 4. Correct partial volume effects 5. Same with no 2, but boundary effects are minimized
Segmentation between minerals with significant contrast.	1. Maximum entropy thresholding (Reyes et al., 2017) 2. Unsupervised classification (Chauhan et al., 2016b) 3. Supervised classification (Chauhan et al., 2016b)	1. Useful for minerals that are less abundant in the sample 2. Rapid classification between rock matrix and mineral phases 3. Similar to number 2, but less rapid.
Segmentation between minerals with lacking contrast	1. Local thresholding using gradient information (Godel, 2013) 2. Lower energy scanning (Kyle et al., 2008) 3. Using smaller sample size (Bam et al., 2019) 4. Dual energy scanning and calibration with pure minerals (Ghorbani et al., 2011) 5. Calibration of thresholding values with SEM-EDS dataset (Reyes et al., 2017)	1. Enhanced phase boundary detection useful for capturing small inclusions 2. At energy of 180 keV bornite and chalcopyrite could be segmented 3. Reduce beam hardening effect 4. Sphalerite, pyrite, galena and silicates were able to be segmented. 5. Chalcopyrite and pyrite were distinguished

- Mineralogy. Minerals are the building blocks of ores in process streams, and it is of a great importance for evaluating mineral processing behaviors. Mineralogical information can be extracted in 3D using methods presented in Table 2.1. One aspects that is also of importance is the statistical reliability of mineral liberation analysis. While it is true that the 3D mineral liberation eliminates the sterological bias exhibited in 2D mineral liberation (therefore requiring multiple cross sections), the number of particles evaluated in a 3D mineral liberation analysis should also be sufficiently large for statistically sound result.

- Particle size. The effect of particle size on mineral processing operations such as comminution, flotation, and gravity separation is widely studied. It is considered as the most important factor in mineral processing together with mineralogy. While the methods of granulometry by opening for extracting particle size distribution is well established, there is still lack of studies that actually compare these 2D-3D particle size information and their effect on mineral processing models.

- Grain size. The grain size distribution could be used as a textural descriptors especially useful for breakage modelling (Evans et al., 2015). Jardine et al. (2018) have also stated that their 3D GLCM textural analysis could not captured the grain size information which could be useful for textural descriptors. Grain size has also been shown to hold some significances in evaluating grain-scale leaching behaviour using μCT systems (Lin et al., 2016b).

- Particle shape. In contrast to size, the significance of shape for mineral processing operations is less studied. Several researchers have indicated the effect of particle

shape to flotation using various shape descriptors such as roundness (Wen and Xia, 2017), elongation ratio (Ma et al., 2018), flatness (Triffett and Bradshaw, 2008). Shape descriptor such as roundness also describe the surface texture (more rough or smooth), which in turns affects particle-bubble attachment in flotation process (Koh et al., 2009). Particle shape has also been used to get some idea about breakage mechanism and breakage modelling (Little et al., 2016, 2017).

- Grain shape and orientation. These information can also be used for textural descriptors. The shape and orientation of vesicles have been demonstrated to hold significance for textural analysis of volcanic rocks (Zandomeneghi et al., 2010).

- Spatial relationship between grains / phases. This information is also key for describing rock textures, and the possibility of quantifying such relationship through 3D methods shown in Figure 2.15 would be useful in classification of different ore texture types. Extending the classification of ore textures by including the metallurgical response of these ore textures is the cornerstone of geometallurgy. This can be achieved by quantifying the texture and using it in a process simulation (Koch, 2017) or by performing metallurgical tests for different ore textures (proxy approach) (Lund et al., 2015).

- Surface exposure. The amount and distribution of the mineral grains on the particle's surface have been reported to affect the flotation recovery (Wang et al., 2017). The amount of mineral grains exposed on the surface is also useful to calculate the interfacial area, which in turns gives some idea for the prevailing breakage mechanism (Garcia et al., 2009). In leaching, recovery and kinetics have been shown to vary depending on the location of the grain relative to the surface; exposed grains leached faster than locked grains (Lin et al., 2016b; Fagan-Endres et al., 2017).

2.4 Challenges and Gaps

After comprehensively reviewing the potential of μCT systems for mineral characterization, several challenges and gaps for future development are identified as follows:

- It can be suggested that the bottleneck of μCT mineral characterization lies on the mineral segmentation; different mineral phases often exhibit low contrast, making it difficult for segmentation. This issue has been addressed by several researchers as shown in Table 2.1. The review suggested that additional information from calibration or SEM-EDS is needed to properly extract the mineralogical information from the data, which somehow compromises one of the advantages of μCT in less sample preparation. Moreover, in cases where significant contrast do exist, partial volume effects prevail (Wang et al., 2017), especially for particulate samples. Future works should evaluate how can μCT extract mineralogical information independently and

accurately, and if such extraction is not possible then what additional data can be used effectively as an additional information.

- Particle size effect's on mineral processing operations is understood to be significant, and μCT offers a more accurate representation of such data. Several researchers (Reyes et al., 2017; Evans et al., 2015) have evaluated the difference between 2D and 3D grain size distribution, which in turns affect the expected liberation size of the ore. Evans et al. (2015) have stated that the difference may entails some errors in the design of grinding circuit, but there is still lack of studies that evaluate to how such error could affect the grinding process and how it varies with different ore types. If geometallurgy is a predictive discipline, then this difference in size distribution between 2D-3D data should readily be quantified with how it will affect the downstream process (recovery) and even the profitability.

- As it has been noted by Koh et al. (2009), the challenge in evaluating particle shape's effect on mineral processing lies on the characterization of shape itself as many different shape descriptors exist. With μCT system, these shape descriptors can be evaluated more accurately, as in previous studies 2D measurement techniques have been used. The review suggested that effect of particle shape on flotation varies significantly with ore types; coal flotation has been reported to be affected by particle shape (Wen and Xia, 2017; Ma et al., 2018), while the same was not observed on chalcopyrite (Vizcarra et al., 2011) and UG2 ores (Little et al., 2017). More studies are required to get more information about shape effects on flotation. Furthermore, these varying results beg the question whether other factors such as mineralogy and texture plays more role in flotation, especially in the case of chalcopyrite and UG2 ores. Therefore, a proper texture and mineralogy classification is indeed needed to isolate these two factors so that the effect of shape can be accurately identified.

- Connected to the previous point, texture classification in the context of geometallurgy is important due to the understanding that texture plays significant role in mineral processing operations. With the availability of 3D data, the notion of texture should be expanded from spatial variability of grains (stationary textures) to include surface exposure of grains by adding the third (z) dimension. This would open up more ideas in evaluating the effect of textures in mineral processing. While surface exposure effects have been evaluated and quantified (e.g. on flotation and leaching processes), the same cannot be said for stationary textures. Proper 3D quantification of textures and utilization of such quantified information for predicting process behaviour is the research front that needed to be opened up in geometallurgy.

Chapter 3

Machine learning for mineral segmentation of µCT data

This chapter addresses one of challenges identified in Chapter 2, which is mineral segmentation. The focus of the chapter would be in the method development and the applicability of such method through case study.

3.1 Background

As it has been identified in Chapter 2, mineral segmentation remains one of the defining challenge in establishing µCT as an automated mineralogical system. This is due to similar attenuation between mineral phases, limited resolution, and lack of automated mineralogical software. Broadly speaking, this challenge has been addressed through two major methods :

- Pre-scanning methods, refer mostly to all measures that are done during and before scanning as well as in reconstruction step. This could include optimization of scanning conditions as well as calibration with pure minerals. Optimization of scanning conditions include sample size, scanning energy, and even the use of filters.

- Post-scanning methods, refer to image processing procedures applied to the acquired µCT dataset. This basically include all sort of image processing techniques such as thresholding, partial volume correction, image filtering, machine learning, etc. It also includes any combination of additional data from other analytical tools

(microscopy, SEM-EDS, visual observation) as a reference for obtaining mineralogical information from μCT data.

Machine learning is one of the promising avenue of attack in extracting mineralogical information from μCT data. In general, machine learning is defined as the use of mathematical models to interpret the underlying patterns in a dataset. By learning this pattern, a computer system can make predictions or classifications on the dataset. Machine learning can be divided into unsupervised and supervised learning. Supervised learning means that the user pre-defines the underlying pattern of the data, and the computer builds a prediction model based on the pre-defined pattern (training data). Unsupervised learning lets the computer interpret the pattern by itself without user's supervision.

Cortina-Januchs et al. (2011) have applied machine learning techniques to extract the pore spaces from μCT image of soils. Compilations of both supervised and unsupervised techniques such as K-means, Fuzzy C-means, Self Organized Maps (SOM), Artificial Neural Network (ANN) were used and their performances evaluated. Chauhan et al. (2016b,a) extended the study further for segmentation between pore, matrix, and mineral phase in rock μCT data by evaluating other supervised technique such as Support Vector Machine (SVM) and ensemble classifiers (boosting and bagging). The argument put forward by Chauhan was that ANN used in Cortina-Januchs et al. (2011) is more biased towards priori information (training data), therefore it is generally anticipated that it would achieve high accuracy. By using more unbiased techniques such as SVM and ensemble classifiers, the generality of the classifier can be evaluated.

For ore samples, Tiu (2017) evaluated random forest classification for segmenting between chalcopyrite and pyrite in a 3D drill core image, using SEM-EDS mineral map as training data. Similarly, Wang et al. (2015) also employed random forest classification to segment ore particles from the background, due to unsatisfactory results obtained from simple thresholding and watershed segmentation methods. Nevertheless, there is still lack of studies regarding the use of machine learning specifically for mineral segmentation of μCT data.

In this Chapter, the application of various machine learning techniques in mineral segmentation of a μCT dataset is evaluated. Both supervised and unsupervised techniques are included. Additionally, an automated image registration technique is introduced to align a Back Scattered Electron (BSE) mineral map with a corresponding slice in a 3D μCT data, which is then used as the training data to classify the other μCT slices. Furthermore, besides using grayscale values as the dataset, the possibility of classification using features such as edges, corners, and blobs (regions with similar grayscale values) is also evaluated. The accuracy and computational costs of these methods are evaluated and compared to give insight on the most suitable method for various tasks related to mineral segmentation of a μCT dataset.

3.2 Experimental methodology

3.2.1 Ore samples

The drill core sample used in this study was obtained from Boliden's Aitik copper mine in Northern Sweden, shown in Figure 3.1. The deposit is described as a metamorphosed porphyry Cu-Au deposit, with chalcopyrite, pyrite, and pyrrhotite as the main sulfide minerals; magnetite and ilmenites were found as the oxide minerals (Wanhainen et al., 2003). Other minerals that can be found in the deposit include quartz, amphibole, biotite, garnet, tourmaline, and zeolites.

Figure 3.1: Map of Sweden, showing mines in operation as of January 2019. The sample originated from Aitik deposit shown as the red star in the northern region of Sweden. Map taken from `www.sgu.se`

3.2.2   Image acquisition with µCT

A cylindrical sample with a diameter of 25 mm was analyzed using a Zeiss Xradia 510 Versa 3D microscope at Luleå University of Technology (LTU), Sweden. The whole sample was placed in the scanning chamber and measured under the scanning conditions summarized in Table 3.1. Reconstruction of projections was done with beam hardening correction. ORS Dragonfly®software was used for volume rendering and visualization of the 3D image. The scanning conditions used in this study were optimized so that a good image with reasonable acquisition time could be achieved. The µCT volume of the sample is shown in Figure 3.2.

Table 3.1: Scanning conditions

Voltage	160 kV
Power	10 W
Exposure time	14 s
Objective	0.4x
Bin	1
Filters	Zeiss HE3 filter
No. of projections	2201
Spatial resolution	13 µm
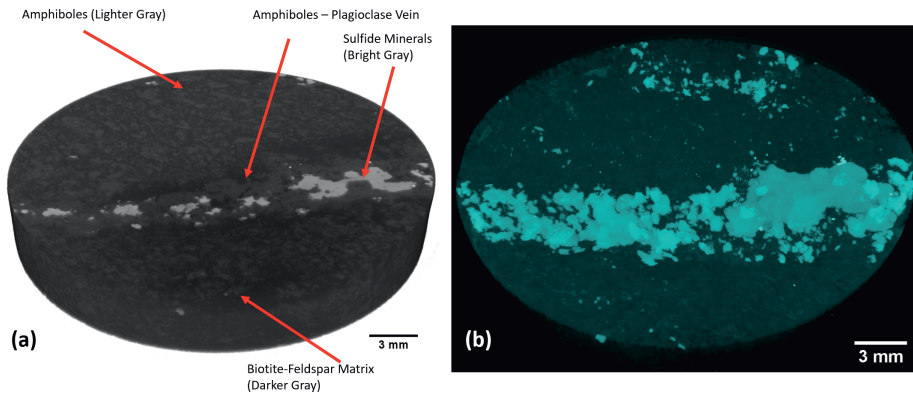
Figure 3.2: (A) µCT volume of the sample, showing clear amphibole phenocrysts (lighter gray) inside biotite-feldspar matrix (darker gray). A high intensity amphibole-plagioclase vein with rich chalcopyrite and pyrite grains (bright gray) is also observed in the sample. (B) µCT volume showing chalcopyrite and pyrite grains as well as their vein mineralization (cyan) inside the drill core volume

Despite the use of filters and beam hardening corrections during reconstruction phase, the final 3D image acquired in this study still possessed some artifacts, most notably that the grayscale values varies significantly for the biotite-feldspar matrix throughout the slices (vertically) as shown in Figure 3.3.
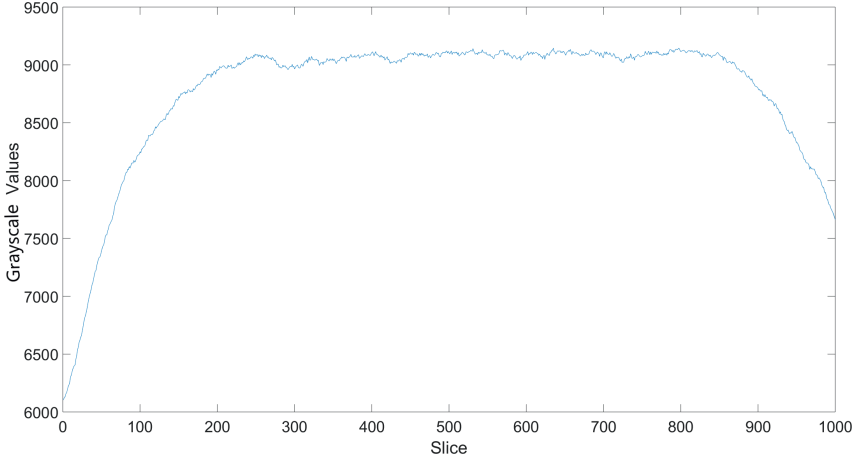
Figure 3.3: Plot of biotite-feldspar matrix average grayscale values of each slice, showing significant variation in the top and bottom hundred slices. Despite the fact that the matrix's grayscale values are different for each slice, the variation should be small (as seen in the plateau in the middle slices). Significant variation in the top and bottom slices is most likely associated with the beam hardening effect

This problem can be seen as an uneven illumination problem, and it can be addressed using top hat filtering (Wang et al., 2014). This is achieved by morphologically opening (removing) the grains from the slice, thereby obtaining an estimation image of the biotite-feldspar matrix. This image is then represents the unevenly illuminated background which must be homogenized. The homogenization is done basically by replacing this background with the correct and constant background taken from one of the middle slices.

The top hat filtering affects all grayscale values of all the phases in the slice, which can lower the contrast between the matrix and the grains. Therefore, following the filtering process, contrast adjustment was performed. The adjustment was done by simply stretching the range of the grayscale values of the images up until the phase contrast is sufficient for segmentation. A comparison of uncorrected and corrected (after contrast adjustment) slice is shown in Figure 3.4.
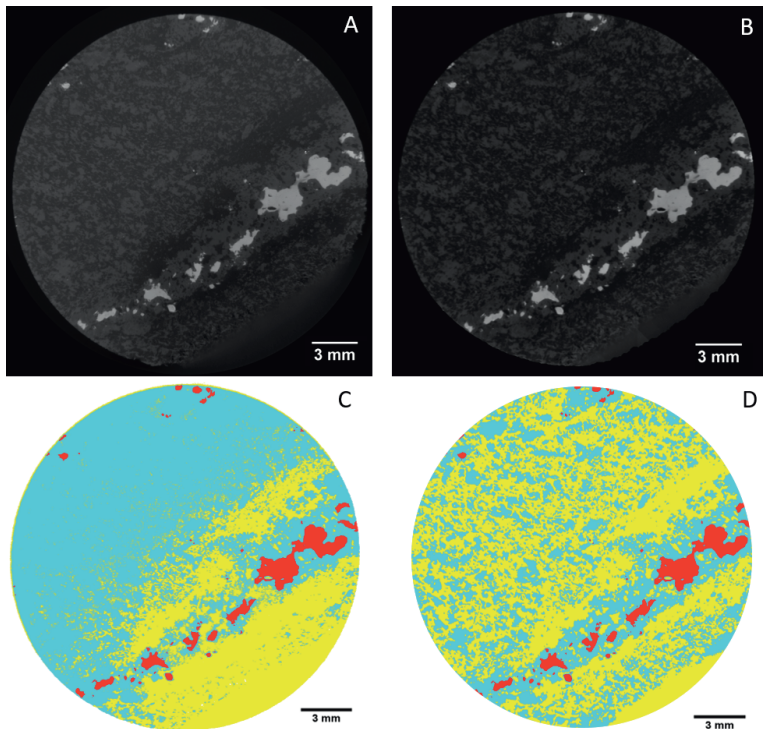
Figure 3.4: Correction of grayscale values showing (A) original slice, (B) corrected slice, (C) segmented image of original slice (A), (D) segmented image of corrected slice (B). Clear improvement is seen in the segmentation results (D) as compared to (C)

3.2.3   SEM-EDS as a reference data

SEM-EDS analysis was performed on top part of the cylindrical sample after the µCT, as a comparison and reference. The cylindrical sample was mounted in epoxy resin and polished prior to SEM-EDS analysis. A Zeiss Merlin FEG-SEM system was used for SEM analysis, and Aztec Energy 2.2 software from Oxford Instruments was used for EDS analysis. The resulting back-scattered electron (BSE) image was subjected to mineral mapping. The BSE image has a resolution of 3 µm per pixel, allowing sharper contrast and better segmentation between phases. Based on EDS measurements, mineral mapping of the BSE image was performed using the Trainable Weka Segmentation (Arganda-Carreras et al., 2017) in the Fiji/ImageJ software (Schindelin et al., 2012). The resulting BSE mineral map is shown in Figure 3.5.
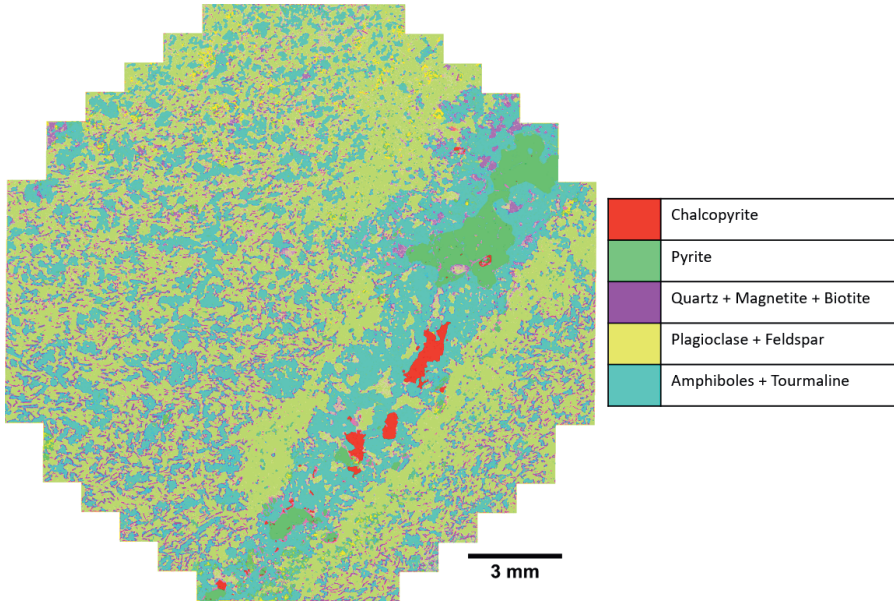
Figure 3.5: Simplified mineral map of BSE image. Due to the high resolution the BSE image, fine-grained minerals of quartz, magnetite, and biotite are also detected. These fine-grained mineral phases are grouped together

3.2.4   Machine learning classification algorithm

Both unsupervised and supervised classification algorithms are evaluated. The following system configuration is used for performing the classification and image processing: Intel®Core™i7-7500U CPU @2.7 GHz, 2904 MHz, 2 Core(s) and 4 logical processors, 24GB RAM and 64-bit OS. The implemented machine learning algorithms are as follows, and detailed explanation about these algorithms have been discussed in Chapter 2.

- K-means clustering (unsupervised). The determination of the number of clusters (K or C in case of FCM) for these algorithms must be initiated by the user. Looking at Figure 3.5, it could be expected that six clusters exist in the mineral map, which corresponds to six mineral groups and one background. Nevertheless, the value of K could be lower as well, for example the mineral group "Quartz + Magnetite + Biotite" could be unclassified due to the low amount of such minerals in the dataset. In order to be sure with the selection of the number of the clusters, various K values were evaluated. The evaluation is done by performing internal validation using sum of squared error.

- Fuzzy C-means clustering (unsupervised). The number of cluster (C) is determined

in similar fashion as in K-mean clustering. The fuzzifier constant is set to two.

- Random forest (supervised). The determination of number of trees (ntree) is done by evaluating the random forest classification using different ntree values. In general, more trees would lead to better performance and lower error at the expense of computational cost. By running several random forest classification using different ntree values, one can determine an optimum point where no significant improvement in performance is obtained when the ntree is increased (Oshiro et al., 2012). Nevertheless, Breiman (2001) stated that while using more trees is often unnecessary and computationally expensive, it does not harm the model.

- k-nearest neighbors (kNN) (supervised). Similar to other algorithms evaluated in this study, the determination of optimum number of neighbors is not straightforward (Naidoo et al., 2012). Small number of neighbors would increase the noise effect on the result, while large number of neighbors could supress the noise effect at a higher computational cost. Some methods have been developed elsewhere to determine optimum number of neighbors (Thanh Noi and Kappas, 2018; Hall et al., 2008), but essentially one could also try similar approach as in previous algorithms.

3.2.4.1 Feature-based supervised classification

The previously mentioned classification algorithms classify the voxels based on their grayscale values. An alternative to that is by using features of the voxels instead. Such features could be edges, corners, or blobs in the image. These features are extracted by convoluting the image using kernel functions, thereby generating a feature map of the image to be classified. Example of a Sobel kernel (Sobel, 2014) which extract the vertical (y-direction) edges in the image is shown in Equation 3.1. Rotating the kernel 90° would produce a new kernel for extracting the horizontal (x-direction) edges in the image. The modified image is referred as a feature map, in which different feature maps can be generated by convoluting the image with different kernels.

$$\begin{bmatrix} 1 & 2 & 1 \\ 0 & 0 & 0 \\ -1 & -2 & -1 \end{bmatrix} \tag{3.1}$$

In order to add another dimension in the feature based classification, the image can also be scaled in a Gaussian scale-space representation. This simply means that beside the xy space, the image is also represented as a family of images blurred with Gaussian filter of varying standard deviations (σ), or commonly referred as varying scales ($t = \sigma^2$) (Lindeberg, 2007). This then gives the possibility to extract the same feature (edges, blobs) but on a different scales. The scale itself affects the features that can be extracted from the image; at larger scales (higher standard deviation and more blurred) the image would lose details on smaller gangue grains while conversely at smaller scales more features

from smaller grains can be extracted. Mathematical illustration of feature extraction at different scales is shown in Figure 3.6.

a)

200	150	0	80	0
10	20	0	50	10
50	123	12	34	20
87	35	56	67	90
98	21	89	5	100

Image

$*$

0.07	0.12	0.07
0.12	0.20	0.12
0.07	0.12	0.07

Gaussian Kernel
($\sigma = 1$)

$=$

138.73	92.22	51.02	33.18	21.66
76.00	58.81	39.22	27.97	22.01
55.06	51.09	41.75	37.11	39.45
73.13	61.39	50.32	53.19	64.62
75.76	59.16	48.96	58.51	76.63

Image at scale 1
($t = \sigma^2 = 1$)

$*$

1	2	1
0	0	0
-1	-2	-1

Sobel Kernel
(Vertical)

$=$

0	1	0	0	0
0	0	0	0	0
0	0	0	0	0
0	0	0	0	0
0	0	0	0	0

Feature Map
(Scale 1)

b)

200	150	0	80	0
10	20	0	50	10
50	123	12	34	20
87	35	56	67	90
98	21	89	5	100

Image

$*$

0.10	0.12	0.10
0.12	0.13	0.12
0.10	0.12	0.10

Gaussian Kernel
($\sigma = 2$)

$=$

129.51	83.72	57.11	26.49	24.65
86.91	61.97	48.88	24.11	24.19
53.19	45.18	43.68	37.54	42.50
72.29	63.07	49.40	52.63	59.94
72.46	64.41	44.42	64.91	73.82

Image at scale 4
($t = \sigma^2 = 4$)

$*$

1	2	1
0	0	0
-1	-2	-1

Sobel Kernel
(Vertical)

$=$

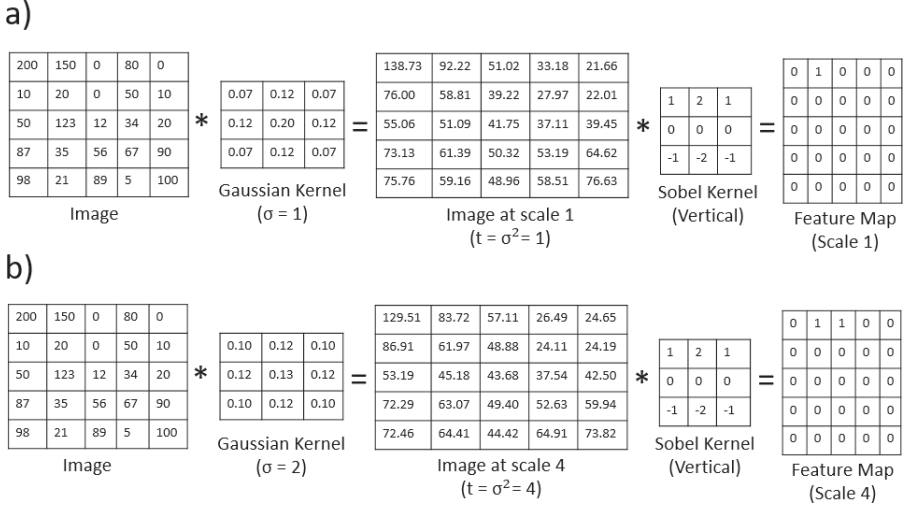| 0	1	1	0	0
0	0	0	0	0
0	0	0	0	0
0	0	0	0	0
0	0	0	0	0

Feature Map
(Scale 4)

Figure 3.6: Feature extraction in Gaussian scale-space, showing (a) Sobel feature extraction from image at scale 1 and (b) Sobel feature extraction from image at scale 4. The image is convoluted with Gaussian kernel of varying standard deviation, creating multiple images in different scales. The feature is extracted from the images in different scales, creating feature maps of different scales. The feature map in (b) is different from (a), which indicates that different image scales generate different feature maps

After collecting the feature maps at different scales, these features are matched with the training data. Then a classifier is built based on the training information, and consequently has more criteria to classify a voxel by looking at these different features. This of course comes with a cost; the classification process would be more computationally expensive. Feature based classification is shown in Figure 3.7

In this study, feature-based classification is performed to evaluate its applicability compared to grayscale-based classification. Edge features are extracted using 3 x 3 Sobel filter (both horizontal and vertical), while blobs and corners are extracted with difference of 3 x 3 Gaussians (Lindeberg, 2015) and the determinant of Hessian matrix (Lindeberg, 2013). Random forest classifier was trained using these features and the training data. All the feature extraction methods and random forest classifiers are available in the Trainable Weka Segmentation in Fiji/ImageJ. Some examples of these features extracted from the drill core μCT slice is shown in Figure 3.8
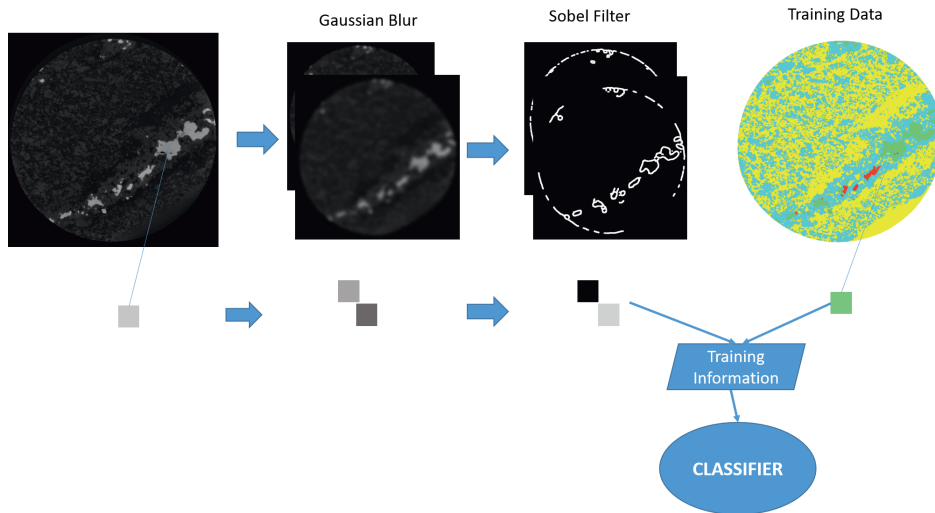
Figure 3.7: Feature-based classification. The image is blurred with Gaussian filter at varying standard deviations, representing various scales of the original image. The edge features are then extracted at different scales using Sobel filter, producing two feature maps of the mineral grains in the drill core (here the edge images are dilated for easier viewing). The two features are then matched with the training data, so that it can be used to train a classifier
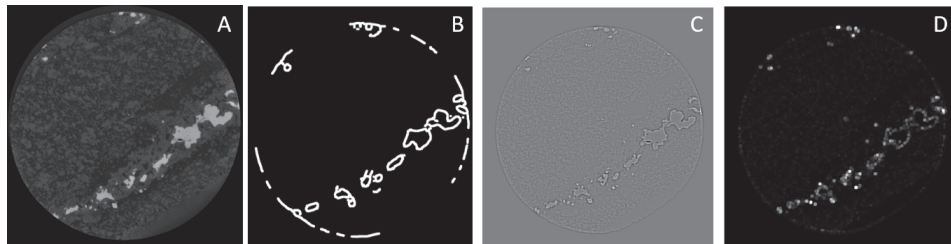
Figure 3.8: Example of feature maps used in this study, showing (A) original μCT slice, (B) Sobel Edge features, (C) Difference of Gaussians blob features, and (D) Hessian corner (and blob) features. These feature maps were fed to the classification scheme in Fig. 11 so that the applicability of each feature map in supervised classification of pyrite and chalcopyrite phases could be evaluated

3.2.4.2   Statistical methods in evaluating the classifiers

Statistical measures were taken to evaluate the performance of the classifiers by comparing to the ground truth. K-fold cross validation was used to evaluate the supervised classifiers. The method randomly sub-sampled the training data into K sub-samples. The training was done so that classifiers was trained based on the K - 1 of the sub-samples,

holding out one sub-sample for validation. The training is then repeated K amount of times with all sub-samples, in which after each training, validation was performed with the hold-out subsample, producing K amount of validation results. These K validation results were then averaged to evaluate the overall performance of the classifier. In this study, 10 fold cross validation was performed.

The ground truth is used to validate the classified voxels. In the study, the goal is to identify chalcopyrite out of the sulfide voxels (which consisted of chalcopyrite and pyrite), so the term positive is used for chalcopyrite, while negative is used for pyrite. Some statistical measures that can be calculated for validation are as follows:

- The True Positive Rate (TPR) and False Negative Rate (FNR), shown in Equation 3.2

$$TPR = \frac{correctly\ classified\ chalcopyrite\ voxels}{all\ chalcopyrite\ voxels} = 1 - FNR \qquad (3.2)$$

- The True Negative Rate (TNR) and False Positive Rate (FPR), shown in Equation 3.3

$$TNR = \frac{correctly\ classified\ pyrite\ voxels}{all\ pyrite\ voxels} = 1 - FPR \qquad (3.3)$$

- The overall accuracy (OA), shown in Equation 3.4

$$OA = \frac{correctly\ classified\ voxels}{all\ voxels} = 1 - FNR \qquad (3.4)$$

Furthermore, the behavior of the classifier could be adjusted by changing the probability threshold (P). A classifier returns the score on how confident it is in classifying a voxel to each respective category. This score varies from 0 to 1, in which if the score for chalcopyrite is x, then for pyrite it will be $1 - x$. The classifier will only classify a voxel ($v_{x,y,z}$) as chalcopyrite only if the score is higher than the probability threshold, as shown in Equation 3.4

$$x > P(v_{x,y,z}|chalcopyrite) \Rightarrow v_{x,y,z} = chalcopyrite \qquad (3.5)$$

Varying the threshold would lead to different TPR and TNR values. An ideal classifier would be able to identify all chalcopyrite (TPR = 1) while at the same time identify all pyrite (TNR = 1). These differrnt TPR and TNR values can be plotted to build a receriver operating characteristic (ROC) curve. The curve gives an information on the discrimination ability of the classifiers as the probability threshold is varied:

- Increasing threshold means that the classifier would only classify a voxel as chalcopyrite if it is very confident in doing so. This would lead to lower TPR, as the

"borderline" voxels (that have similar characteristics to pyrite) would not be classified as chalcopyrite, leading to decrease of correctly classified chalcopyrite voxels.

- Decreasing the threshold results in less sensitive classifiers. It would classify voxels as chalcopyrite even if it is not very confident. This would naturally increase the TPR, but at the same time more pyrite voxels would be mis-classified to chalcopyrite.

- The area under the ROC curve (AUC) also gives an idea about the classifier's performance. The aforementioned accuracy measures (TPR, TNR, OA) only gives information about the classifier in one operating point of probability threshold, AUC gives an idea about the classifier's performance over a range of probability threshold values (Bradley, 1997).

The confidence score of the classifiers can be obtained as follows:

- The confidence score of random forest classifier is based on the fraction of total of number of trees that vote for chalcopyrite.

- For kNN classifier, similar method is also applied. The confidence score is the fraction of the k nearest neighbors that belongs to chalcopyrite.

3.2.5   Image registration and creation of ground truth

Since that BSE mineral map in Figure 3.5 is acquired from different set of instruments (therefore different image characteristic), a method must be devised on how to directly use the mineral map information on Figure 3.5 to train the classifiers. The most straightforward way would be to manually annotate the corresponding µCT slice according to the BSE mineral map, but this is quite laborious. In this study, image registration is employed to align the BSE mineral map to the corresponding µCT slice. Image registration refers to the transformation of an image into a specified coordinate systems (Brown, 1992). The alignment of both images allows automated annotation of the pixels in the µCT slice based on the BSE mineral map, creating a ground truth to train the classifiers.

The image registration technique is based on matching the features between two images. Speeded up robust features (SURF) (Bay et al., 2008) is used to extract these features. SURF algorithm extract mostly blobs (voxel regions that differ from surrounding regions) in the image, which in this case the blobs would be the mineral grains. Example of the features detected using SURF algorithm is shown in Figure 3.9, while the whole procedure of alignment and image registration is shown in Figure 3.10

The registration procedure shown in Figure 3.10 did produce a good match especially within the vein area (sulphide phase). Nevertheless, some mismatches can be seen particularly in the right of the vein. These mismatches can be explained by the fact that
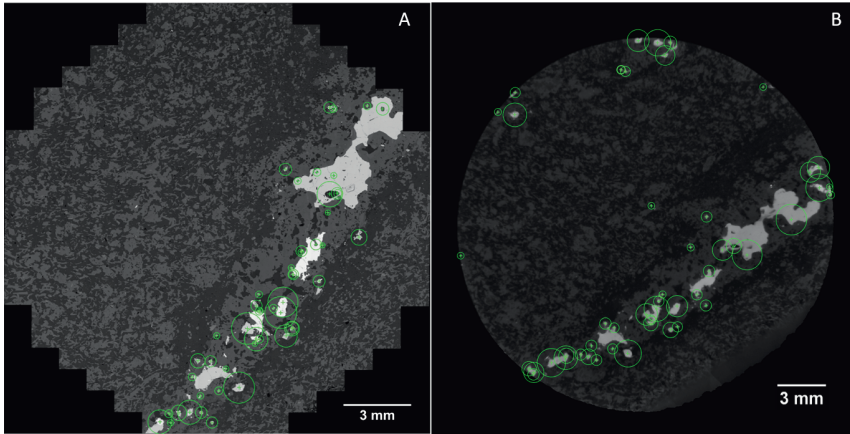
Figure 3.9: Detected SURF features (denoted in green circles) from (A) BSE image (resolution 3 μm) and (B) μCT slice (resolution 13 μm). These features corresponds well with the sulfide grains in the core. The points of interest from both images are matched, so that a transformation matrix that could align both images can be calculated

such registration procedure would not be accurate if the thin section for SEM-EDS is not cut perfectly parallel with the μCT slice plane. While this issue can be addressed using 2D-to-3D registration scheme, it would be more complex than the current proposed algorithm.

Around 84.4% of the sulphide pixels in the BSE mineral map was accurately matched with the corresponding sulphide pixels in the μCT slice. Out of this, 92.8% of the chalcopyrite pixels in the BSE mineral map was accurately matched. The registration and annotation procedure shown in Figure 3.10 was quite fast; it took around 7 s to create the fully annotated training data shown in Figure 3.10(C).

3.2.5.1 Ground truth for test data

In order to evaluate the generality of the classifiers, the classifiers are tested with an "unseen data", i.e. data that have never been used for training. Since cross-validation was used for training the classifiers, this means that all parts of the training data shown in Figure 3.10 have already been used. An independent test data is therefore created from another μCT slice.
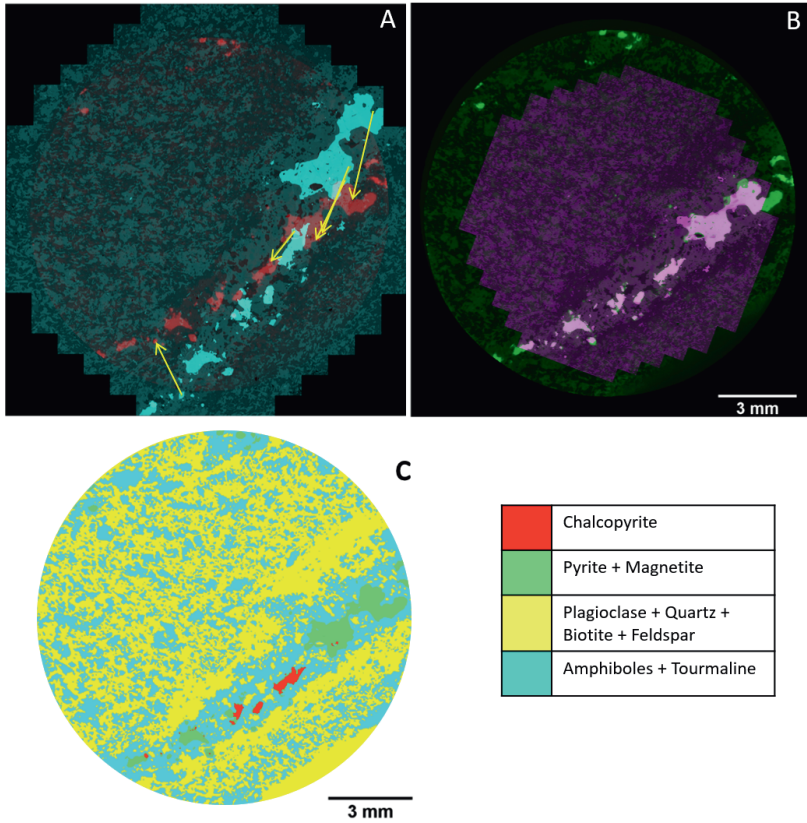
Figure 3.10: Image alignment and training data creation, showing (A) Matched feature points between two images with arrows showing the transformation direction, (B) both images aligned, magenta for BSE image, and green for the μCT slice, and (C) 2DμCT slice for training data, with chalcopyrite pixels annotated based on alignment with BSE mineral map. The same color coding would be used throughout this chapter, except if other information is given

Then, the question becomes how to create the ground truth for another μCT slice, since the ground truth for the test data must also be known for validation. Since the μCT data in this study has a relatively high spatial resolution (13 μm), this means that adjacent μCT slice represents 13 μm distance in the drill core. It can then be suggested two adjacent μCT slices would not differ greatly. Therefore, the same transformation matrix obtained from the previous image registration procedure can be used to align the BSE mineral map to the adjacent μCT slice. The adjacent μCT slice then is automatically annotated to create the ground truth which would not be used to train the classifiers, but used later in the testing part. This test data is shown in Figure 3.11.
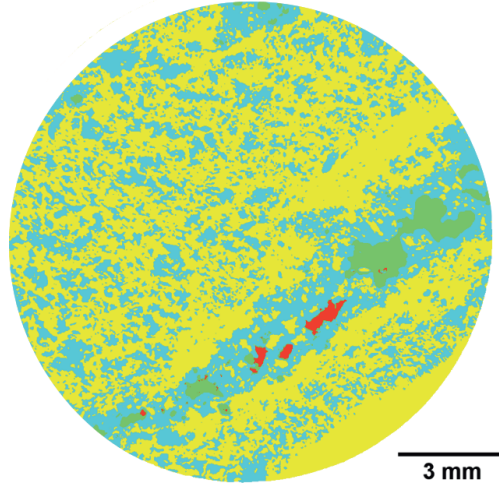
Figure 3.11: Test data. The pixels were annotated using the same procedure shown in Figure 3.10. Approximately 84.6% of sulfide pixels and 92.8% of the chalcopyrite pixels in the BSE image were accurately matched with the sulfide pixels in the µCT slice. Mineral color legend is the same as in Figure 3.10(C)

3.3 Results and discussion

The histogram of µCT dataset in this study is shown in Figure 3.12. While peaks gangue and sulphide mineral groups are visible, differentiating mineral phases within this group is not straightforward. Several different machine learning algorithms are evaluated to tackle this problem.

3.3.1 Unsupervised classification

3.3.1.1 Determination of number of clusters

The relationship between classification error and number of clusters is shown Figure 3.13. The problem with using error metrics such as Sum of Squared Error (SSE) is that in classification problems, the error always goes down if the cluster is increased. In the extreme point, when the cluster numbers equal number of pixels, the error would go to zero (as the distance between the pixel and cluster centroid is zero), but it would defeat the purpose of clustering.

Therefore, the optimum number of clusters can be defined as the point where no significant decrease in error is obtained. Such point could be obtained by considering the point
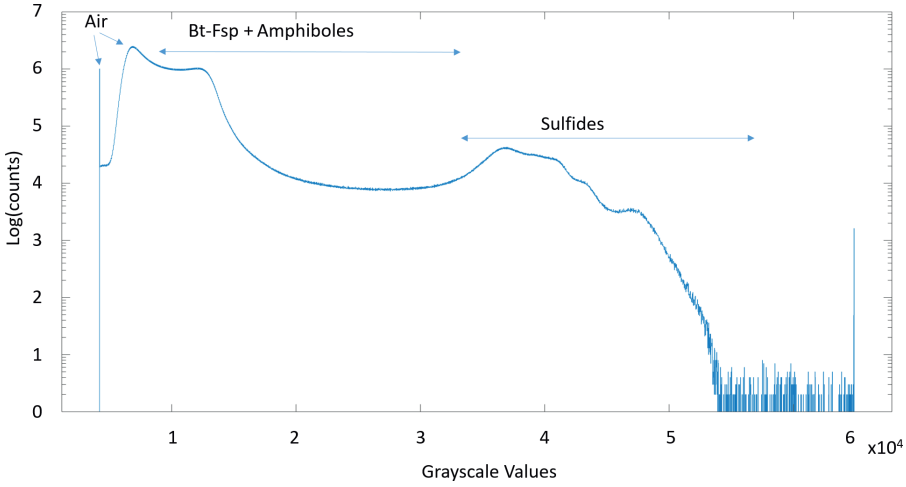
Figure 3.12: Histogram of μCT *dataset (after illumination correction). Major visible peaks represent air, gangue minerals (Biotite, Feldspars, Amphiboles), as well as the sulfide minerals (chalcopyrite and pyrite)*

where the tangent of the curve starts to level out (plateau is reached), often referred as the "elbow" of the curve (Bholowalia and Kumar, 2014) as shown in Figure 3.13. In order to illustrate this further, some results of the K-means classification are shown in 3.14.
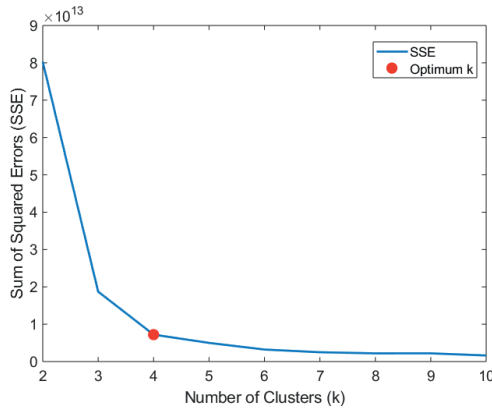
Figure 3.13: Relationship between SSE and K*, with the optimum value of* K *indicated by the red dot*
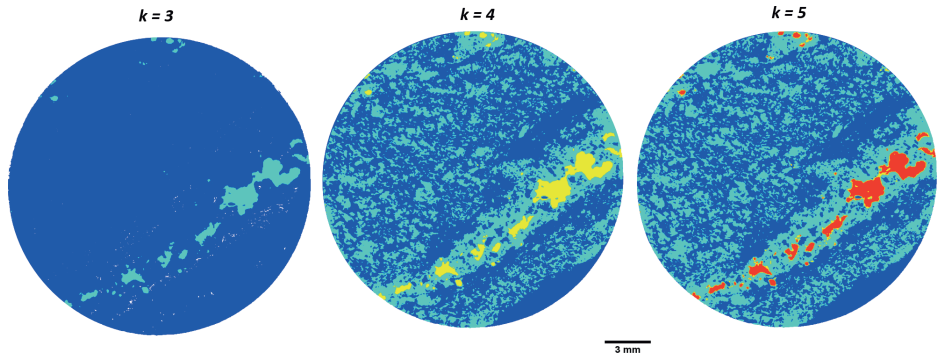
Figure 3.14: Some results of the K-means classification with different K values. Adding a new clusters from three to four clusters produced a new information in the new cluster (a phase was separated to the new cluster), but increasing to five clusters did not produce any new information (no phase was separated further)

Table 3.2: Phase percentage of the mineral maps from both K-means and FCM, showing minimal difference between the classifiers. Minor differences exist in comparison to BSE mineral map due to difference in spatial resolution between the 2D µCT slice and BSE image, but overall both techniques show good correspondence

Color	Phase	K-means (%)	FCM (%)	BSE Mineral Map (%)
	Chalcopyrite, Pyrite, Magnetite	3.4	3.4	4.4
	Plagioclase, Quartz, Biotite, Feldspar	57.8	57.3	55.7
	Amphiboles, Tourmaline	38.8	39.3	39.9

3.3.1.2   Results of K-means and FCM classification

Using $K = 4$, the results of both K-means and FCM are shown in Figure 3.15 and Table 3.2. Both classifications are performed until the centroids are stable within less than 0.1% difference. The time required is calculated with one µCT slice corresponding to 2008 x 2048 pixels, with K-means and FCM requiring 4.5 and 11.9 s respectively. Similar results were obtained for both classification techniques with K-means requiring slightly less time. The pixel differences between both classification algorithms are mostly localized in the phase boundaries, as shown in Figure 3.15.

One thing remain clear, both unsupervised classification techniques did not succeed in segmenting between chalcopyrite and pyrite, as compared to the BSE mineral map in Figure 3.5. Therefore the use of supervised classification technique is evaluated next.
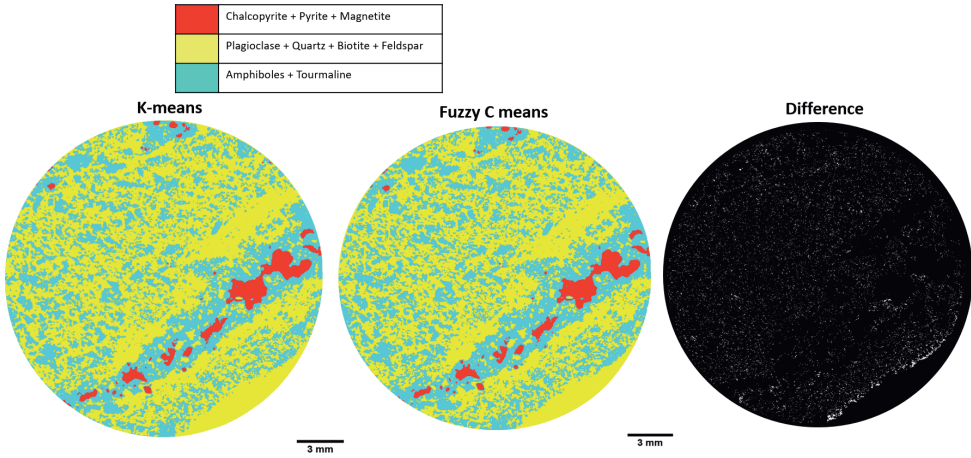
Figure 3.15: Mineral mapping using unsupervised classification (k-means and FCM). Three phases were identified. The "Difference" image shows a binary image with pixels that are classified differently in the two classification schemes, which corresponds to 86,838 pixels, or 2.11% out of the total 2008×2048 pixels in the image

3.3.2   Supervised classification

3.3.2.1   Tuning of classifiers' parameters

Both OA and AUC is used to evaluate the classifiers' performance. While OA is the most straightforward metric to evaluate the classifier's performance, it cannot assess the performance of specific classes (Thanh Noi and Kappas, 2018). Furthermore, as the training data is imbalanced (chalcopyrite class is less than pyrite class), the OA value might be deceiving as the rare class might be classified poorly (He and Garcia, 2008). Therefore AUC is also taken to evaluate the classifiers in order to take into account the class imbalance in the dataset. After performing classification repeatedly using various classifiers' parameters, the value of OA and AUC for both classifiers are shown in Figure 3.16 and 3.17.

The performance of both classifiers was increased up until a certain level in which further increase of the complexity of the classifiers would not necessarily give better performance. One noticeable difference between kNN and random forest classifier is that while increasing ntree in random forest would always lead to better or similar performance, the same cannot be said kNN classifier. As shown in Figure 3.16, the AUC of kNN decreases when k is increased. The decrease in OA is less clear in Figure 3.17, but around 0.2% decrease was observed. Therefore in kNN, there exists an "optimum" point where the increase of k would worsen the predictive capability of the classifier.
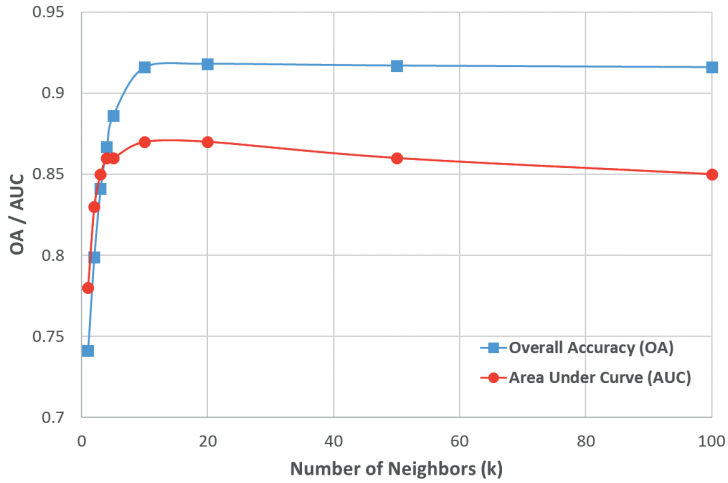
Figure 3.16: Effect of k to the performance of the kNN classifier
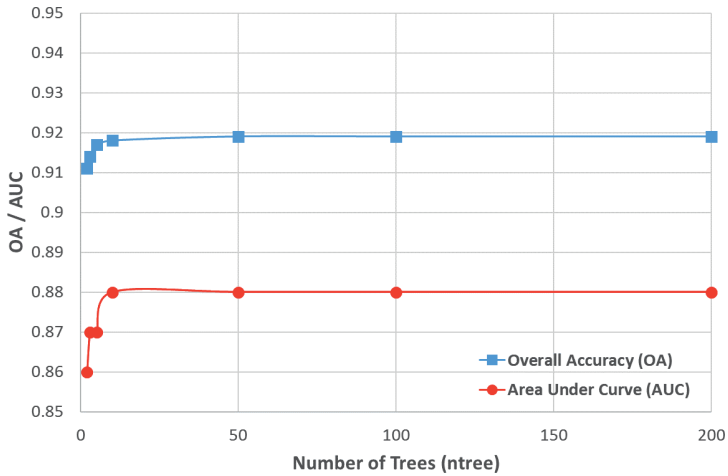
Figure 3.17: Effect of ntree to the performance of random forest classifier

Besides the accuracy, the computational cost must also be considered when determining the optimum parameter for the classifiers. This is shown in Figure 3.18. In general the random forest classifier is considerably more complex than kNN classifier, as shown by the training time. Additionally, increasing the number of trees in random forest led to significant increase of computational complexity. This increase was less prevalent for kNN classifiers, especially for less than 50 neighbors. Based on the accuracy and computational time, the optimum number of tree (ntree) is determined to be 10, while
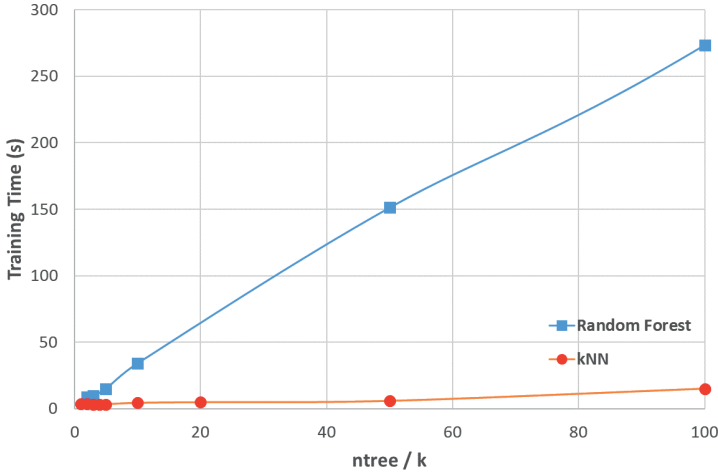
Figure 3.18: Effect of ntree and k to the training time of random forest and kNN classifier respectively. Training time was obtained based on MATLAB implementation of supervised classification with 10-fold cross-validation

the optimum number of neighbors (k) is determined to be 20.

3.3.2.2   Grayscale-based classification

The grayscale values of each phase in the training data in Figure 3.10(C) was used to train the classifiers. Observe that since the ground truth creation procedure in Figure 3.10 only able to define chalcopyrite phase, the classification performed only concerns between pyrite and chalcopyrite. The total training data then becomes 88,980 pixels, which 13.5% out of the data belongs chalcopyrite, and the rest is pyrite. Cross-valdiation (10-fold) is used to evaluate the trained classifiers; results are given in Figure 3.19 and Table 3.3.

Table 3.3: Training performance of different algorithms in grayscale-based classification

Algorithm	Training time (s)	TPR (%)	TNR (%)
kNN (k = 20)	4.9	60	97
Random Forest (ntree = 10)	34.2	60	97

After the classifiers are trained, they are evaluated against the test data. The total test data are 88,644 pixels, in which around 14% of those are chalcopyrite. The test data is independent of the training data, so that the generality and robustness of the classifiers can be evaluated. The results of the classifier's testing are shown in Figure 3.20 and Table 3.4
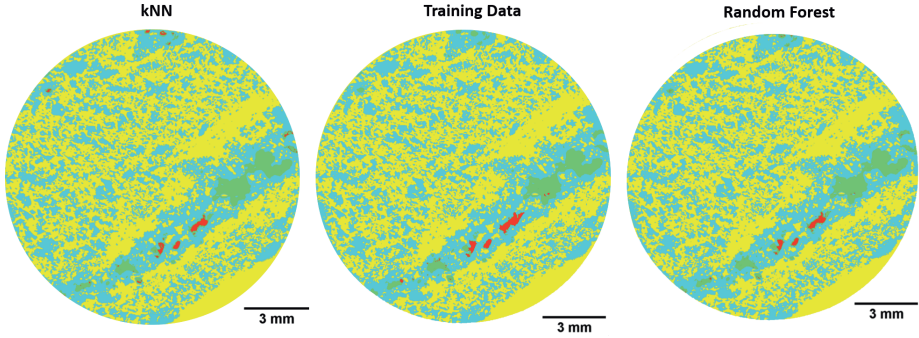
Figure 3.19: Comparison of grayscale-based classified training data with the ground truth
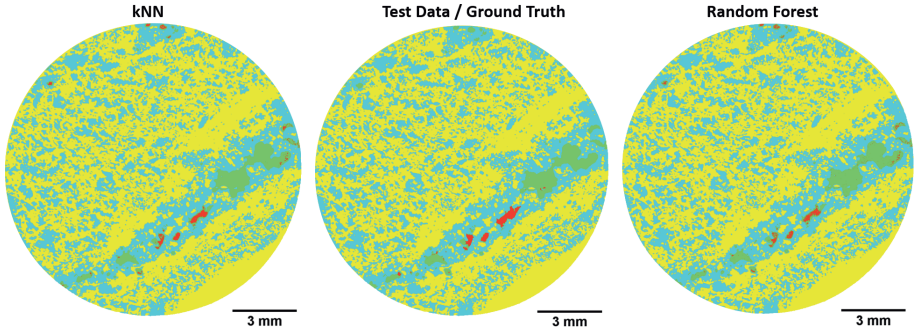
Figure 3.20: Comparison of classified test data with the ground truth

Generally, a classifier is considered as robust if the testing performance is similar as the training performance (Xu and Mannor, 2012). By comparing Table 3.3 and 3.4, it can be seen that the accuracy of the classifiers decrease as they are evaluated on the test data. kNN classifiers showed better robustness as its testing performance fared better than random forest classifiers. The training time of kNN classifier is also significantly lower than that of random forest, which is explainable due to the nature of kNN classifier as lazy learning.

One noticeable result is that while the true negative of the classifiers are high, the same cannot be said for the true positive. This means that the classifiers only succeed 50-60% of the time in identifying the chalcopyrite pixels. This can be explained due to the fatc that there is a significant overlap between the grayscale values of the chalcopyrite and pyrite as shown in Figure 3.21. Due to this overlap, this means that the grayscale values of chalcopyrite and pyrite are not mutually exclusive; some of the pixels have the grayscale values that could be classified as both chalcopyrite and pyrite.

Table 3.4: *Testing performance of different algorithms in grayscale-based classification. The testing time is taken as the time required by the classifiers to classify the test data.*

Algorithm	Testing time (s)	TPR (%)	TNR (%)
kNN (k = 20)	0.4	57	96
Random Forest (ntree = 10)	0.5	50	95
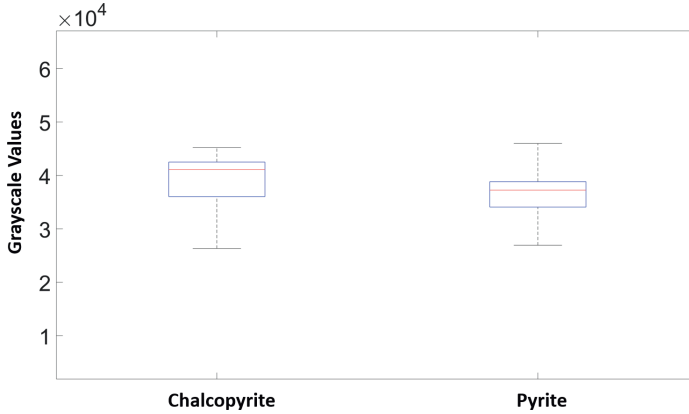
Figure 3.21: *Boxplot of grayscale values of chalcopyrite and pyrite obtained from the training data, showing a considerable overlap between the phases making it difficult to segment these phases based on their grayscale values*

3.3.2.3   Feature-based classification

Due to this overlap, it might be useful to try to use the features instead to classify between the chalcopyrite and pyrite. Therefore, classifiers are trained using features extracted from the training data in Figure 3.10(C), and subsequently tested against the independent test data (Figure 3.11). The results are shown in Figure 3.22 and Table 3.5.

Table 3.5: *Classification performance of different feature extractors. Random forest was used as the classifier. All 4,112,385 pixels in the training data were used to create the feature vectors, hence the increase in training time. The true positive and true negative is based on the testing with the test data*

Feature Extractor	Training time	TPR (%)	TNR (%)
Sobel filter	3h 35m 8s	60	96
Determinant of Hessian	5h 36m 39s	57	97
Differences of Gaussian	4h 59m 8s	53	97

Feature-based classification was also found to be unsatisfactory. Features such as edges,
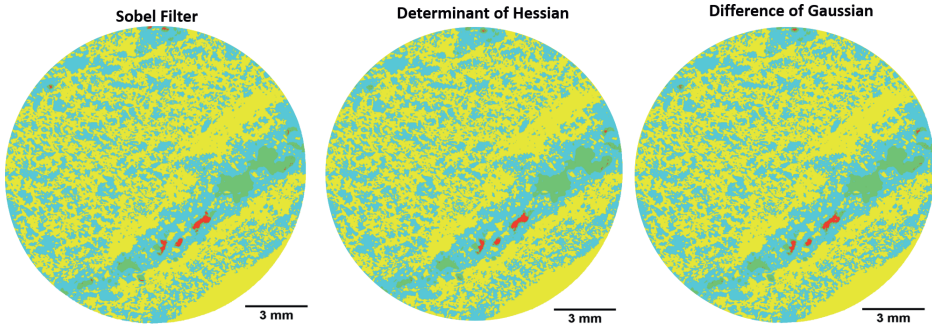
Figure 3.22: Classified test data using feature-based classifications

corners, and blobs of chalcopyrite and pyrite pixels were not found to be the discriminating factor between both phases. Nevertheless, comparing between Table 3.4 (for random forest classification) and 3.5, the performance of feature-based classification as relatively better. This indicates that by using features extracted in different scales, one can build a classifier that generalizes better than using solely the grayscale values. However, it should be noted that feature-based classifications require significantly longer training time than grayscale-based classifications.

3.3.3   Evaluation of performance and results

Unsupervised classification was found to be satisfactory to classify between the gangue, background, and the sulphide minerals with results showing good correspondence with the BSE mineral map while requiring short computational time. It needs to be noted that the difference in grayscale values between these phases are clear enough so that unsupervised classification can be performed. Nevertheless, supervised classification is needed to segment between chalcopyrite and pyrite within the sulphide phases.

Using the BSE mineral map as a reference and training data, chalcopyrite and pyrite can be segmented using supervised classifiers to some extent, as seen in Table 3.4 and 3.5. As discussed earlier, the behavior of the classifiers can be altered to obtain favorable accuracy, and this is illustrated through the ROC curve shown in Figure 3.23. This behaviour change is shown by moving the red dot along the curve in Figure 3.23. It is therefore clear that there would be no point where the classifiers could classify all pyrite and chalcopyrite voxels correctly, i.e. by reaching 100% TPR and 0% FPR (top left corner of the graph). Furthermore, due to the class imbalance (pyrite being higher than chalcopyrite), the classifier tends to decrease the false positive rate, as the 1% misclassified pyrite weighs higher in the overall accuracy than 1% chalcopyrite being correctly classified.
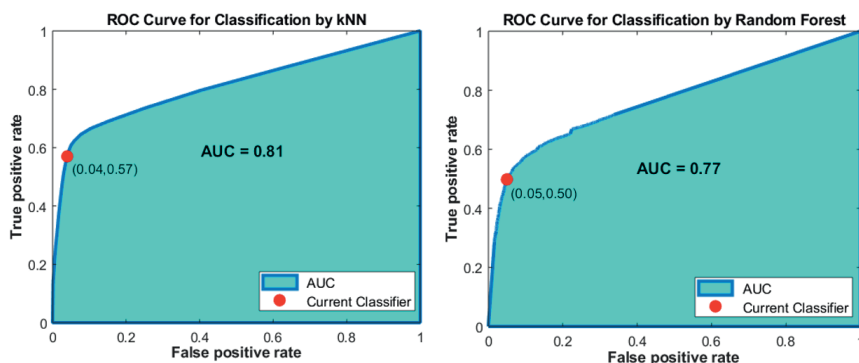
Figure 3.23: ROC curve for Random Forest and kNN classifiers. The curve describes the relationship between FPR and TPR, with the red dot indicates the current classifier. The test data was used to generate the curve

Feature based classification did not significantly increase the classifiers' performance as seen in Table 3.5. This is due to the fact that features such as edges, corners, and blobs were also built based on the grayscale values of the pixels, with addition of their relationship to other pixels in the neighborhood. Since the original grasycale values of the pixels were too similar and almost indistinguishable, the features would also be difficult to discriminate. Nevertheless, feature based classification tends to generalize better than the grayscale-based classification.

Another notable difference between feature-based and grayscale-based classification can be seen in Figure 3.24. In grayscale-based classification, the voxels' grayscale value is the sole criteria in classifying pyrite and chalcopyrite. This leads to many scattered chalcopyrite voxels in the pyrite grain shown in Figure 3.24(A). This phenomena was not observed in feature-based classification, as shown in Figure 3.24(B). Feature-based classification is especially well suited when dealing with grain boundaries (Wang et al., 2015), as it uses features that could represent grains (voxel regions) when segmenting between minerals. This in turns produces better segmentation between the grains in the ore.

Nevertheless, a significant difference is observed when evaluating the mineralogical result of 3D µCT data and the conventional 2D BSE mineral map. The mineralogical results given Table 7 shows the typical stereological error exhibited by 2D based analysis in overestimating the mineralogy. The difference in 2D µCT slice and 2D SEM-EDS can be explained by the loss of details in the µCT due to lower spatial resolution.

Figure 3.24: *Comparison of random forest classified mineral map showing chalcopyrite (red), pyrite (green), and gangue (gray), using (A) grayscale based classification, and (B) feature (determinant of Hessian) based classification. While grayscale based classification operates on individual voxels, determinant of Hessian operates based on blobs/region of voxels, which resulted in better segmentation between grains as shown in (B)*

Table 3.6: *Simplified mineralogy (by area or volume) obtained from SEM and µCT. Note: kNN=k Nearest Neighbors, RF=Random Forest, SF=Sobel Filter followed by RF, DoH=Determinant of Hessian followed by RF, and DoG=Difference of Gaussians followed by RF*

Minerals	2D SEM-EDS (%)	2D µCT (%)	3D µCT (%)				
			kNN	RF	SF	DoH	DoG
Amphiboles Tourmaline	39.92	39.29	37.26	37.26	40.33	40.33	40.33
Plagioclase Quartz Biotite Feldspar	55.67	57.28	59.47	59.47	56.77	56.77	56.77
Pyrite Magnetite	3.7	3.00	2.90	2.91	2.73	2.72	2.73
Chalcopyrite	0.71	0.43	0.37	0.36	0.17	0.18	0.17

3.4 Conclusion

In order to address the challenge of mineral segmentation using µCT, the application of machine learning algorithms have been presented in this Chapter. The main findings of this study are as follows:

- Unsupervised classification provided a rapid and satisfactory segmentation between gangue and sulphide minerals that differs significantly in grayscale values. In determining the optimum number of clusters, several classification runs were performed

and the SSE is evaluated. The optimum number of clusters is obtained when the decrease in error becomes less significant. The result suggested that the performance of both K-means and FCM is similar, but with K-means requiring less computational time.

- Supervised classification was found to address the issue of segmentation between chalcopyrite and pyrite phases to a certain extent. Using directly the voxel values in grayscale-based classification offers a simple and rapid approach in segmenting these minerals with reasonable accuracy. The results suggested that kNN performed better than random forest classifiers in all aspect; it generalized better and require less computational time. The classifiers parameters were also tuned by running several runs of classification, in which the optimum parameters were determined as the point where further increase of classifiers' complexity leads to insignificant performance gain.

- Feature based classification offers a better alternative in segmenting between the mineral grains. The results of this study also suggested that feature-based classifiers generalized better than grayscale-based classifiers. Feature-based classifiers could be an alternative when textural information such as grain size and shape needs to be extracted after the segmentation.

These concluding points are summarized in Table 3.7

Table 3.7: Applicability of the various categories of machine learning techniques

Method	Applicability	Notes
Unsupervised	Segmentation between gangues and sulphides (differs signifiicantly in grayscale values)	Rapid, simple, and straightforward approach when reference data is not available
Supervised	Segmentation between chalcopyrite and pyrite (similar grayscale values)	Limited by the overlapping grayscale values despite the use of reference data
Feature-based	Addresses the grain morphology better	Limited by the expensive computational cost

Besides the machine learning applications, a methodology to create ground truth for training and testing data based on SEM-EDS measurement has also been presented. The methodology is relatively rapid (around 7s) and largely automated; the user only needs to specify which μCT slice corresponds to BSE mineral map. This need could also be alleviated by quantifying the errors of the BSE-μCT feature matching process, and the μCT slice that has the lowest error would be determined as the corresponding slice.

Another advantage of this method is that it works on pixel-level i.e. information of each pixel that belongs to a phase can be transferred to a μCT slice, therefore allowing the definition of multi-mineral grains. Moreover, since it is based on features, it is more robust to characteristic differences between the images. Therefore, the methodology can potentially be used as a tool to combine mineralogical information from different sets of analytical equipments such as hyperspectral or microscopy image in order to assist

the μCT mineral segmentation process. Nevertheless, the methodology is limited on the parallel cutting of the μCT sample for the thin section, as it must be cut exactly in parallel to achieve perfect correspondence between the two images.

The main limitation of the application of machine learning in μCT dataset lies on the dataset itself, particularly whether the grayscale values of mineral phases in the sample are different enough to be segmented. In this study, due to the significant overlaps in the grayscale values between chalcopyrite and pyrite, the classifier could not fully differentiate between the two phases. Increasing the classifier's sensitivity to one phase will decrease the sensitivity to the other phase.

This study shows clearly that the data processing method of μCT analysis can only achieve accuracy as high as the dataset itself allows. If the scanning conditions are not optimized, then the downstream data processing of the μCT image would not be fully accurate. It is therefore very important to acquire a reliable dataset where the minerals can be segmented accurately. If the phases in the dataset have a clear difference in grayscale values, then even a simple unsupervised classification should produce satisfactory results.

CHAPTER 4

Conclusion and Future Work

In this chapter, the preliminary conclusions and plans for future work in the scope of the PhD work are presented.

4.1 Conclusion

Some concluding remarks can be drawn by connecting the main body of the licentiate which presented in Chapter 2 and 3 to the thesis objectives and research questions presented in Chapter 1. The research questions are broken down into several parts so that answers can be given accordingly to each part of the question.

1. How can mineralogical information be extracted accurately using μCT systems?
   The mineralogical information can be extracted using various different segmentation techniques such as thresholding, watershed, and machine learning techniques. Otsu thresholding can be used for simple cases where the minerals exhibits significant difference in grayscale values, while maximum entropy thresholding can be used in similar cases but when the mineral is not abundant in the sample. Watershed segmentation is particularly useful for particulate samples. Image features such as edges, blobs, and corners can be used as an alternative to grayscale values for the basis of the segmentation, and it has been shown further in the case study in Chapter 3 that it could address the grains and particles morphology better. In more challenging cases where the grayscale values of the minerals are similar, machine learning techniques can be used. However, the case study presented in Chapter 3 revealed that machine learning is as good as the μCT dataset itself; if the there exist a considerable overlap in grayscale values between the minerals,

it would be very difficult to fully separate the minerals even if additional data from SEM-EDS is used to guide the segmentation. This work suggested that the key to obtaining accurate mineralogical information lies on the optimization of the scanning conditions so that the minerals in the μCT dataset are distinguishable with simple segmentation techniques.

2. How can structural texture information be extracted accurately using μCT systems?
   Structural texture information such as grain and particle morphology can be extracted from 3D μCT data using various techniques. Granulometry by opening is the most widely used technique to extract size distribution information from the 3D data. Shape information of the particles (or grains) can be extracted by approximation using regular objects such as polygons and spheres, or analytically by mapping the particles in a spherical coordinate system. The orientation of the grains in ores can be extracted using mean intercept length. The accuracy of these techniques are largely dependent to the preceding mineral segmentation techniques, as the particles and grains are defined first by the segmentation process.

3. How can stationary texture information be extracted accurately using μCT systems?
   Stationary textures can be extracted quantitatively from 3D μCT data using GLCM and LBP. The former has been shown to be useful for classification of 3D drill core textures, while the latter for textural classification of carbonate rocks. Further studies needs to be devoted to evaluate the applicability of these techniques for texture quantification and classification of various different ore types.

4. How can surface texture information be extracted accurately using μCT systems?
   Surface texture such as mineral exposure can be extracted from 3D image using distance transformation as well as matching the marching-cube vertices between the particles and the mineral grains. The concept of mineral exposure is unique to 3D image, and certainly is one of the most promising aspect of 3D μCT mineral characterization.

5. How to use the extracted (3D) ore properties from μCT data in a geometallurgical program?
   The literature review conducted in the Chapter 2 suggested the relevances of these 3D ore properties in geometallurgy. The information of shape and interfacial area of the progeny particles could be used for breakage modelling, which is a key step in particle-based geometallurgy. Mineralogy and texture information (structural, stationary, and surface) could be used to as a parameter in process modelling, in which empirical models could be be generated through experiments in the framework of proxy-based geometallurgy. The ore particles before, during, and after the experiments could be subjected to μCT analysis, in which then the process modelling can be coupled with the 3D ore properties. The quantification and classification of mineral textures for geometallurgy could be enriched by the use of 3D information.

These textural classes represent different ore types that are expected to behave differently in the process, therefore the need of more accurate information to describe textures so that more comprehensive process prediction could be performed.

4.2 Future work

Coming back to the framework of this study given in Figure 1.4, an illustration of the future plan of this PhD is shown in Figure 4.1. In the near future, the work should be orientated to evaluate the potential quantification methods of ore textures with 3D µCT. After the textures are quantified, classification of different textures would be performed and validated with the core logging information. This work is denoted as "FW1" in the Figure 4.1. Further, the work should also evaluate the reliability of µCT systems in liberation measurements of ore particles and comparing it with traditional automated mineralogical systems. This work is denoted as "FW2" in the Figure 4.1. Up until the writing of this licentiate thesis, some new drill core materials have been obtained as well as imaged with µCT. These 3D images represented different ore types, so the plan is to perform some texture quantification of these various ore types and evaluate how these different ore types can be classified. With some information about textures and mineralogy, a suitable ore type can be selected for comminution and liberation measurement.
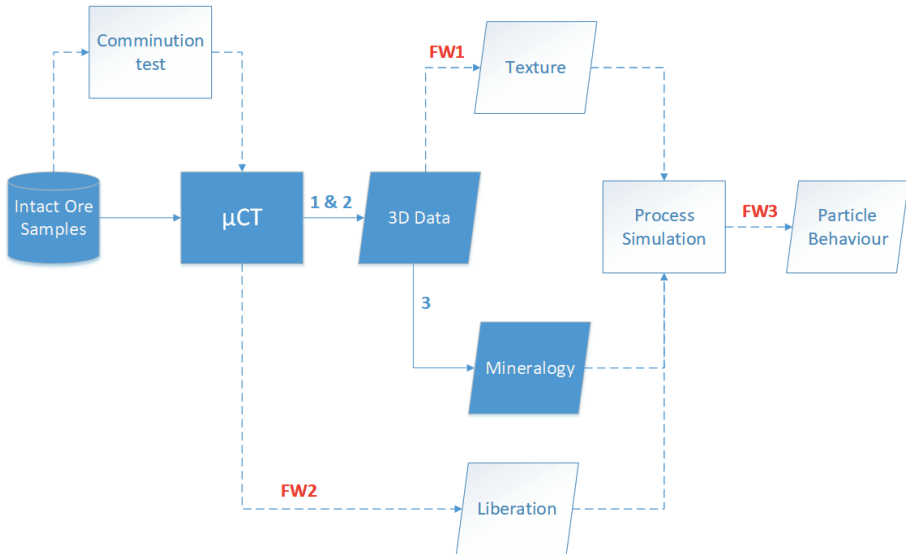
Figure 4.1: Future tasks in the scope of the PhD work

Finally to complete the scope of geometallurgy and using all the µCT data processing methods that have been reviewed and developed, the 3D µCT particle data would be used in a particle-based process simulation so that the particle behavior could be predicted. As a benchmark, the same process simulation should be performed but using 2D particle data. The particle tracking technique developed by Lamberg and Vianna (2007) which has been implemented in the particle-based process modelling of wet low intensity magnetic separator (WLIMS) operations by Parian et al. (2016) could be a useful starting point in working with the 3D particle-based process modelling and simulation. This work is denoted as "FW3" in Figure 4.1. The software implementation of particle tracking algorithm by Lamberg and Vianna (2007) has been largely done together with Outotec during the secondment period. Sampling campaign has also been performed in Pyhäsalmi flotation circuit in Finland (a photo taken during the campaign is shown in Figure 4.2), in which the samples could be used for the particle-based process modelling. The samples then can be imaged with µCT and subsequently used to perform the particle-based process simulation using 3D data.

Figure 4.2: Sampling of flotation cells in Pyhäsalmi concentrator plant, Finland

References

Aasly, K. and Ellefmo, S. (2014). Geometallurgy applied to industrial minerals operations. *Mineralproduksjon*, 5:21–34.

Alikarami, R., Andò, E., Gkiousas-Kapnisis, M., Torabi, A., and Viggiani, G. (2015). Strain localisation and grain breakage in sand under shearing at high mean stress: insights from in situ X-ray tomography. *Acta Geotechnica*, 10(1):15–30.

Alves dos Santos, N. (2018). Modelling flotation per size liberation class – Part 3 – Modelling recoveries using particle surface area. *Minerals Engineering*, 129:15–23.

Alves dos Santos, N. and Galery, R. (2018). Modelling flotation per size liberation class – Part 2 – Evaluating flotation per class. *Minerals Engineering*, 129:24–36.

Andrä, H., Combaret, N., Dvorkin, J., Glatt, E., Han, J., Kabel, M., Keehm, Y., Krzikalla, F., Lee, M., and Madonna, C. (2013). Digital rock physics benchmarks—Part I: Imaging and segmentation. *Computers & Geosciences*, 50:25–32.

Arganda-Carreras, I., Kaynig, V., Rueden, C., Eliceiri, K. W., Schindelin, J., Cardona, A., and Sebastian Seung, H. (2017). Trainable Weka Segmentation: a machine learning tool for microscopy pixel classification. *Bioinformatics*, 33(15):2424–2426.

Arthur, D. and Vassilvitskii, S. (2007). k-means++: The advantages of careful seeding. In *Proceedings of the eighteenth annual ACM-SIAM symposium on Discrete algorithms*, pages 1027–1035. Society for Industrial and Applied Mathematics.

Artioli, G., Cerulli, T., Cruciani, G., Dalconi, M. C., Ferrari, G., Parisatto, M., Rack, A., and Tucoulou, R. (2010). X-ray diffraction microtomography (XRD-CT), a novel tool for non-invasive mapping of phase development in cement materials. *Analytical and Bioanalytical Chemistry*, 397(6):2131–2136.

Baklanova, O. E. and Baklanov, M. A. (2016). Methods and Algorithms of Image Recognition for Mineral Rocks in the Mining Industry. In *International Conference in Swarm Intelligence*, pages 253–262. Springer.

Bam, L., Miller, J., Becker, M., de Beer, F., and Basson, I. (2016). *X-ray Computed Tomography – Determination of Rapid Scanning Parameters for Geometallurgical Analysis of Iron Ore*.

Bam, L. C., Miller, J. A., Becker, M., and Basson, I. J. (2019). X-ray computed tomography: Practical evaluation of beam hardening in iron ore samples. *Minerals Engineering*, 131:206–215.

Barbery, G. (1991). *Mineral liberation: measurement, simulation and practical use in mineral processing*. Québec: Éditions GB.

Bay, H., Ess, A., Tuytelaars, T., and Van Gool, L. (2008). Speeded-up robust features (SURF). *Computer vision and image understanding*, 110(3):346–359.

Berger, M. (2010). XCOM: photon cross sections database. *http://www. nist. gov/pml/data/xcom/index. cfm*.

Bholowalia, P. and Kumar, A. (2014). EBK-means: A clustering technique based on elbow method and k-means in WSN. *International Journal of Computer Applications*, 105(9).

Brabant, L., Vlassenbroeck, J., De Witte, Y., Cnudde, V., Boone, M. N., Dewanckele, J., and Van Hoorebeke, L. (2011). Three-Dimensional Analysis of High-Resolution X-Ray Computed Tomography Data with Morpho+. *Microscopy and Microanalysis*, 17(2):252–263.

Bradley, A. P. (1997). The use of the area under the ROC curve in the evaluation of machine learning algorithms. *Pattern Recognition*, 30(7):1145–1159.

Breiman, L. (2001). Random forests. *Machine learning*, 45(1):5–32.

Brown, L. G. (1992). A survey of image registration techniques. *ACM computing surveys (CSUR)*, 24(4):325–376.

Bullard, J. W. and Garboczi, E. J. (2013). Defining shape measures for 3D star-shaped particles: Sphericity, roundness, and dimensions. *Powder Technology*, 249:241–252.

Canny, J. (1986). A computational approach to edge detection. *IEEE Transactions on Pattern Analysis and Machine Intelligence*, (6):679–698.

Cantatore, A. and Müller, P. (2011). Introduction to computed tomography. Technical report, DTU Mechanical Engineering.

Cepuritis, R., Garboczi, E. J., Jacobsen, S., and Snyder, K. A. (2017). Comparison of 2-D and 3-D shape analysis of concrete aggregate fines from VSI crushing. *Powder Technology*, 309:110–125.

Cepuritis, R., Jacobsen, S., Pedersen, B., and Mørtsell, E. (2016). Crushed sand in concrete – Effect of particle shape in different fractions and filler properties on rheology. *Cement and Concrete Composites*, 71:26–41.

Chauhan, S., Rühaak, W., Khan, F., Enzmann, F., Mielke, P., Kersten, M., and Sass, I. (2016a). Processing of rock core microtomography images: Using seven different machine learning algorithms. *Computers & Geosciences*, 86:120–128.

Chauhan, S., Rhaak, W., Anbergen, H., Kabdenov, A., Freise, M., Wille, T., and Sass, I. (2016b). Phase segmentation of X-ray computer tomography rock images using machine learning techniques: an accuracy and performance study. *Solid Earth*, 7(4):1125–1139.

Chun, B. and Xiaoyue, L. (2009). The edge detection technology of CT image for study the growth of rock crack. In *2009 ISECS International Colloquium on Computing, Communication, Control, and Management*, volume 4, pages 286–288.

Cnudde, V. and Boone, M. N. (2013). High-resolution X-ray computed tomography in geosciences: A review of the current technology and applications. *Earth-Science Reviews*, 123:1–17.

Cortina-Januchs, M. G., Quintanilla-Dominguez, J., Vega-Corona, A., Tarquis, A. M., and Andina, D. (2011). Detection of pore space in CT soil images using artificial neural networks. *Biogeosciences*, 8(2):279–288.

De Berg, M., Van Kreveld, M., Overmars, M., and Schwarzkopf, O. C. (2000). Computational geometry. In *Computational geometry*, pages 1–17. Springer.

Deng, H., Fitts, J. P., and Peters, C. A. (2016). Quantifying fracture geometry with X-ray tomography: Technique of Iterative Local Thresholding (TILT) for 3D image segmentation. *Computational Geosciences*, 20(1):231–244.

Dobson, J. K., Harrison, T. S., Lin, Q., Ní Bhreasail, A., Fagan-Endres, A. M., Neethling, J. S., Lee, D. P., and Cilliers, J. J. (2017). Insights into Ferric Leaching of Low Grade Metal Sulfide-Containing ores in an Unsaturated Ore Bed Using X-ray Computed Tomography. *Minerals*, 7(5).

Dominy, S., O'Connor, L., Parbhakar-Fox, A., Glass, H., and Purevgerel, S. (2018). Geometallurgy—A Route to More Resilient Mine Operations. *Minerals*, 8(12):560.

Donskoi, E., Poliakov, A., Holmes, R., Suthers, S., Ware, N., Manuel, J., and Clout, J. (2016). Iron ore textural information is the key for prediction of downstream process performance. *Minerals Engineering*, 86:10–23.

Ducheyne, P., Healy, K., Hutmacher, D. W., Grainger, D. W., and Kirkpatrick, C. J. (2017). *Comprehensive Biomaterials II*. Elsevier.

Duran, B. S. and Odell, P. L. (2013). *Cluster analysis: a survey*, volume 100. Springer Science & Business Media.

Evans, C., Wightman, E., and Yuan, X. (2015). Quantifying mineral grain size distributions for process modelling using X-ray micro-tomography. *Minerals Engineering*, 82:78–83.

Fagan-Endres, M. A., Cilliers, J. J., Sederman, A. J., and Harrison, S. T. (2017). Spatial variations in leaching of a low-grade, low-porosity chalcopyrite ore identified using X-ray μCT. *Minerals Engineering*, 105:63–68.

Fandrich, R., Gu, Y., Burrows, D., and Moeller, K. (2007). Modern SEM-based mineral liberation analysis. *International Journal of Mineral Processing*, 84(1):310–320.

Fandrichi, R., Schneider, C., and Gay, S. (1998). Two stereological correction methods: Allocation method and kernel transformation method. *Minerals Engineering*, 11(8):707–715.

Fatima, A., Venkatesh, A., Mukherjee, R., Agrawal, A., Singh, B., Sarkar, P., Kashyap, Y., and Shripathi, T. (2019). 3D spatial distribution of ore mineral phases using high resolution synchrotron micro-computed tomography (μCT) combined with optical microscopy. *Applied Radiation and Isotopes*, 148:49–59.

Garboczi, E. J. (2002). Three-dimensional mathematical analysis of particle shape using X-ray tomography and spherical harmonics: Application to aggregates used in concrete. *Cement and Concrete Research*, 32(10):1621–1638.

Garboczi, E. J. and Bullard, J. W. (2017). 3D analytical mathematical models of random star-shape particles via a combination of X-ray computed microtomography and spherical harmonic analysis. *Advanced Powder Technology*, 28(2):325–339.

Garcia, D., Lin, C. L., and Miller, J. D. (2009). Quantitative analysis of grain boundary fracture in the breakage of single multiphase particles using X-ray microtomography procedures. *Minerals Engineering*, 22(3):236–243.

Gay, S. L. and Morrison, R. D. (2006). Using Two Dimensional Sectional Distributions to Infer Three Dimensional Volumetric Distributions – Validation using Tomography. *Particle & Particle Systems Characterization*, 23(3-4):246–253.

Ghorbani, Y., Becker, M., Petersen, J., Morar, S. H., Mainza, A., and Franzidis, J.-P. (2011). Use of X-ray computed tomography to investigate crack distribution and mineral dissemination in sphalerite ore particles. *Minerals Engineering*, 24(12):1249–1257.

Godel, B. (2013). High-resolution X-ray computed tomography and its application to ore deposits: From data acquisition to quantitative three-dimensional measurements with case studies from Ni-Cu-PGE deposits. *Economic Geology*, 108(8):2005–2019.

Gottlieb, P., Wilkie, G., Sutherland, D., Ho-Tun, E., Suthers, S., Perera, K., Jenkins, B., Spencer, S., Butcher, A., and Rayner, J. (2000). Using quantitative electron microscopy for process mineralogy applications. *JOM*, 52(4):24–25.

Gu, Y., Schouwstra, R. P., and Rule, C. (2014). The value of automated mineralogy. *Minerals Engineering*, 58:100–103.

Guntoro, P. I., Tiu, G., Ghorbani, Y., Lund, C., and Rosenkranz, J. (2019). Application of machine learning techniques in mineral phase segmentation for X-ray microcomputed tomography (µCT) data. *Minerals Engineering*, 142:105882.

Guven, O. and Çelik, M. S. (2016). Interplay of Particle Shape and Surface Roughness to Reach Maximum Flotation Efficiencies Depending on Collector Concentration. *Mineral Processing and Extractive Metallurgy Review*, 37(6):412–417.

Hall, P., Park, B. U., and Samworth, R. J. (2008). Choice of neighbor order in nearest-neighbor classification. *Ann. Statist.*, 36(5):2135–2152.

Haralick, R. M. and Shanmugam, K. (1973). Textural features for image classification. *IEEE Transactions on systems, man, and cybernetics*, (6):610–621.

He, H. and Garcia, E. A. (2008). Learning from imbalanced data. *IEEE Transactions on Knowledge & Data Engineering*, (9):1263–1284.

Henley, K. J. (1983). ORE-DRESSING MINERALOGY - A REVIEW OF TECHNIQUES, APPLICATIONS AND RECENT DEVELOPMENTS. Number 7, pages 175–200, The Australian Mineral Development, Lab, Geological Services Div,, Adelaide, Aust, The Australian Mineral Development Lab, Geological Services Div, Adelaide, Aust. Geological Soc of South Africa.

Hepner, G., Logan, T., Ritter, N., and Bryant, N. (1990). Artificial neural network classification using a minimal training set- Comparison to conventional supervised classification. *Photogrammetric Engineering and Remote Sensing*, 56(4):469–473.

Herbig, M., King, A., Reischig, P., Proudhon, H., Lauridsen, E. M., Marrow, J., Buffière, J.-Y., and Ludwig, W. (2011). 3-D growth of a short fatigue crack within a polycrystalline microstructure studied using combined diffraction and phase-contrast X-ray tomography. *Acta Materialia*, 59(2):590–601.

Iassonov, P., Gebrenegus, T., and Tuller, M. (2009). Segmentation of X-ray computed tomography images of porous materials: A crucial step for characterization and quantitative analysis of pore structures. *Water Resources Research*, 45(9).

Jardine, M. A., Miller, J. A., and Becker, M. (2018). Coupled X-ray computed tomography and grey level co-occurrence matrices as a method for quantification of mineralogy and texture in 3D. *Computers and Geosciences*, 111:105–117.

Kapur, J. N., Sahoo, P. K., and Wong, A. K. C. (1985). A new method for gray-level picture thresholding using the entropy of the histogram. *Computer vision, graphics, and image processing*, 29(3):273–285.

Kastner, J., Harrer, B., Requena, G., and Brunke, O. (2010). A comparative study of high resolution cone beam X-ray tomography and synchrotron tomography applied to Fe- and Al-alloys. *NDT & E International*, 43(7):599–605.

Kaya, E., Hogg, R., and Kumar, S. (2002). Particle shape modification in comminution. *KONA Powder and Particle Journal*, 20(March):188–195.

Ketcham, R. A. and Hanna, R. D. (2014). Beam hardening correction for X-ray computed tomography of heterogeneous natural materials. *Computers & Geosciences*, 67:49–61.

Kikuchi, S., Nonaka, K., Asakawa, N., Shiozawa, D., and Nakai, Y. (2017). Change of misorientation of individual grains in fatigue of polycrystalline alloys by diffraction contrast tomography using ultrabright synchrotron radiation. *Procedia Structural Integrity*, 3:402–410.

King, A., Reischig, P., Adrien, J., Peetermans, S., and Ludwig, W. (2014). Polychromatic diffraction contrast tomography. *Materials Characterization*, 97:1–10.

King, R. and Schneider, C. (1998). Stereological correction of linear grade distributions for mineral liberation. *Powder Technology*, 98(1):21–37.

Koch, P.-H. (2017). *Particle generation for geometallurgical process modeling*. PhD thesis, Minerals and Metallurgical Engineering, Department of Civil, Environmental and Natural Resources Engineering, Luleå University of Technology.

Koch, P.-H., Lund, C., and Rosenkranz, J. (2019). Automated drill core mineralogical characterization method for texture classification and modal mineralogy estimation for geometallurgy. *Minerals Engineering*, 136:99–109.

Koh, P., Hao, F., Smith, L., Chau, T., and Bruckard, W. (2009). The effect of particle shape and hydrophobicity in flotation. *International Journal of Mineral Processing*, 93(2):128–134.

Kong, D. and Fonseca, J. (2017). Quantification of the morphology of shelly carbonate sands using 3D images. *Géotechnique*, 68(3):249–261.

Kyle, J. R. and Ketcham, R. A. (2015). Application of high resolution X-ray computed tomography to mineral deposit origin, evaluation, and processing. *Ore Geology Reviews*, 65:821–839.

Kyle, J. R., Mote, A. S., and Ketcham, R. A. (2008). High resolution X-ray computed tomography studies of Grasberg porphyry Cu-Au ores, Papua, Indonesia. *Mineralium Deposita*, 43(5):519–532.

Laforce, B., Masschaele, B., Boone, M. N., Schaubroeck, D., Dierick, M., Vekemans, B., Walgraeve, C., Janssen, C., Cnudde, V., Van Hoorebeke, L., and Vincze, L. (2017). Integrated Three-Dimensional Microanalysis Combining X-Ray Microtomography and X-Ray Fluorescence Methodologies. *Analytical Chemistry*, 89(19):10617–10624.

Lamberg, P. (2011). Particles-the bridge between geology and metallurgy. In *Konferens i mineralteknik 2011: 08/02/2011-09/02/2011*. Luleå tekniska universitet.

Lamberg, P. and Vianna, S. (2007). A technique for tracking multiphase mineral particles in flotation circuits. In *Meeting of the Southern Hemisphere on Mineral Technology: 20/11/2007-24/11/2007*, pages 195–202. Universidade Federal de Ouro Preto.

Lätti, D. and Adair, B. (2001). An assessment of stereological adjustment procedures. *Minerals Engineering*, 14(12):1579–1587.

Leroy, S., Dislaire, G., Bastin, D., and Pirard, E. (2011). Optical analysis of particle size and chromite liberation from pulp samples of a UG2 ore regrinding circuit. *Minerals Engineering*, 24(12):1340–1347.

Lewiner, T., Lopes, H., Vieira, A. W., and Tavares, G. (2003). Efficient Implementation of Marching Cubes' Cases with Topological Guarantees. *Journal of Graphics Tools*, 8(2):1–15.

Liddell, K. C. (2005). Shrinking core models in hydrometallurgy: What students are not being told about the pseudo-steady approximation. *Hydrometallurgy*, 79(1-2):62–68.

Limaye, A. (2012). Drishti: a volume exploration and presentation tool. *Developments in X-ray Tomography VIII*, 8506:85060X.

Lin, C. L. and Miller, J. D. (1996). Cone beam X-ray microtomography for three-dimensional liberation analysis in the 21st century. *International Journal of Mineral Processing*, 47(1-2):61–73.

Lin, C. L. and Miller, J. D. (2005). 3D characterization and analysis of particle shape using X-ray microtomography (XMT).

Lin, C. L. and Miller, J. D. (2010). Advances in X-ray computed tomography (CT) for improved coal washability analysis. In *16th International Coal Preparation Congress, ICPC 2010*.

Lin, C. L., Videla, A. R., Yu, Q., and Miller, J. D. (2010). Characterization and analysis of Porous, Brittle solid structures by X-ray micro computed tomography. *JOM*, 62(12):86–89.

Lin, Q., Barker, D. J., Dobson, K. J., Lee, P. D., and Neethling, S. J. (2016a). Modelling particle scale leach kinetics based on X-ray computed micro-tomography images. *Hydrometallurgy*, 162:25–36.

Lin, Q., Neethling, S. J., Courtois, L., Dobson, K. J., and Lee, P. D. (2016b). Multi-scale quantification of leaching performance using X-ray tomography. *Hydrometallurgy*, 164:265–277.

Lin, Q., Neethling, S. J., Dobson, K. J., Courtois, L., and Lee, P. D. (2015). Quantifying and minimising systematic and random errors in X-ray micro-tomography based volume measurements. *Computers & Geosciences*, 77:1–7.

Lindeberg, T. (2007). Scale-space. *Wiley Encyclopedia of Computer Science and Engineering*, pages 2495–2504.

Lindeberg, T. (2013). Image Matching Using Generalized Scale-Space Interest Points BT - Scale Space and Variational Methods in Computer Vision. pages 355–367, Berlin, Heidelberg. Springer Berlin Heidelberg.

Lindeberg, T. (2015). Image Matching Using Generalized Scale-Space Interest Points. *Journal of Mathematical Imaging and Vision*, 52(1):3–36.

Lishchuk, V., Koch, P.-H., Ghorbani, Y., and Butcher, A. R. (2020). Towards integrated geometallurgical approach: Critical review of current practices and future trends. *Minerals Engineering*, 145:106072.

Lishchuk, V., Lamberg, P., and Lund, C. (2015). Classification of geometallurgical programs based on approach and purpose. In *SGA 2015: 24/08/2015-27/08/2015*.

Little, L., Mainza, A. N., Becker, M., and Wiese, J. (2017). Fine grinding: How mill type affects particle shape characteristics and mineral liberation. *Minerals Engineering*, 111:148–157.

Little, L., Mainza, A. N., Becker, M., and Wiese, J. G. (2016). Using mineralogical and particle shape analysis to investigate enhanced mineral liberation through phase boundary fracture. *Powder Technology*, 301:794–804.

Lobos, R., Silva, J. F., Ortiz, J. M., Díaz, G., and Egaña, A. (2016). Analysis and Classification of Natural Rock Textures based on New Transform-based Features. *Mathematical Geosciences*, 48(7):835–870.

Lotter, N., Evans, C., and Engstrőm, K. (2018a). Sampling – A key tool in modern process mineralogy. *Minerals Engineering*, 116:196–202.

Lotter, N. O. (2011). Modern Process Mineralogy: An integrated multi-disciplined approach to flowsheeting. *Minerals Engineering*, 24(12):1229–1237.

Lotter, N. O., Baum, W., Reeves, S., Arrué, C., and Bradshaw, D. J. (2018b). The business value of best practice process mineralogy. *Minerals Engineering*, 116:226–238.

Lund, C. and Lamberg, P. (2014). Geometallurgy–A tool for better resource efficiency. *European Geologist Magazine*, 37:39–43.

Lund, C., Lamberg, P., and Lindberg, T. (2013). Practical way to quantify minerals from chemical assays at Malmberget iron ore operations – An important tool for the geometallurgical program. *Minerals Engineering*, 49:7–16.

Lund, C., Lamberg, P., and Lindberg, T. (2015). Development of a geometallurgical framework to quantify mineral textures for process prediction. *Minerals Engineering*, 82:61–77.

Ma, G., Xia, W., and Xie, G. (2018). Effect of particle shape on the flotation kinetics of fine coking coal. *Journal of Cleaner Production*, 195:470–475.

Martínez-Martínez, J., Benavente, D., and Del Cura, M. A. G. (2007). Petrographic quantification of brecciated rocks by image analysis. Application to the interpretation of elastic wave velocities. *Engineering Geology*, 90(1-2):41–54.

Masad, E., Saadeh, S., Al-Rousan, T., Garboczi, E., and Little, D. (2005). Computations of particle surface characteristics using optical and X-ray CT images. *Computational Materials Science*, 34(4):406–424.

Mees, F., Swennen, R., Van Geet, M., and Jacobs, P. (2003). Applications of X-ray computed tomography in the geosciences. *Geological Society, London, Special Publications*, 215(1):1–6.

Miller, J. and Lin, C. (1988). Treatment of polished section data for detailed liberation analysis. *International Journal of Mineral Processing*, 22(1-4):41–58.

Miller, J. D. and Lin, C. L. (2016). Opportunities for plant-site 3D coarse particle characterization with automated high-speed X-ray tomography. *Minerals & Metallurgical Processing*, 33(2):53–57.

Miller, J. D. and Lin, C. L. (2018). X-ray tomography for mineral processing technology-3D particle characterization from mine to mill. *Minerals & Metallurgical Processing*, 35(1):1–12.

Miller, J. D., Lin, C. L., and Cortes, A. B. (1990). A review of X-ray computed tomography and its applications in mineral processing. *Mineral Procesing and Extractive Metallurgy Review*, 7(1):1–18.

Miller, J. D., Lin, C. L., Garcia, C., and Arias, H. (2003). Ultimate recovery in heap leaching operations as established from mineral exposure analysis by X-ray microtomography. *International Journal of Mineral Processing*, 72(1):331–340.

Müter, D., Pedersen, S., Sørensen, H. O., Feidenhans'l, R., and Stipp, S. L. S. (2012). Improved segmentation of X-ray tomography data from porous rocks using a dual filtering approach. *Computers & Geosciences*, 49:131–139.

Mwanga, A., Lamberg, P., and Rosenkranz, J. (2014). Liberability: A new approach for measuring ore comminution behavior. In *Process Mineralogy: 17/11/2014-19/11/2014*.

Naidoo, L., Cho, M., Mathieu, R., and Asner, G. (2012). Classification of savanna tree species, in the Greater Kruger National Park region, by integrating hyperspectral and LiDAR data in a Random Forest data mining environment. *ISPRS Journal of Photogrammetry and Remote Sensing*, 69:167–179.

Ojala, T., Pietikäinen, M., and Harwood, D. (1996). A comparative study of texture measures with classification based on featured distributions. *Pattern Recognition*, 29(1):51–59.

Olivo, A. and Castelli, E. (2014). X-ray phase contrast imaging: From synchrotrons to conventional sources. *Rivista del Nuovo Cimento*, 37(9):467–508.

Oshiro, T. M., Perez, P. S., and Baranauskas, J. A. (2012). How Many Trees in a Random Forest? In Perner, P., editor, *Machine Learning and Data Mining in Pattern Recognition*, pages 154–168, Berlin, Heidelberg. Springer Berlin Heidelberg.

Otsu, N. (1979). A threshold selection method from gray-level histograms. *IEEE transactions on systems, man, and cybernetics*, 9(1):62–66.

Pamukcu, A. S., Gualda, G. A. R., and Rivers, M. L. (2013). Quantitative 3D petrography using X-ray tomography 4: Assessing glass inclusion textures with propagation phase-contrast tomography. *Geosphere*, 9(6):1704–1713.

Parian, M., Lamberg, P., and Rosenkranz, J. (2016). Developing a particle-based process model for unit operations of mineral processing – WLIMS. *International Journal of Mineral Processing*, 154:53–65.

Parian, M., Mwanga, A., Lamberg, P., and Rosenkranz, J. (2018). Ore texture breakage characterization and fragmentation into multiphase particles. *Powder Technology*, 327:57–69.

Peng, R., Yang, Y., Ju, Y., Mao, L., and Yang, Y. (2011). Computation of fractal dimension of rock pores based on gray CT images. *Chinese Science Bulletin*, 56(31):3346.

Pérez-Barnuevo, L., Lévesque, S., and Bazin, C. (2018). Automated recognition of drill core textures: A geometallurgical tool for mineral processing prediction. *Minerals Engineering*, 118:87–96.

Pérez-Barnuevo, L., Pirard, E., and Castroviejo, R. (2013). Automated characterisation of intergrowth textures in mineral particles. A case study. *Minerals Engineering*, 52:136–142.

Pierret, A., Capowiez, Y., Belzunces, L., and Moran, C. J. (2002). 3D reconstruction and quantification of macropores using X-ray computed tomography and image analysis. *Geoderma*, 106(3-4):247–271.

Pirard, E., Califice, A., Léonard, A., and Gregoire, M. (2009). Multiscale shape analysis of particles in 3D using the calypter.

Pita, F. and Castilho, A. (2017). Separation of plastics by froth flotation. The role of size, shape and density of the particles. *Waste Management*, 60:91–99.

Prewitt, J. M. S. (1970). Object enhancement and extraction. *Picture processing and Psychopictorics*, 10(1):15–19.

Rahimov, K., AlSumaiti, A. M., AlMarzouqi, H., and Jouini, M. S. (2017). Use of Local Binary Pattern in Texture Classification of Carbonate Rock Micro-CT Images.

Reyes, F., Cilliers, J. J., and Neethling, S. J. (2019). Quantifying mineral liberation by grade and surface exposure using X-ray micro-tomography for flotation processes. In *29th International Mineral Processing Congress, IMPC*, Moscow. Canadian Institute of Mining, Metallurgy and Petroleum.

Reyes, F., Lin, Q., Cilliers, J. J., and Neethling, S. J. (2018). Quantifying mineral liberation by particle grade and surface exposure using X-ray microCT. *Minerals Engineering*, 125:75–82.

Reyes, F., Lin, Q., Udoudo, O., Dodds, C., Lee, P. D., and Neethling, S. J. (2017). Calibrated X-ray micro-tomography for mineral ore quantification. *Minerals Engineering*, 110:122–130.

Russell, S. J. and Norvig, P. (2016). *Artificial intelligence: a modern approach*. Malaysia; Pearson Education Limited,.

Schindelin, J., Arganda-Carreras, I., Frise, E., Kaynig, V., Longair, M., Pietzsch, T., Preibisch, S., Rueden, C., Saalfeld, S., and Schmid, B. (2012). Fiji: an open-source platform for biological-image analysis. *Nature methods*, 9(7):676.

Schlüter, S., Sheppard, A., Brown, K., and Wildenschild, D. (2014). Image processing of multiphase images obtained via X-ray microtomography: a review. *Water Resources Research*, 50(4):3615–3639.

Serra, J. (1983). *Image analysis and mathematical morphology*. Academic Press, Inc.

Serra, J. and Soille, P. (2012). *Mathematical morphology and its applications to image processing*, volume 2. Springer Science & Business Media.

Shi, Y. and Yan, W. M. (2015). Segmentation of irregular porous particles of various sizes from X-ray microfocus computer tomography images using a novel adaptive watershed approach. *Géotechnique Letters*, 5(4):299–305.

Siddique, M., Bakr, A., Arif, R. B., Khan, M. M. R., and Ashrafi, Z. (2018). Implementation of Fuzzy C-Means and Possibilistic C-Means Clustering Algorithms, Cluster Tendency Analysis and Cluster Validation. *arXiv preprint arXiv:1809.08417*.

Sobel, I. (2014). *An Isotropic 3x3 Image Gradient Operator*.

Spencer, S. and Sutherland, D. (2000). Stereological correction of mineral liberation grade distributions estimated by single sectioning of particles. *Image Anal. Stereol.*, 19(3):175–182.

Sun, J., Yu, T., Xu, C., Ludwig, W., and Zhang, Y. (2018). 3D characterization of partially recrystallized Al using high resolution diffraction contrast tomography. *Scripta Materialia*, 157:72–75.

Sutherland, D. (2007). Estimation of mineral grain size using automated mineralogy. *Minerals Engineering*, 20(5):452–460.

Suuronen, J.-P. and Sayab, M. (2018). 3D nanopetrography and chemical imaging of datable zircons by synchrotron multimodal X-ray tomography. *Scientific Reports*, 8(1):4747.

Takahashi, H. and Sugiyama, T. (2019). Application of non-destructive integrated CT-XRD method to investigate alteration of cementitious materials subjected to high temperature and pure water. *Construction and Building Materials*, 203:579–588.

Thanh Noi, P. and Kappas, M. (2018). Comparison of Random Forest, k-Nearest Neighbor, and Support Vector Machine Classifiers for Land Cover Classification Using Sentinel-2 Imagery. *Sensors*, 18(1).

Tiu, G. (2017). *Classification of Drill Core Textures for Process Simulation in Geometallurgy : Aitik Mine, Sweden*. PhD thesis, EMerald Program.

Toda, H., Takijiri, A., Azuma, M., Yabu, S., Hayashi, K., Seo, D., Kobayashi, M., Hirayama, K., Takeuchi, A., and Uesugi, K. (2017). Damage micromechanisms in dual-phase steel investigated with combined phase- and absorption-contrast tomography. *Acta Materialia*, 126:401–412.

Tøgersen, M. K., Kleiv, R. A., Ellefmo, S., and Aasly, K. (2018). Mineralogy and texture of the Storforshei iron formation, and their effect on grindability. *Minerals Engineering*, 125:176–189.

Triffett, B. and Bradshaw, D. (2008). The role of morphology and host rock lithology on the flotation behaviour of molybdenite at Kennecott Utah Copper. Australasian Institute of Mining and Metallurgy.

Tungpalan, K., Wightman, E., and Manlapig, E. (2015). Relating mineralogical and textural characteristics to flotation behaviour. *Minerals Engineering*, 82:136–140.

Ueda, T. (2019). Experimental validation of a statistical reliability method for the liberation distribution measurement of ore particles. *Minerals Engineering*, 140:105880.

Ueda, T., Oki, T., and Koyanaka, S. (2016). Statistical effect of sampling particle number on mineral liberation assessment. *Minerals Engineering*, 98:204–212.

Ueda, T., Oki, T., and Koyanaka, S. (2017). Comparison of seven texture analysis indices for their applicability to stereological correction of mineral liberation assessment in binary particle systems. *Minerals*, 7(11).

Ueda, T., Oki, T., and Koyanaka, S. (2018a). A general quantification method for addressing stereological bias in mineral liberation assessment in terms of volume fraction and size of mineral phase. *Minerals Engineering*, 119:156–165.

Ueda, T., Oki, T., and Koyanaka, S. (2018b). Numerical analysis of the general characteristics of stereological bias in surface liberation assessment of ore particles. *Advanced Powder Technology*, 29(12):3327–3335.

Ueda, T., Oki, T., and Koyanaka, S. (2018c). Statistical reliability of the liberation distribution of ore particles with respect to number of particle measurements. *Minerals Engineering*, 126:82–88.

Van Dalen, G., Koster, M. W., Dalen, G. V., and Koster, M. W. (2012). 2D & 3D particle size analysis of micro-CT images. *Unilever Research and Development, The Netherlands*.

Van Geet, M., Swennen, R., and Wevers, M. (2000). Quantitative analysis of reservoir rocks by microfocus X-ray computerised tomography. *Sedimentary Geology*, 132(1):25–36.

Van Geet, M., Volckaert, G., and Roels, S. (2005). The use of microfocus X-ray computed tomography in characterising the hydration of a clay pellet/powder mixture. *Applied Clay Science*, 29(2):73–87.

Vapnik, V., Guyon, I., and Hastie, T. (1995). Support vector machines. *Mach. Learn*, 20(3):273–297.

Vecchio, I., Schladitz, K., Godehardt, M., and Heneka, M. J. (2012). 3D GEO-METRIC CHARACTERIZATION OF PARTICLES APPLIED TO TECHNICAL CLEANLINESS. *Image Analysis & Stereology; Vol 31, No 3 (2012)DO - 10.5566/ias.v31.p163-174*.

Viermetz, M., Birnbacher, L., Willner, M., Achterhold, K., Pfeiffer, F., and Herzen, J. (2018). High resolution laboratory grating-based X-ray phase-contrast CT. *Scientific Reports*, 8(1):15884.

Vizcarra, T., Harmer, S., Wightman, E., Johnson, N., and Manlapig, E. (2011). The influence of particle shape properties and associated surface chemistry on the flotation kinetics of chalcopyrite. *Minerals Engineering*, 24(8):807–816.

Vlassenbroeck, J., Dierick, M., Masschaele, B., Cnudde, V., Van Hoorebeke, L., and Jacobs, P. (2007). Software tools for quantification of X-ray microtomography at the UGCT. *Nuclear Instruments and Methods in Physics Research Section A: Accelerators, Spectrometers, Detectors and Associated Equipment*, 580(1):442–445.

Voigt, M., Miller, J., Bbosa, L., Govender, R., Bradshaw, D., Mainza, A., and Becker, M. (2019). Developing a 3D mineral texture quantification method of drill core for geometallurgy. *Journal of the Southern African Institute of Mining and Metallurgy*, 119(4):347–353.

Wadell, H. (1932). Volume, Shape, and Roundness of Rock Particles. *The Journal of Geology*, 40(5):443–451.

Wang, G., Wang, Y., Li, H., Chen, X., Lu, H., Ma, Y., Peng, C., Wang, Y., and Tang, L. (2014). Morphological Background Detection and Illumination Normalization of Text Image with Poor Lighting. *PLOS ONE*, 9(11):e110991.

Wang, Y., Lin, C., and Miller, J. (2015). Improved 3D image segmentation for X-ray tomographic analysis of packed particle beds. *Minerals Engineering*, 83:185–191.

Wang, Y., Lin, C. L., and Miller, J. D. (2017). Quantitative analysis of exposed grain surface area for multiphase particles using X-ray microtomography. *Powder Technology*, 308:368–377.

Wanhainen, C., Broman, C., and Martinsson, O. (2003). *The Aitik Cu-Au-Ag deposit in northern Sweden: A product of high salinity fluids*, volume 38.

Wen, B. and Xia, W. (2017). Effect of particle shape on coal flotation. *Energy Sources, Part A: Recovery, Utilization, and Environmental Effects*, 39(13):1390–1394.

Whiteman, E., Lotter, N., and Amos, S. (2016). Process mineralogy as a predictive tool for flowsheet design to advance the Kamoa project. *Minerals Engineering*, 96-97:185–193.

Wightman, E., Evans, C. L., Wightman, E. M., and Yuan, X. (2015). Quantifying mineral grain size distributions for process modelling using X-ray micro-tomography. *Minerals Engineering*, 82:78–83.

Wu, A.-x., Yang, B.-h., Xi, Y., and Jiang, H.-c. (2007). Pore structure of ore granular media by computerized tomography image processing. *Journal of Central South University of Technology*, 14(2):220–224.

Xia, W., Ma, G., Bu, X., and Peng, Y. (2018). Effect of particle shape on bubble-particle attachment angle and flotation behavior of glass beads and fragments. *Powder Technology*, 338:168–172.

Xu, H. and Mannor, S. (2012). Robustness and generalization. *Machine Learning*, 86(3):391–423.

Xu, W., Dhawan, N., Lin, C.-L., and Miller, J. D. (2013). Further study of grain boundary fracture in the breakage of single multiphase particles using X-ray microtomography procedures. *Minerals Engineering*, 46-47:89–94.

Yang, B.-h., Wu, A.-x., Narsilio, G. A., Miao, X.-x., and Wu, S.-y. (2017). Use of high-resolution X-ray computed tomography and 3D image analysis to quantify mineral dissemination and pore space in oxide copper ore particles. *International Journal of Minerals, Metallurgy, and Materials*, 24(9):965–973.

Yildirim, B. G., Bradshaw, D., Powell, M., Evans, C., and Clark, A. (2014). Development of an effective and practical Process Alteration Index (PAI) for predicting metallurgical responses of Cu porphyries. *Minerals Engineering*, 69:91–96.

Zaitoun, N. M. and Aqel, M. J. (2015). Survey on image segmentation techniques. *Procedia Computer Science*, 65:797–806.

Zandomeneghi, D., Voltolini, M., Mancini, L., Brun, F., Dreossi, D., and Polacci, M. (2010). Quantitative analysis of X-ray microtomography images of geomaterials: Application to volcanic rocks. *Geosphere*, 6(6):793–804.

Zhang, J. and Subasinghe, N. (2012). Extracting ore texture information using image analysis. *Transactions of the Institutions of Mining and Metallurgy, Section C: Mineral Processing and Extractive Metallurgy*, 121(3):123–130.

Zhao, B., Wang, J., Coop, M. R., Viggiani, G., and Jiang, M. (2015). An investigation of single sand particle fracture using X-ray micro-tomography. *Géotechnique*, 65(8):625–641.

Part II - Papers

Paper 1

USE OF X-RAY MICRO-COMPUTED TOMOGRAPHY (µCT) FOR 3-D ORE CHARACTERIZATION: A TURNING POINT IN PROCESS MINERALOGY

P.I. Guntoro [1], Y. Ghorbani [1, *], J. Rosenkranz [1]

[1] *Dept. of Civil, Environmental and Natural Resources Eng., Luleå University of Technology, Sweden*
(*Corresponding author: yousef.ghorbani@ltu.se)

ABSTRACT

In recent years, automated mineralogy has become an essential enabling technology in the field of process mineralogy, allowing better understanding between mineralogy and the beneficiation process. Recent developments in X-ray micro-computed tomography (µCT) as a non-destructive technique have indicated great potential to become the next automated mineralogy technique. µCT's main advantage lies in its ability to allow 3-D monitoring of internal structure of the ore at resolutions down to a few hundred nanometers, thereby eliminating the stereological error encountered in conventional 2-D analysis. Driven by the technological and computational progress, the technique is continuously developing as an analysis tool in ore characterization and subsequently it foreseen that µCT will become an indispensable technique in the field of process mineralogy. Although several software tools have been developed for processing µCT dataset, but the main challenge in µCT data analysis remains in the mineralogical analysis, where µCT data often lacks contrast between mineral phases, making segmentation difficult. In this paper, an overview of some current applications of µCT in ore characterization is reviewed, alongside with it potential implications to process mineralogy. It also describes the current limitations of its application and concludes with outlook on the future development of 3-D ore characterization.

Keywords: X-ray micro-tomography (µCT), process mineralogy, ore mineral characterization.

INTRODUCTION

Process Mineralogy

Process mineralogy is defined as the study of mineral characteristics and properties with relation to their beneficiation process. The beneficiation process defined here can range from ore beneficiation, metallurgical process, as well as environmental and waste management (Henley, 1983; Lotter et al., 2018a). The key here is that by evaluating the characteristics of the minerals on a representative sample of an ore, one could determine the optimum processing route of such ore based on the characteristics of the minerals (both gangue and valuable minerals) in the ore. As the characteristics of the ore is determined by the sample analyzed, sampling becomes ever increasingly important in terms of process mineralogy (Lotter et al., 2018b).

In contrast to traditional separation between mineral processing and mineralogy, where troubleshooting of processes are often focused more on process parameters; process mineralogy aims to combine both field so both the characteristics of ore and process parameters can be taken into account when designing and troubleshooting mineral processes. Process mineralogy requires combination of knowledge from geology, mineralogy, metallurgy, and mineral processing. This can be illustrated in Figure 1.
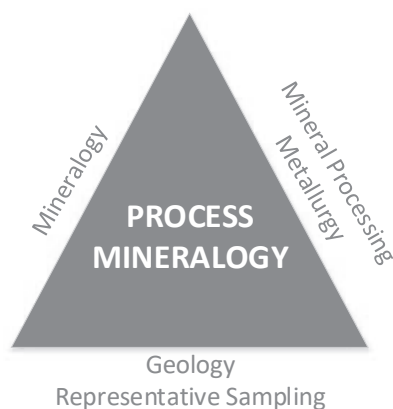
Figure 1. Interdisciplinary of fields in process mineralogy (altered from Lotter et al. (2018, 2002)).

Several instruments and analytical techniques have been developed over the years to evaluate mineralogical characteristics of an ore sample. The development of automated quantitative mineralogical techniques such as Mineral Liberation Analyser (MLA) and Quantitative Evaluation of Minerals by Scanning Electron Microscopy (QEMSCAN) was a significant breakthrough in process mineralogy, as mineral characteristics of ore samples could now be analyzed in an automated, rapid, and statistically reliable way (Fandrich et al., 2007; Gottlieb et al., 2000; Sutherland and Gottlieb, 1991). With such system, information about mineral liberation (Fandrich et al., 2007), size and shape (Leroy et al., 2011; Sutherland, 2007), and stationary textures (Pérez-Barnuevo et al., 2013, 2018; Tøgersen et al., 2018) could be obtained and quantified. This information has been demonstrated to hold significant role in evaluating ore beneficiation processes such as flotation (Alves dos Santos, 2018; Alves dos Santos and Galery, 2018; dos Santos and Galery, 2018; Tungpalan et al., 2015) and comminution (Little et al., 2017, 2016; Tøgersen et al., 2018).

X-ray Tomography for Ore Characterization

While MLA and QEMSCAN offer a rapid data acquisition and processing, it possesses an obvious weakness due to loss of dimensionality. Particles and ore samples are three-dimensional (3D) objects, while automated mineralogical techniques produced a two-dimensional (2D) cross section analysis of the ore samples. This phenomenon is known as stereological bias / error, in which the mineral liberation may be overestimated, as the cross section of the sample might not represent the actual state of the particles (Lätti and Adair, 2001) as shown in Figure 2. Over the years, several correction methods have been developed to address this error in regards to mineral liberation and texture of the particles (Fandrichi et al., 1998; Ueda et al., 2018a, 2018b).
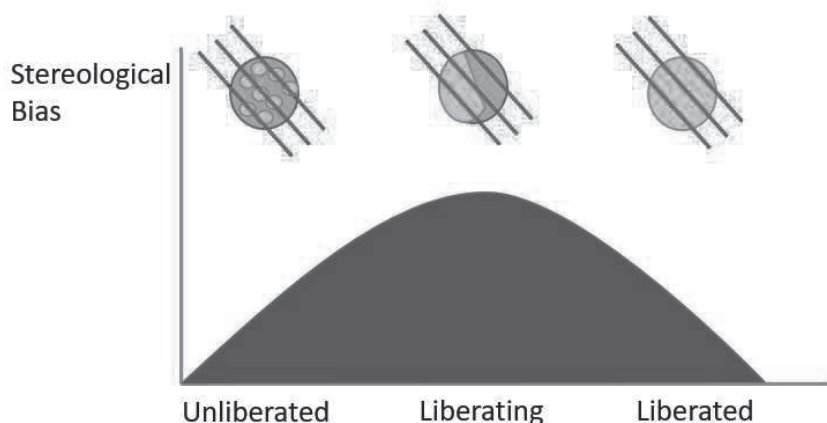
Figure 2. The effect of stereological bias on different type of particles with varying degree of liberation by Spencer and Sutherland (2000). The possible cross-sections analyzed is indicated by the red lines crossing the particles.

This inherent bias gives way to the development of instruments that are capable of acquiring 3D data from an ore sample. Over the last decades, the development of X-ray microcomputed tomography (µCT) in geosciences have received wide attentions. The main advantage of µCT lies on its ability to non-destructively analyze the 3D interior of an object. Several reviews have been done in evaluating µCT application in geosciences (Cnudde and Boone, 2013; Mees et al., 2003), particularly in relation to ore characterization and mineral processing (Kyle and Ketcham, 2015; Miller et al., 1990).

Using µCT, 3D properties of an ore sample such as porosity (Lin and Miller, 2005; Peng et al., 2011; Yang et al., 2017; Zandomeneghi et al., 2010), mineralogy (Ghorbani et al., 2011; Reyes et al., 2017; Tiu, 2017), mineral liberation (Lin and Miller, 1996; Reyes et al., 2018), as well as size and shape (Cepuritis et al., 2017; Lin and Miller, 2005; Masad et al., 2005) could be obtained. Additionally, as 3D data offer additional information about depth, surface properties of an ore can also be evaluated, in which such parameter is important for leaching, flotation, and to some extent grinding (Miller et al., 2003; Tøgersen et al., 2018; Wang et al., 2017; Xia, 2017).

Recent development in µCT instruments also allows in-situ experiments to be carried while scanning is performed, therefore obtaining the so-called four-dimensional (4D) data, which consist of three dimensional of space plus one dimension of time. With such settings, the evolution of ore samples during experiments can be obtained so that the relation of the mineralogical characteristics of the ore to the process can be draw. Such settings have been implemented for example in evaluating ore breakage (L. Wang et al., 2015; Wang et al., 2018) and leaching (Ghorbani et al., 2011). If the key in process mineralogy lies in drawing the relations between mineralogy and mineral processing, then in-situ experiments with µCT scanning could offer a valuable dataset for process mineralogy.

The main limitation of µCT scanning lies on the principle of the X-ray scanning, where minerals are differentiated by their respective attenuation to the X-ray beam. This is reflected in the grayscale intensity of the final image. The attenuation of each materials varies depending on the minerals density, atomic number, as well as the energy of the X-ray beam (Omoumi et al., 2015). This phenomena creates a trade-off situation, where one has to optimize the beam energy so that sufficient contrast between minerals could be obtained. Using lower energy beam often means better contrast, as the attenuation is more dependent on the atomic number of the minerals due to photoelectric effect, but it requires

longer exposure time. Using higher energy would mean less exposure time, but the attenuation is now more dependent on density due to Compton effect, therefore making mineral differentiation difficult as many minerals have similar density.

CASE STUDIES

Ore Structural Characterization with µCT

At the early stages, µCT analysis of ore samples was more focused on structural analysis, which includes pore, shape, as well as size analysis. Analysis with µCT could obtain several information of the ore which includes porosity and crack (Deng et al., 2016; Lin and Miller, 2005; Peng et al., 2011; Yang et al., 2017; Zandomeneghi et al., 2010), particle and grain size distribution (Tiu, 2017) as well as particle shape descriptors such as solidity, elongation, flatness, and aspect ratio (Vecchio et al., 2012; Zhao et al., 2015).

Pore and crack analysis is one of the most common application of µCT. While pore and crack analysis is less emphasized in mineralogy, it holds a significant role in petroleum (Markussen et al., 2019) and construction engineering (Yang et al., 2019). Nevertheless, pore and crack analysis is often indispensable when dealing with processes such as leaching, especially in cases with packed particle bed samples, where connectivity of the pores could help in understanding the permeability of the ore (Deng et al., 2016; Wu et al., 2007).

Most of the automated mineralogy technique could produce analysis on particle size and shape, but as said earlier, these parameters often not used in process mineralogy due to the stereological error. Particle and grain size distribution analysis using µCT is quite well established, as several researchers have optimized the image processing algorithm in acquiring such distribution analysis (Lux et al., 2011; Pierret et al., 2002). One of the most commonly used algorithm is granulometry morphological opening, illustrated in Figure 3.
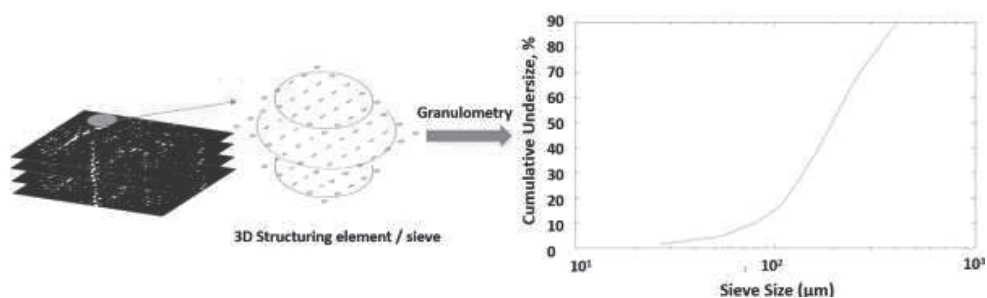

Figure 3. Grain size distribution in 3D as obtained from µCT analysis with granulometry technique. The technique uses a structuring element acting as a sieve, where grain smaller than the sieve is removed. The sieve size is then increased gradually, so the cumulative undersize can be obtained.

Particle and grains are irregular objects; therefore, a descriptor of shape is often needed when describing such parameters. With µCT system, such descriptors could be better acquired, as now the 3D data is available. Most of the available shape descriptors in 3D follow the same logic as the one commonly available in 2D. Particle and grain shapes in 3D can be described with convex hull (Pamukcu et al., 2013; Zhao et al., 2015), bounding box (Vecchio et al., 2012) as well as relation to sphere shapes (Pirard et al., 2009; Van Dalen et al., 2012). Example of bounding box and convex hull of a mineral grain is shown in Figure 4.
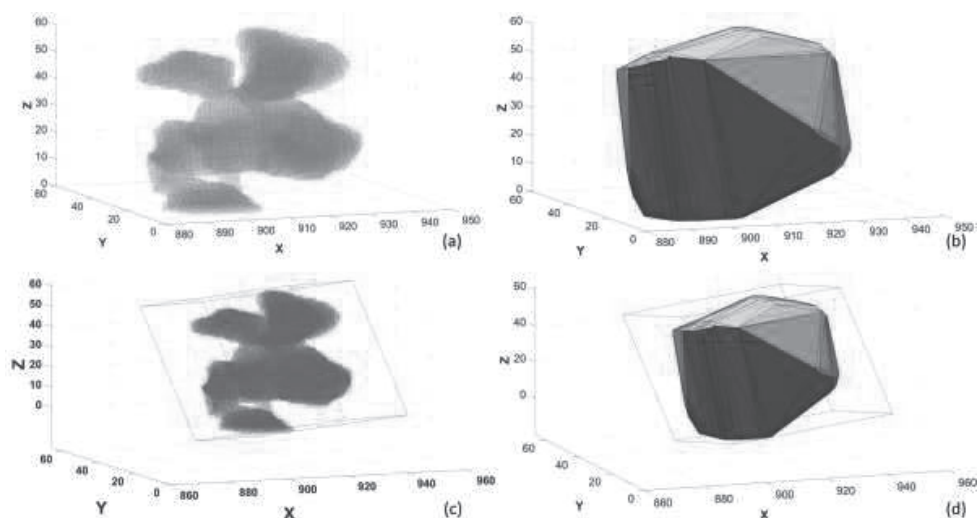
Figure 4. Bounding box and convex hull of an irregular grain. (a) Scatter plots representing the grain; (b) convex hull of the particle; (c) minimum bounding box of the grain; (d) minimum bounding box of the convex hull. Due to the high irregularity (non-convex) particle, convex objects such as polygons often are not the best when describing such particle.

While it is obvious that particle size is of an importance when dealing with most of mineral processes, the effect of shape is not so obvious. It is clear that the choice of comminution equipment affects greatly the progeny particle shape, which then indicates that grain shape could be an important indicator in modelling the breakage mechanism that occurs in the particle (Little et al., 2017, 2016). With flotation, several researchers have analyzed the effect of particle shape (Ma et al., 2018; Pita and Castilho, 2017; Xia et al., 2018), and it is clear that the effect of shape is intertwined with the particle composition and size; in some cases the effect of shape is minimum while in others its effect is more prevalent.

Ore Mineralogical Characterization with μCT

The use of μCT in mineralogical characterization is relatively limited, although it is outlined as one of the future characterization technique in process mineralogy (Baum, 2014). Mineralogical characterization with μCT is often limited to simple mineralogy, such as differentiating the gangue and valuable mineral phases. In these cases, simple thresholding technique such as Otsu could work (Andrä et al., 2013; Yang et al., 2017). Limitations do exist especially if the sample is heterogeneous (Yang et al., 2017), or consist of fine particles with high density / high atomic number, as then the boundary between particles and the background might not be segmented properly due to partial volume effect (Y. Wang et al., 2015).

Several researchers have applied different techniques in dealing with multi-mineral ore samples, especially those that contains minerals with similar attenuations. Such problems can be anticipated earlier by optimizing the scanning conditions through reduction of sample size (Bam et al., 2019; Kyle and Ketcham, 2015), using lower scanning energy (Reyes et al., 2017), or using dual energy scanning (Ghorbani et al., 2011). In other cases, such problem could be addressed later at the data processing stage, such as using machine-learning techniques (Chauhan et al., 2016; Tiu, 2017) as well as combination with SEM-EDS of XRF (Laforce et al., 2017; Reyes et al., 2017; Suuronen and Sayab, 2018; Tiu, 2017). Despite all the steps need to be performing mineralogical analysis with μCT, the

mineralogical result does show considerable difference with traditional automated mineralogy techniques (Reyes et al., 2017; Tiu, 2017). Example of the usage of machine-learning in µCT mineralogical analysis is shown in Figure 5.
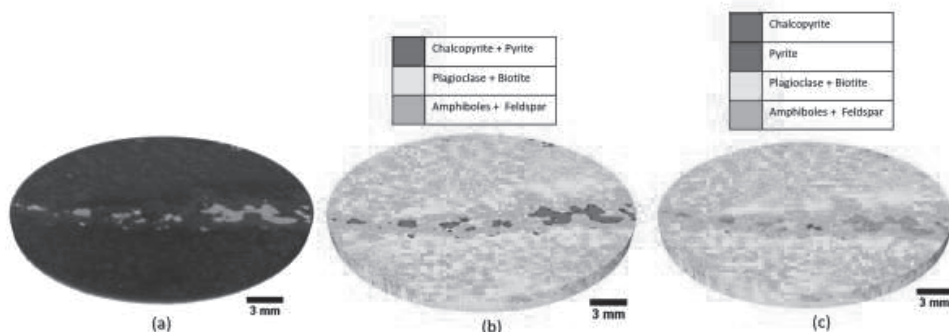

Figure 5. Comparison of different machine learning techniques in mineralogical analysis. (a) Original 3D image of a drill core; (b) Unsupervised machine learning classification; (c) Supervised machine learning classification. By supervised the learning user can better specify the minerals, as in this example pyrite is lacking contrast.

Ore Texture Characterization with µCT

Textural measures such as grain size is well known to have effect to the downstream processes, especially in terms of liberation size (Lotter et al., 2018a). Another equally important texture measure is the spatial distribution (pattern) of different minerals in the ore, often referred as stationary textures (Lobos et al., 2016). While grain size is quantifiable, stationary textures is often descriptive and qualitative. Recent developments are leaning toward the quantification of stationary textures with the help of microscopy based techniques (Donskoi et al., 2016; Koch, 2017; Lund et al., 2015), accounting both grain size and spatial relationship of minerals. Stationary textures have been shown to affect the ore behavior in mineral processes (Butcher, 2010; Dey et al., 2017; Tøgersen et al., 2018) and it has been used as an important measure in geometallurgy (Lund et al., 2015; Pérez-Barnuevo et al., 2018).

µCT analysis opens up a new potential in analyzing textures, especially stationary textures, as now the spatial relationship of minerals can be described in 3D, which in turns leads to better understanding of its effect to the downstream processes (Becker et al., 2016). Additionally, information about surface texture of the ore could be obtained as well, in which parameter such as grain surface exposure affecting leaching processes (Miller et al., 2003; Wang et al., 2017); surface hardness affecting grinding processes (Tøgersen et al., 2018); as well as surface roughness affecting flotation process (Xia, 2017).

In general, µCT ore texture analysis is very limited, as it requires a comprehensive mineralogical analysis, in which µCT has a limitation. Several researchers have tried to use µCT to describe texture better (Barnes et al., 2018, 2017), while others have used µCT data to quantify stationary textures (Jardine et al., 2018). Example of texture quantification in 3D is shown in Figure 6.
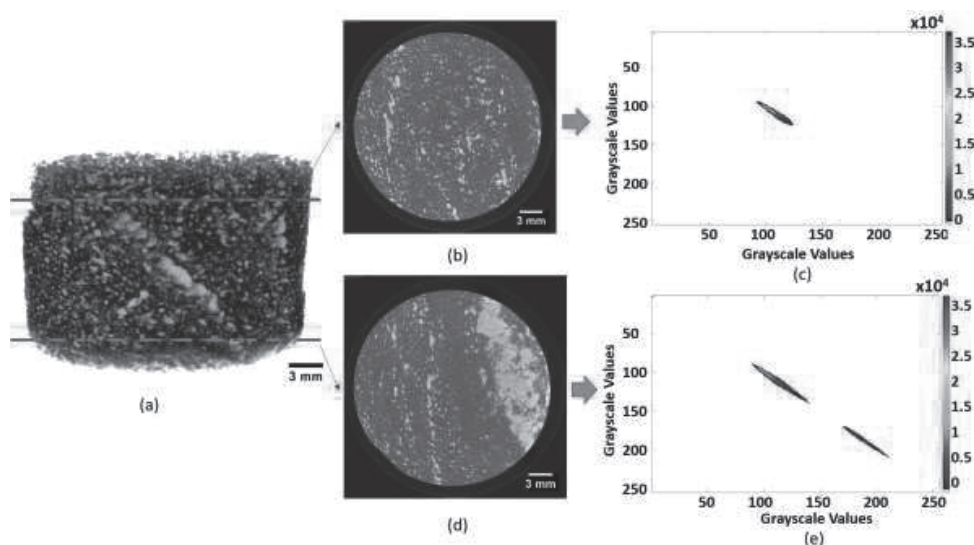
Figure 6. Textural analysis of 3D drill core image acquired from μCT. (a) Original 3D image of a drill core; (b) and (c) Two μCT slices showing different textures; (d) and (e) shows the texture heat map of the slices. The heat map reveals the association of each pixels in the image; more association between high grayscale value pixels means more sulphide mineralization, as shown in (e).

CONCLUSION

The future is wide open for μCT in process mineralogy. Additional dimension in μCT analysis allows better characterization of ore, leading to better understanding of ore behavior in the downstream processes. Future work shall be emphasized to accelerate μCT application in ore characterization through development of both instrumentation and data processing workflow. Development of instrumentation could include sub-micron resolution, in-situ experiments, and combination with μCT other instruments such as XRF, EDS, and XRD. Development of the data processing includes better reconstruction techniques, optimized algorithm to handle large datasets, as well as benchmarking data processing techniques applied in other field of material science.

REFERENCES

Alves dos Santos, N., 2018. Modelling flotation per size liberation class – Part 3 – Modelling recoveries using particle surface area. Miner. Eng. 129, 15–23. https://doi.org/10.1016/J.MINENG.2018.08.036

Alves dos Santos, N., Galery, R., 2018. Modelling flotation per size liberation class – Part 2 – Evaluating flotation per class. Miner. Eng. 129, 24–36. https://doi.org/10.1016/J.MINENG.2018.09.013

Andrä, H., Combaret, N., Dvorkin, J., Glatt, E., Han, J., Kabel, M., Keehm, Y., Krzikalla, F., Lee, M., Madonna, C., 2013. Digital rock physics benchmarks—Part I: Imaging and segmentation. Comput. Geosci. 50, 25–32.

Bam, L.C., Miller, J.A., Becker, M., Basson, I.J., 2019. X-ray computed tomography: Practical evaluation of beam hardening in iron ore samples. Miner. Eng. 131, 206–215. https://doi.org/10.1016/J.MINENG.2018.11.010

Barnes, S.J., Le Vaillant, M., Lightfoot, P.C., 2017. Textural development in sulfide-matrix ore breccias in the Voisey's Bay Ni-Cu-Co deposit, Labrador, Canada. Ore Geol. Rev. 90, 414–438. https://doi.org/10.1016/j.oregeorev.2017.03.019

Barnes, S.J., Staude, S., Le Vaillant, M., Piña, R., Lightfoot, P.C., 2018. Sulfide-silicate textures in magmatic Ni-Cu-PGE sulfide ore deposits: Massive, semi-massive and sulfide-matrix breccia ores. Ore Geol. Rev. 101, 629–651. https://doi.org/10.1016/J.OREGEOREV.2018.08.011

Baum, W., 2014. Ore characterization, process mineralogy and lab automation a roadmap for future mining. Miner. Eng. 60, 69–73. https://doi.org/10.1016/J.MINENG.2013.11.008

Becker, M., Jardine, M.A., Miller, J.A., Harris, M., 2016. X-ray Computed Tomography–a Geometallurgical Tool for 3D Textural Analysis of Drill Core?, in: Proceedings of the 3rd AusIMM International Geometallurgy Conference. pp. 15–16.

Butcher, A., 2010. A practical guide to some aspects of mineralogy that affect flotation. Flotat. Plant Optim. 16, 83–93.

Cepuritis, R., Garboczi, E.J., Jacobsen, S., Snyder, K.A., 2017. Comparison of 2-D and 3-D shape analysis of concrete aggregate fines from VSI crushing. Powder Technol. 309, 110–125. https://doi.org/https://doi.org/10.1016/j.powtec.2016.12.037

Chauhan, S., Rühaak, W., Khan, F., Enzmann, F., Mielke, P., Kersten, M., Sass, I., 2016. Processing of rock core microtomography images: Using seven different machine learning algorithms. Comput. Geosci. 86, 120–128. https://doi.org/https://doi.org/10.1016/j.cageo.2015.10.013

Cnudde, V., Boone, M.N., 2013. High-resolution X-ray computed tomography in geosciences: A review of the current technology and applications. Earth-Science Rev. 123, 1–17.

Deng, H., Fitts, J.P., Peters, C.A., 2016. Quantifying fracture geometry with X-ray tomography: Technique of Iterative Local Thresholding (TILT) for 3D image segmentation. Comput. Geosci. 20, 231–244. https://doi.org/10.1007/s10596-016-9560-9

Dey, S., Mohanta, M.K., Singh, R., 2017. Mineralogy and textural impact on beneficiation of goethitic ore. Int. J. Min. Sci. Technol. 27, 445–450. https://doi.org/10.1016/J.IJMST.2017.03.017

Donskoi, E., Poliakov, A., Holmes, R., Suthers, S., Ware, N., Manuel, J., Clout, J., 2016. Iron ore textural information is the key for prediction of downstream process performance. Miner. Eng. 86, 10–23. https://doi.org/10.1016/j.mineng.2015.11.009

dos Santos, N.A., Galery, R., 2018. Modelling flotation per size liberation class – Part 1 – Minimizing the propagation of experimental errors in the estimate of flotation recovery. Miner. Eng. 128, 254–265. https://doi.org/10.1016/J.MINENG.2018.07.003

Fandrich, R., Gu, Y., Burrows, D., Moeller, K., 2007. Modern SEM-based mineral liberation analysis. Int. J. Miner. Process. 84, 310–320. https://doi.org/https://doi.org/10.1016/j.minpro.2006.07.018

Fandrichi, R.G., Schneider, C.L., Gay, S.L., 1998. Two stereological correction methods: Allocation method and kernel transformation method. Miner. Eng. 11, 707–715. https://doi.org/10.1016/S0892-6875(98)00057-0

Ghorbani, Y., Becker, M., Petersen, J., Morar, S.H., Mainza, A., Franzidis, J.-P., 2011. Use of X-ray computed tomography to investigate crack distribution and mineral dissemination in sphalerite ore particles. Miner. Eng. 24, 1249–1257. https://doi.org/https://doi.org/10.1016/j.mineng.2011.04.008

Gottlieb, P., Wilkie, G., Sutherland, D., Ho-Tun, E., Suthers, S., Perera, K., Jenkins, B., Spencer, S., Butcher, A., Rayner, J., 2000. Using quantitative electron microscopy for process mineralogy applications. JOM 52, 24–25. https://doi.org/10.1007/s11837-000-0126-9

Henley, K.J., 1983. ORE-DRESSING MINERALOGY - A REVIEW OF TECHNIQUES, APPLICATIONS AND RECENT DEVELOPMENTS., in: J.P.R., de V., P.A., C. (Eds.), . Geological Soc of South Africa, The Australian Mineral Development, Lab, Geological Services Div,, Adelaide, Aust, The Australian Mineral Development Lab, Geological Services Div, Adelaide, Aust, pp. 175–200.

Jardine, M.A., Miller, J.A., Becker, M., 2018. Coupled X-ray computed tomography and grey level co-occurrence matrices as a method for quantification of mineralogy and texture in 3D. Comput. Geosci. 111, 105–117. https://doi.org/10.1016/j.cageo.2017.11.005

Koch, P.-H., 2017. Particle generation for geometallurgical process modeling. Licent. thesis / Luleå Univ. Technol. Luleå tekniska universitet, Minerals and Metallurgical Engineering, Department of Civil, Environmental and Natural Resources Engineering, Luleå University of Technology.

Kyle, J.R., Ketcham, R.A., 2015. Application of high resolution X-ray computed tomography to mineral

deposit origin, evaluation, and processing. Ore Geol. Rev. 65, 821–839. https://doi.org/10.1016/j.oregeorev.2014.09.034

Laforce, B., Masschaele, B., Boone, M.N., Schaubroeck, D., Dierick, M., Vekemans, B., Walgraeve, C., Janssen, C., Cnudde, V., Van Hoorebeke, L., Vincze, L., 2017. Integrated Three-Dimensional Microanalysis Combining X-Ray Microtomography and X-Ray Fluorescence Methodologies. Anal. Chem. 89, 10617–10624. https://doi.org/10.1021/acs.analchem.7b03205

Lätti, D., Adair, B.J.I., 2001. An assessment of stereological adjustment procedures. Miner. Eng. 14, 1579–1587. https://doi.org/10.1016/S0892-6875(01)00176-5

Leroy, S., Dislaire, G., Bastin, D., Pirard, E., 2011. Optical analysis of particle size and chromite liberation from pulp samples of a UG2 ore regrinding circuit. Miner. Eng. 24, 1340–1347.

Lin, C.L., Miller, J.D., 2005. 3D characterization and analysis of particle shape using X-ray microtomography (XMT). Powder Technol. https://doi.org///doi.org/10.1016/j.powtec.2005.04.031

Lin, C.L., Miller, J.D., 1996. Cone beam X-ray microtomography for three-dimensional liberation analysis in the 21st century. Int. J. Miner. Process. 47, 61–73.

Little, L., Mainza, A.N., Becker, M., Wiese, J., 2017. Fine grinding: How mill type affects particle shape characteristics and mineral liberation. Miner. Eng. 111, 148–157. https://doi.org/10.1016/j.mineng.2017.05.007

Little, L., Mainza, A.N., Becker, M., Wiese, J.G., 2016. Using mineralogical and particle shape analysis to investigate enhanced mineral liberation through phase boundary fracture. Powder Technol. 301, 794–804. https://doi.org/https://doi.org/10.1016/j.powtec.2016.06.052

Lobos, R., Silva, J.F., Ortiz, J.M., Díaz, G., Egaña, A., 2016. Analysis and Classification of Natural Rock Textures based on New Transform-based Features. Math. Geosci. 48, 835–870.

Lotter, N.O., Baum, W., Reeves, S., Arrué, C., Bradshaw, D.J., 2018a. The business value of best practice process mineralogy. Miner. Eng. 116, 226–238. https://doi.org/10.1016/J.MINENG.2017.05.008

Lotter, N.O., Evans, C.L., Engstrőm, K., 2018b. Sampling – A key tool in modern process mineralogy. Miner. Eng. 116, 196–202. https://doi.org/10.1016/J.MINENG.2017.07.013

Lotter, N.O., Whittaker, P.J., Kormos, L., Stickling, J.S., Wilkie, G.J., 2002. The development of process mineralogy at Falconbridge Limited and application to the Raglan Mill. CIM Bull. 95, 85–92.

Lund, C., Lamberg, P., Lindberg, T., 2015. Development of a geometallurgical framework to quantify mineral textures for process prediction. Miner. Eng. 82, 61–77. https://doi.org/https://doi.org/10.1016/j.mineng.2015.04.004

Lux, J., Delisée, C., Thibault, X., 2011. 3D characterization of wood based fibrous materials: an application. Image Anal. Stereol. 25, 25–35.

Ma, G., Xia, W., Xie, G., 2018. Effect of particle shape on the flotation kinetics of fine coking coal. J. Clean. Prod. 195, 470–475. https://doi.org/10.1016/J.JCLEPRO.2018.05.230

Markussen, Ø., Dypvik, H., Hammer, E., Long, H., Hammer, Ø., 2019. 3D characterization of porosity and authigenic cementation in Triassic conglomerates/arenites in the Edvard Grieg field using 3D micro-CT imaging. Mar. Pet. Geol. 99, 265–281. https://doi.org/10.1016/j.marpetgeo.2018.10.015

Masad, E., Saadeh, S., Al-Rousan, T., Garboczi, E., Little, D., 2005. Computations of particle surface characteristics using optical and X-ray CT images. Comput. Mater. Sci. 34, 406–424. https://doi.org/https://doi.org/10.1016/j.commatsci.2005.01.010

Mees, F., Swennen, R., Van Geet, M., Jacobs, P., 2003. Applications of X-ray computed tomography in the geosciences. Geol. Soc. London, Spec. Publ. 215, 1–6.

Miller, J.D., Lin, C.L., Cortes, A.B., 1990. A review of X-ray computed tomography and its applications in mineral processing. Miner. Procesing Extr. Metall. Rev. 7, 1–18.

Miller, J.D., Lin, C.L., Garcia, C., Arias, H., 2003. Ultimate recovery in heap leaching operations as established from mineral exposure analysis by X-ray microtomography. Int. J. Miner. Process. 72, 331–340.

Omoumi, P., Becce, F., Racine, D., Ott, J., Andreisek, G., Verdun, F., 2015. Dual-Energy CT: Basic Principles, Technical Approaches, and Applications in Musculoskeletal Imaging (Part 1), Seminars in musculoskeletal radiology. https://doi.org/10.1055/s-0035-1569253

Pamukcu, A.S., Gualda, G.A.R., Rivers, M.L., 2013. Quantitative 3D petrography using X-ray tomography 4: Assessing glass inclusion textures with propagation phase-contrast tomography. Geosphere 9, 1704–1713.

Peng, R., Yang, Y., Ju, Y., Mao, L., Yang, Y., 2011. Computation of fractal dimension of rock pores based on gray CT images. Chinese Sci. Bull. 56, 3346. https://doi.org/10.1007/s11434-011-4683-9

Pérez-Barnuevo, L., Lévesque, S., Bazin, C., 2018. Automated recognition of drill core textures: A geometallurgical tool for mineral processing prediction. Miner. Eng. 118, 87–96. https://doi.org/https://doi.org/10.1016/j.mineng.2017.12.015

Pérez-Barnuevo, L., Pirard, E., Castroviejo, R., 2013. Automated characterisation of intergrowth textures in mineral particles. A case study. Miner. Eng. 52, 136–142. https://doi.org/10.1016/J.MINENG.2013.05.001

Pierret, A., Capowiez, Y., Belzunces, L., Moran, C.J., 2002. 3D reconstruction and quantification of macropores using X-ray computed tomography and image analysis. Geoderma 106, 247–271.

Pirard, E., Califice, A., Léonard, A., Gregoire, M., 2009. Multiscale shape analysis of particles in 3D using the calypter.

Pita, F., Castilho, A., 2017. Separation of plastics by froth flotation. The role of size, shape and density of the particles. Waste Manag. 60, 91–99. https://doi.org/10.1016/J.WASMAN.2016.07.041

Reyes, F., Lin, Q., Cilliers, J.J., Neethling, S.J., 2018. Quantifying mineral liberation by particle grade and surface exposure using X-ray microCT. Miner. Eng. 125, 75–82. https://doi.org/10.1016/J.MINENG.2018.05.028

Reyes, F., Lin, Q., Udoudo, O., Dodds, C., Lee, P.D., Neethling, S.J., 2017. Calibrated X-ray micro-tomography for mineral ore quantification. Miner. Eng. 110, 122–130. https://doi.org/10.1016/j.mineng.2017.04.015

Spencer, S., Sutherland, D., 2000. Stereological correction of mineral liberation grade distributions estimated by single sectioning of particles. Image Anal. Stereol. 19, 175–182.

Sutherland, D., 2007. Estimation of mineral grain size using automated mineralogy. Miner. Eng. 20, 452–460. https://doi.org/10.1016/J.MINENG.2006.12.011

Sutherland, D.N., Gottlieb, P., 1991. Application of automated quantitative mineralogy in mineral processing. Miner. Eng. 4, 753–762. https://doi.org/10.1016/0892-6875(91)90063-2

Suuronen, J.-P., Sayab, M., 2018. 3D nanopetrography and chemical imaging of datable zircons by synchrotron multimodal X-ray tomography. Sci. Rep. 8, 4747. https://doi.org/10.1038/s41598-018-22891-9

Tiu, G., 2017. Classification of Drill Core Textures for Process Simulation in Geometallurgy : Aitik Mine, Sweden. EMerald Program.

Tøgersen, M.K., Kleiv, R.A., Ellefmo, S., Aasly, K., 2018. Mineralogy and texture of the Storforshei iron formation, and their effect on grindability. Miner. Eng. 125, 176–189. https://doi.org/10.1016/j.mineng.2018.06.009

Tungpalan, K., Wightman, E., Manlapig, E., 2015. Relating mineralogical and textural characteristics to flotation behaviour. Miner. Eng. 82, 136–140. https://doi.org/10.1016/J.MINENG.2015.02.005

Ueda, T., Oki, T., Koyanaka, S., 2018a. A general quantification method for addressing stereological bias in mineral liberation assessment in terms of volume fraction and size of mineral phase. Miner. Eng. 119, 156–165. https://doi.org/10.1016/J.MINENG.2018.01.034

Ueda, T., Oki, T., Koyanaka, S., 2018b. Numerical analysis of the general characteristics of stereological bias in surface liberation assessment of ore particles. Adv. Powder Technol. 29, 3327–3335. https://doi.org/10.1016/J.APT.2018.09.010

Van Dalen, G., Koster, M.W., Dalen, G. Van, Koster, M.W., 2012. 2D & 3D particle size analysis of micro-CT images. Unilever Res. Dev. Netherlands. https://doi.org/10.1007/s10509-008-9775-x

Vecchio, I., Schladitz, K., Godehardt, M., Heneka, M.J., 2012. 3D GEOMETRIC CHARACTERIZATION OF PARTICLES APPLIED TO TECHNICAL CLEANLINESS. Image Anal. & Stereol. Vol 31, No 3 (2012)DO - 10.5566/ias.v31.p163-174 .

Wang, L., Ooi, J.Y., Butler, I., 2015. Interpretation of Particle Breakage under Compression Using X-ray Computed Tomography and Digital Image Correlation. Procedia Eng. 102, 240–248.

https://doi.org/10.1016/J.PROENG.2015.01.138

Wang, Y., Li, C., Hou, Z., Yi, X., Wei, X., 2018. In Vivo X-ray Computed Tomography Investigations of Crack Damage Evolution of Cemented Waste Rock Backfills (CWRB) under Uniaxial Deformation. Minerals 8, 539.

Wang, Y., Lin, C.L., Miller, J.D., 2017. Quantitative analysis of exposed grain surface area for multiphase particles using X-ray microtomography. Powder Technol. 308, 368–377. https://doi.org/10.1016/j.powtec.2016.11.047

Wang, Y., Lin, C.L., Miller, J.D., 2015. Improved 3D image segmentation for X-ray tomographic analysis of packed particle beds. Miner. Eng. 83, 185–191. https://doi.org/10.1016/j.mineng.2015.09.007

Wu, A., Yang, B., Xi, Y., Jiang, H., 2007. Pore structure of ore granular media by computerized tomography image processing. J. Cent. South Univ. Technol. 14, 220–224.

Xia, W., 2017. Role of surface roughness in the attachment time between air bubble and flat ultra-low-ash coal surface. Int. J. Miner. Process. 168, 19–24. https://doi.org/10.1016/J.MINPRO.2017.09.006

Xia, W., Ma, G., Bu, X., Peng, Y., 2018. Effect of particle shape on bubble-particle attachment angle and flotation behavior of glass beads and fragments. Powder Technol. 338, 168–172. https://doi.org/10.1016/J.POWTEC.2018.07.024

Yang, B., Wu, A., Narsilio, G.A., Miao, X., Wu, S., 2017. Use of high-resolution X-ray computed tomography and 3D image analysis to quantify mineral dissemination and pore space in oxide copper ore particles. Int. J. Miner. Metall. Mater. 24, 965–973. https://doi.org/10.1007/s12613-017-1484-4

Yang, X., Kuru, E., Gingras, M., Iremonger, S., 2019. CT-CFD integrated investigation into porosity and permeability of neat early-age well cement at downhole condition. Constr. Build. Mater. 205, 73–86. https://doi.org/10.1016/J.CONBUILDMAT.2019.02.004

Zandomeneghi, D., Voltolini, M., Mancini, L., Brun, F., Dreossi, D., Polacci, M., 2010. Quantitative analysis of X-ray microtomography images of geomaterials: Application to volcanic rocks. Geosphere 6, 793–804.

Zhao, B., Wang, J., Coop, M.R., Viggiani, G., Jiang, M., 2015. An investigation of single sand particle fracture using X-ray micro-tomography. Géotechnique 65, 625–641.

Paper 2

X-ray Microcomputed Tomography (μCT) for Mineral Characterization: A Review of Data Analysis Methods

Pratama Istiadi Guntoro *, Yousef Ghorbani, Pierre-Henri Koch and Jan Rosenkranz

MiMeR—Minerals and Metallurgical Engineering, Luleå University of Technology, SE-971 87 Luleå, Sweden;
yousef.ghorbani@ltu.se (Y.G.); pierre-henri.koch@ltu.se (P.-H.K.); jan.rosenkranz@ltu.se (J.R.)

* Correspondence: pratama.istiadi.guntoro@ltu.se, Tel.: +46-920-493-235

Abstract: The main advantage of X-ray microcomputed tomography (μCT) as a non-destructive imaging tool lies in its ability to analyze the three-dimensional (3D) interior of a sample, therefore eliminating the stereological error exhibited in conventional two-dimensional (2D) image analysis. Coupled with the correct data analysis methods, μCT allows extraction of textural and mineralogical information from ore samples. This study provides a comprehensive overview on the available and potentially useful data analysis methods for processing 3D datasets acquired with laboratory μCT systems. Our study indicates that there is a rapid development of new techniques and algorithms capable of processing μCT datasets, but application of such techniques is often sample-specific. Several methods that have been successfully implemented for other similar materials (soils, aggregates, rocks) were also found to have the potential to be applied in mineral characterization. The main challenge in establishing a μCT system as a mineral characterization tool lies in the computational expenses of processing the large 3D dataset. Additionally, since most of the μCT dataset is based on the attenuation of the minerals, the presence of minerals with similar attenuations limits the capability of μCT in mineral segmentation. Further development on the data processing workflow is needed to accelerate the breakthrough of μCT as an analytical tool in mineral characterization.

Keywords: X-ray microcomputed tomography; data analysis; mineral characterization; texture; mineralogy

1. Introduction

Following the widespread development of X-ray microcomputed tomography (μCT) in medical applications and in diverse industrial applications, potential applications of μCT have been reviewed within the geosciences [1,2], especially for mineral characterization [3,4]. Being a non-destructive technique, which allows for three-dimensional (3D) analysis of an object, μCT systems offer a new depth of information that has not been available with conventional two-dimensional (2D)-based microscopy analysis. Several studies have investigated the application of μCT in performing mineral characterization, which includes pore analysis [5–10], liberation and grain exposure analysis [11–15], crack and breakage analysis [14,16,17], as well as mineral segmentation analysis [3,17–19].

While work towards identifying further potential applications of μCT continues, several studies have also been focusing on development of data processing to better analyze μCT datasets [9,18,20–26]. A typical data processing tool of μCT images in relation to mineral characterization can be generalized into several steps that are illustrated in Figure 1.
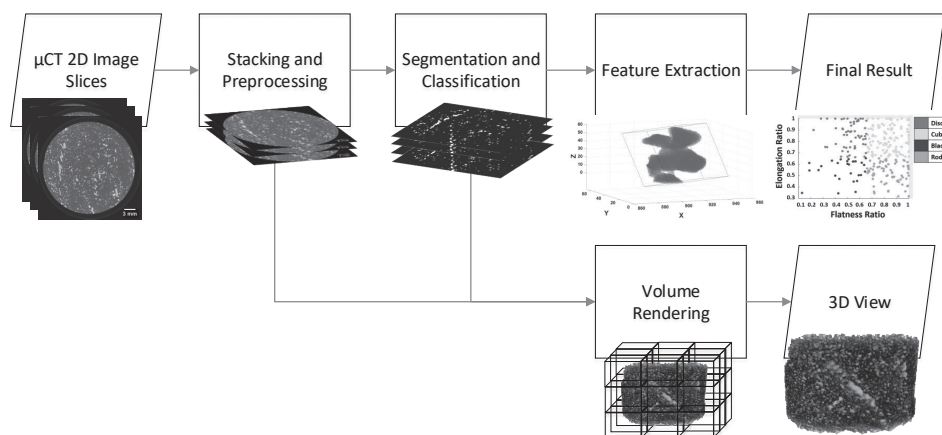
Figure 1. Typical workflow involved in μCT data analysis for mineral characterization. The resulting 2D μCT slices are stacked and preprocessed into a 3D image. Segmentation and classification are performed so that a volume of interest (VOI) can be analyzed further. In relation to mineral characterization, this VOI usually represents a phase in the sample (an example here is the sulphide phase), so that features of that phase can be extracted (an example here is the grain shape). Volume rendering is done to produce a 3D view on a 2D display screen.

Many reviews have been conducted with regard to μCT applications [1–4,11]. Such reviews mostly analyze the applicability and performance of μCT systems for different cases of mineral analysis. Potential new applications were identified through addressing the advancement made in the μCT instruments, such as dual-energy μCT [1,17], in situ experiments during acquisition [27,28], the use of diffraction and phase contrast modes [29,30], as well as sub-micron resolution [1,31,32].

While the applicability and usage of μCT in mineral characterization has been reviewed, there seems to be lack of studies in evaluating the data analysis methods involved in processing μCT datasets. This review aims to address just that; it aims to thoroughly discuss various μCT data analysis methods, their limitations, as well as their application in mineral characterization. By exploring the data analysis methods, this review can be a reference in determining which data analysis methods shall be implemented in various cases of mineral characterization using μCT systems.

The primary sources of studies for this review are those that apply laboratory μCT systems in characterizing ore samples. Moreover, this review focuses mainly on absorption-contrast mode tomography, as this is the conventional mode in laboratory μCT systems. As the objective of this review is also to further explore potential data analysis methods that can be applied in mineral characterization, other μCT applications in similar materials, such as different types of rocks, sands, powders, and aggregates, are also considered. Some other materials that are less similar to ore samples, such as composites, soils, and artificial fibrous networks, are also evaluated. Medical application of μCT systems are not considered as the nature of the system is different compared to the one used in material science. The algorithms in each step shown in Figure 1 are systematically evaluated alongside examples of cases and applications.

2. μCT Measurement and Data Acquisition

During acquisition, the sample for the μCT measurement is exposed to the incident X-ray beam and rotated through 180° to obtain a number of projections (typically between 600 to 3600 projections). These projections are then reconstructed to create 2D slices (projection images) of the measured volume. The pixels in the 2D slices retain spatial information about their originating volume elements (voxels) so that the slices could be stacked to recreate the 3D volume of the

specimen. These 2D slices are also the "raw data" that could be put in the μCT data processing workflow in Figure 1. An illustrative image describing the processes involved in μCT measurement and data acquisition is shown in Figure 2.
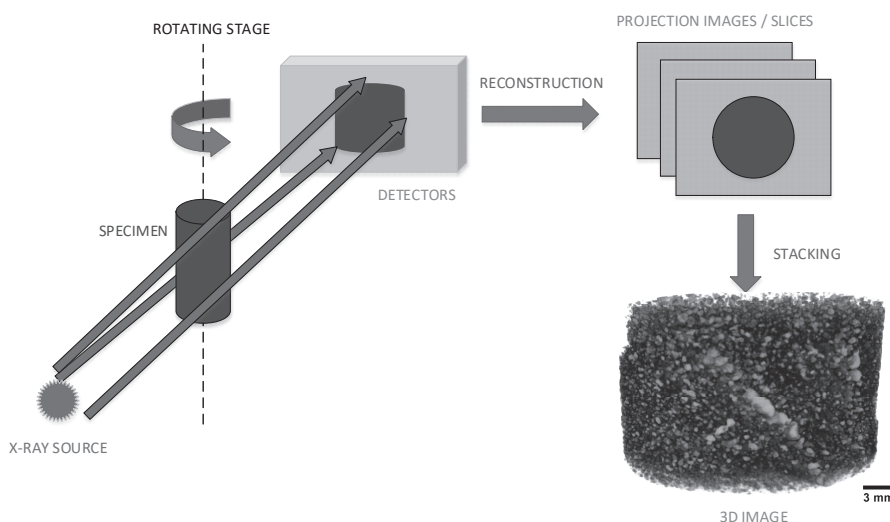
Figure 2. Specimen analysis and data acquisition using μCT. The X-ray beam originates from a small focal spot and illuminates a planar detector. The specimen is fixed in a stage, and rotated to obtain several projections over a range of angles and positions. The 2D image slices are reconstructed from these projections, whereas afterwards it can be stacked and rendered to create the 3D volume for displaying purposes.

The μCT configuration shown in Figure 2 resembles the most widely used modern laboratory cone beam scanning configuration. Other configurations, such as fan beam, near-parallel beam, as well as synchrotron-based μCT, are not the main focus in this review; interested readers are referred to other reviews [1,3,33].

2.1. Measurements

The principle of μCT is similar to other X-ray based analysis, whereas it records the differences in X-ray attenuation by the object. Attenuation is described as the proportion of the X-ray that interacts with the material and represented by the gray intensities in the reconstructed slice images. The interaction between the material and the X-ray beam decreases the intensity of the X-ray as it passes through the volume. This decrease of intensity is described by the Beer–Lambert Law:

$$I(x) = I^0 \times e^{-\mu x} \tag{1}$$

where $I(x)$ is the intensity measured at the detector (units: mass time^{-3}), I^0 is the intensity of original incident beam from the X-ray source, x is the length of the X-ray path within the material, and μ is the attenuation coefficient of the material (units: length^{-1}), which depends on the material atomic number and density.

Due to the stage rotation, the beam angle (α) is varied, which in turn affects the attenuation coefficient. Deriving from Equation (1), the correlation between the beam angle and attenuation coefficient (μ) for a given length of X-ray path (L) is given below:

$$\ln \frac{I(L,x)}{I^0(\alpha)} = - \int_0^L \mu(x,\alpha)dx \tag{2}$$

The attenuation coefficient is then related to its theoretical values for different ore minerals (μ_C). The theoretical values can be calculated as a function of the X-ray energy (ε, units: mass length^2 time^{-2}), and mineral density (ϱ, units: mass length^{-3}). Such calculation is given in Equation (3).

$$\mu_C(\varepsilon) = \rho \times \mu_{mass}(\varepsilon) \tag{3}$$

μ_{mass} refers to the mass attenuation coefficient which depends on the X-ray energy used in the measurement. The dependency of μ_{mass} on energy can be expressed by Equation (4) [34], in which a and b are the energy-dependent coefficients, and Z is the bulk atomic number of the material.

$$\mu_{mass} = a + b\frac{Z^{3.8}}{\varepsilon^{3.2}} \tag{4}$$

Depending on the energy spectrum, different attenuation mechanisms prevail. In lower energy spectra (50–100 keV), photoelectric absorption predominates, in which the incoming X-ray photon ejects the inner electron by occupying the inner shell of the atom. This imbalance causes the electron from the outer shell to jump to the inner shell. The resulting μ based on this mechanism is proportional to Z^{4-5}. In the higher energy range (up to 5–10 MeV), Compton scattering is more prevalent, in which the incoming photon only interacts with the outer electron and deflects it to a different direction. This mechanism yields attenuation coefficient (μ) that is proportional to Z. As it suggests by the relation of μ with Z, photoelectric absorption is highly dependent on the atomic number of the material, while Compton scattering strongly depends on density of the material (it is less dependent on the atomic number) [35]. Both mechanisms are illustrated in Figure 3.
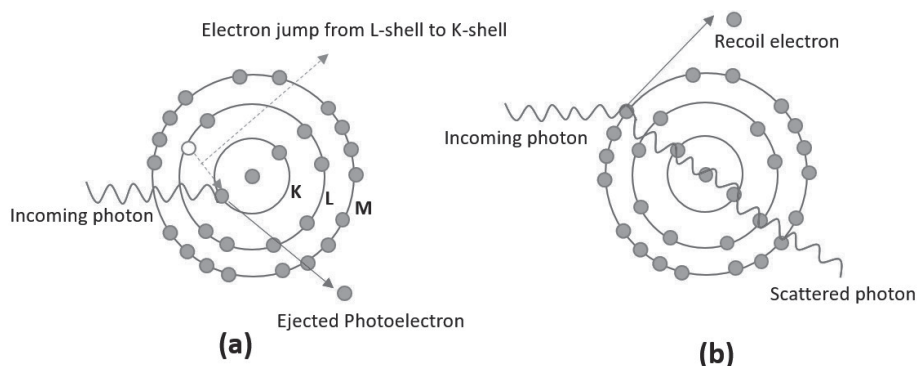
Figure 3. Interaction of X-ray photons to the subjected atom, showing: (**a**) photoelectric absorption; and (**b**) Compton scattering.

The dependence of the X-ray attenuation coefficient to the energy spectrum poses a trade-off in differentiating mineral phases within the sample. Higher energy means a better penetrative capability of the X-ray beam which, in turn, results in a better signal-to-noise ratio, but it often becomes less sensitive in differentiating mineral phases in the rock sample. Decreasing the energy could overcome this limitation, but this also decreases the penetrative capability of the X-ray, therefore requiring longer exposure time to achieve good signal-to-noise ratio. This could further be explained by the circumstance that in lower energy spectra, the resulting μ is proportional to Z^{4-5}, which means that it is much more sensitive to changes in the atomic number, therefore better in differentiating phases in the sample. This is compared to having higher energy spectra in which μ is only proportional to Z, which then the difference in μ is more driven by density differences between the materials due to Compton effect. This principle is the key in differentiating minerals using μCT; by using lower energy, contrasts between minerals with similar densities can be achieved as it is driven more by the difference in atomic number. The dependence of attenuation coefficient of

minerals to the X-ray energy is available in some databases, such as XCOM, managed by National Institute of Science and Technology (NIST) [36].

In fact, several researchers have addressed this issue of differentiating minerals by optimizing the scanning conditions of the μCT system. The use of lower energy spectra was evaluated by Reyes et al. [18] in which, at 50 kV, copper sulphide minerals were able to be distinguished from pyrite, with the help of SEM-EDS measurement as reference data. Reduction of sample size was also evaluated [3,37], as lower energy means longer acquisition time; reducing sample size is an alternative way to achieve reasonable acquisition time while at the same time minimizing the beam hardening effect. Such an effect makes attenuation of the same minerals differ depending on the location within the sample, therefore limiting the accuracy of the mineral differentiation [18]. Kyle et al. [38] has demonstrated that at scanning energy of 180 keV, differentiation of chalcopyrite and bornite is possible using smaller cores (≤22 mm), while Bam et al. [37] have also demonstrated that, at similar energy level, the beam hardening effect is minimized when the apatite-magnetite core sample size is reduced to 17 mm.

A calibration step prior to μCT data acquisition can also be performed in order to distinguish between minerals. This can be achieved by measuring pure minerals with known density, so that correlation between the attenuation coefficient and density is obtained, or by using dual-energy scanning so that the density of the material can be obtained directly through the relation between attenuation coefficients in two different energy levels [17,39]. However, the latter case is known to be sensitive to noise [40]. Such calibration could also be performed after acquisition by correlating the μCT data to SEM-EDS data [18,19] or XRF mapping [41,42].

The spatial resolution of the μCT system is also critical to produce good results as well as good signal-to-noise ratios. Spatial resolution defines how the volume is discretized, i.e., the volume over which Equation (2) is integrated. In other words, this resolution is the size of the smallest detectable object with μCT. Typically, a μCT scanner would have spatial resolution ranging from 10–50 μm [43]. Some newer generations of cone beam μCT systems are even able to reach below 1 μm, or even further, which is often termed as sub-μCT [44]. It is worth noting that higher resolution will lead to better results, but longer exposure time is needed as a higher number of projections is required to achieve such high resolution. In order to reduce cost, samples are often scanned at a lower resolution first, then afterwards its region of interest is determined where high-resolution scanning is carried out.

Some artifacts could be present during μCT measurement and data acquisition. Artifacts are defined as part of the reconstructed μCT slice images which did not originate from the original sample. Artifacts could originate from the physical interaction between the materials and the X-ray beam, or from the scanning process (detectors). These artifacts have been thoroughly discussed by several other workers [3,37,45,46]. The artifacts that regularly occurred with industrial (non-medical) μCT system are summarized in Table 1.

Table 1. Summary of artifacts that occur with an industrial μCT system.

Type of Artifact	Associated with	Source	Solution
Cupping artifacts, streaks and dark bands	Physical artifact	Beam hardening—Unequal absorption of photons in the polychromatic X-ray beam	Digital filtering, calibration correction, linearization
Ring Artifact	Scanning artifact	Deviation of the detectors	Recalibration of the detectors, Digital filtering
Partial volume effect– Limited resolution effect	Physical artifact	Voxel comprised of several phases, yielding an average CT values of those phases	Interpolation, using higher spatial resolution

It is worth noting that the artifacts and limitations described earlier are mostly found when using the laboratory based μCT configurations. For example, the beam hardening effect can be avoided by

the use of a monochromatic (synchrotron) source [47]. A synchrotron source also offers higher photon flux, allowing more rapid acquisition time, less image noise, and higher spatial resolution in comparison with laboratory μCT systems.

Moreover, some of the issues of mineral differentiation with μCT can be alleviated by the use of other contrast modes such as diffraction-contrast tomography (DCT) and phase-contrast tomography (PCT), which is mainly available only in synchrotron sources. Both contrast modes have found applications mostly in analysis of microstructures in crystalline samples, as it allows the high contrast between phases [48–53]. Synchrotron systems also open up possibilities of complimentary tomography methods such as X-ray diffraction microtomography (XRD-CT) and X-ray Fluorescence microtomography (XRF-CT). XRD-CT finds applications mostly in evaluating crystalline materials [54,55], while XRF-CT could be used to detect small features, such as inclusions in geological samples [48,56].

While these properties of synchrotron μCT systems make it clearly superior to laboratory μCT system, the access to such systems is generally limited due to high operational costs [1]. The current technology of laboratory μCT systems has not yet met the level of synchrotron source [37], but recent developments have extended their capabilities further. For example, recent works [29,30,57] have demonstrated the possibilities to perform PCT and DCT with laboratory μCT systems.

2.2. Reconstruction

Reconstruction is the process of creating μCT image slices from the projections obtained from the μCT measurement. The projections from μCT measurements are reconstructed, mainly by solving Equation (2) for all angles and positions using appropriate mathematical transformations [23]. The most widely used reconstruction method in μCT systems is the filtered back projection (FBP), which is based on Radon transformation. In FBP, all the projection values from the measurement are placed back into the appropriate position in the X-ray path/line between the source and detectors depending on its acquisition angle (α).

Prior to the back projection, these values are convoluted with a filter to remove blurring. Mathematical derivations and detailed explanations of the FBP method are available elsewhere [58]. With the cone beam scanning configurations, modification from the traditional convolution filter and back-projection based method is needed. Most of the cone beam μCT systems make use of the FBP reconstruction methods developed by Feldkamp [59], i.e., the Feldkamp, Davis, Kress (FDK) method.

It can be concluded that back projection is accurate only if the projection values are precise and clear without any noise. In real applications, the measurements often result in a probability distribution of the projection values; a single projection value in a given position and angle is almost impossible to achieve. A direct back projection of such values could result in reconstruction artifacts in the final image.

The iterative reconstruction method is another reconstruction method that can overcome the limitations of FBP. The method allows input of prior information about the μCT system to the algorithm, improving the accuracy of the method. The method itself is based on iteratively forward projecting the image and back projecting the projection values until convergence. Usually an initial estimate about the image is produced and forward-projected to estimate the projection values. The projection values are then compared with the actual measurement. The initial image estimate is then improved based on the back-projection values. These procedures are repeated until a convergence between the actual and estimated projection values is achieved. While this method can overcome the noise limitations, it is well known to be computationally intensive and slow compared to the traditional back projection method. Several studies [60–62] have been conducted to improve this iterative method, mainly aiming to lower its computational cost.

After the reconstruction, the reconstruction values or CT numbers are obtained, in which such values correspond to the grayscales in the reconstructed images. These numbers are linearly related to the attenuation coefficients of the material in each position. In medical systems, a relative scaling of this CT number is used which often termed as the Hounsfield Units (HU). The scaling is based on the attenuation of water (assigned at 0 HU) and air (assigned at −1000 HU). In the case of ore samples,

often time a mineral phase would not have a single CT value, rather it would have a distribution of CT values. This is mostly caused by natural variation of chemical composition in the rocks itself due to weathering, solid solutions, zoning, etc.

3. Pre-Processing

The projection images are then stacked into a 3D dataset, which is a stack of 2D slice images. The pre-processing step is usually necessary in order to prepare the dataset for the subsequent steps.

3.1. Filtering

Filters are mathematical algorithms that are implemented in each pixel and its neighbors. These filters typically attempt to replace any pixel value that is inconsistent with its neighbors. The simplest approach is by convoluting a kernel (matrix) to the image. The kernel holds some values that would modify the image, and depending on the values, several tasks, such as denoising, blurring, sharpening, and edge detection, can be performed. The dimension of the kernel can be two or three dimensions depending on the image. Examples of these filters are listed below:

- Denoising and blurring filters, such as Gaussian and mean filters. As the name suggests, the typical drawback of these filters is that it blurs the image, including the phase boundaries which are critical in the segmentation process. This drawback is avoided by using edge-preserving filters, such as median, non-local mean, and bilateral filters. Some researchers have applied variation of these filters in their specific cases of μCT analysis of rock samples [9,21,63].
- Sharpening and edge detection filters, such as Laplacian filters, Sobel, Canny filters, Robert, and Prewitt filters [64–66]. These filters are typically used in rock μCT analysis especially in crack and pore detection [8,67], watershed segmentation [68], as well as feature extraction for supervised classification [15,19,22].

4. Segmentation and Classification

Segmentation refers to the grouping of digital image into several segments by identification and isolation of pixels that have the same features into a single category [69]. There are many different image segmentation methods, and several investigators have made reviews about their performances and applications [70–72]. More than a hundred segmentation algorithms based on these methods have also been developed, with many of them combining two or more methods. In this paper, the discussion will focus on methods that have been applied in μCT data analysis of ore samples.

4.1. Histogram Analysis

The most common segmentation method is based on the histogram analysis of grayscale intensities of the pixels in the image; an example is shown in Figure 4. The histogram provides the distribution of the grayscale level of each pixels in the image, therefore giving an idea regarding the different phases contained in the image. By analyzing the histogram of an image, one can obtain global information about the grayscale levels in the image. The analysis itself can be varying, including geometrical shape analysis of the histogram, entropy analysis between two classes, histogram deconvolution, as well as similarity attributes within one classes [73,74]. Histogram analysis can be used for μCT volumes in cases such as background removal [75], and to some extent pore extraction from rocks [7,8,74].
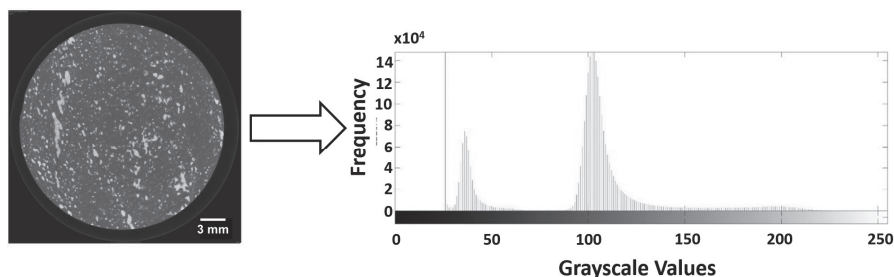
Figure 4. Histogram of gray values of a 2D slice. The two peaks indicate a clear threshold value for separating two classes, which in this case are the background (left peak) and the drill core (right peak). Note that further thresholding for the phases within the drill core would be challenging as it seems difficult to separate the right peak into several peaks (phases).
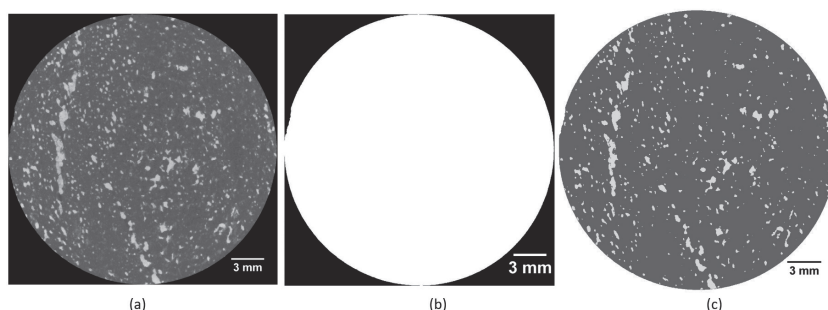
4.2. Thresholding

Thresholding is a common term to describe the introduction of threshold/limit value on an image, thereby segmenting the features that are below the threshold and others that are above the threshold value. The value is usually the grayscale intensity of the pixels. Thresholding is often used in the first step of image processing in order to extract the volume of interest from the whole volume. There are two major types of thresholding algorithms:

- Global thresholding, where the threshold value is determined from the entire image properties, for example by analyzing the whole histogram of the image as in Figure 4.
- Local thresholding, which means that instead of considering the whole image, only a certain part of the image is considered as a basis in setting a threshold value.

In the case of global thresholding, an optimal threshold value must be chosen in order to obtain a good result. Some algorithms exist that can optimize the threshold value based on the image input, one of them developed by Otsu [75]. It remains a widely used algorithm in setting a threshold value for 3D µCT image analysis [6,18,20,76,77], especially in terms of segmenting between pores/air and mineral matrix. The Otsu thresholding method is an effective way in differentiating mineral phases and the pore space, however it may not works perfectly when the sample is heterogeneous and the volume of interest (VOI) is large; such large volume shall be sub-sampled to produce a suitable VOI that represent the whole volume [6]. Additionally, Otsu thresholding might not work properly in cases where boundaries between high density/high atomic number and low density materials exist, as the boundaries may not be thresholded properly due to the partial volume effect [22].

Otsu thresholding can also be extended to obtain multiple thresholds, so that more than two phases can be separated in the µCT volume [78,79]. An example of this is shown in Figure 5.

Another commonly used algorithm for determining a global threshold value is the maximum entropy algorithm [80]. This algorithm is mostly used in segmenting between the grains and mineral matrix [76,77]. In studies by Lin et al. [77], the Otsu algorithm was used to distinguish ore particles from the air, while the maximum entropy algorithm was used to identify the metal sulphide grains within the mineral matrix. The reasoning behind this was that the occurrences of metal sulphide in the matrix is minimum, so that the sulphide peaks could not be clearly identified in the histogram.

Figure 5. Otsu thresholding, showing: (**a**) Original slice of drill core stack from μCT; (**b**) global thresholding with Otsu; and (**c**) multi-level thresholding with Otsu. It can be seen that directly using global thresholding will only intercept the drill core volumes from the background; multilevel thresholding is needed to extract the mineral grains from the drill core.

Local thresholding sets the value based on a local domain of voxels within a volume. This method is considered as a refinement of the global thresholding method based on local spatial information [7]. Deng et al. [26] applied an improved local thresholding algorithm that was capable of distinguishing between fractures and pores in rock matrix in a 3D μCT image. In his work, a fracture mask was initially created using connectivity operator in which local thresholding is performed within the mask. Based on local thresholding, a new fracture mask is obtained. This is repeated until the fracture mask volume is stabilized.

A gradient line computing the gradients of the image intensity intercepted by the line can be used also as a local domain where thresholds value should be based on. The threshold value is then based on the points where the calculated gradients are high, indicating the phase boundaries. Such a technique is referred to as gradient-based segmentation, and has been applied in mineral phase segmentation in μCT ore analysis [23]. Nevertheless, such a method would require the user to determine the locations of the lines to get them intercept as many phases as possible, thereby increasing the number of phases that can be segmented using the thresholds.

The eventual determination of a threshold value could also be done arbitrarily by the user. Arbitrary here means that the user visually estimates the threshold value. This could be done, for example, by visually determining the phase boundaries or taking the average grayscale values of the phases that have been visually determined by the user. Such a method has been implemented in porosity analysis, in which it was found that such method was in agreement with the experimental measurement [74]. The limitation of such a technique is that it is very subjective as the threshold determination depends very much on the user.

4.3. Region Growing

Another segmentation technique is the region growing method. The method is initialized by selecting a pixel, followed by the addition of the neighboring pixels to the initial pixel based on their similarity in grayscale values, thereby creating a region with similar grayscales. The process is repeated until all pixels can be categorized into a region. Grayscale intensities of the pixels are used as the similarity criteria [81,82] and, in other cases, gradients between neighboring pixels can also be used [23].

The region growing method is combined with edge detection in the widely used watershed segmentation. Watershed segmentation considers a grayscale image as a topographic surface, where the height of the surface is defined as the grayscale intensities of the image. The term "watershed" typically refers to a ridge that divides areas drained by different river system. This watershed line separates the catchment basins, which are typically the features that are segmented.

The common problem with watershed is the over segmentation, in which every regional minimum is transformed into its own basin, also segmenting features that are not of interest. Several

researchers have developed a way to overcome this problem, including by introducing markers to the image [83,84], merging the regions [85], denoising and edge enhancement [86], as well as combining watershed segmentation with wavelet transformation [87] and the topological gradient approach [88].

Marker-controlled watershed segmentation has been applied to 3D µCT images for several analyses by Miller et al. [22,89,90]. 3D watershed segmentation has been applied to different types of µCT image analysis, including coal washability analysis [89], air bubble sizes [90], as well as analysis of particle beds [22]. Wang et al. [22] identified that 3D watershed segmentation works best for mineral particles greater than the scale parameter (particle size/voxel size ratio of 30) and density lower than 4.0 g/cc. An example of marker-controlled watershed segmentation to separate touching grains is shown in Figure 6.
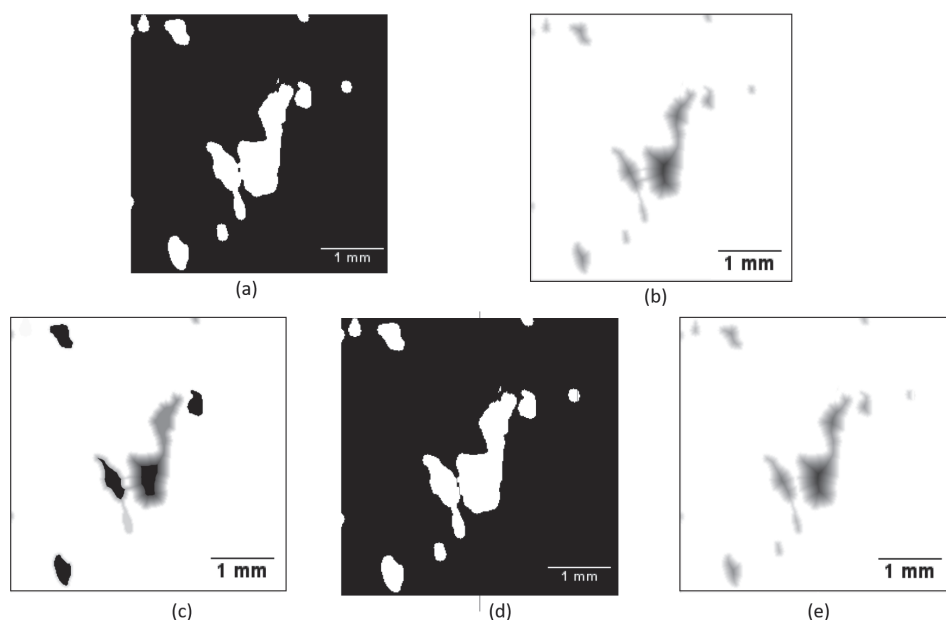
Figure 6. Marker-controlled watershed segmentation process. (**a**) Binary image showing touching grains; (**b**) distance transformation of (**a**), showing two grains are connected with each other; (**c**) Markers are introduced by imposing a minima for each grain; (**d**) watershed segmentation of (**c**), showing a thin ridge is now formed between two grains; and (**e**) the distance transform of (**d**) showing the grains are no longer connected.

The markers introduced in Figure 6 were obtained by filtering out the minima that are less than a certain threshold value to avoid over-segmentation. Such a method has a clear drawback, if the grain sizes in the image are highly varied, it would be difficult to find a threshold value that could remove all unwanted minima without removing the minima of interest [91]. An alternative to such a technique is by taking into account the topography of the minima; instead of setting a threshold value on the minima, such a threshold value is set as a fraction of the zone around the minima [92]. The goal would then to find a fraction value (0 to 1) to set that zone fraction to be the same as the minima, i.e., to flatten down the basin zone to the level of its minima. The watershed transform would then consider the flattened basin to be part of the adjacent basin, therefore merging both basins to avoid over-segmentation. While such a procedure is less affected by grain size (basin depth), the procedure is still affected by the grain shape (basin topography), therefore making it unsuitable for highly elongated grains [91].

The major challenge with the previously described marker-controlled watershed segmentation is clear: it would be difficult to obtain a global threshold value that could balance between under-segmentation and over-segmentation. Kong and Fonseca [91] proposed an iterative technique based on information obtained at a local level. Initially the method used a similar method as in Figure 6, but then it is followed by iteratively performing watershed segmentation in each basin zone to identify potential new basins within the zone. This simply means that each segmentation is adapted according to the properties of each basin. The method has been demonstrated to be capable of segmenting grains with varying sizes and shapes.

4.4. Unsupervised Classification

Classification is defined as the partitioning of a set of elements into several clusters (or classes) based on their similarity [93]. In terms of image analysis, the sets of elements are the pixels in the image. Unsupervised classifications mean that the classification algorithm is automated by the computer, without any training or supervision from the users. However, users can have some degree of controls in this technique by specifying the number of classes, maximum iterations, as well as the endpoint of the classification (i.e., how much of the data that needs to be classified).

K-means clustering, is a clustering technique that segments the image in K numbers of clusters based on a certain criteria [94]. The K-means technique is one of the most commonly used technique in clustering of images, and it has been applied both in microscopic images [93,95], as well as 3D μCT images of rocks [25].

The K-means algorithm calculates the distance between pixel values and its nearest centroid of the cluster. This algorithm continues until the mean square root error of the distance reaches a minimum value, meaning that there are no more pixels that need to be assigned to the nearest clusters. The performance of K-means algorithm is very much affected by the initial selection of centroids as well as the selection of distance function. Poor selection of initial centroids will lead to the algorithm terminating without finding the global minimum of the objective function (after only finding a local minimum) [70]. Arthur and Vassilvitskii [96] have developed an algorithm that would improve the initial selection of centroids, by using a weighted probability distribution that is proportional to the distance between the newly selected centroid and the previous centroid. Their method is often referred to as K-means++. An example of a K-means segmented drill core volume, alongside with multi-level Otsu thresholding is shown in Figure 7.

K-means clustering has been applied in rock pore matrix analysis using μCT by Chauhan et al. (2016) [97]. Rock samples used were Andesite, Berea sandstone, as well as Rotliegend sandstone. In Chauhan's work, the performance of K-means clustering was compared with other unsupervised algorithms, such as fuzzy-C means (FCM) and self-organized maps (SOM).

A fuzzy set is defined as a set of data with no distinctive boundary [72]. In contrast to K-means in which each pixel can only be a member of one cluster, a pixel in the FCM scheme can be a member of multiple clusters depending on the fuzzifier constant, in which it acts as a weighting factor in the calculation of the distance between pixels and their centroids. A larger constant would decrease the weight, leading to fuzzier classification. If the constant is decreased to its limit value of 1, the FCM scheme simplifies into K-means.

The performance evaluation of the classifier is based on the entropy and purity of the clusters. The entropy of a cluster defines how the pixel values are distributed within the K number of clusters—in other words how likely a pixel value is misplaced in another cluster. Meanwhile, purity refers to the frequency of the most common category in each cluster.

A clustering technique is good if the purity is high, while the entropy is low. In Chauhan's study, the K-means clustering technique was found to outperform other unsupervised techniques in terms of both entropy and purity, as well as computational speed. Chauhan also found that the porosity value of the rock obtained from unsupervised classification corresponded well with the experimental values obtained from pycnometer measurements.
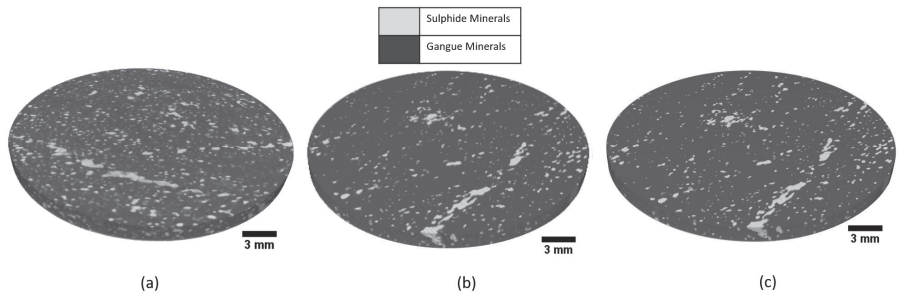
Figure 7. (**a**) Original drill core volume obtained from μCT; (**b**) multilevel Otsu thresholding, showing 10% of sulphide mineral grain content; and (**c**) K-means segmented image, showing 6.3% of sulphide mineral grains content. While the images look similar, there exists a relatively significant difference between the amount of grains segmented using both techniques.

4.5. Supervised Classification

In a supervised classification technique, the user trains the computer to classify the image based on the training dataset. This can be done by selecting a sample of pixels and assigning them to a specific class, in which the computer will use this as a reference in classifying other images. Supervised classification has been used to some extent in rock μCT images [19,22,25,97]. Comparison of supervised and unsupervised classification is shown in Figure 8.
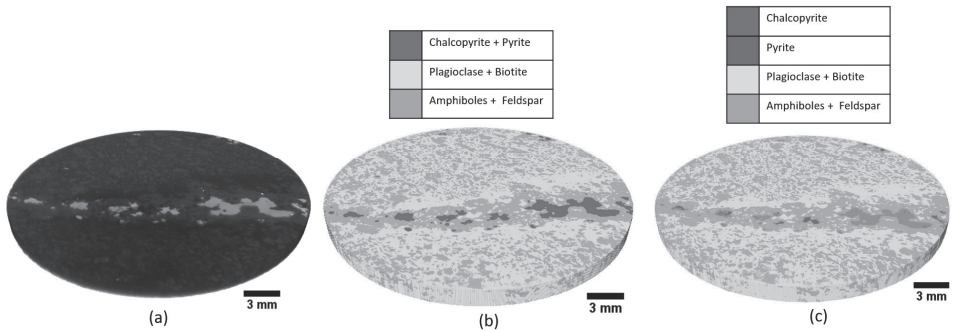

Figure 8. (**a**) Original 3D data of the drill core; (**b**) unsupervised classification performed on the data; and (**c**) supervised classification performed on the data. In (**b**), both chalcopyrite and pyrite grains are regarded as one phase, i.e., unsupervised classification could not distinguish further between the phases. In (**c**) both phases could be segmented using supervised classification depending on how the user trains the classifier.

A classification tree is a supervised classification technique where the computer builds a decision tree with a binary test in each of the branches. This tree is grown until a certain point when no new information can be obtained from the training dataset. Random forest is then a technique where multiples of these classification trees are built based on different subsamples of the training data, allowing the building of classification trees based on different parts of the training data. Such a technique mainly aims to prevent overfitting of the trees to the training data; it ensures the generality of the classification tree. Random forest then classifies pixels by majority voting of the classification trees [98].

An artificial neural network (ANN) is simply a large number of simple and interconnected processors (neurons) working in parallel in a network [99]. The neurons simply calculate the probability of the image to be categorized as an object. This is done by assigning weights to the

elements of the input image (the nodes) and summing those weighted elements, which then if the sum is higher than a certain threshold (or bias) it will be sent to the next layers. This is continued until the output layer, where it returns the probability of the input to be an object. During the training phase, the user inputs a training dataset for the network. The network then adjusts the weights of each nodes by computing the loss function which measures the difference between the true class of a pixel in the training set with the output value predicted by the network [100].

The main issues with ANNs are that they require a significantly larger amount nodes when larger images are fed and it is not translation-invariant (meaning that it depends on the orientation of the original training data). Convolutional neural networks (CNNs) are an alternative where the full-size image is convoluted first using several different filters to produce feature maps. The strength of a CNN is that, instead of using pre-defined filters, these filters could also be trained according to the user needs. In most cases the feature maps are then downsampled (pooling) so that the only the most important information of the feature maps is preserved and fed to the network. These sets of convolution and pooling can be repeated several times until small enough feature maps can be inputted to the network. There exist several convolutional neural network architectures that have been developed and trained, and can perform various image recognition tasks [101–103]. An illustration of a neural network and a convolutional neural network is shown in Figure 9.
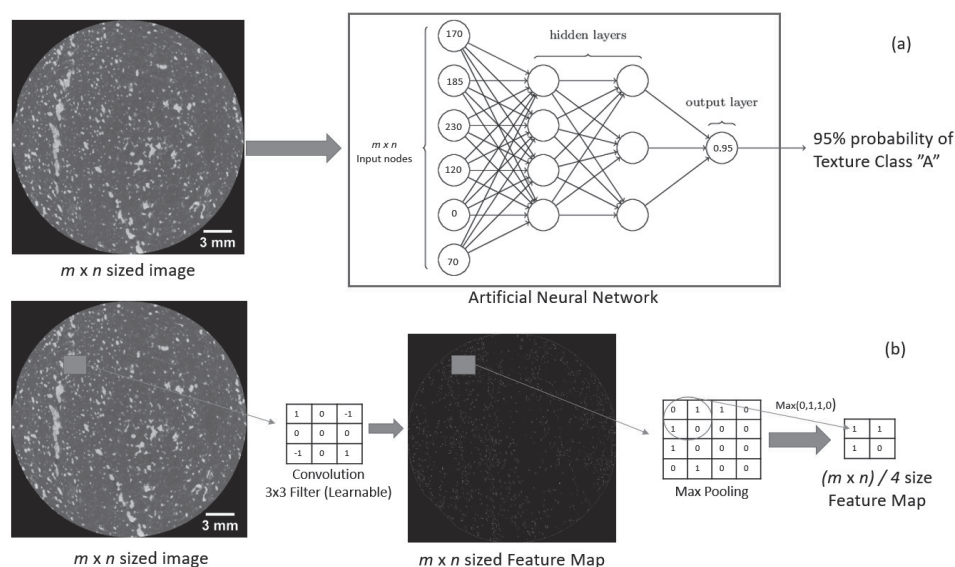
Figure 9. (**a**) ANN applied on a μCT drill core slice images; (**b**) CNN applied on a μCT drill core slice images. In an ANN each pixel in the image is inputted directly, creating an m × n amount of input nodes, which is very large for typical μCT slice images. In a CNN the image is convoluted first with filters to produce feature maps. These filters can be more than one and are learnable during the training phase. The feature map is then pooled, for example by taking maximum values in a 2 × 2 neighborhood, so it is downsized by the factor of four. This scheme represents the neural network application in image recognition (recognizing the texture class of a drill core slice) while, for phase segmentation, the input can be changed to the mask image of each phase.

A support vector machine (SVM) [104] is a supervised classification technique that projects the training dataset to a feature space of higher dimension using a kernel function, so that the dataset can be segmented using a linear classifier [105]. The linear classifier is set so that it leaves the largest possible fraction of points of the same class in the same side while maximizing the distance between the different classes from the linear classifier [106].

The use of supervised classification in μCT data analysis has been limited, especially in ore mineral cases. Chauhan et al. [25,97] extensively explored different supervised classification techniques, such as ANN and least square–SVM in segmenting between rock matrix, minerals, and pores in an μCT image of Andesite rock sample. Cortina-Januchs et al. [107] used an ANN to classify pores in a μCT images of soil. Tiu [19] utilized a random forest classifier in the Trainable Weka Segmentation (TWS) tool [108] to classify mineral phases in a μCT image of a Cu-Au drill core samples. A random forest classifier is also used by Wang et al. [22], as the marker-controlled watershed segmentation did not perform well for fine and low density particles.

From Chauhan's study, it was concluded that both ANN and LS–SVM classification techniques yielded a porosity analysis which is in a good agreement with experimental pycnometer measurements (relative differences of less than 1%). Furthermore, it was also concluded that LS–SVM is superior compared to ANN due to its capability in identifying generalized patterns. However, this is compromised by its extensive computational requirements, where LS–SVM took 10 times longer to process the same μCT dataset compared to the ANN.

Tiu [19] attempted to classify mineral phases in a μCT drill core image using a random forest classifier with different feature extraction algorithms (i.e., the convolution steps similar to CNN). Using a SEM-EDS mineral map as the training dataset, Tiu validated the resulting classification with the same 2D μCT slice that was analyzed by SEM-EDS. The differences between the mineral map obtained by SEM-EDS and the supervised classification was minimal, in which it underestimates chalcopyrite content by 0.2% and overestimates pyrite content by 0.2%. It was further added that the performance of such supervised classification techniques is heavily dependent on the training dataset, so care must be taken when applying such classifiers to an inherently different dataset.

In relation to the 3D watershed segmentation by Wang et al. [22], supervised classification was performed to overcome the limitations of the current watershed algorithm. Instead of using thresholding for extracting the particles from the background, a trainable feature based classification was employed using the TWS tool [108] which is based on a random forest classifier. It was found that around a 10–15% decrease in calculation error was obtained when the supervised classification was used instead of thresholding in the watershed segmentation.

5. Feature Extraction

The resulting data from segmentation is most often in the form of a labeled image, in which each label represents a segmented phase. These phases would have some features that a machine vision can extract. The process of feature extraction reduces the dataset into features of interest. Hence, such a process could also be called dimensionality reduction [109]. With a smaller dataset, the computational expense of the subsequent data processing can be reduced.

These features in terms of mineral characterization are often related to the textures of the ore minerals. Texture in terms of ore geology is referred as the relative size, shape, and spatial interrelationship between grains and internal features of grains in a rock. Size, shape, and orientation of the grains in minerals are referred as structural texture, while the spatial relation between the grains (pattern) are referred as stationary textures [110].

The concept of structural textures is quite easily understandable; by having grain shape, size, and orientation information of an ore, one could distinguish different types of ore texture. With the use of μCT, more accurate 3D information on these textures can be obtained as well as quantified through a variation of data analysis methods. On the other hand, stationary textures are often described qualitatively using experiences and textural archetypes. Recent developments are leaning towards the use of computer vision and image analysis techniques to quantitatively extract stationary textures of rocks [110–113]. Extending these techniques into 3D data would open up a new depth of information in describing texture of ore minerals.

5.1. Distance Transformation

Distance transform simply transforms a binary image into a function of the distance of each pixel to the nearest non-feature pixels (the zero-valued pixels in the binary image) [114]. Such transform

function has been demonstrated to be extendable to 3D [115]. Distance transform has found many applications in relation to ore characterization with μCT, most notably in analyzing structures of pores, grains, and particles [22,116–119].

One application of distance transform in segmentation of touching particles and grains [22,118,119] has already been shown in Figure 6. With the information of the distance of each voxel to the background, one could estimate the center of each grain by taking the voxels with maximum distance value. Inverting the distance map would produce a minima at the center of the grains, which can then be used as a basis for specifying a marker for the watershed segmentation.

Distance transform is also important in evaluating surface exposure of mineral grains in a particle, which has been applied in μCT analysis of leaching experiments [117,119]. Mineral voxels that have low distance value (closer to surface) would be leached faster, i.e., the leaching kinetics and recovery is dependent on the position of the minerals relative to the surface. Throughout the leaching period, the number of mineral voxels would be decreased gradually due to dissolution, and this decrease could be used to evaluate the leaching recovery. Coupled with distance transformation, the dependency of leaching recovery to the mineral's distance from the particle surface can be evaluated.

The shape and structure of a feature could also be evaluated with distance transformation. The skeleton of a feature could be defined as the ridges (local extrema) in a distance function. The skeleton is particularly useful when analyzing pore space and connectivity in a sample, which can be used to evaluate the permeability of the sample [6,120]. Evaluating the maximum inscribed sphere along these skeleton voxels allows comparison of surface topology between the feature and a sphere, giving an idea on the bluntness of the feature [116].

5.2. Mathematical Morphology

Mathematical morphology [121,122] is one of the tools that analyze the spatial structure of voxels in a 3D dataset. This technique usually takes binary image as an input, in which the structure of the volume of interest is analyzed. Morphological image analysis makes uses of a structuring element to extract morphological features of the image, in which the structuring elements are operated on the entire volume. Morphological image analysis has been used in various applications for μCT volumes, especially in quantifying size and structures of pores, grains, and particles in a sample [19,123–126].

The shape of the structuring elements defines what kind of features can be extracted from the volume. Furthermore, by manipulating the size of the structuring elements, the size function of the features could also be extracted. Morphological opening is an operation that removes any of the elements in the image that are smaller than the size of the structuring element. Morphological opening is then analogous to sieve analysis performed for powder samples, where particles smaller than the sieve are passed through the sieve. Sieves of increasing size are stacked vertically to get the size distribution. This is done in morphological image opening where the structuring element size is incrementally increased, which is often termed as granulometry by opening [121,122], compare Figure 10. This operation has been implemented in various μCT 3D volumes, including cellulosic fibrous network [124,125], as well as in ore samples [19,120].
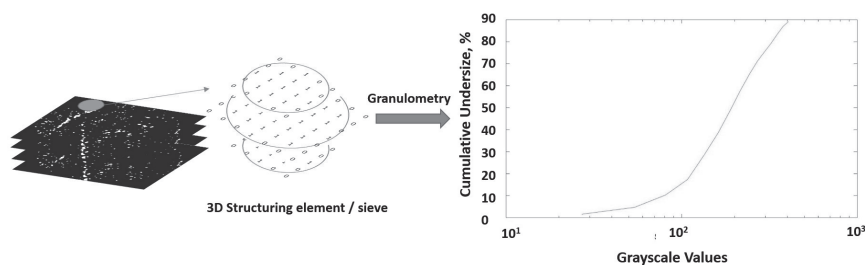
Figure 10. Granulometry by opening. A structuring element/sieve is operated on the stack of binary images, in which here represents the mineral grains in the ore sample. After operation, the grains

smaller than the sieve are removed. The sieve size is then increased, and the distribution of the grains based on their sieve passing size is plotted. The structuring element in here is a stack of 2D structuring elements, mimicking a 3D structuring element.

Limitations do exist in granulometry, as it is highly dependent on the shape and size of the structuring elements and on how the features can be interpreted. Lux et al. [125] argued that in a fibrous network, the pore size distribution using granulometry does not correspond to actual respiratory pore sizes, but rather as a minimum distance between the fibers. Tiu [19] stated that the grains in the measurements are more defined as a set of voxels containing similar gray values as defined by the previous segmentation, so it is also highly dependent on how it was segmented previously. The shape of the structuring elements also defines the computational costs; spherical structuring element (which often describes grain and pore quite well), is quite computationally extensive as by increasing its radius, the voxels processed increased to the power of three of the incremental radius [123]. This for example can be overcome by using a 32-faced polyhedron, which could reasonably estimate the shape of a sphere [123].

Several other different tools exist in mathematical morphology. These tools allow textural extraction from the 3D dataset including:

- Local orientation of textures. This is achieved by opening of the image using a line structuring element and rotating the structuring element to get directional information of the image. Such information is useful to obtain information about the isotropy of textures. It has been used in analyzing 3D datasets of fibrous networks [125].
- Global orientation of textures. While the combination of local orientations could give a good estimation on the global orientation, methods for directly determining global orientation also exist. The mean intercept length (MIL) is the most popular method to obtain this information. It generates several parallel lines in a certain direction in which the number of intercepts of the lines with the textures can be used for estimating the orientation. Such a method has been used in analyzing orientation of pores and vesicles in CT images of volcanic rocks [10].
- Skeleton of the textures. In addition to using the distance transform, the skeleton of the texture could also be obtained by eroding the features up to a certain point where its homotopy is still preserved. Such a technique is often referred to as morphological thinning.
- Shape descriptors of textures through Minkowski functionals. The Minkowski functionals are geometric measures applied to binary structures, in which for n dimensional plane, $n + 1$ of such functional exists. Such functionals have been applied in 3D pore analysis of soil structure [126]. These functionals are:

$$M_o(X) = V(X) \tag{5}$$

The zeroth functional, Equation (5), calculates the mass of the object:

$$M_1(X) = \int_{\delta X} ds \tag{6}$$

The first functional, Equation (6), is the integral over the surface δX of the unit. This is simply the total surface area of the object (units: length^2):

$$M_2(X) = \frac{1}{2} \int_{\delta X} \left[\frac{1}{r1} + \frac{1}{r2} \right] ds \tag{7}$$

The second functional, Equation (7), is the mean curvature (units: length^{-1}) of the surface area obtained from the previous functional. Both $r1$ and $r2$ define the minimum and maximum radius of the curvature:

$$M_3(X) = \int_{\delta X} \frac{1}{r1r2} ds \tag{8}$$

The third functional, Equation (8), is the total curvature, which can be used to measure the topological properties of the object (convex, concave, or saddle).

5.3. Computational Geometry

One of the key features of μCT is that it can extract the three-dimensional representation of the samples, i.e., it is not subject to stereological error as in 2D-based image analysis. This permits more accurate geometrical representations of the sample, which then can be further exploited in order to extract shape representations (sphericity, surface area, aspect ratio, etc.) of the sample. Computational geometry is a systematic study of algorithms and data structures for geometric objects [127], allowing users to extract features using the geometrical properties of the object.

The shapes of ore particles and grains are often irregular, i.e., a method is needed to approximate the shape of such objects using geometrical objects. One of the geometrical objects that can be used to approximate particles are a set of polygons. This can be achieved using the three major concepts in computational geometry: convex hull, Voronoi diagram, and Delaunay triangulation. Formal definitions of these concepts are available elsewhere [127], but essentially all of these concepts make uses of convex polygons in order to represent an object, i.e., the object is tessellated into a set of convex polygons so that the properties of the object can be approximated from the properties of the polygons. One of the properties that can be obtained is the surface area of the object, which is useful to deduce the sphericity of the object.

Another way is to create a geometrical object that would bound all parts of the irregular shape inside it. This bounding object can be minimized so that it could better represent the sample. In computational geometry this is termed the minimum bounding object problem, and the bounding object can be a sphere or a box. The properties of the bounding object can describe features of the shape bounded by it. Furthermore, many of shape descriptors can be calculated if the major, minor, and intermediate dimensions of the object is known, e.g., the aspect ratio, elongation index, and flatness index [118]. This is illustrated in Figure 11.
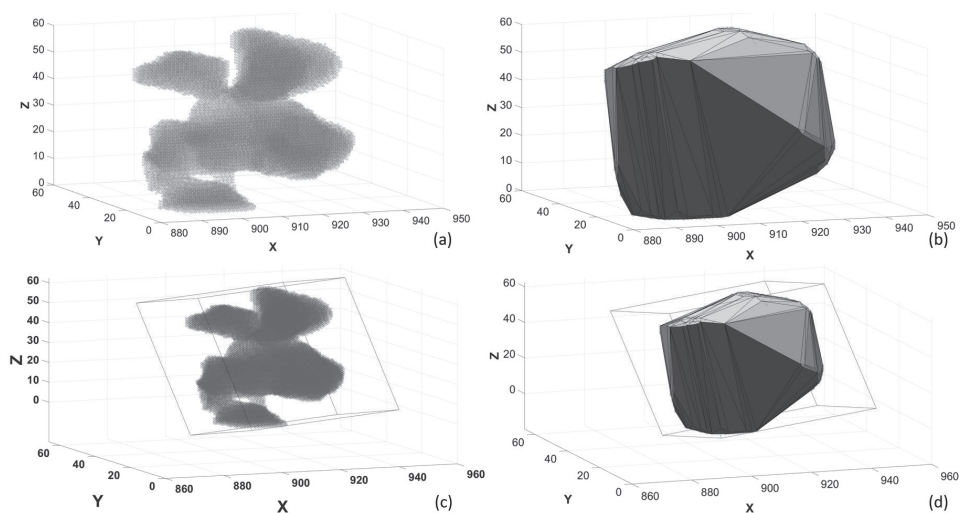
Figure 11. Using geometry to extract shape features of a particle. (**a**) Scatter plots representing the particle; (**b**) convex hull of the particle; (**c**) minimum volume bounding box of the particle, which is the same as the bounding box for the convex hull (**d**). From the convex hull, convex surface area and solidity (ratio of convex volume and actual volume of a particle) can be obtained, while from the bounding box, major, intermediate, and minor dimensions of the particle can be obtained.

Computational geometry has been applied mainly in extracting shape parameters of a 3D volume obtained from μCT. Vecchio et al. [128] described the applications of bounding box in describing different types of particle shape, and the errors associated with it. Zhao et al. [118] investigated shape descriptors of a particle before and after fracture using convex hull of that particle,

particularly its solidity. Pamukcu et al. [129] have used convex hulls to analyze glass inclusions in an igneous rock, in which it was stated such a method cannot properly describe non-convex inclusions. This limitation for non-convex particles is even illustrated in Figure 11, where the particle shown is non-convex, and the convex hull of the particle differs significantly from the original particle. In general, this is the main limitation of computational geometry; errors always arise when regular objects (polygons) are used to estimate an irregular object (rock particles, grains).

In addition to polygons, spheres have also been used in approximating size and shape. The maximum inscribed sphere has been used by Van Dalen et al. [130] to measure the local thickness of a particle. By inscribing a sphere in each point of a particle, the thickness of that point can be obtained by the diameter of the maximum inscribed sphere at that point. The maximum inscribed sphere applied in a 3D distance transform map has been used to generate a new shape descriptor for particles called the bluntness index [116]. The index was able to distinguish blunt particles (spheroid) and sharp particles (cuboid) at a resolution as low as 5000 voxels per particle. Other uses of spheres includes maximum equivalent sphere diameter in describing melt inclusion sizes in garnets [131] as well as evaluating platinum and precious metal grains in various types of Cu-sulphide texture [132].

5.4. Domain Transfer Function

As mentioned earlier, besides structural textures, stationary textures and patterns of the grains in the ore are also of interest. Stationary textures can be evaluated directly as the spatial relationship of the grayscale values of the voxels in the image, meaning that it does not require segmentation or classification of the mineral phases beforehand. On the other hand, such textures can also be evaluated as the spatial distribution of the mineral grains, which then would require segmentation between the mineral grains and the rock matrix prior to obtaining such distribution.

The spatial pattern of the phases can often be readily detectable by looking the image in another way, i.e., by transforming the image from spatial domain to frequency domain. Moreover, some mathematical operations are simpler in another domain, making the operation computationally less consumptive. This is the basic concept behind the Fourier series, in which it describes a function in a frequency domain through summation of simple sine waves. The Fourier series are especially well suited in analyzing the periodical nature of an image.

The Fourier method measures an object through a profile function, describing its radius (R) in different angles from 0° to 360°, as shown in Equation (9), in which a_n and b_n are the Fourier coefficients:

$$R(\theta) = a_0 + \sum_{n=1}^{\infty} a_n \cos(n\theta) + b_n \sin(\theta) \qquad (9)$$

The value of n represents the number of harmonics, and different values describe different properties (signatures) of the object, namely form/shape ($n \leq 4$), angularity ($5 \leq n \leq 25$), and texture ($26 \leq n \leq 180$) [133]. In other words, two objects with similar shape will have the similar Fourier series at lower frequency harmonics ($n \leq 4$), but at higher frequency ($26 \leq n \leq 180$), their Fourier series are not necessarily similar; they depend on the surface textures of the objects [134]. In a three-dimensional plane, the spherical harmonic series is used instead, which is analogous to the Fourier series in 2D case [135]. Spherical harmonics has found its application in three-dimensional μCT analysis of shape and surface textures of aggregate particles [134–137].

Wavelet transform has a concept similar to Fourier, differing that the function still retains some of its spatial information while having also some new information about its frequency. There are several different wavelet families, with each of them having its own functional properties [138]. Wavelets, especially the discrete wavelet transform, has find its application in image processing, especially in image compression [139] and removing noise [140,141]. A discrete function of $f(n)$ can be represented as a weighted summation of wavelet function $\psi(n)$ (mother wavelet) as well as the $\varphi(n)$ scaling function (father wavelet), displayed in Equation (10):

$$f(n) = \frac{1}{\sqrt{M}} \sum_{k} W_{\varphi}(j_0, k) \varphi_{j_0,k}(n) + \frac{1}{\sqrt{M}} \sum_{j=j_0}^{\infty} \sum_{k} W_{\psi}(j, k) \psi_{j,k}(n) \qquad (10)$$

Wavelets have been used extensively in describing rock textures in 2D images [110,142–144], yet their use in 3D textural analysis is almost non-existent. In 3D µCT analysis, wavelets have also been used as an alternative for edge detection operators in measuring crack growth in rock CT volumes [67]. Similarly, Katunin et al. [145] used 3D wavelet transform to identify and classify different types of defects in composite structures.

The frequency information in an ore sample that is obtained by wavelet and Fourier analysis can offer a new type of information that could be useful in analyzing stationary textures, as it gives information on the spatial relationship of the phases in an ore, i.e., on how the phases are distributed over the space of the ore. Such information would be of utmost benefit when having 3D µCT data readily available.

*5.5. Spatial Statistics and Co-Occurrence Matrices*

Some textures have similar patterns that are observable across the whole volume. This makes the texture simpler to detect as it will have similar statistics across the volume. These kinds of textures can be addressed with spatial statistics as well as co-occurrence matrices. Local binary pattern, or LBP [146], is one of the algorithms that evaluates the variability of the image spatially by using kernel operators. In this algorithm, a 3 × 3 convolution kernel is operated on the image. The kernel performs comparison of each pixel with its 8-neighborhoods, and label them accordingly. If the center pixel is greater than its neighbors, it will be assigned label 1, otherwise 0. Afterwards, there will be a total of 2^8 possible combinations of the output, and the histogram of this output is plotted to obtain a textural descriptor. Despite its well-known application in describing textural features, LBP has mostly been used for medical CT images [147,148], and only recently it has been applied by Rahimov et al. for classifying different textures of CT image of carbonate rocks [149]. Rahimov's work considered textural classes based on the spatial correlation between the pores of different sizes and the solid phases. A similar method could potentially be applied in classifying textures based on spatial relationship between mineral phases in the sample, which is more relevant in terms of mineral characterization.

Spatial statistical tools such as co-variance and variograms can also be used to quantify stationary textures. Such tools define variability of two points in a texture, which is very useful when inferring the probability of the two points to belong to the same phase. It has also been used in 3D dataset of a fibrous network [125]. An example of these variograms is shown in Figure 12.

Co-occurrence and autocorrelation features are another approach to extract textures from an image. Gray level co-occurrence matrices (GLCM) [150] are a quite well known image processing technique that measures how the gray level varies between the neighboring pixels. A GLCM is composed of an n × n matrix, in which n is the number of possible grayscale values in an image, i.e., 256 for an eight-bit grayscale image. The matrix shows how many times a pair of voxel values co-exists in a neighborhood, as well as the directional adjacency of such pairs. In a 3D volume, a voxel would have 26 neighborhood voxels and 13 specific directions of voxel pairs. This is illustrated for a simple 3 × 3 × 3 volume in Figure 13.
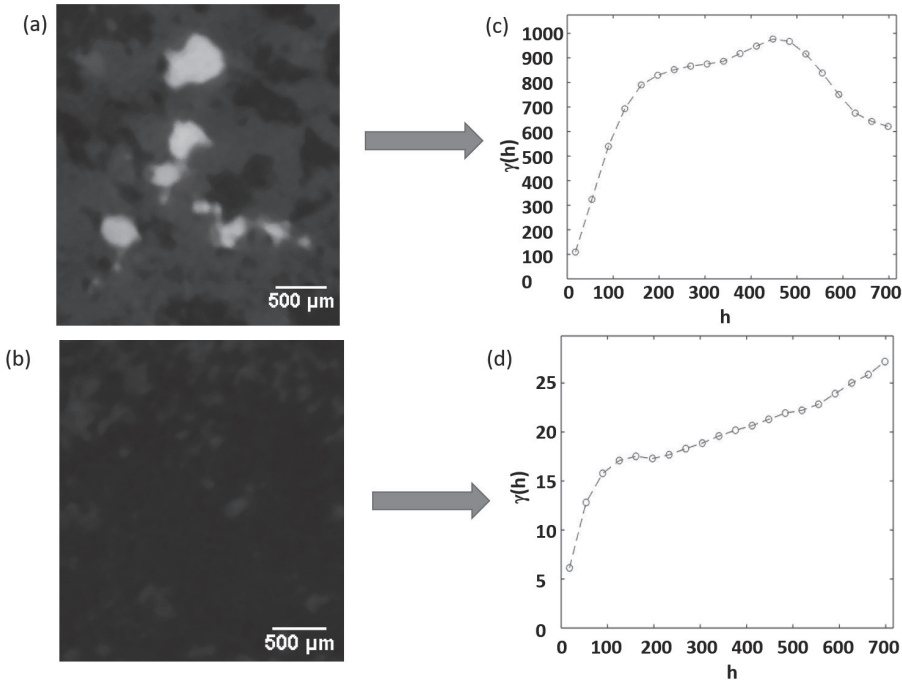
Figure 12. Semi-variogram for different textures, computed using a total 10,000 points in the texture. The variogram explains the relation between the variance (γ(h)) against the distance of two points in the texture (h), grouped in a bin width of 20. Texture (**a**) is more varied than (**b**), which explains the higher variance in the variogram (**c**) in comparison to (**d**). The variogram of texture (**a**) exhibits a cyclic nature due to the somewhat periodical occurrence of sulphide phases. Texture (**b**) exhibits upward trend in variance due to occurrence of amphiboles (light grey) in the top part of the texture.
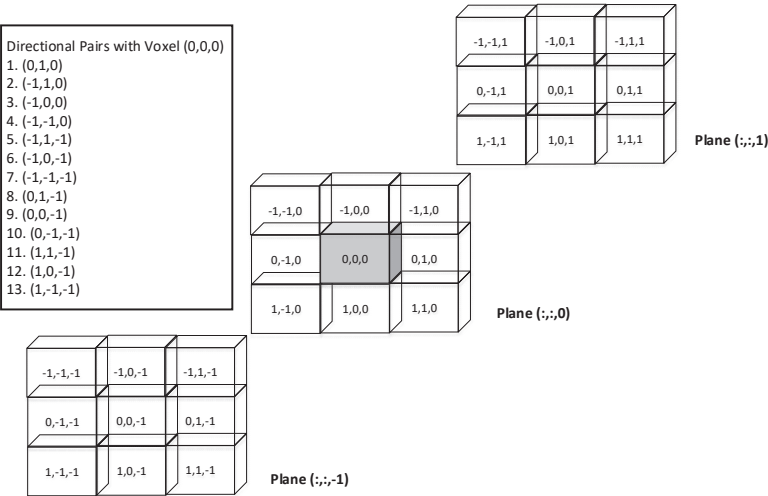
Figure 13. Neighborhood and directional voxel pairs in relation to GLCM analysis, adapted from Jardine et al. [24]. All three planes are in a 26-connected neighborhood of voxels, in which there exist 13 unique directional pairs with the origin voxel (0, 0, 0). Keep in mind that mirrored direction does

not count as a unique direction, e.g., direction (0, 1, 0) has the same direction with (0, −1, 0), direction (0, 0, −1) has the same as (0, 0, 1), and so on.

The GLCM of an ore sample can be analyzed as such, as it shows us the correlations between gray values in a given direction. It is able to show how often a gray value co-exist together with another gray values, thereby giving an idea of how the host rock phase (lower gray values) associate with its mineral grains (higher gray values). Such correlations are shown in Figure 14.
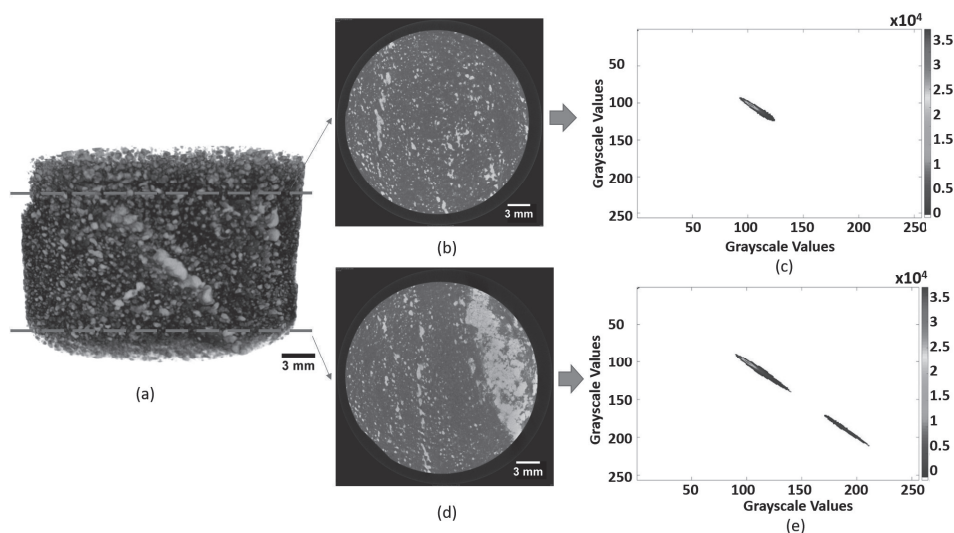
Figure 14. Relation of GLCM matrix on direction 1 (0,1,0) to the texture of a drill core. (**a**) Drill core volume showing horizontal slices, (**b**) and (**d**). Horizontal slices of the drill core, (**c**) and (**e**), are the GLCM matrices as a heat map, alongside its legend showing red for high frequency and blue for low. The results clearly show difference in the GLCM as slice (**d**) has more sulphide mineralization as compared to slice (**b**). This can be seen as the higher correlation frequency between the brighter phases, which usually indicates the sulphide minerals.

Furthermore, the GLCM can also be quantified using the available 14 GLCM statistical parameters. Four of these parameters are related to stationary textures, namely energy, correlation, contrast, and homogeneity. The GLCM technique has recently been applied to 3D µCT drill core images [24], where it was shown that there exists correlations between various textures and their respective GLCM statistics. However, such statistics captured only the bulk mineralogy (stationary textures); structural textures, such as coarse versus fine grained, were not observed to be correlated with the statistics. Such a technique is also very much dependent on the voxel pair direction chosen when calculating the GLCM, especially in cases where the ore texture is anisotropic. In such cases, several voxel pair directions might be needed to adequately quantify the textural characteristic of the sample, which consequently increase the computational expense of the GLCM technique [24].

6. Summary of Data Analysis Methods

In this section, the methods that have been reviewed are summarized together with their related applications and case studies on mineral characterization. A flow diagram showing the applicability of these methods is shown in Figure 15.

- Cases such as grain, pore, or particle size distribution analysis with µCT have been evaluated. These cases are most conveniently addressed using granulometry by opening. Improvements toward computational speed of such methods in 3D datasets have mostly been addressed by modification of the structuring element used.

- Shape analysis using μCT is more common for particulate samples; less emphasis has been put on grain shape analysis of intact ore. In these cases, computational geometry has been used, but there is always an error associated with it. Spherical harmonic series is another alternative, but it is yet more complex due to its analytical approach. Minkowski functionals allow straightforward calculations of shape descriptors, but they are limited to surface properties and topology of the shape.

- Mineral phase segmentation can be addressed well using thresholding and unsupervised classification, provided that the target phases have enough attenuation contrasts. Additional measures must be taken when attempting to segment minerals with similar attenuations, in which such measures include dual energy μCT scanning, using lower voltage and smaller sample size, and using additional information acquired from another dataset (SEM-EDS, XRF). A more detailed summary on mineral phase segmentation with μCT is provided in Table 2.

- Stationary texture analysis in 3D has been addressed using kernel operators (such as LBP), covariance and variograms, as well as co-occurrence matrices (such as GLCM). Such techniques are potentially capable to quantify stationary textures. As these techniques rely on spatial statistics, it is restricted to textures with similar statistics across the volume (isotropic and homogenous textures). Textures with high variability across the volume might be difficult to be accurately represented. Wavelet techniques could be an alternative in texture analysis, but its current development is lagging behind, especially for 3D μCT datasets.

- Structural analysis, such as fractures, cracks, and pores, with μCT systems has also been evaluated by several researchers. The skeleton transform technique has been used in evaluating pore connectivity in a leaching column filled with ore particles. Cracks and fractures in a rock sample could be detected using wavelet analysis, or using local thresholding with a fracture mask. The latter technique has been shown to be capable of distinguishing fractures/cracks from pores.
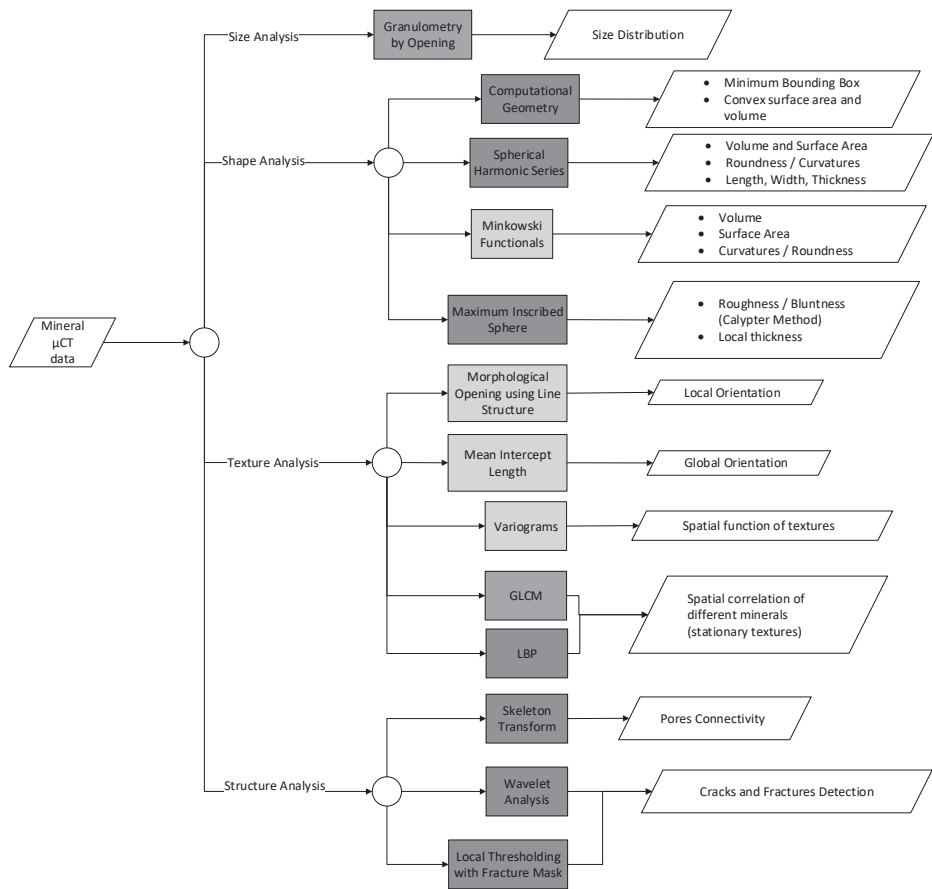
Figure 15. Workflow showing different alternatives in characterization of ore sample using a μCT system and the resulting information. The colors indicate the applicability of the methods. Green indicates that the methods have been implemented for μCT analysis of ore samples. Blue is for methods that have not been implemented specifically for μCT mineral characterization but have been implemented for similar materials such as dirt particles, aggregates, metal powders, and rocks. Yellow is for methods that have only been implemented for μCT analysis of materials that have little similarity to ore samples, such as soil and fibrous networks.

Table 2. Summary of phase segmentation techniques applied in mineral characterization using μCT system.

Case	Techniques	Applicability
Segmentation between air (background or pores) and solid materials	1. Otsu global thresholding [6,21,77,119] 2. Marker-controlled watershed segmentation [20,22,89,119] 3. Adaptive watershed segmentation [91,92] 4. ANN [107] 5. Feature-based random forest classifier [22]	1. Implemented in most cases due to its simplicity 2. Used to address touching particles 3. Used for sample with highly varied particle size and shape 4. Used for soil samples where the contrast is low 5. Similar to number 2, but better result for finer particle sizes as it defines the particle boundaries better

Segmentation between mineral phases with significant contrast	1. Maximum entropy thresholding [18] 2. Unsupervised classification (K-Means, FCM, SOM) [25,97] 3. Supervised classification (ANN and SVM) [25,97]	1. Segmentation between the sulphides with the gangues 2. Segmentation between pore, rock matrix, and mineral phases of andesite rock samples. 3. Similar to number 2
Segmentation between mineral phases with less significant contrast	1. Feature-based random forest classifier, trained with SEM dataset [19] 2. Local thresholding using gradient information for enhanced detection of phase boundary [23] 3. Low energy μCT scanning followed by maximum entropy thresholding, calibrated with SEM dataset [18] 4. Using smaller sample size for the μCT scanning [37,38] 5. Dual energy μCT scanning with calibration to pure minerals [17] 6. Combination of μCT scanning with XRF analysis (mainly available in synchrotron-based μCT systems) [48,56] 7. Correlating μCT data with XRF maps [41,42]	1. Segmentation between chalcopyrite and pyrite in drill core samples from porphyry Cu-Au deposit 2. Segmentation between bornite, PdCu, silicate inclusion, Fe-Ti oxide. Especially suited for fine inclusions. 3. Segmentation between copper sulphides and pyrite in porphyry copper ore is achieved using 50 kV voltage, with additional help of SEM-EDS data. 4. Bornite and chalcopyrite are able to be distinguished with small core size (≤22 mm) 5. Sphalerite, pyrite, galena, and silicate gangues were able to be distinguished in 3D after calibration with high purity samples. 6. Virtual slices of the 3D μCT volume is subjected to XRF to reveal chemical composition, inclusion mineralogy, and structure of perlite and zircon minerals. 7. The chemical composition obtained from XRF maps is used as a complementary data for the 3D μCT data

7. Conclusion and Outlook

In general, the applications of μCT in mineral characterization are in still development. One key to improve the application of μCT systems is by developing the data processing workflow so that features of the samples can be extracted, described, and classified in an accurate and efficient manner. Several conclusions and outlooks can be drawn from this review:

- In general, size, shape, and structural analysis of ore samples using μCT have been evaluated extensively by several researchers, as these parameters are best analyzed in 3D. Various data analysis methods devoting to evaluate these parameters are available with varying degree of accuracy and complexity. In relation to mineral characterization, an adequate estimation of size and shape of particulate samples could be useful in evaluating the processing behavior of such ore samples (more relevant to the field of process mineralogy and geometallurgy). Estimation on cracks and pores would be a good addition, as it could affect mineral liberation during comminution.

- It can be suggested that the bottleneck of mineral characterization with μCT lies in the mineral segmentation and mapping. Most of the μCT applications in mineral characterization are highly limited to segmentation between the major phases, such as pores, gangues, and valuable minerals (high density phases). The establishment of μCT as a rapid, standalone, and automated mineralogical analysis is challenging, as the result of this study indicates that additional information (SEM-EDS, XRF, calibration with pure minerals, dual energy) are required to effectively segment between different mineral phases in the μCT dataset. Future works should also include how to effectively combine this additional information to the μCT data processing workflow.

- Mineral texture analysis using μCT is a potential yet to be explored. Textural analysis with μCT systems is more prevalent with cases of soil, fibrous materials, as well as aggregates. In such materials the notion of texture is mostly limited to structural textures, such as morphology,

surface texture (topology), and orientation. While these types of textures can be of importance in mineral characterization, the stationary textures (spatial patterns of the mineral grains) are also of interest. Various techniques have been developed to extract and quantify 3D stationary textures of ore samples. However, such techniques are currently limited to the computational expense of processing the large 3D dataset; further development is needed to optimize the computational performances of such techniques.

Author Contributions: P.I.G. conducted the literature review and tested some of the methods to available μCT datasets. Y.G. mainly focused more on latest applications of μCT and its relation to mineral characterization. P.-H.K. mainly contributed to the theoretical framework in image processing. J.R. supervised the project and contributed mainly to the conclusion section.

Conflicts of Interest: The authors declare no conflict of interest.

References

1. Cnudde, V.; Boone, M.N. High-resolution X-ray computed tomography in geosciences: A review of the current technology and applications. *Earth-Sci. Rev.* **2013**, *123*, 1–17.
2. Mees, F.; Swennen, R.; Van Geet, M.; Jacobs, P. Applications of X-ray computed tomography in the geosciences. *Geol. Soc. Lond. Spec. Publ.* **2003**, *215*, 1–6.
3. Kyle, J.R.; Ketcham, R.A. Application of high resolution X-ray computed tomography to mineral deposit origin, evaluation, and processing. *Ore Geol. Rev.* **2015**, *65*, 821–839, doi:10.1016/j.oregeorev.2014.09.034.
4. Miller, J.D.; Lin, C.L.; Cortes, A.B. A review of X-ray computed tomography and its applications in mineral processing. *Miner. Procesing Extr. Metall. Rev.* **1990**, *7*, 1–18.
5. Lin, C.L.; Miller, J.D. 3D characterization and analysis of particle shape using X-ray microtomography (XMT). *Powder Technol.* **2005**, *154*, 61–69.
6. Yang, B.; Wu, A.; Narsilio, G.A.; Miao, X.; Wu, S. Use of high-resolution X-ray computed tomography and 3D image analysis to quantify mineral dissemination and pore space in oxide copper ore particles. *Int. J. Miner. Metall. Mater.* **2017**, *24*, 965–973, doi:10.1007/s12613-017-1484-4.
7. Iassonov, P.; Gebrenegus, T.; Tuller, M. Segmentation of X-ray computed tomography images of porous materials: A crucial step for characterization and quantitative analysis of pore structures. *Water Resour. Res.* **2009**, *45*, doi:10.1029/2009WR008087.
8. Peng, R.; Yang, Y.; Ju, Y.; Mao, L.; Yang, Y. Computation of fractal dimension of rock pores based on gray CT images. *Chin. Sci. Bull.* **2011**, *56*, 3346, doi:10.1007/s11434-011-4683-9.
9. Müter, D.; Pedersen, S.; Sørensen, H.O.; Feidenhans'l, R.; Stipp, S.L.S. Improved segmentation of X-ray tomography data from porous rocks using a dual filtering approach. *Comput. Geosci.* **2012**, *49*, 131–139, doi:10.1016/j.cageo.2012.06.024.
10. Zandomeneghi, D.; Voltolini, M.; Mancini, L.; Brun, F.; Dreossi, D.; Polacci, M. Quantitative analysis of X-ray microtomography images of geomaterials: Application to volcanic rocks. *Geosphere* **2010**, *6*, 793–804.
11. Lin, C.L.; Miller, J.D. Cone beam X-ray microtomography for three-dimensional liberation analysis in the 21st century. *Int. J. Miner. Process.* **1996**, *47*, 61–73.
12. Miller, J.D.; Lin, C.L.; Garcia, C.; Arias, H. Ultimate recovery in heap leaching operations as established from mineral exposure analysis by X-ray microtomography. *Int. J. Miner. Process.* **2003**, *72*, 331–340.
13. Miller, J.D.; Lin, C.-L.; Hupka, L.; Al-Wakeel, M.I. Liberation-limited grade/recovery curves from X-ray micro CT analysis of feed material for the evaluation of separation efficiency. *Int. J. Miner. Process.* **2009**, *93*, 48–53.
14. Reyes, F.; Lin, Q.; Cilliers, J.J.; Neethling, S.J. Quantifying mineral liberation by particle grade and surface exposure using X-ray microCT. *Miner. Eng.* **2018**, *125*, 75–82, doi:10.1016/j.mineng.2018.05.028.
15. Wang, Y.; Lin, C.L.; Miller, J.D. Quantitative analysis of exposed grain surface area for multiphase particles using X-ray microtomography. *Powder Technol.* **2017**, *308*, 368–377, doi:10.1016/j.powtec.2016.11.047.
16. Garcia, D.; Lin, C.L.; Miller, J.D. Quantitative analysis of grain boundary fracture in the breakage of single

multiphase particles using X-ray microtomography procedures. *Miner. Eng.* **2009**, *22*, 236–243.

17. Ghorbani, Y.; Becker, M.; Petersen, J.; Morar, S.H.; Mainza, A.; Franzidis, J.-P. Use of X-ray computed tomography to investigate crack distribution and mineral dissemination in sphalerite ore particles. *Miner. Eng.* **2011**, *24*, 1249–1257, doi:10.1016/j.mineng.2011.04.008.

18. Reyes, F.; Lin, Q.; Udoudo, O.; Dodds, C.; Lee, P.D.; Neethling, S.J. Calibrated X-ray micro-tomography for mineral ore quantification. *Miner. Eng.* **2017**, *110*, 122–130, doi:10.1016/j.mineng.2017.04.015.

19. Tiu, G. Classification of Drill Core Textures for Process Simulation in Geometallurgy: Aitik Mine, New Boliden. M.Sc. Thesis, Luleå University of Technology, Sweden, 2017.

20. Andrä, H.; Combaret, N.; Dvorkin, J.; Glatt, E.; Han, J.; Kabel, M.; Keehm, Y.; Krzikalla, F.; Lee, M.; Madonna, C. Digital rock physics benchmarks—Part I: Imaging and segmentation. *Comput. Geosci.* **2013**, *50*, 25–32.

21. Andrä, H.; Combaret, N.; Dvorkin, J.; Glatt, E.; Han, J.; Kabel, M.; Keehm, Y.; Krzikalla, F.; Lee, M.; Madonna, C. Digital rock physics benchmarks—Part II: Computing effective properties. *Comput. Geosci.* **2013**, *50*, 33–43.

22. Wang, Y.; Lin, C.L.; Miller, J.D. Improved 3D image segmentation for X-ray tomographic analysis of packed particle beds. *Miner. Eng.* **2015**, *83*, 185–191, doi:10.1016/j.mineng.2015.09.007.

23. Godel, B. High-resolution X-ray computed tomography and its application to ore deposits: From data acquisition to quantitative three-dimensional measurements with case studies from Ni-Cu-PGE deposits. *Econ. Geol.* **2013**, *108*, 2005–2019.

24. Jardine, M.A.; Miller, J.A.; Becker, M. Coupled X-ray computed tomography and grey level co-occurrence matrices as a method for quantification of mineralogy and texture in 3D. *Comput. Geosci.* **2018**, *111*, 105–117, doi:10.1016/j.cageo.2017.11.005.

25. Chauhan, S.; Rühaak, W.; Khan, F.; Enzmann, F.; Mielke, P.; Kersten, M.; Sass, I. Processing of rock core microtomography images: Using seven different machine learning algorithms. *Comput. Geosci.* **2016**, *86*, 120–128, doi:10.1016/j.cageo.2015.10.013.

26. Deng, H.; Fitts, J.P.; Peters, C.A. Quantifying fracture geometry with X-ray tomography: Technique of Iterative Local Thresholding (TILT) for 3D image segmentation. *Comput. Geosci.* **2016**, *20*, 231–244, doi:10.1007/s10596-016-9560-9.

27. Alikarami, R.; Andò, E.; Gkiousas-Kapnisis, M.; Torabi, A.; Viggiani, G. Strain localisation and grain breakage in sand under shearing at high mean stress: Insights from in situ X-ray tomography. *Acta Geotech.* **2015**, *10*, 15–30.

28. Dobson, J.K.; Harrison, T.S.; Lin, Q.; Ní Bhreasail, A.; Fagan-Endres, A.M.; Neethling, J.S.; Lee, D.P.; Cilliers, J.J. Insights into Ferric Leaching of Low Grade Metal Sulfide-Containing ores in an Unsaturated Ore Bed Using X-ray Computed Tomography. *Minerals* **2017**, *7*, 85, doi:10.3390/min7050085.

29. King, A.; Reischig, P.; Adrien, J.; Peetermans, S.; Ludwig, W. Polychromatic diffraction contrast tomography. *Mater. Charact.* **2014**, *97*, 1–10, doi:10.1016/J.MATCHAR.2014.07.026.

30. Olivo, A.; Castelli, E. X-ray phase contrast imaging: From synchrotrons to conventional sources. *La Rivista Del Nuovo Cimento* **2014**, *37*, 467–508, doi:10.1393/ncr/i2014-10104-8.

31. Dierick, M.; Van Loo, D.; Masschaele, B.; Van den Bulcke, J.; Van Acker, J.; Van Hoorebeke, L. Recent micro-CT scanner developments at UGCT. *Nucl. Instrum. Methods Phys. Res. Sect. B Beam Interact. Mater. Atoms* **2014**, *324*, 35–40, doi:10.1016/J.NIMB.2013.10.051.

32. Lau, S.H.; Miller, J.; Lin, C.-L. *3D Mineralogy, Texture and Damage Analysis of Multiphase Mineral Particles with a High Contrast, Submicron Resolution X-ray Tomography System*; Xradia Inc: Pleasanton, CA, USA, 2012; pp. 2726–2736.

33. Fusseis, F.; Xiao, X.; Schrank, C.; De Carlo, F. A brief guide to synchrotron radiation-based microtomography in (structural) geology and rock mechanics. *J. Struct. Geol.* **2014**, *65*, 1–16, doi:10.1016/J.JSG.2014.02.005.

34. Han, I.; Demir, L.; Şahin, M. Determination of mass attenuation coefficients, effective atomic and electron numbers for some natural minerals. *Radiat. Phys. Chem.* **2009**, *78*, 760–764, doi:10.1016/j.radphyschem.2009.03.077.

35. Omoumi, P.; Becce, F.; Racine, D.; Ott, J.; Andreisek, G.; Verdun, F. Dual-Energy CT: Basic Principles, Technical Approaches, and Applications in Musculoskeletal Imaging (Part 1). *Semin. Musculoskelet. Radiol.* **2015**, *19*, 421-43, doi: 10.1055/s-0035-1569253.

36. Berger, M. XCOM: Photon Cross Sections Database. 2010. Available online: http//www. nist.

gov/pml/data/xcom/index.cfm (accessed on 9 March 2019).

37. Bam, L.C.; Miller, J.A.; Becker, M.; Basson, I.J. X-ray computed tomography: Practical evaluation of beam hardening in iron ore samples. *Miner. Eng.* **2019**, *131*, 206–215, doi:10.1016/j.mineng.2018.11.010.

38. Kyle, J.R.; Mote, A.S.; Ketcham, R.A. High resolution X-ray computed tomography studies of Grasberg porphyry Cu-Au ores, Papua, Indonesia. *Miner. Depos.* **2008**, *5*, 519–532, doi:10.1007/s00126-008-0180-8.

39. Van Geet, M.; Swennen, R.; Wevers, M. Quantitative analysis of reservoir rocks by microfocus X-ray computerised tomography. *Sediment. Geol.* **2000**, *132*, 25–36, doi:10.1016/S0037-0738(99)00127-X.

40. Van Geet, M.; Volckaert, G.; Roels, S. The use of microfocus X-ray computed tomography in characterising the hydration of a clay pellet/powder mixture. *Appl. Clay Sci.* **2005**, *29*, 73–87, doi:10.1016/j.clay.2004.12.007.

41. Lai, P.; Moulton, K.; Krevor, S. Pore-scale heterogeneity in the mineral distribution and reactive surface area of porous rocks. *Chem. Geol.* **2015**, *411*, 260–273, doi:10.1016/J.CHEMGEO.2015.07.010.

42. Barnes, S.J.; Le Vaillant, M.; Lightfoot, P.C. Textural development in sulfide-matrix ore breccias in the Voisey's Bay Ni-Cu-Co deposit, Labrador, Canada. *Ore Geol. Rev.* **2017**, *90*, 414–438, doi:10.1016/j.oregeorev.2017.03.019.

43. Ducheyne, P.; Healy, K.; Hutmacher, D.W.; Grainger, D.W.; Kirkpatrick, C.J. *Comprehensive Biomaterials II*; Elsevier: Amsterdam, The Netherlands, 2017; ISBN 0081006926.

44. Kastner, J.; Harrer, B.; Requena, G.; Brunke, O. A comparative study of high resolution cone beam X-ray tomography and synchrotron tomography applied to Fe- and Al-alloys. *NDT E Int.* **2010**, *43*, 599–605, doi:10.1016/j.ndteint.2010.06.004.

45. Boas, F.E.; Fleischmann, D. CT artifacts: Causes and reduction techniques. *Imaging Med.* **2012**, doi:10.2217/iim.12.13.

46. Schwarz, T. Artifacts in CT. In *Veterinary Computed Tomography*; John Wiley & Sons, Ltd.: Hoboken, NJ, USA, 2011; pp. 35–55, ISBN 9781118785676.

47. Wildenschild, D.; Vaz, C.M.P.; Rivers, M.L.; Rikard, D.; Christensen, B.S.B. Using X-ray computed tomography in hydrology: Systems, resolutions, and limitations. *J. Hydrol.* **2002**, *267*, 285–297, doi:10.1016/S0022-1694(02)00157-9.

48. Suuronen, J.-P.; Sayab, M. 3D nanopetrography and chemical imaging of datable zircons by synchrotron multimodal X-ray tomography. *Sci. Rep.* **2018**, *8*, 4747, doi:10.1038/s41598-018-22891-9.

49. Sun, J.; Yu, T.; Xu, C.; Ludwig, W.; Zhang, Y. 3D characterization of partially recrystallized Al using high resolution diffraction contrast tomography. *Scr. Mater.* **2018**, *157*, 72–75, doi:10.1016/j.scriptamat.2018.08.001.

50. Kikuchi, S.; Nonaka, K.; Asakawa, N.; Shiozawa, D.; Nakai, Y. Change of misorientation of individual grains in fatigue of polycrystalline alloys by diffraction contrast tomography using ultrabright synchrotron radiation. *Procedia Struct. Integr.* **2017**, *3*, 402–410, doi:10.1016/j.prostr.2017.04.058.

51. Herbig, M.; King, A.; Reischig, P.; Proudhon, H.; Lauridsen, E.M.; Marrow, J.; Buffière, J.-Y.; Ludwig, W. 3-D growth of a short fatigue crack within a polycrystalline microstructure studied using combined diffraction and phase-contrast X-ray tomography. *Acta Mater.* **2011**, *59*, 590–601, doi:10.1016/J.ACTAMAT.2010.09.063.

52. King, A.; Herbig, M.; Ludwig, W.; Reischig, P.; Lauridsen, E.M.; Marrow, T.; Buffière, J.Y. Non-destructive analysis of micro texture and grain boundary character from X-ray diffraction contrast tomography. *Nucl. Instrum. Methods Phys. Res. Sect. B Beam Interact. Mater. Atoms* **2010**, *268*, 291–296, doi:10.1016/J.NIMB.2009.07.020.

53. Toda, H.; Takijiri, A.; Azuma, M.; Yabu, S.; Hayashi, K.; Seo, D.; Kobayashi, M.; Hirayama, K.; Takeuchi, A.; Uesugi, K. Damage micromechanisms in dual-phase steel investigated with combined phase- and absorption-contrast tomography. *Acta Mater.* **2017**, *126*, 401–412, doi:10.1016/J.ACTAMAT.2017.01.010.

54. Artioli, G.; Cerulli, T.; Cruciani, G.; Dalconi, M.C.; Ferrari, G.; Parisatto, M.; Rack, A.; Tucoulou, R. X-ray diffraction microtomography (XRD-CT), a novel tool for non-invasive mapping of phase development in cement materials. *Anal. Bioanal. Chem.* **2010**, *397*, 2131–2136, doi:10.1007/s00216-010-3649-0.

55. Takahashi, H.; Sugiyama, T. Application of non-destructive integrated CT-XRD method to investigate alteration of cementitious materials subjected to high temperature and pure water. *Constr. Build. Mater.* **2019**, *203*, 579–588, doi:10.1016/J.CONBUILDMAT.2019.01.128.

56. Laforce, B.; Masschaele, B.; Boone, M.N.; Schaubroeck, D.; Dierick, M.; Vekemans, B.; Walgraeve, C.; Janssen, C.; Cnudde, V.; Van Hoorebeke, L.; et al. Integrated Three-Dimensional Microanalysis Combining X-Ray Microtomography and X-Ray Fluorescence Methodologies. *Anal. Chem.* **2017**, *89*, 10617–10624,

doi:10.1021/acs.analchem.7b03205.

57. Viermetz, M.; Birnbacher, L.; Willner, M.; Achterhold, K.; Pfeiffer, F.; Herzen, J. High resolution laboratory grating-based X-ray phase-contrast CT. *Sci. Rep.* **2018**, *8*, 15884, doi:10.1038/s41598-018-33997-5.

58. Dudgeon, D.E.; Mersereau, R.M. *Multidimensional Digital Signal Processing Prentice-Hall Signal Processing Series*; Prentice-Hall: Englewood Cliffs, NJ, USA, 1984.

59. Feldkamp, L.A.; Davis, L.C.; Kress, J.W. Practical cone-beam algorithm. *J. Opt. Soc. Am. A* **1984**, *1*, 612–619.

60. Lin, Q.; Andrew, M.; Thompson, W.; Blunt, M.J.; Bijeljic, B. Optimization of image quality and acquisition time for lab-based X-ray microtomography using an iterative reconstruction algorithm. *Adv. Water Resour.* **2018**, *115*, 112–124, doi:10.1016/j.advwatres.2018.03.007.

61. Zhuge, X.; Palenstijn, W.J.; Batenburg, K.J. TVR-DART: A More Robust Algorithm for Discrete Tomography From Limited Projection Data With Automated Gray Value Estimation. *IEEE Trans. Image Process.* **2016**, *25*, 455–468, doi:10.1109/TIP.2015.2504869.

62. Myers, G.R.; Kingston, A.M.; Varslot, T.K.; Turner, M.L.; Sheppard, A.P. Dynamic tomography with a priori information. *Appl. Opt.* **2011**, *50*, 3685–3690, doi:10.1364/AO.50.003685.

63. Brabant, L.; Vlassenbroeck, J.; De Witte, Y.; Cnudde, V.; Boone, M.N.; Dewanckele, J.; Van Hoorebeke, L. Three-Dimensional Analysis of High-Resolution X-Ray Computed Tomography Data with Morpho+. *Microsc. Microanal.* **2011**, *17*, 252–263, doi:10.1017/S1431927610094389.

64. Canny, J. A computational approach to edge detection. *IEEE Trans. Pattern Anal. Mach. Intell.* **1986**, 679–698.

65. Prewitt, J.M.S. Object enhancement and extraction. *Pict. Process. Psychopictorics* **1970**, *10*, 15–19.

66. Sobel, I. *An Isotropic 3x3 Image Gradient Operator*; 2014. Avaliable Online: https://www.researchgate.net/publication/239398674_An_Isotropic_3x3_Image_Gradient_Operator (accessed on 14 March 2019).

67. Chun, B.; Xiaoyue, L. The edge detection technology of CT image for study the growth of rock crack. In Proceedings of the 2009 ISECS International Colloquium on Computing, Communication, Control, and Management, Sanya, China, 8–9 August 2009; Volume 4, pp. 286–288.

68. Schlüter, S.; Sheppard, A.; Brown, K.; Wildenschild, D. Image processing of multiphase images obtained via X-ray microtomography: A review. *Water Resour. Res.* **2014**, *50*, 3615–3639.

69. Martínez-Martínez, J.; Benavente, D.; Del Cura, M.A.G. Petrographic quantification of brecciated rocks by image analysis. Application to the interpretation of elastic wave velocities. *Eng. Geol.* **2007**, *90*, 41–54.

70. Kaur, D.; Kaur, Y. Various Image Segmentation Techniques: A Review. *Int. J. Comput. Sci. Mob. Comput.* **2014**, *3*, 809–814.

71. Yogamangalam, R.; Karthikeyan, B. Segmentation techniques comparison in image processing. *Int. J. Eng. Technol.* **2013**, *5*, 307–313.

72. Zaitoun, N.M.; Aqel, M.J. Survey on image segmentation techniques. *Procedia Comput. Sci.* **2015**, *65*, 797–806.

73. Sezgin, M.; Sankur, B. Survey over image thresholding techniques and quantitative performance evaluation. *J. Electron. Imaging* **2004**, *13*, 146–166.

74. Kaczmarczyk, J.; Dohnalik, M.; Zalewska, J.; Cnudde, V. *The Interpretation of X-ray Computed Microtomography Images of Rocks as an Application of Volume Image Processing and Analysis*; 2010. Available Online: https://biblio.ugent.be/publication/1020385/file/1020401.pdf (accessed on 14 March 2019).

75. Otsu, N. A threshold selection method from gray-level histograms. *IEEE Trans. Syst. Man. Cybern.* **1979**, *9*, 62–66.

76. Lin, Q.; Barker, D.J.; Dobson, K.J.; Lee, P.D.; Neethling, S.J. Modelling particle scale leach kinetics based on X-ray computed micro-tomography images. *Hydrometallurgy* **2016**, *162*, 25–36.

77. Lin, Q.; Neethling, S.J.; Dobson, K.J.; Courtois, L.; Lee, P.D. Quantifying and minimising systematic and random errors in X-ray micro-tomography based volume measurements. *Comput. Geosci.* **2015**, *77*, 1–7.

78. Fan, S.-K.S.; Lin, Y. A multi-level thresholding approach using a hybrid optimal estimation algorithm. *Pattern Recognit. Lett.* **2007**, *28*, 662–669, doi:10.1016/j.patrec.2006.11.005.

79. Huang, D.-Y.; Wang, C.-H. Optimal multi-level thresholding using a two-stage Otsu optimization approach. *Pattern Recognit. Lett.* **2009**, *30*, 275–284, doi:10.1016/j.patrec.2008.10.003.

80. Kapur, J.N.; Sahoo, P.K.; Wong, A.K.C. A new method for gray-level picture thresholding using the entropy of the histogram. *Comput. Vis. Graphics Image Process.* **1985**, *29*, 273–285.

81. Gonzalez, R.C.; Woods, R.E. *Digital Image Processing*; Prentice Hall: New Jersey, USA, 2002.

82. Ketcham, R.A. Computational methods for quantitative analysis of three-dimensional features in

geological specimens. *Geosphere* **2005**, *1*, 32–41.

83. Meyer, F.; Beucher, S. Morphological segmentation. *J. Vis. Commun. Image Represent.* **1990**, *1*, 21–46.

84. Wang, D.; Vallotton, P. Improved marker-controlled watershed segmentation with local boundary priors. In Proceedings of the 2010 25th International Conference of Image and Vision Computing New Zealand, Queenstown, New Zealand, 8–9 November 2010; pp. 1–6.

85. Vincent, L.; Soille, P. Watersheds in digital spaces: An efficient algorithm based on immersion simulations. *IEEE Trans. Pattern Anal. Mach. Intell.* **1991**, *6*, 583–598.

86. Weickert, J. Efficient image segmentation using partial differential equations and morphology. *Pattern Recognit.* **2001**, *34*, 1813–1824.

87. Jung, C.R.; Scharcanski, J. Robust watershed segmentation using wavelets. *Image Vis. Comput.* **2005**, *23*, 661–669.

88. Belaid, L.J.; Mourou, W. Image segmentation: A watershed transformation algorithm. *Image Anal. Stereol.* **2011**, *28*, 93–102.

89. Lin, C.L.; Miller, J.D. Advances in X-ray computed tomography (CT) for improved coal washability analysis. In Proceedings of the 16th International Coal Preparation Congress, ICPC 2010, Lexington, KY, USA, 25–30 April 2010.

90. Lin, C.L.; Videla, A.R.; Yu, Q.; Miller, J.D. Characterization and analysis of Porous, Brittle solid structures by X-ray micro computed tomography. *JOM* **2010**, *62*, 86–89.

91. Kong, D.; Fonseca, J. Quantification of the morphology of shelly carbonate sands using 3D images. *Géotechnique* **2017**, *68*, 249–261, doi:10.1680/jgeot.16.p.278.

92. Shi, Y.; Yan, W.M. Segmentation of irregular porous particles of various sizes from X-ray microfocus computer tomography images using a novel adaptive watershed approach. *Géotechnique Lett.* **2015**, *5*, 299–305, doi:10.1680/jgele.15.00100.

93. Baklanova, O.E.; Baklanov, M.A. Methods and Algorithms of Image Recognition for Mineral Rocks in the Mining Industry. In *International Conference in Swarm Intelligence*; Springer: Berlin/Heidelberg, Germany, 2016; pp. 253–262.

94. Duran, B.S.; Odell, P.L. *Cluster Analysis: A Survey*; Springer Science & Business Media: Berlin/Heidelberg, Germany, 2013; Volume 100.

95. Baklanova, O.E.; Shvets, O.Y. Methods and algorithms of cluster analysis in the mining industry: Solution of tasks for mineral rocks recognition. In Proceedings of the 2014 International Conference on Signal Processing and Multimedia Applications (SIGMAP), Vienna, Austria, 28–30 August 2014; pp. 165–171.

96. Arthur, D.; Vassilvitskii, S. k-means++: The advantages of careful seeding. In *Proceedings of the Eighteenth Annual ACM-SIAM Symposium on Discrete Algorithms*; Society for Industrial and Applied Mathematics: Philadelphia, PA, USA, 2007; pp. 1027–1035.

97. Chauhan, S.; Rühaak, W.; Anbergen, H.; Kabdenov, A.; Freise, M.; Wille, T.; Sass, I. Phase segmentation of X-ray computer tomography rock images using machine learning techniques: An accuracy and performance study. *Solid Earth* **2016**, *7*, 1125–1139.

98. Pal, M. Random forest classifier for remote sensing classification. *Int. J. Remote Sens.* **2005**, *26*, 217–222.

99. Hepner, G.; Logan, T.; Ritter, N.; Bryant, N. Artificial neural network classification using a minimal training set- Comparison to conventional supervised classification. *Photogramm. Eng. Remote Sens.* **1990**, *56*, 469–473.

100. Koch, P.-H. Particle Generation for Geometallurgical Process Modeling. Ph.D. Thesis, Luleå Tekniska Universitet: Minerals and Metallurgical Engineering, Department of Civil, Environmental and Natural Resources Engineering, Luleå University of Technology, Luleå, Sweden, 2017.

101. LeCun, Y.; Bottou, L.; Bengio, Y.; Haffner, P. Gradient-based learning applied to document recognition. *Proc. IEEE* **1998**, *86*, 2278–2324.

102. Krizhevsky, A.; Sutskever, I.; Hinton, G.E. Imagenet classification with deep convolutional neural networks. In *Advances in Neural Information Processing Systems*; 2012; pp. 1097–1105. Available Online: https://papers.nips.cc/paper/4824-imagenet-classification-with-deep-convolutional-neural-networks.pdf (accessed on 14 March 2019).

103. Szegedy, C.; Liu, W.; Jia, Y.; Sermanet, P.; Reed, S.; Anguelov, D.; Erhan, D.; Vanhoucke, V.; Rabinovich, A. Going Deeper with Convolutions. 2014, arXiv:1409.4842. Available Online: https://arxiv.org/pdf/1409.4842.pdf (accessed on 14 March 2019).

104. Vapnik, V.; Guyon, I.; Hastie, T. Support vector machines. *Mach. Learn.* **1995**, *20*, 273–297.

105. Anthony, G.; Greg, H.; Tshilidzi, M. Classification of images using support vector machines. 2007,

arXiv:0709.3967. Available Online: https://arxiv.org/ftp/arxiv/papers/0709/0709.3967.pdf (accessed on 14 March 2019).

106. Chapelle, O. Support Vector Machines et Classification D'Images. Master's Thesis, Ecole Normale Supérieure de Lyon, Lyon, France, 1998.

107. Cortina-Januchs, M.G.; Quintanilla-Dominguez, J.; Vega-Corona, A.; Tarquis, A.M.; Andina, D. Detection of pore space in CT soil images using artificial neural networks. *Biogeosciences* **2011**, *8*, 279–288, doi:10.5194/bg-8-279-2011.

108. Arganda-Carreras, I.; Kaynig, V.; Rueden, C.; Eliceiri, K.W.; Schindelin, J.; Cardona, A.; Sebastian Seung, H. Trainable Weka Segmentation: A machine learning tool for microscopy pixel classification. *Bioinformatics* **2017**, *33*, 2424–2426.

109. Wang, H.-Y.; Yang, Q.; Qin, H.; Zha, H. Dirichlet component analysis: Feature extraction for compositional data. In Proceedings of the 25th international conference on Machine Learning, Helsinki, Finland, 5–9 July 2008; pp. 1128–1135.

110. Lobos, R.; Silva, J.F.; Ortiz, J.M.; Díaz, G.; Egaña, A. Analysis and Classification of Natural Rock Textures based on New Transform-based Features. *Math. Geosci.* **2016**, *48*, 835–870.

111. Parian, M.; Mwanga, A.; Lamberg, P.; Rosenkranz, J. Ore texture breakage characterization and fragmentation into multiphase particles. *Powder Technol.* **2018**, *327*, 57–69, doi:10.1016/j.powtec.2017.12.043.

112. Pérez-Barnuevo, L.; Pirard, E.; Castroviejo, R. Textural descriptors for multiphasic ore particles. *Image Anal. Stereol.* **2012**, *31*, 175–184.

113. Zhang, J.; Subasinghe, N. Extracting ore texture information using image analysis. *Trans. Inst. Min. Metall. Sect. C Miner. Process. Extr. Metall.* **2012**, *121*, 123–130, doi:10.1179/1743285512Y.0000000011.

114. Borgefors, G. Distance transformations in digital images. *Comput. Vis. Graphics Image Process.* **1986**, *34*, 344–371, doi:10.1016/S0734-189X(86)80047-0.

115. Borgefors, G. Distance transformations in arbitrary dimensions. *Comput. Vis. Graphics Image Process.* **1984**, *27*, 321–345, doi:10.1016/0734-189X(84)90035-5.

116. Pirard, E.; Califice, A.; Léonard, A.; Gregoire, M. *Multiscale Shape Analysis of Particles in 3D Using the Calypter*; 2009. Available Online: https://orbi.uliege.be/bitstream/2268/22089/1/PUB_09_01_EP%203D%20calypter%20v21.pdf (accessed on 14 March 2019).

117. Fagan-Endres, M.A.; Cilliers, J.J.; Sederman, A.J.; Harrison, S.T.L. Spatial variations in leaching of a low-grade, low-porosity chalcopyrite ore identified using X-ray μCT. *Miner. Eng.* **2017**, *105*, 63–68, doi:10.1016/j.mineng.2017.01.010.

118. Zhao, B.; Wang, J.; Coop, M.R.; Viggiani, G.; Jiang, M. An investigation of single sand particle fracture using X-ray micro-tomography. *Géotechnique* **2015**, *65*, 625–641.

119. Lin, Q.; Neethling, S.J.; Courtois, L.; Dobson, K.J.; Lee, P.D. Multi-scale quantification of leaching performance using X-ray tomography. *Hydrometallurgy* **2016**, *164*, 265–277, doi:10.1016/j.hydromet.2016.06.020.

120. Wu, A.; Yang, B.; Xi, Y.; Jiang, H. Pore structure of ore granular media by computerized tomography image processing. *J. Cent. South Univ. Technol.* **2007**, *14*, 220–224.

121. Serra, J. *Image Analysis and Mathematical Morphology*; Academic Press, Inc.: Cambridge, MA, USA, 1983; ISBN 0126372403.

122. Serra, J.; Soille, P. *Mathematical Morphology and Its Applications to Image Processing*; Springer Science & Business Media: Berlin/Heidelberg, Germany, 2012; Volume 2; ISBN 9401110409.

123. Pierret, A.; Capowiez, Y.; Belzunces, L.; Moran, C.J. 3D reconstruction and quantification of macropores using X-ray computed tomography and image analysis. *Geoderma* **2002**, *106*, 247–271.

124. Faessel, M.; Delisée, C.; Bos, F.; Castéra, P. 3D Modelling of random cellulosic fibrous networks based on X-ray tomography and image analysis. *Compos. Sci. Technol.* **2005**, *65*, 1931–1940.

125. Lux, J.; Delisée, C.; Thibault, X. 3D characterization of wood based fibrous materials: An application. *Image Anal. Stereol.* **2011**, *25*, 25–35.

126. Vogel, H.-J.; Weller, U.; Schlüter, S. Quantification of soil structure based on Minkowski functions. *Comput. Geosci.* **2010**, *36*, 1236–1245, doi:10.1016/j.cageo.2010.03.007.

127. De Berg, M.; Van Kreveld, M.; Overmars, M.; Schwarzkopf, O.C. Computational geometry. In *Computational Geometry*; Springer: Berlin/Heidelberg, Germany, 2000; pp. 1–17.

128. Vecchio, I.; Schladitz, K.; Godehardt, M.; Heneka, M.J. 3D Geometric characterization of particles applied

to technical cleanliness. *Image Anal. Stereol.* **2012**, *31*, 163–174.

129. Pamukcu, A.S.; Gualda, G.A.R.; Rivers, M.L. Quantitative 3D petrography using X-ray tomography 4: Assessing glass inclusion textures with propagation phase-contrast tomography. *Geosphere* **2013**, *9*, 1704–1713.

130. Van Dalen, G.; Koster, M.W.; Dalen, G. Van; Koster, M.W. *2D & 3D Particle Size Analysis of Micro-CT Images*; Unilever Research and Development Netherlands: Vlaardingen, The Netherlands, 2012; doi:10.1007/s10509-008-9775-x.

131. Parisatto, M.; Turina, A.; Cruciani, G.; Mancini, L.; Peruzzo, L.; Cesare, B. Three-dimensional distribution of primary melt inclusions in garnets by X-ray microtomography. *Am. Mineral.* **2018**, *103*, 911–926.

132. Duran, C.J.; Barnes, S.J.; Pleše, P.; Kudrna Prašek, M.; Zientek, M.L.; Pagé, P. Fractional crystallization-induced variations in sulfides from the Noril'sk-Talnakh mining district (polar Siberia, Russia). *Ore Geol. Rev.* **2017**, *90*, 326–351, doi:10.1016/j.oregeorev.2017.05.016.

133. Wang, L.B.; Frost, J.D.; Lai, J.S. Three-dimensional digital representation of granular material microstructure from X-ray Tomography imaging. *J. Comput. Civ. Eng.* **2004**, *18*, 28–35, doi:10.1061/(ASCE)0887-3801(2004)18:1(28).

134. Masad, E.; Saadeh, S.; Al-Rousan, T.; Garboczi, E.; Little, D. Computations of particle surface characteristics using optical and X-ray CT images. *Comput. Mater. Sci.* **2005**, *34*, 406–424, doi:10.1016/j.commatsci.2005.01.010.

135. Garboczi, E.J. Three-dimensional mathematical analysis of particle shape using X-ray tomography and spherical harmonics: Application to aggregates used in concrete. *Cem. Concr. Res.* **2002**, *32*, 1621–1638, doi:10.1016/S0008-8846(02)00836-0.

136. Cepuritis, R.; Garboczi, E.J.; Jacobsen, S.; Snyder, K.A. Comparison of 2-D and 3-D shape analysis of concrete aggregate fines from VSI crushing. *Powder Technol.* **2017**, *309*, 110–125, doi:10.1016/j.powtec.2016.12.037.

137. Garboczi, E.J.; Bullard, J.W. 3D analytical mathematical models of random star-shape particles via a combination of X-ray computed microtomography and spherical harmonic analysis. *Adv. Powder Technol.* **2017**, *28*, 325–339, doi:10.1016/j.apt.2016.10.014.

138. Nava, E. *Wavelets: Theory and Applications*; University of Malaga: Malaga, Spain, 2006.

139. Mulcahy, C. Image compression using the Haar wavelet transform. *Spelman Sci. Math. J.* **1997**, *1*, 22–31.

140. Antonini, M.; Barlaud, M.; Mathieu, P.; Daubechies, I. Image coding using wavelet transform. *IEEE Trans. Image Process.* **1992**, *1*, 205–220.

141. Walker, J.S. Wavelet-based image processing. *Appl. Anal.* **2006**, *85*, 439–458.

142. Lepistö, L.; Kunttu, I.; Visa, A. Rock image classification using color features in Gabor space. *J. Electron. Imaging* **2005**, *14*, 040503.

143. Tessier, J.; Duchesne, C.; Bartolacci, G. A machine vision approach to on-line estimation of run-of-mine ore composition on conveyor belts. *Miner. Eng.* **2007**, *20*, 1129–1144.

144. Perez, C.A.; Estévez, P.A.; Vera, P.A.; Castillo, L.E.; Aravena, C.M.; Schulz, D.A.; Medina, L.E.; Estévez, P.A.; Vera, P.A.; Castillo, L.E.; et al. Ore grade estimation by feature selection and voting using boundary detection in digital image analysis. *Int. J. Miner. Process.* **2011**, *101*, 28–36, doi:10.1016/j.minpro.2011.07.008.

145. Katunin, A.; Dańczak, M.; Kostka, P. Automated identification and classification of internal defects in composite structures using computed tomography and 3D wavelet analysis. *Arch. Civ. Mech. Eng.* **2015**, *15*, 436–448, doi:10.1016/j.acme.2014.08.002.

146. Ojala, T.; Pietikäinen, M.; Harwood, D. A comparative study of texture measures with classification based on featured distributions. *Pattern Recognit.* **1996**, *29*, 51–59, doi:10.1016/0031-3203(95)00067-4.

147. Sorensen, L.; Shaker, S.B.; De Bruijne, M. Quantitative analysis of pulmonary emphysema using local binary patterns. *IEEE Trans. Med. Imaging* **2010**, *29*, 559–569.

148. Murala, S.; Maheshwari, R.P.; Balasubramanian, R. Directional binary wavelet patterns for biomedical image indexing and retrieval. *J. Med. Syst.* **2012**, *36*, 2865–2879.

149. Rahimov, K.; AlSumaiti, A.M.; AlMarzouqi, H.; Jouini, M.S. Use of Local Binary Pattern in Texture Classification of Carbonate Rock Micro-CT Images. In Proceedings of the SPE Kingdom of Saudi Arabia Annual Technical Symposium and Exhibition, Dammam, Saudi Arabia, 24–27 April 2017.

150. Haralick, R.M.; Shanmugam, K. Textural features for image classification. *IEEE Trans. Syst. Man. Cybern.* **1973**, *3*, 610–621.

Paper 3

Application of machine learning techniques in mineral phase segmentation for X-ray microcomputed tomography (μCT) data

Pratama Istiadi Guntoro[a,*], Glacialle Tiu[b], Yousef Ghorbani[a], Cecilia Lund[a], Jan Rosenkranz[a]

[a] *Division of Minerals and Metallurgical Engineering, Luleå University of Technology, SE-971 87 Luleå, Sweden*
[b] *Division of Geosciences and Environmental Engineering, Luleå University of Technology, SE-971 87 Luleå, Sweden*

ABSTRACT

X-ray microcomputed tomography (μCT) offers a non-destructive three-dimensional analysis of ores but its application in mineralogical analysis and mineral segmentation is relatively limited. In this study, the application of machine learning techniques for segmenting mineral phases in a μCT dataset is presented. Various techniques were implemented, including unsupervised classification as well as grayscale-based and feature-based supervised classification. A feature matching method was used to register the back-scattered electron (BSE) mineral map to its corresponding μCT slice, allowing automatic annotation of minerals in the μCT slice to create training data for the classifiers. Unsupervised classification produced satisfactory results in terms of segmenting between amphibole, plagioclase, and sulfide phases. However, the technique was not able to differentiate between sulfide phases in the case of chalcopyrite and pyrite. Using supervised classification, around 50–60% of the chalcopyrite and 97–99% of pyrite were correctly identified. Feature based classification was found to have a poorer sensitivity to chalcopyrite, but produced a better result in segmenting between the mineral grains, as it operates based on voxel regions instead of individual voxels. The mineralogical results from the 3D μCT data showed considerable difference compared to the BSE mineral map, indicating stereological error exhibited in the latter analysis. The main limitation of this approach lies in the dataset itself, in which there was a significant overlap in grayscale values between chalcopyrite and pyrite, therefore highly limiting the classifier accuracy.

1. Introduction

There has been growing interest in X-ray microcomputed tomography (μCT) application in geosciences, due to its non-destructive nature that allows three-dimensional (3D) analysis of an object. μCT could potentially eliminate stereological errors generated by conventional two-dimensional microscopy analysis used for ore and rock samples, allowing more accurate analysis of the samples. Rapid development of μCT systems currently allows spatial resolution down to nanometer scale (Ghorbani et al., 2011; Yang et al., 2017), as well as enabling in-situ experiments to be performed during acquisition, thereby acquiring time-based 3D data (Ghorbani et al., 2011; Lin et al., 2016a, 2016b). These developments make μCT a more attractive analytical technique for rock samples.

Various applications of μCT systems in geoscience have been studied, including mineral liberation and grain analysis, pore and fracture analysis, and to some degree, texture analysis (Garcia et al., 2009; Ghorbani et al., 2011; Jardine et al., 2018; Lin and Miller, 2005, 1996).

Reviews discussing current and potential applications of μCT system in geosciences have also been published (Cnudde and Boone, 2013; Guntoro et al., 2019; Kyle and Ketcham, 2015; Maire and Withers, 2014; Mees et al., 2003; Miller et al., 1990). Nevertheless, the current use of μCT for ore samples is more focused towards structural analysis of the samples, such as analysis of pores and fractures (Deng et al., 2016; Ghorbani et al., 2011; Müter et al., 2012). Other uses include particle size distribution analysis (Wightman et al., 2015) and particle shape analysis (Lin and Miller, 2005). In a recent study, textural analysis of mineral phases in a drill core sample was conducted using a μCT system through the correlation and association indices between volume elements (voxels) in the 3D dataset (Jardine et al., 2018).

Being able to use μCT to generate a 3D structural analysis as well as gaining mineralogical information of the ore sample at the same time would add value to the technique as well as its potential uses. This is where μCT is currently limited due to challenges including: similar attenuations between mineral phases, limited resolution, and lack of automated mineralogical analysis software. Both pre- and post-scanning

---

techniques aiming to obtain a reliable 3D mineralogical analysis have been evaluated by several researchers (Bam et al., 2019; Ghorbani et al., 2011; Kyle et al., 2008; Reyes et al., 2017; Tiu, 2017; Wang et al., 2015).

Pre-scanning techniques refer mostly to optimization of the scanning conditions as well as calibration with pure minerals. Scanning conditions can be adjusted to increase the attenuation contrasts between minerals, which often means using lower voltage and/or reducing sample size. Reyes et al. (2017) have shown that segmentation between chalcopyrite and pyrite was still found to be difficult when using voltage as low as 50 kV. Kyle et al. (2008) have shown that bornite, chalcopyrite, and magnetite minerals could be differentiated with smaller-diameter (≤ 22 mm) core samples at scanning energy of 180 KeV. Additionally, using smaller sample size could also suppress the beam hardening effect (Bam et al., 2019), which can contribute to segmentation inaccuracies (Reyes et al., 2017).

Calibration with high purity mineral samples in combination with dual energy μCT scanning has been demonstrated by Ghorbani et al. (2011). By calibrating the μCT system with minerals with known density, a correlation that relates density with the attenuation coefficient can be obtained. The density of the material can also be determined directly through the relation between attenuation coefficients obtained from scanning at two different energy levels. Ghorbani et al. (2011) combined both procedures so that the measured density from dual energy scanning (130 and 200 kV) can be compared against the real density of the calibration samples. Using such procedures, Ghorbani et al. (2011) successfully differentiated pyrite, quartz, and sphalerite minerals in the sample.

Post-scanning techniques refer to the image processing procedures applied to the acquired μCT dataset. If the differences in attenuations are significant enough, simple thresholding techniques such as the one developed by Otsu (1979) can be used to set a threshold between the grayscale values and subsequently differentiate the phases. This method has been used in segmenting pores/air and the mineral matrix, as well as heavy and light minerals (Andrä et al., 2013; Lin et al., 2016a, 2015; Reyes et al., 2017; Yang et al., 2017). In cases where the attenuation differences are insignificant, cross-correlation of the μCT dataset to other dataset such as dataset obtained from Scanning Electron Microscope with Energy Dispersive X-ray Spectroscopy (SEM-EDS) has been shown to be capable of distinguishing minerals with similar attenuations such as copper sulfides and pyrite (Reyes et al., 2017; Tiu, 2017).

Another promising approach in differentiating between mineral phases is the use of machine learning techniques. In general, machine learning is defined as the use of mathematical models to interpret the underlying patterns in a dataset. By learning this pattern, a computer system can make predictions or classifications on the dataset (Sutharan, 2016). Machine learning can be divided into unsupervised and supervised learning. Supervised learning means that the user predefines the underlying pattern of the data, and the computer builds a prediction model based on the pre-defined pattern (training data). Unsupervised learning lets the computer interpret the pattern by itself without user's supervision.

Several recent studies have evaluated the use of machine learning in the segmentation of mineral phases in μCT dataset. Chauhan et al. (2016a, 2016b) evaluated the performances of various machine learning algorithm for μCT datasets, focusing mostly on the segmentation of pores from the rock matrix. Both unsupervised and supervised algorithms were evaluated, including K-means, Fuzzy C-means, Self-Organized Maps (SOM), Artificial Neural Network (ANN), as well Support Vector Machines (SVM). Tiu (2017) evaluated the use of supervised classification (random forest) in segmentation between chalcopyrite and pyrite in a drill core sample, using SEM-EDS mineral map as training data. Wang et al. (2015), used feature-based random forest classification to segment multiphase particulate samples from the background, in which they concluded that the resulting segmentation from simple thresholding technique was not satisfactory.

Fig. 1. Map of Sweden, showing mines in operation as of August 2018. The sample originated from Aitik deposit shown as the red star in the northern region of Sweden. Map taken from www.sgu.se. (For interpretation of the references to color in this figure legend, the reader is referred to the web version of this article.)

This study systematically evaluates the application of different machine learning techniques in mineral segmentation to a μCT dataset. Both unsupervised and supervised learning techniques are included in this study. Additionally, an automated image registration technique is introduced to align a Back Scattered Electron (BSE) mineral map with a corresponding slice in a 3D μCT data, which is then used as the training data to classify the other μCT slices. Furthermore, besides using grayscale values as the dataset, the possibility of classification using

Table 1
Textural characteristics of the sample analyzed (Tiu, 2017).

Textural description	Ore mineralogy	Gangue mineralogy	Vein intensity
Dark greenish colored rock, with coarse (1–5 mm) amphibole phenocrysts in a quartz-feldspar-biotite matrix.	Chalcopyrite and pyrite occur in veins. Magnetite occurs as fine-grained dissemination	Amphiboles, feldspars, and biotite occur as the major gangue minerals	High amphibole-plagioclase vein containing chalcopyrite, pyrite and some magnetite minerals

features such as edges, corners, and blobs (regions with similar grayscale values) is also evaluated. The accuracy and computational costs of these methods are evaluated and compared to give insight on the most suitable method for specific tasks related to mineral segmentation of a µCT dataset.

2. Material and methods

2.1. Ore samples

The drill core sample used in this study was obtained from Boliden's Aitik copper mine in Northern Sweden, shown in Fig. 1.

The deposit is described as a metamorphosed porphyry Cu-Au deposit, with chalcopyrite, pyrite, and pyrrhotite as the main sulfide minerals; magnetite and ilmenites were found as the oxide minerals (Wanhainen et al., 2003). Other minerals that can be found in this deposit include quartz, amphibole, biotite, garnet, tourmaline, and zeolites. The textural description of this sample is provided in Table 1, while a µCT volume of the sample is shown in Fig. 2.

2.2. X ray microcomputed tomography (µCT) and image acquisition

A cylindrical sample with a diameter of 25 mm was analyzed using a Zeiss Xradia 510 Versa 3D microscope at Luleå University of Technology (LTU), Sweden. The whole sample was placed in the scanning chamber and measured under the scanning conditions summarized in Table 2. Reconstruction of projections was done with beam hardening correction. ORS Dragonfly® software was used for volume rendering and visualization of the 3D image. The scanning conditions used in this study were optimized so that a good image with reasonable acquisition time could be achieved.

Despite the use of filters and beam hardening corrections during reconstruction phase, the final 3D image acquired in this study still

Table 2
Experimental conditions of the µCT scanning.

|	
Voltage	160 kV
Power	10 W
Exposure time	14 s
Objective	0.4x
Bin	1
Filters	Zeiss HE3 filter (as provided by the manufacturer)
No. of projections	2201
Spatial resolution	13 µm

possessed some artifacts, most notably that the grayscale value varies significantly for the biotite-feldspar matrix throughout the slices (vertically) as shown in Fig. 3. This does not necessarily mean that the matrix grayscale values in the top and bottom slices are homogenously darker than the middle slices; the grayscale value of the matrix also varies horizontally in a single slice, as shown in Fig. 4.

This problem can be seen as an uneven illumination problem, which can be addressed using top hat filtering (Wang et al., 2014). Top hat filtering is achieved by morphologically opening (removing) the grains from the slice, thereby obtaining an image estimation of biotite-feldspar matrix without any amphibole, chalcopyrite and pyrite grains. This image estimation represents the unevenly illuminated "background", in which the goal is to homogenize this "background". This is achieved by replacing the image by the "correct" and constant background, obtained from one of the middle slices where variation in the biotite-feldspar matrix does not exist, as illustrated in Fig. 5.

While the aforementioned procedure affects all the grayscale values of all phases, it focuses on correcting the biotite-feldspar matrix, so adjustment is needed for the other phases. This is done by increasing the contrast between phases, so that the difference between phases is clear enough to segment. A comparison of an uncorrected and corrected image is shown in Fig. 6.
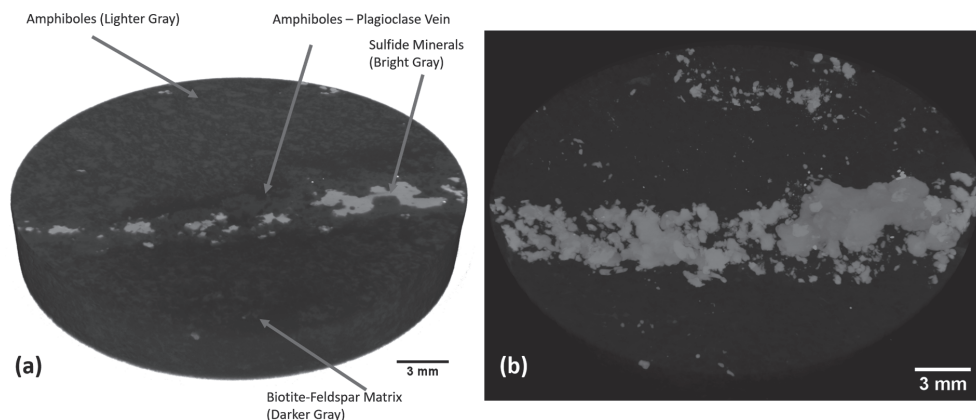
Fig. 2. (A) µCT volume of the sample, showing clear amphibole phenocrysts (lighter gray) inside biotite-feldspar matrix (darker gray). A high intensity amphibole-plagioclase vein with rich chalcopyrite and pyrite grains (bright gray) is also observed in the sample. (B) µCT volume showing chalcopyrite and pyrite grains as well as their vein mineralization (cyan) inside drill core volume. (For interpretation of the references to color in this figure legend, the reader is referred to the web version of this article.)
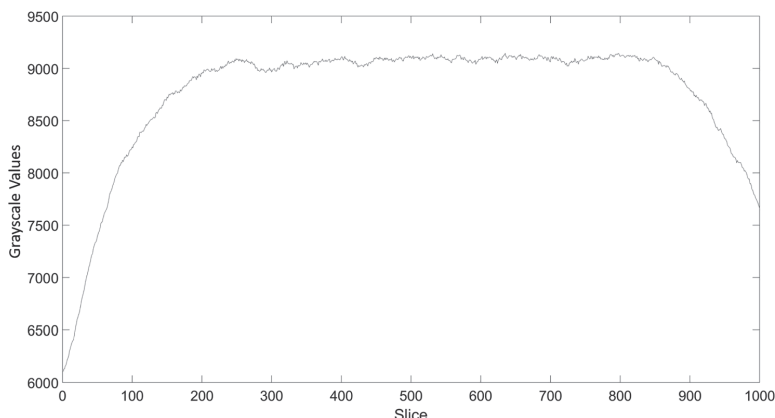
Fig. 3. Plot of biotite-feldspar matrix average grayscale values of each slice, showing significant variation in the top and bottom hundred slices. Despite the fact that the matrix's grayscale values are different for each slice, the variation should be small (as seen in the plateau in the middle slices). Significant variation in the top and bottom slices is most likely associated with the beam hardening effect.

2.3. SEM-EDS and mineral mapping

SEM-EDS analysis was performed on the top part of the cylindrical sample after the μCT measurement, as a comparison and reference. The cylindrical sample was mounted in epoxy resin and polished prior to SEM-EDS analysis. A Zeiss Merlin FEG-SEM system was used for SEM analysis, and Aztec Energy 2.2 software from Oxford Instruments was used for EDS analysis.

The resulting Back Scattered Electron (BSE) image was subjected to mineral mapping. The BSE image has a resolution of 3 μm per pixel, allowing sharper contrast and better segmentation between phases. Based on the EDS measurements, mineral mapping of the BSE image was performed using the Trainable Weka Segmentation (Arganda-Carreras et al., 2017) in the Fiji/ImageJ software (Schindelin et al.,
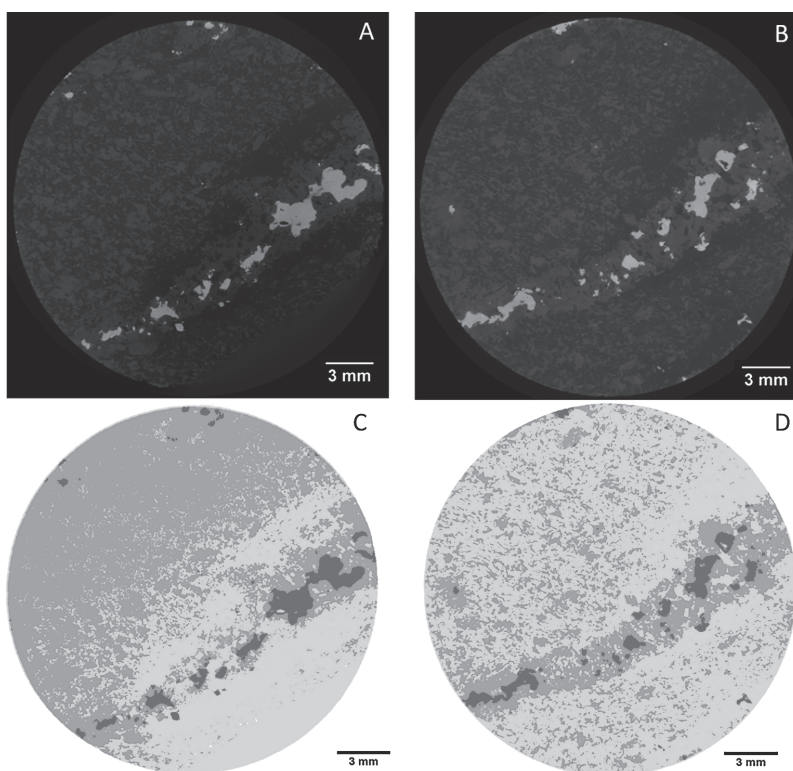
Fig. 4. Variation of grayscale values in one of the top slices, showing (A) top slice, (B) middle slice, (C) segmented image of top slice, (D) segmented image of middle slice. The grayscale value of biotite-feldspar matrix in (A) varies, in which it is getting darker from top left to bottom right, as shown in the segmented image (C). In contrast with the middle slice, the matrix is homogenous, as seen in (B), producing better segmentation result in (D).
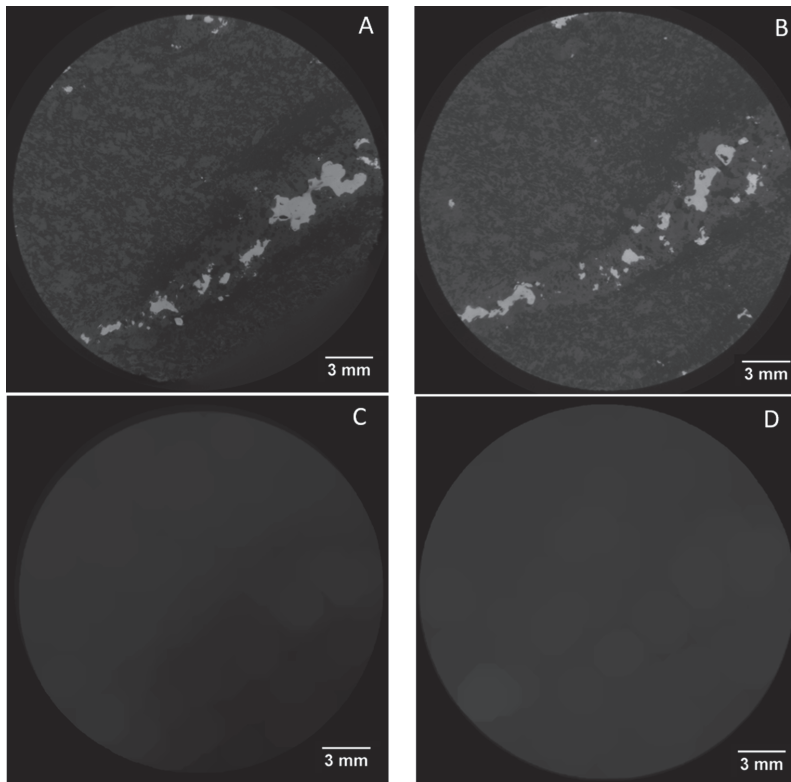
Fig. 5. An image estimation of the biotite-feldspar matrix showing (A) top slice, (B) middle slice, (C) image estimation of biotite-feldspar matrix of (A), (D) image estimation of biotite-feldspar matrix of (B). The grayscale values of (C) is unevenly varied compared to (D). The image (D) is used as the "correct" grayscale value for the matrix, in which grayscale variation practically does not exist.

2012). The resulting mineral map is shown in Fig. 7.

2.4. Machine learning classification algorithms

In this study, both unsupervised and supervised classification algorithms were evaluated for mineral segmentation of the μCT dataset. Image processing and classifications were performed by compilation of tools in MATLAB® as well as in ImageJ/Fiji (Schindelin et al., 2012). The following system configuration is used for data processing: Intel® Core™ i7-7500U CPU @2.7 GHz, 2904 MHz, 2 Core(s) and 4 logical processors, 24 GB RAM and 64-bit OS. The implemented machine learning algorithms are listed as follows:

- *K*-means clustering (unsupervised). This technique aims to classify the dataset into *k* number of clusters containing voxels with similar grayscale values (Duran and Odell, 2013). The user initiates the clustering by setting the number of clusters (*k*) as well as the initial guess of the grayscale value of the cluster centroids (c_k). The squared Euclidean distance between each voxel in the dataset to the initial centroids are calculated in Eq. (1).

- Fuzzy C-means clustering (FCM) (unsupervised). A fuzzy set is defined as a set of data with no distinctive boundary (Zaitoun and Aqel, 2015). In contrast to *k*-means clustering in which each pixel can only be a member of one cluster, a pixel in a FCM scheme can be a member of multiple clusters, depending on the fuzzifier constant

(m). This constant affects the distance calculation (d_{FCM}), which in turns affects how a voxel is classified to a cluster centroid (c_k), as shown in Eq. (3).

$$d_{k-means} = ||v_{(x,y,z)} - c_k||^2 \tag{1}$$

In which $v_{(x,y,z)}$ is the grayscale value of a voxel in a three-dimensional xyz coordinate. Each voxel is then classified to the nearest centroid, i.e. the centroid that has the least squared distance to the voxel. Afterwards, new centroids can be calculated by averaging the grayscale values of the voxels in each cluster. The process is re-iterated until the cluster centroids stabilize around a certain value. The determination of *k* is often arbitrary, or in some cases based on prior knowledge about the dataset. In this study, based on the mineral map in Fig. 7, six clusters could be expected to exist in the dataset, i.e. *k* = 6, which corresponds to the five different mineral groups and one background. However, the value of k could be lower as well, as for example the mineral group of "Quartz + Magnetite + Biotite" could be unclassified due to the relatively low amount of such minerals in the dataset. Proper determination of k often requires running of several k-means classification with different *k* values, then evaluating the results accordingly (trial and error). In this study, an evaluation is done by visual checking combined with evaluating the sum squared of errors (SSE) between each pixel and its cluster centroid, shown in Eq. (2). For each pixel $i = 1, \cdots, n$, the squared error is the squared difference between the pixel and the centroid of its assigned cluster $c(k|x_i)$, $k = 2, \cdots, K$.
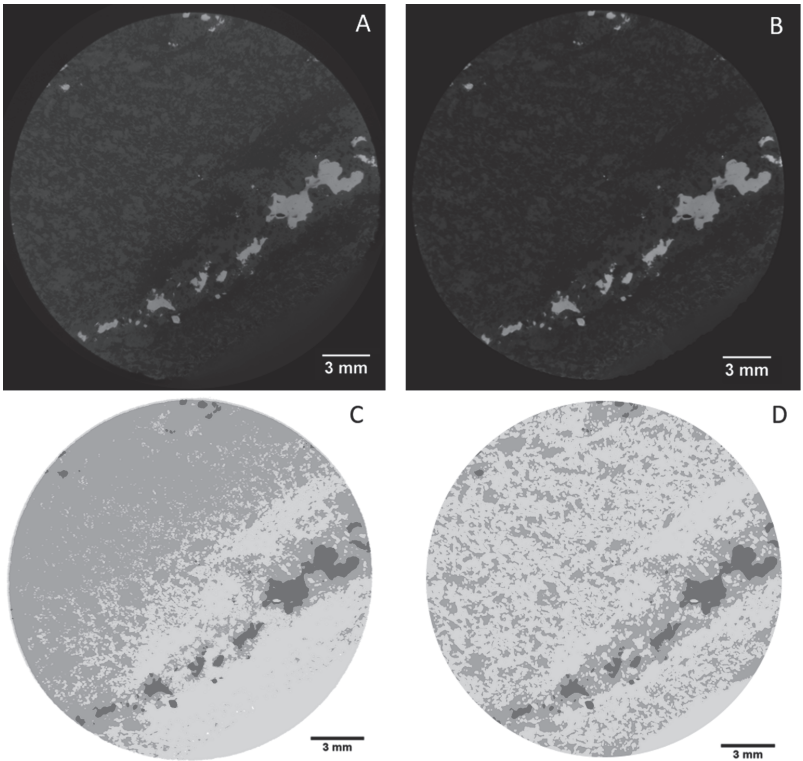
Fig. 6. Correction of grayscale values showing (A) original slice, (B) corrected slice, (C) segmented image of original slice (A), (D) segmented image of corrected slice (B). Clear improvement is seen in the segmentation results (D) as compared to (C).
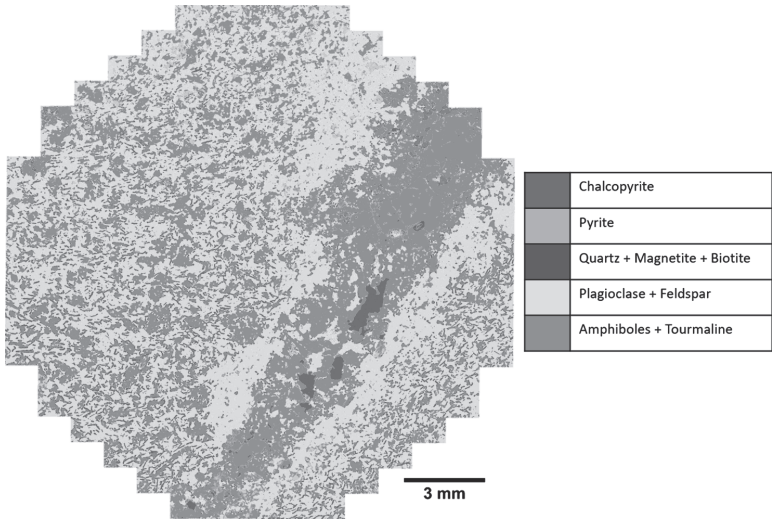

Fig. 7. Simplified mineral map of BSE image. Due to the high resolution the BSE image, fine-grained minerals of quartz, magnetite, and biotite are also detected. These fine-grained mineral phases are grouped together.

The maximum number of clusters was set to ten, i.e. $K = 10$, representing nine mineral phases in Fig. 7 with one background phase.

$$SSE = \sum_{i=1}^{n} (x_i - c(k|x_i))^2 \qquad (2)$$

$$d_{FCM} = w_k^m \cdot d_{k-means}; \quad \frac{1}{w_k} = \sum_{j=1}^{c} \left(\frac{||v_{(x,y,z)} - c_k||}{||v_{(x,y,z)} - c_j||} \right)^{\frac{2}{m-1}} \qquad (3)$$

In which $j = 1, \cdots, c$, with c as the number of clusters (determined in similar fashion as in k-means clustering), $m \in \mathbb{R}$ with $m \geq 1$, and w_k is the weight or the membership function. As it can be seen that large fuzzifier constant leads to smaller weight, i.e. it decreases the weight assigned to clusters that are close to the voxel, which leads to fuzzier classification. In the limit of $m = 1$, the weight increases for clusters that are close to the voxel, indicating less fuzzy classification (similar to k-means). Unless prior knowledge about the dataset is known, the fuzzifier constant is commonly set to 2 (Siddique et al., 2018). In this study, the fuzzifier constant is set to 2.

- Random forest (supervised). This is a classification technique in which multiple classification trees are built by bootstrap aggregating (bagging). Then, the voxel is classified by majority voting of the trees (Breiman, 2001). Classification tree is a decision tree aiming to classify the voxels by asking a yes or no question (binary tests) in each branch of the tree. An example of decision tree is illustrated in Fig. 8. Essentially, a decision tree is built by examining all possible binary splits on the dataset, in which a split is considered optimum when the resulting branches have the lowest impurity. In a random forest technique, these trees are built by repeatedly sampling the training data uniformly and with replacement (bagging). This allows the building of decision trees based on different parts of the training data, thereby reducing the overfitting of the training dataset. Building more trees would lead to better performance and lower error, but at the expense of computational cost. Finding the optimum number of trees (ntree) requires trial and error; by evaluating random forest classification using different number of trees, one can determine the point where no significant improvement in performance is gained if the number of tree is increased (Oshiro et al., 2012). Several studies have suggested various optimum number of trees such as between 64 and 128 (Oshiro et al., 2012), 200 (Feng et al., 2015), and 500 (Thanh Noi and Kappas, 2018). Nevertheless, these numbers are often case-specific, so parameter tuning is required to find the optimum number of trees. Furthermore, while using more than optimum number of trees is unnecessary and computationally expensive, it does not harm the model (Breiman, 2001). The ntree parameter was tuned and varied between 3, 5, 10, 50, 100, and 200.

- k-nearest neighbors (kNN) (supervised). This is a classification that has no prior hypothesis about the training data, but rather generates a hypothesis from the training data itself (Russell and Norvig, 2016). In comparison to random forest where a classifier was build based on training data, kNN directly classifies test voxels by comparing the similar voxels in the training data. This is done by calculating the Euclidean distances between the test voxel to the voxels in training data. Then by looking at the majority of mineral class in the k number of closest voxels to the test voxel, the mineral class of that test voxel can be determined. Similar to the previous machine learning techniques, determination of the ideal k value is not straightforward (Naidoo et al., 2012) and often requires trial and error. Small number of k would increase the noise effect on the result, while larger number of k would suppress the noise effect at the cost of computational power. Methods for optimum determination of k has been evaluated thoroughly elsewhere (Hall et al., 2008; Thanh Noi and Kappas, 2018), but essentially one could also try similar approach as in determining the number of trees in random forest classification. In this study, k is tuned and varied between 1 and 5, as well as 10, 50, and 100. An example of kNN classification is illustrated in Fig. 9.

2.4.1. Supervised feature-based classification

The previous classification techniques classify the voxels based on the grayscale value. In this study, an alternative is also evaluated, in which the voxel is classified by its feature. The features can be edges, corners, or blob / regions in the image. These features are extracted by convoluting the image using kernel functions, thereby generating a feature map of the image to be classified. A kernel is a square matrix that holds some values that would modify the image when the matrix is convoluted with the image (Guntoro et al., 2019). Depending on the values, several tasks such as blurring and edge detection could be performed on the image. Example of a Sobel kernel (Sobel, 2014) which extract the vertical (y-direction) edges in the image is shown in Eq. (4). Rotating the kernel 90° would produce a new kernel for extracting the horizontal (x-direction) edges in the image. The modified image is referred as a feature map, in which different feature maps can be generated by convoluting the image with different kernels.
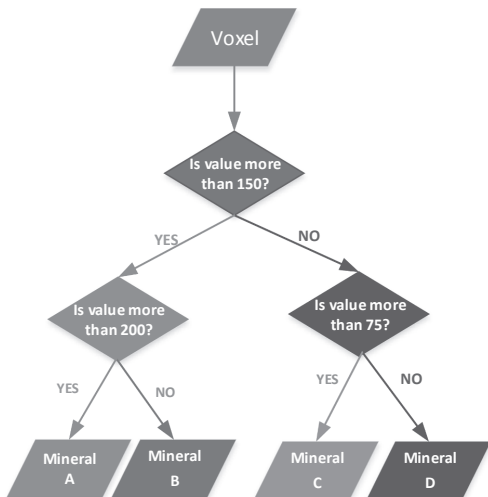

Fig. 8. Example of a classification tree. Sequences of binary decision making branch is built based on training data so that a voxel can be classified into several different minerals.
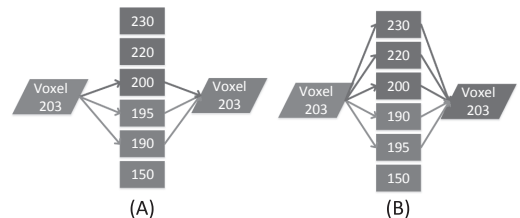

Fig. 9. kNN classification, showing k = 3 (A) and k = 5 (B). Different k will affect how a voxel is classified, in (A) the majority of three closest neighbors are green, therefore the voxel will be classified as green, while in (B) the majority of five closest neighbors are red, therefore the voxel is classified as red. (For interpretation of the references to color in this figure legend, the reader is referred to the web version of this article.)
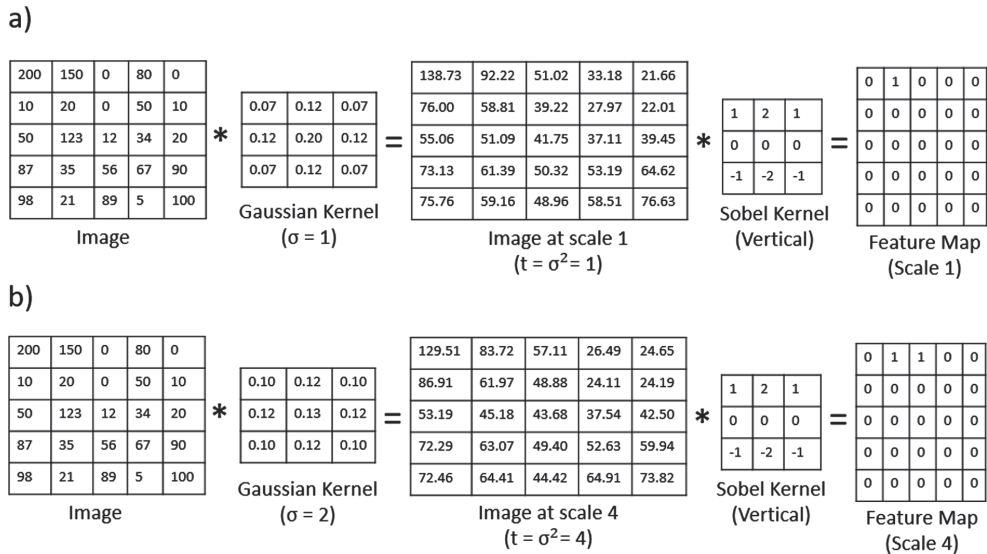
Fig. 10. Feature extraction in Gaussian scale-space, showing (a) Sobel feature extraction from image at scale 1 and (b) Sobel feature extraction from image at scale 4. The image is convoluted with Gaussian kernel of varying standard deviation, creating multiple images in different scales. The feature is extracted from the images in different scales, creating feature maps of different scales. The feature map in (b) is different from (a), which indicates that different image scales generate different feature maps.

$$\begin{bmatrix} 1 & 2 & 1 \\ 0 & 0 & 0 \\ -1 & -2 & -1 \end{bmatrix} \qquad (4)$$

In feature-based classification, the image is represented in a Gaussian scale-space representation, which means that beside xy space, the image is also represented as a family of images blurred with Gaussian filter of varying standard deviations (σ), or commonly referred as varying scales ($t = \sigma^2$) (Lindeberg, 2007). The features are then extracted from the image at different scales, creating feature maps of different scales. These different scales affect the features that may be extracted from the image. At the larger scales, (higher standard deviation and more blurred) the image would lose details on smaller gangue grains. Conversely, at the smaller scales, more features from the smaller grains will be extracted. A mathematical illustration of feature extraction at different scales is shown in Fig. 10.

After collecting the feature maps at different scales, these features are matched with the training data. Then a classifier is built based on the training information, and consequently has more criteria to classify a voxel by looking at these different features. For example, a conventional classifier classifies a voxel as pyrite if it has grayscale value over 200.

$$v_{(x,y,z)} > 200 \Rightarrow v_{(x,y,z)} = pyrite \qquad (5)$$

In feature-based classification, if Sobel filter (G) is used as the feature extractor, then the classifier classifies the voxel as pyrite if the Sobel edge extracted at scale 1 is 1 and the Sobel edge extracted at scale 4 is 0.

$$G^*v_{(x,y,z,t=1)} = 1 \land G^*v_{(x,y,z,t=4)} = 0 \Rightarrow v_{(x,y,z)} = pyrite \qquad (6)$$

This of course comes with a cost; the classifier would be computationally more expensive to build. Feature-based classification is illustrated in Fig. 11.

Feature-based classification was performed to evaluate its applicability compared to grayscale-based classification. Different types of features are extracted from the μCT image, and classification is performed based on these features instead of the grayscale values. Edge features are extracted using 3×3 Sobel filter (both horizontal and vertical), while blobs and corners are extracted with difference of 3×3 Gaussians (Lindeberg, 2015) and the determinant of Hessian matrix (Lindeberg, 2013). Random forest classifier was trained using these features and the training data. The feature extraction methods and random forest classifiers are available in the Trainable Weka Segmentation Plug-in (Arganda-Carreras et al., 2017) in Fiji/ImageJ.

Examples of these features extracted from a drill core μCT slice are shown in Fig. 12.

2.4.2. Statistical methods in evaluating the classifiers

Several statistical measures were used to evaluate the classifiers, in particular regarding the supervised classification. Essentially these statistical measures evaluate the performance of classifiers by comparing to the ground truth. In the case of unsupervised classification, due to the ground truth being unavailable, the classification results was compared directly to the BSE mineral-map instead.

K-fold cross validation was used to evaluate and compare the performance of the supervised classifiers. In principle, the method randomly sub-sampled the training data into K sub-samples. The training was done so that the classifier was trained using $K - 1$ of the sub-samples, in which the remaining one sub-sample was held out for validation. The training is repeated K amount of times with all sub samples, in which after each training, validation was performed with the hold-out subsample, producing K amount of validation results. These K validation results were then averaged to evaluate the overall performance of the classifier. In this study, 10 fold cross validation was performed.

During validation, the accuracy of the classifier could be evaluated by comparing the classified voxels with the ground truth. In this study, the main task for the classifier is to segment between chalcopyrite and pyrite. Thus, some statistical measures could be calculated as follows:

- The percentage of correctly classified chalcopyrite voxels out of all chalcopyrite voxels, this is termed the True Positive Rate (TPR). The percentage of remaining chalcopyrite voxels (which are falsely
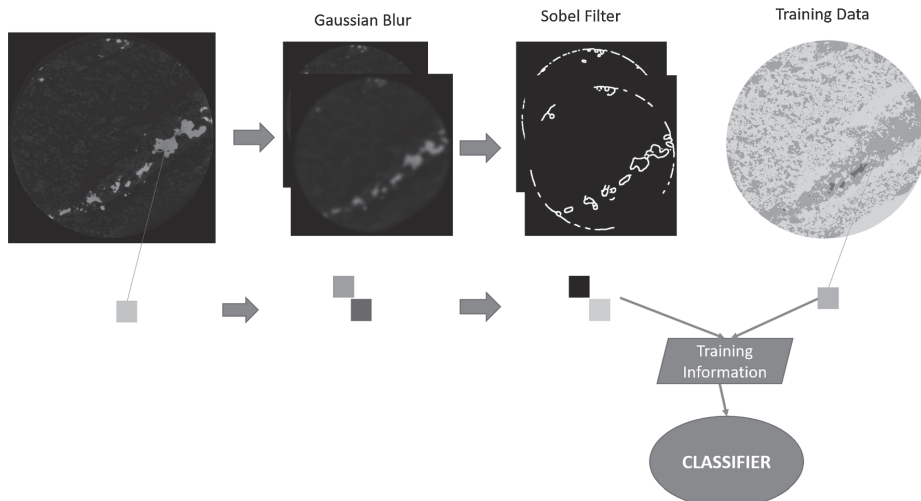
Fig. 11. Feature-based classification. The image is blurred with Gaussian filter at varying standard deviations, representing various scales of the original image. The edge features are then extracted at different scales using Sobel filter, producing two feature maps of the mineral grains in the drill core (here the edge images are dilated for easier viewing). The two features are then matched with the training data, so that it can be used to train a classifier.
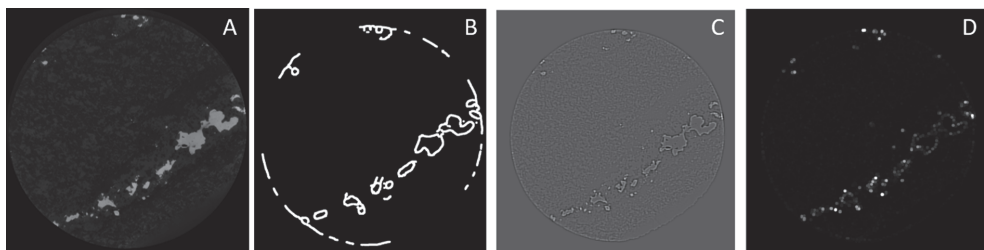
Fig. 12. Example of feature maps used in this study, showing (A) original μCT slice, (B) Sobel Edge features, (C) Difference of Gaussians blob features, and (D) Hessian corner (and blob) features. These feature maps were fed to the classification scheme in Fig. 11 so that the applicability of each feature map in supervised classification of pyrite and chalcopyrite phases could be evaluated.

classified as pyrite) is then called the False Negative Rate (FNR).

$$TPR = \frac{correctly \ classified \ chalcopyrite \ voxels}{All \ chalcopyrite \ voxels} = 1 - FNR \tag{7}$$

- On the other side, the percentage of correctly classified pyrite out of all pyrite voxels is termed True Negative Rate (TNR). Then the percentage of remaining pyrite voxels (which are miss-classified to chalcopyrite) is termed false positive rate (FPR).

$$TNR = \frac{correctly \ classified \ pyrite \ voxels}{All \ pyrite \ voxels} = 1 - FPR \tag{8}$$

- The percentage of all correctly classified voxels out of all voxels is termed Overall Accuracy (OA).

$$OA = \frac{correctly \ classified \ voxels}{All \ voxels} \tag{9}$$

Furthermore, the behavior of the classifier could be adjusted by changing the probability threshold (P). During validation and prediction, a classifier returns the scores on how confident it is in classifying a voxel to each respective category. The confidence score varies from 0 to 1, in which if the score for chalcopyrite is x, then for pyrite the score is $1 - x$. The classifier then identify a voxel as chalcopyrite only if its score is higher than the probability threshold.

$$x > P(v_{(x,y,z)}|chalcopyrite) \Rightarrow v_{(x,y,z)} = chalcopyrite \tag{10}$$

By varying this threshold, the sensitivity of classifier can be adjusted, therefore producing different TPR and TNR. An ideal classifier is a classifier that is able to correctly identify all chalcopyrite (TPR = 1), while at the same time correctly identify the pyrite as well (TNR = 1). By plotting the different TPR data (x-axis) against FPR data (y-axis), a receiver operating characteristic (ROC) curve can be drawn. The ROC curve tells the discrimination ability of a binary classifier as its probability threshold is varied:

- If the threshold is increased, it will only classify a voxel as a chalcopyrite only when it is very confident. In most cases, it will lead to decrease of FPR (as less pyrite will be misclassified as chalcopyrite). However, the proportion of the chalcopyrite correctly identified from the actual chalcopyrite (TPR) would also decrease, i.e. the classifier is now "strict" in identifying the chalcopyrite voxels
- Decreasing the threshold results in a less sensitive classifier, it now classifies a voxel as chalcopyrite even if it is not confident. This will lead to increase in TPR (as more chalcopyrite is correctly identified). However, at the same time, more pyrite is also being incorrectly

identified as chalcopyrite, leading to an increase in FPR. Simply, the classifier is now "lenient" in identifying the chalcopyrite voxels.

- Additionally, the area under the ROC curve, often abbreviated as AUC, also gives an idea on the classifiers' performance. While the aforementioned accuracy measures (TPR, TNR, OA) are valid for one operating point of the classifier (fixed probability threshold), the AUC can give an alternative measure on the classifiers' performance. This measure is invariant to the selected probability threshold (Bradley, 1997).

Nevertheless, getting the confidence score from the classifiers can be non-trivial. This is especially true when the classifier only predicts the class of the data (discrete classifier), instead of predicting the probability of the data to belong to a certain class (probabilistic classifier) (Majnik and Bosnić, 2013). The confidence score for both kNN and random forest classifier can be obtained as follows:

- In random forest classification, the standard method of obtaining confidence score is by simply calculating the fraction of total number of trees that vote for a specific class, although some other methods exist (Li, 2013). By default, random forest classifier assign a class by majority voting of the trees, in which majority is defined as more than 50%. This 50% is then the default probability threshold, which can be varied to change the behavior of the classifier.
- kNN classifier (in its basic form) can be categorized as discrete classifier, which means a method must be devised to obtain the confidence scores. The score can be associated to the fraction of the k nearest neighbors that belongs to a specific class (Majnik and Bosnić, 2013). Similar to the random forest classifier, kNN assign a class by majority (more than 50%) of classes found within the k nearest neighbors. This 50% threshold is then varied to change the classifier's behavior.

2.5. Image registration and creation of ground truth

Image registration refers to the transformation of an image into a specified coordinate system (Brown, 1992). The specified coordinate system can be in the form of a target image, where the transformed image is aligned with the target. The process involves matching both target and transforming images, which can be based on either the grayscale values or the features of the images.

As the reference data in Fig. 7 has different properties than the μCT image, a method must be devised on how to use the mineral information in Fig. 7 as the ground truth for the machine-learning classifications of the μCT images. Manually annotating the pixels in the μCT slice according to the mineral map in Fig. 7 is laborious, so there is a need for an automated annotation technique. In this study, the BSE image is registered to the corresponding μCT slice, so that a transformation matrix can be obtained. Using the transformation matrix, the BSE mineral map in Fig. 7 can be aligned to the μCT slice. The alignment of both images allows automated annotation of pixels in the μCT slice based on the BSE mineral map, therefore creating the ground truth for evaluating the performance of the classifiers.

Speeded up robust features (SURF) developed by Bay et al. (2008) were used to extract and match features of the BSE mineral map and its corresponding μCT image slice for the subsequent image registration. The algorithm essentially detects blobs (voxel regions that differ from the surrounding regions) in the image, in which in this case the algorithm could detect mineral grains. This is done by searching for points of interest with the maximum change of grayscale values in the surrounding voxels. This is accomplished by taking the use Hessian Matrix, which is used to describe the local curvatures in multivariable functions (an image here is considered a discrete function with two space variables). Detection of SURF features is shown in Fig. 13. Using such features allows alignment of two similar images with different

characteristics, and so is well suited to this study where the two images were acquired from different instruments.

2.5.1. Creation of ground truth for training data

Using image registration, a training μCT slice can be created based on the BSE mineral map. This is illustrated in Fig. 14.

The registration procedure did produce a good match within the vein area (sulfide phases), despite some mismatches seen particularly in the right part of the vein. These mismatches can be explained by the fact that such procedure struggles when the thin section for SEM-EDS is not cut perfectly parallel with the μCT slice plane. While this issue can be addressed by 2D-to-3D registration scheme rather than 2D-to-2D, such scheme is considerably more complex.

The SURF algorithm detected mainly the sulfide grains (Fig. 13), and the alignment was done mainly by matching the features between these grains in the two images. Around 84.4% of the sulfide (chalcopyrite and pyrite) pixels in the BSE image was accurately matched with the corresponding sulfide pixels in the μCT slice. Additionally, 92.8% of the chalcopyrite pixels in the BSE image was accurately matched to the sulfide phases in the μCT slice. The registration and annotation procedure was quite fast; it took around 7 s to create the fully annotated training data shown in Fig. 14(C).

With relatively good correspondence obtained for the sulfide pixels, the registration procedure was also good enough to identify the chalcopyrite phases in the μCT slice. Additionally, the registration scheme could also identify chalcopyrite phases within a pyrite grain (multimineral grains), as the mineral information was transferred on a pixel level rather than grain level. Therefore, the training data shown in Fig. 14(C) as constructed using multiple information: the gangue minerals were defined from unsupervised classification while the chalcopyrite minerals was defined from the image registration procedure.

### 2.5.2. Creation of ground truth for test data

In order to evaluate the generality and robustness of the classifiers, the trained classifiers were tested with an "unseen" data, i.e. data that have never been used for training. Since cross-validation was used for validation in the training session, this means that all parts of the training data in Fig. 14 have already been used. While it is possible to hold out part of the training data for independent testing, this means reducing the amount of training data used in the training session. As the chalcopyrite phase in our dataset is relatively low in proportion, holding out a part of this phase could lead to the classifiers not properly trained in classifying chalcopyrite. Therefore, an independent test data was created from another μCT slice.

The ground truth of the test data should also be known so that the classifiers can be evaluated properly. Since the μCT data in this study has a relatively high spatial resolution (13 μm), the data variation between the slices is not very significant; adjacent μCT slices represent a 13 μm distance in the drill core sample. This means that using the same transformation matrix obtained from the image registration in Fig. 14, the BSE mineral map could be aligned to the μCT slice that is adjacent to the training data, creating the ground truth of the μCT slice. The adjacent μCT slice can then be used as an independent test data, as this slice has never been used before to train the classifiers. The test data is shown in Fig. 15.
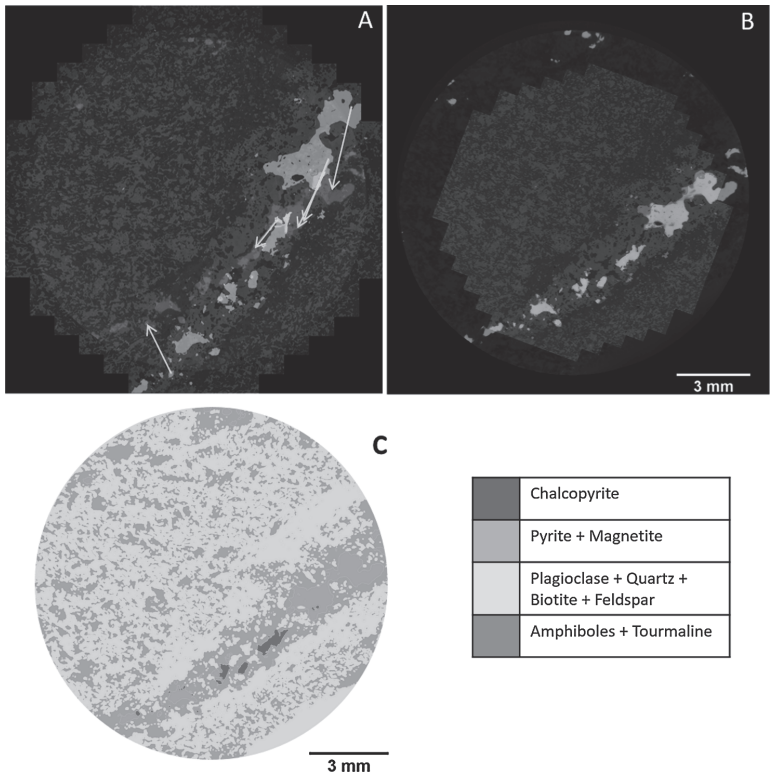
3. Results and discussion

The histogram of the μCT dataset used in this study is shown in Fig. 16.

While peaks of gangue and sulfide mineral groups are visible, differentiating mineral phases within this group was not straightforward. Several different machine learning algorithms were evaluated in order to tackle the segmentation problem, beginning with the simplest unsupervised based classification with no training data required.
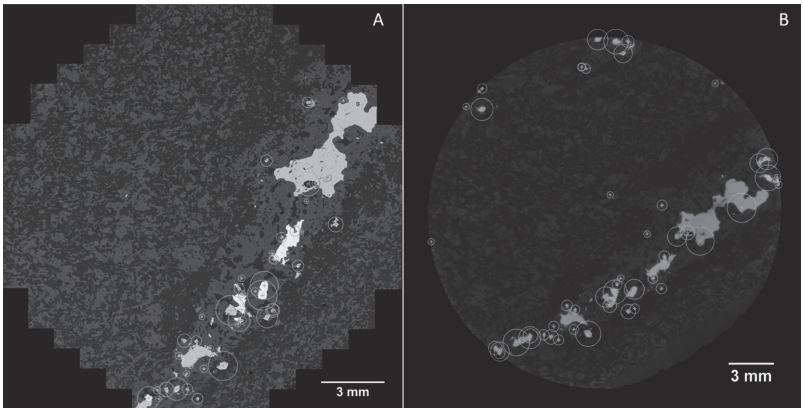
Fig. 13. Detected SURF features from (A) BSE image (resolution 3 μm) and (B) μCT slice (resolution 13 μm). These features corresponds well with the sulfide grains in the core. The points of interest from both images are matched, so that a transformation matrix that could align both images can be calculated.

	Chalcopyrite
	Pyrite + Magnetite
	Plagioclase + Quartz + Biotite + Feldspar
	Amphiboles + Tourmaline

Fig. 14. Image alignment and training data creation, showing (A) Matched feature points between two images with arrows showing the transformation direction, (B) both images aligned, magenta for BSE image, and green for the μCT slice, and (C) 2D μCT slice for training data, with chalcopyrite pixels annotated based on alignment with BSE mineral map. While the registration procedure returned a good match with the vein area of the slice, it returned a poor match with the phenocrysts and gangue area. (For interpretation of the references to color in this figure legend, the reader is referred to the web version of this article.)
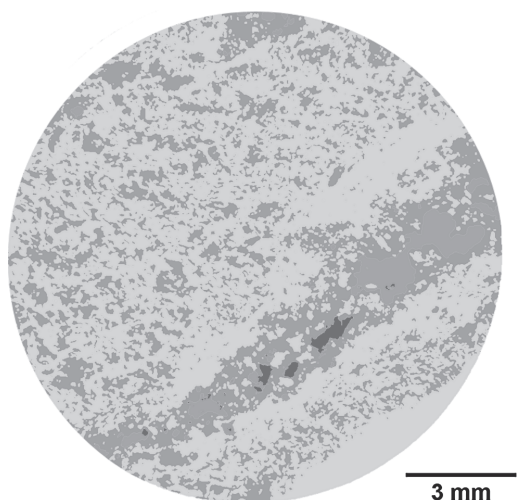
Fig. 15. Test data. The pixels were annotated using the same procedure shown in Fig. 14. Approximately 84.6% of sulfide pixels and 92.8% of the chalcopyrite pixels in the BSE image were accurately matched with the sulfide pixels in the μCT slice. Mineral color legend is the same as in Fig. 14(C).

3.1. Unsupervised classification

The selection of *k* value is discussed first, followed by the results of both *k*-means and FCM.

3.1.1. Determination of the number of clusters (k)

The relationship between SSE and number of clusters is shown in Fig. 17.

Determining the optimum number of clusters can be ambiguous, as the SSE always decreases up to the point of zero error where the number of clusters is the same as the number of pixels (each pixel has its own cluster). However, such condition would defeat the purpose of clustering, which is to group large datasets into several clusters. The optimum number of clusters can be defined as the point where no significant decrease of error is obtained when the number of clusters is increased. Obtaining such point can be illustrated in Fig. 17, where the
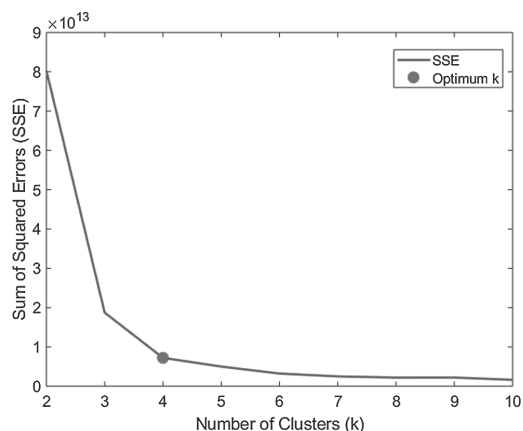

Fig. 17. Relationship between SSE and k, with the optimum value of k indicated by the red dot. (For interpretation of the references to color in this figure legend, the reader is referred to the web version of this article.)

tangent of the point gradually decreases as the number of cluster increases. The point where the tangent starts to level out (plateau) can be taken as the optimum point, often referred as the "elbow" of the curve (Bholowalia and Kumar, 2014). Using the elbow of the curve, the optimum number of clusters is determined as 4, representing 3 mineral groups and 1 background. In order to evaluate this further, some results of the *k*-means classification are shown in Fig. 18.

3.1.2. Results of k-means and FCM classification

Using *k = 4*, the results of both *k*-means and FCM are shown in Fig. 19 and Table 3.

Both classifications were performed until cluster means are stable within less than 0.1% relative difference. The time required is calculated for one μCT slice corresponding to 2008 × 2048 pixels, with *k-means* and FCM requiring 4.5 and 11.9 s respectively. Both techniques give similar results in mineral classification, but *k*-means requires less time to classify the input data. The pixel differences between both classification results do not show a clear tendency to a certain phase, the differences occur mostly in phase boundaries, as shown in the lower right hand corner of the "Difference" image in Fig. 19.
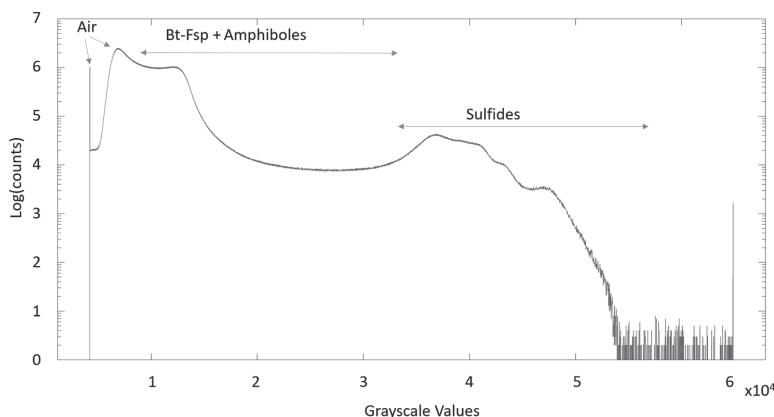
Fig. 16. Histogram of μCT dataset (after illumination correction). Major visible peaks represent air, gangue minerals (Biotite, Feldspars, Amphiboles), as well as the sulfide minerals (chalcopyrite and pyrite).
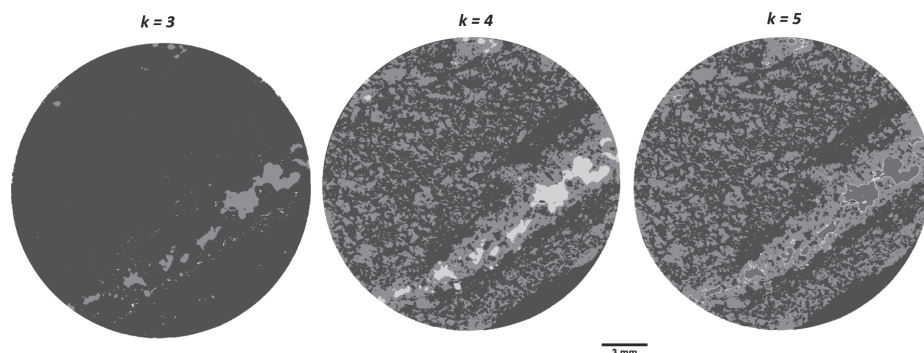
Fig. 18. Some results of the k-means classification with different k values. Adding a new clusters from three to four clusters produced a new information in the new cluster (a phase was separated to the new cluster), but increasing to five clusters did not produce any new information (no phase was separated further).

In general, both classification results show good correspondence with the BSE mineral map. However, both methods fail to differentiate between chalcopyrite and pyrite, compared to the BSE mineral map in Fig. 7. Other minerals such as quartz and magnetite are also not segmented, but this is due to the lower resolution of μCT in comparison to the BSE image (3 μm). Therefore, small minerals with a grain size less than the μCT resolution (13 μm) cannot be accurately segmented.

3.2. Supervised classification

In order to address the segmentation between chalcopyrite and pyrite, two approaches in supervised classification were evaluated in this study, namely grayscale-based classification and feature-based classification. Before moving on to classification results, the tuning of classifiers' parameters is discussed first.

#### 3.2.1. Tuning of classifiers' parameters

By evaluating the effect of varying classifiers' parameters to their performance, one could identify the set of parameters that gave the best performance while maintaining reasonable computational complexities. While OA is one of the most popular metrics in assessing classifier's performance, it is not capable of assessing the performance of specific classes (Thanh Noi and Kappas, 2018). Furthermore, since the

training data was relatively imbalanced in class (chalcopyrite phase is occurs much less frequently than other phases), the OA value might be deceiving as the rare classes may be classified poorly (He and Garcia, 2008). Therefore, AUC value was also used to compensate for the weaknesses of OA, as AUC also takes into account the performance of the classes. The effect of classifiers' parameters to their performance is shown in Figs. 20 and 21 for kNN and random forest classifier respectively.

The performance of both classifiers was increased up until a certain level in which further increase in the complexity of the classifiers would not necessarily give better performance. Additionally, increasing k or ntree means more time required to build and train the classifiers, so a balance between training time and classifiers' performance is required.

One noticeable difference between kNN and random forest classifiers is that while increasing ntree in random forest classifier would always lead to better (or at least similar) performance, the same cannot be said with kNN classifier. As shown in Fig. 20, the AUC of kNN classifier decreases when k is increased. The decrease in OA is less clear in Fig. 20, but around 0.2% decrease was observed. This is in contrast with random forest, where kNN does have a so-called "optimum" number of k, in which further increase of k would worsen the predictive capability of the classifier.

Beside the performance, the training time is also an important factor
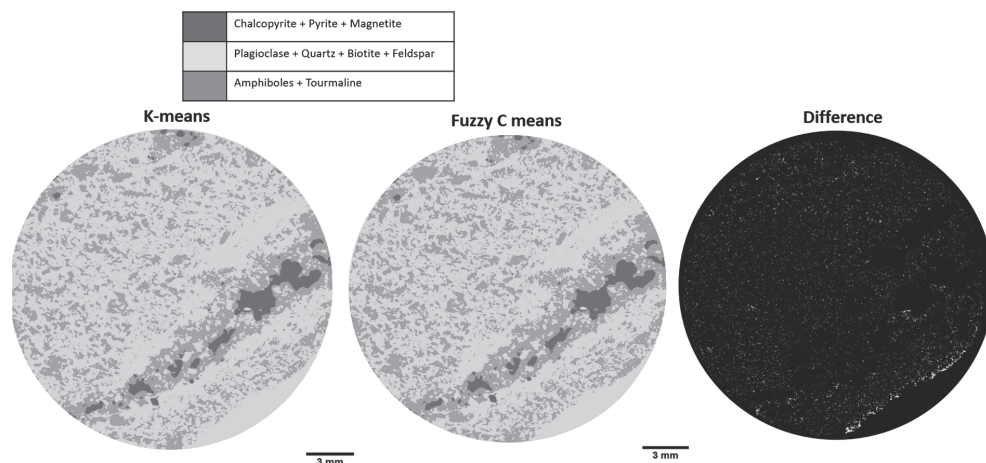
Fig. 19. Mineral mapping using unsupervised classification (k-means and FCM). Three phases were identified. The "Difference" image shows a binary image with pixels that are classified differently in the two classification schemes, which corresponds to 86,838 pixels, or 2.11% out of the total 2008 × 2048 pixels in the image.

Table 3

Phase percentage of mineral maps shown in Fig. 19, showing minimal difference between the classifiers. Minor differences exist in comparison to BSE mineral map due to difference in spatial resolution between the 2D μCT slice and BSE image, but overall both techniques shows good correspondence.

Color	Phase	k-means – Phase (%)	FCM – Phase (%)	BSE Mineral Map – Phase (%)
	Chalcopyrite, Pyrite, Magnetite	3.4%	3.4%	4.4%
	Plagioclase, Quartz, Biotite, Feldspar	57.8%	57.3%	55.7%
	Amphiboles, Tourmaline	38.8%	39.3%	39.9%

Fig. 20. Effect of k to the performance of the kNN classifier.

Fig. 22. Effect of ntree and k to the training time of random forest and kNN classifier respectively. Training time was obtained based on MATLAB® implementation of supervised classification with 10-fold cross-validation.
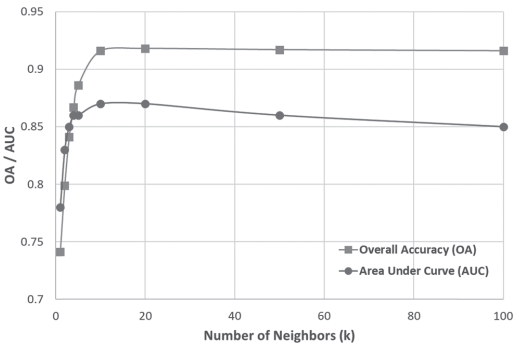
in determining the optimum parameters for the classifiers. The effect of varying classifiers' parameter to their training time is shown in Fig. 22.

In general, random forest classifiers is considerably more complex than kNN classifiers, as shown by the training time. Additionally, increasing the number of trees in random forest led to significant increase of computational complexity. This increase was less prevalent for kNN classifiers, especially for less than 50 neighbors.

Based on the performances and required training time, the optimum number of tree (ntree) for random forest classifier was determined to be 10, while the optimum number of neighbors (k) was determined to be 20. These parameters were then used for the subsequent grayscale-based classification.

3.2.2. Grayscale-based classification

Grayscale values for each phase based on the training data were obtained and used as reference values for the classification process.
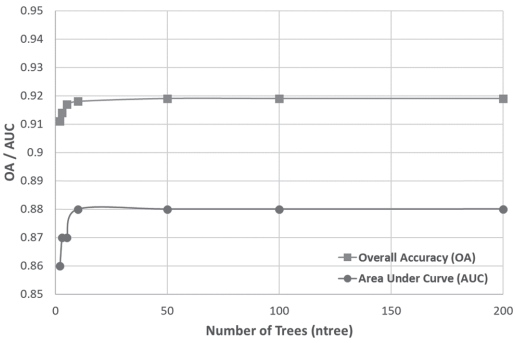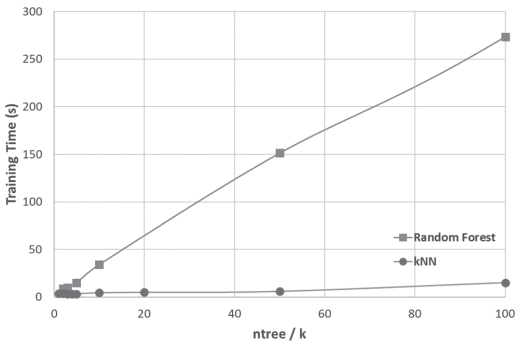

Fig. 21. Effect of ntree to the performance of random forest classifier.

These reference values were then used to train a classification model. The model was then applied to classify the rest of the slices in the 3D image. As only chalcopyrite phases were defined from the BSE mineral map through feature matching, the classification problem mostly concerns binary classification of the sulfide grains as chalcopyrite or pyrite. The pyrite phase referred here includes a small amount of magnetite as well. Therefore, the total training data was reduced to only 88,980 pixels of the original 2048×2008 pixels, corresponding to both the chalcopyrite and pyrite grains in the image. Out of these pixels, 13.5% of them belong to chalcopyrite class, while the remaining belongs to pyrite class. The information about relative frequencies of the classes was used as the prior probability of the classes, meaning that the prior probability of chalcopyrite and pyrite class is 0.135 and 0.865 respectively. The training results are shown in Table 4 and Fig. 23.

The classifiers were then evaluated with test data. The total test data was 88,664 pixels, corresponding to chalcopyrite and pyrite grains in the image. Chalcopyrite accounts for 14% of these pixels. Similarly, the relative frequency information was used as the prior probability of each class. The testing results are given in Table 5 and Fig. 24.

Having an independent test data set is useful in evaluating the generality and robustness of the classifiers. A classifier is robust if the testing performance is similar as the training performance (Xu and Mannor, 2012). By comparing Tables 4 and 5, it can be seen that the accuracy of the classifiers decreases as they are evaluated on unseen test data. This is especially true for the random forest classifier, while

Table 4

Training performance of different algorithms in grayscale-based classification.

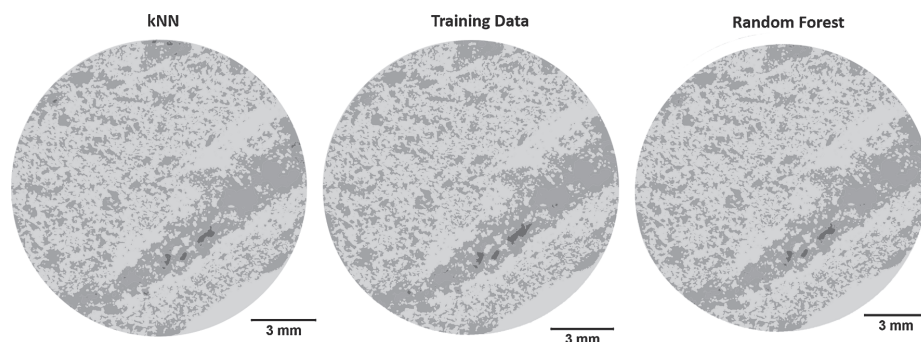| Algorithm	Training time (s)	True positive	True negative
kNN (k = 20)	4.9	60%	97%
Random Forest (ntree = 10)	34.2	60%	97%

Fig. 23. Comparison of grayscale-based classified training data with the ground truth.

Table 5

Testing performance of different algorithms in grayscale-based classification. Testing time is taken as the time required for the classifiers to classify the test data. Performance was assessed by comparing to the ground truth of the test data.

Algorithm	Testing time (s)	True positive	True negative
kNN (k = 20)	0.4	57%	96%
Random forest (ntree = 10)	0.5	50%	95%

kNN classifier showed better robustness and generalization capability.

While both classifiers have relatively high true negative values, the TPRs for chalcopyrite are still relatively low. The classifiers only succeed 50–60% of the time when identifying a pixel that should belong to chalcopyrite. This could be explained by the fact that there is an overlap in grayscale values between chalcopyrite and pyrite, which means that some pixels could be classified as both chalcopyrite and pyrite based on their grayscale values, as illustrated in Fig. 25.

3.2.3. Feature-based classification

Feature-based classification was used as a comparison to the grayscale value based classification. The classifiers were trained using the training data and subsequently evaluated using the independent test data in Fig. 15. The results are shown in Table 6 and Fig. 26.

Similar to the classification scheme using grayscale values, classification based on features was also found to be unsatisfactory. Features such as edges, corners, and blobs of the chalcopyrite and pyrite pixels were found not to be the discriminating factor for both phases. Nevertheless, comparing Table 6 to the testing results of grayscale-based classifications in Table 5 (especially the random forest classification), the performance of feature-based classification was relatively

better. This indicates that by using features extracted in different scales, one can build a classifier that generalizes better than using solely the grayscale values. However, it should be noted that feature-based classifications require significantly longer training time than grayscale-based classifications.

3.3. Evaluation of performances and results

When classifying between the gangue, background and the sulfides, unsupervised classification was found to be satisfactory, with results showing good match with the BSE mineral map while requiring short computational time, as seen in Table 3. This is due to the relatively clear difference in grayscale values between these phases. However, supervised classification was needed to differentiate between chalcopyrite and pyrite due to unclear difference between the two phases.

By using BSE mineral map as a reference and training data, chalcopyrite and pyrite can be differentiated to some extent using supervised classification, as seen in Tables 4 and 5. Increasing the classifier's sensitivity (TPR) would lead to the decrease of sensitivity for the pyrite phase (TNR). This limitation is illustrated through the ROC curve obtained from the models in Table 5. (Random Forest and k-nearest neighbor) shown in Fig. 27.

As noted previously, the behavior of the classifiers can be adjusted by changing the probability threshold, which is shown by moving the red dot in Fig. 27 along the ROC curve. Therefore, there would be no condition where the classifier could classify all pyrite and chalcopyrite voxels correctly, i.e. by reaching 100% TPR while at the same time having 0% FPR (top left corner of the graph). A compromise between the two phases is inevitable, mainly due to overlapping grayscale values. Furthermore, as the amount of pixels belonging to pyrite is higher than that of chalcopyrite, the classifier tends to decrease the false
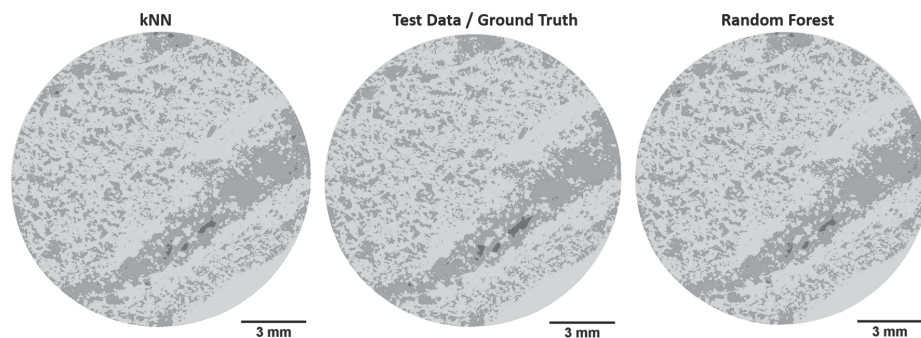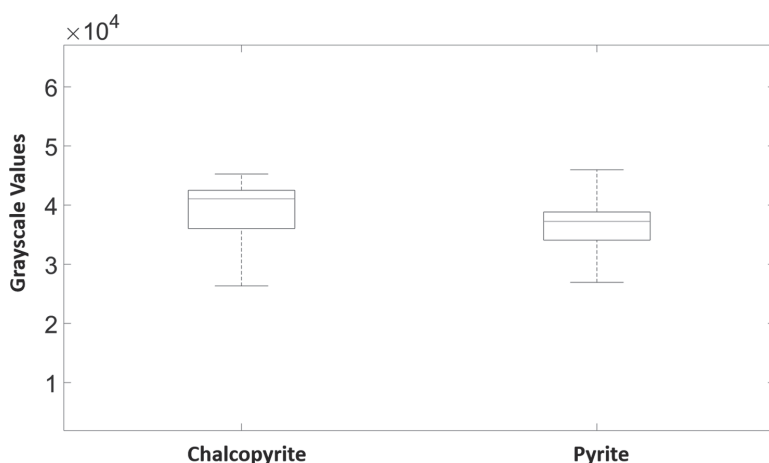

**Fig. 24.** Comparison of classified test data with the ground truth.

Fig. 25. Boxplot of grayscale values of chalcopyrite and pyrite obtained from the training data. Due to the photoelectric effect, chalcopyrite is more attenuating than pyrite despite having lower density, as shown by the first, second (median), and third quartile of chalcopyrite grayscale values being higher than pyrite. However still there is considerable overlap between the phases making it difficult to segment these phases based on their grayscale value.

Table 6
Classification performance of different feature extractors. All 4,112,385 (2008 × 2048) pixels in the training data were used to create the feature vectors. The increase in training data subsequently increased the training time. The true positive and true negative values are based on the testing with the test data.

Feature extractor	Classifier	Training time	True positive	True negative
Sobel filter	Random forest	3 h 53 m 8 s	60%	96%
Determinant of Hessian	Random forest	5 h 36 m 39 s	57%	97%
Difference of Gaussian	Random forest	4 h 59 m 8 s	53%	97%
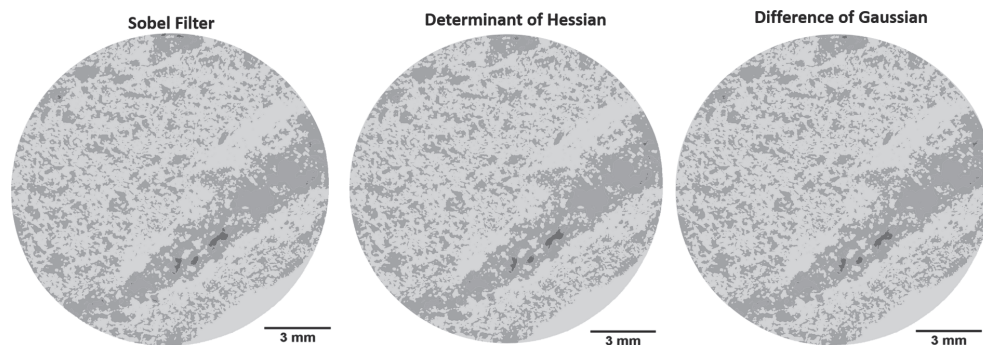
Fig. 26. Classified test data using feature-based classifications.

positive, as 1% of pyrite being misclassified weighs higher in the final accuracy than 1% of chalcopyrite being correctly classified.

Feature-based classification did not increase the classifier's accuracy and precision significantly, as seen in Table 6. This is because these features were also built based on the grayscale values of the pixels, with addition of their relationship to the other pixels in the neighborhood. If the original pixel values were too similar and almost indistinguishable, their features would also be difficult to distinguish. Nevertheless, feature-based classifications tend to generalize better than grayscale-based classification, as shown in Tables 5 and 6.

Another notable difference in result between feature-based and grayscale-based classification can be seen in Fig. 28. In grayscale-based classification, the voxels' grayscale value is the sole criteria in classifying pyrite and chalcopyrite. This leads to many scattered chalcopyrite voxels in the pyrite grain shown in Fig. 28(A). This phenomena was not observed in feature-based classification, as shown in Fig. 28(B). Feature-based classification is especially well suited when dealing with

grain boundaries (Wang et al., 2015), as it uses features that could represent grains (voxel regions) when segmenting between minerals. This in turns produces better segmentation between the grains in the ore.

Nevertheless, a significant difference is observed when evaluating the mineralogical result of 3D μCT data and the conventional 2D BSE mineral map. The mineralogical results given Table 7 shows the typical stereological error exhibited by 2D based analysis in overestimating the mineralogy. The difference in 2D μCT slice and 2D SEM-EDS can be explained by the loss of details in the μCT due to lower spatial resolution.

4. Conclusions

The application of machine learning algorithms to mineral segmentation of 3D μCT image has been presented. It was found that simple unsupervised classification could provide a rapid segmentation
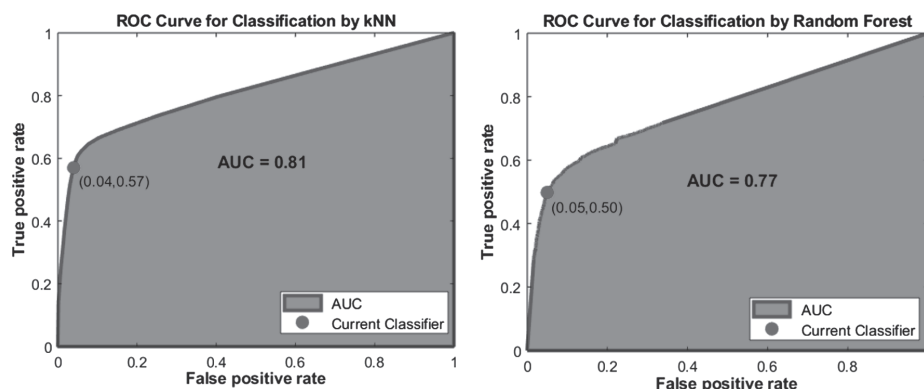
Fig. 27. ROC curve for Random Forest and kNN classifiers. The curve describes the relationship between FPR and TPR, with the red dot indicates the current classifier. The test data was used to generate the curve. (For interpretation of the references to color in this figure legend, the reader is referred to the web version of this article.)
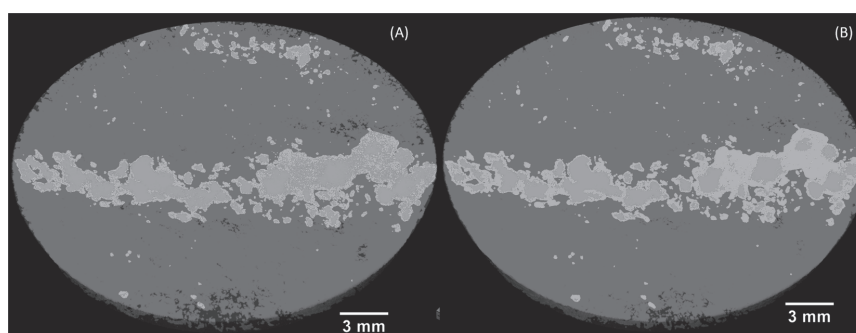
Fig. 28. Comparison of random forest classified mineral map showing chalcopyrite (red), pyrite (green), and gangue (gray), using (A) grayscale based classification, and (B) feature (determinant of Hessian) based classification. While grayscale based classification operates on individual voxels, determinant of Hessian operates based on blobs/region of voxels, which resulted in better segmentation between grains as shown in (B). (For interpretation of the references to color in this figure legend, the reader is referred to the web version of this article.)

Table 7
Simplified mineralogy (by area or volume) obtained from SEM and μCT. Note: kNN = k Nearest Neighbors, RF = Random Forest, SF = Sobel Filter followed by RF, DoH = Determinant of Hessian followed by RF, and DoG = Difference of Gaussians followed by RF.

Minerals	2D – SEM EDS (%)	2D – μCT (%)	3D μCT (%)				
			kNN	RF	SF	DoH	DoG
Amphiboles Tourmaline	39.92	39.29	37.26	37.26	40.33	40.33	40.33
Plagioclase Quartz Biotite Feldspar	55.67	57.28	59.47	59.47	56.77	56.77	56.77
Pyrite Magnetite	3.70	3.00	2.90	2.91	2.73	2.72	2.73
Chalcopyrite	0.71	0.43	0.37	0.36	0.17	0.18	0.17

between gangue and sulfide minerals that has less difference in grayscale values. Unsupervised classification also required significantly less time, as no training and feature extraction was needed. A method in determining the optimum number of clusters in unsupervised classifications has also been presented.

Supervised classification was found to be capable of distinguishing chalcopyrite and pyrite to a certain extent. Using voxel values as the dataset in grayscale-based supervised classification offers a simple and rapid approach in distinguishing the mineral phases with reasonable accuracy. Overall, the results of the grayscale-based classification suggested that kNN classifier performed better than random forest classifier in all aspects; it generalized better and required less training time. The effect of classifiers' parameters to the performance was also evaluated, and it was found that there is an optimum point where further increasing the classifiers' complexity leads to relatively insignificant performance gain.

Feature-based classification added more information about voxel neighborhoods in the classification process, producing better segmentation between the mineral grains. Moreover, the results in this study suggested that feature-based classifiers tend to generalize better than grayscale-based classifiers. Feature-based classification could be a better alternative especially when textural information such as grain size and shape needs to be extracted after the mineral phase segmentation.

Additionally, methodology to align SEM-EDS image to its corresponding μCT slice for phase labelling and training data generation has been presented. The whole process is relatively fast (around 7 s) and largely automated; the user only needs to specify which μCT slice corresponds to the BSE mineral map. The main advantage of the method is that it works on pixel level, i.e. information of each pixel that belongs to a phase can be transferred to a μCT slice, therefore allowing

the definition of multi-mineral grains. Moreover, since it is based on features, it is more robust to characteristic differences between the images. Nevertheless, the methodology is limited on the parallel cutting of the μCT sample for the thin section, as it must be cut exactly in parallel to achieve perfect correspondence between the two images.

The main limitation of the application of machine learning in μCT dataset lies in the dataset itself, particularly whether the grayscale values of mineral phases in the sample are different enough to be segmented. In this study, due to the significant overlaps in grayscale values between chalcopyrite and pyrite, the classifier could not fully differentiate between the two phases. Increasing the classifier's sensitivity to one phase will decrease the sensitivity to the other phase.

As the limitations come from the dataset, improvements must be done during the image acquisition process. Scanning conditions could be optimized so that contrast between phases of interests could be maximized for easier segmentation. Dual energy scanning is one of the alternatives, as it allows direct determination of density or effective atomic number by correlating with attenuation coefficient at different energy levels. Some calibration with pure chalcopyrite and pyrite minerals could also be done prior to image acquisition in order to determine the optimum beam settings for distinguishing both phases. If both phases have a clear difference in grayscale values, then even a simple unsupervised classification should produce satisfactory results.

Acknowledgements

References

Andrä, H., Combaret, N., Dvorkin, J., Glatt, E., Han, J., Kabel, M., Keehm, Y., Krzikalla, F., Lee, M., Madonna, C., 2013. Digital rock physics benchmarks—Part I: Imaging and segmentation. Comput. Geosci. 50, 25–32.

Arganda-Carreras, I., Kaynig, V., Rueden, C., Eliceiri, K.W., Schindelin, J., Cardona, A., Sebastian Seung, H., 2017. Trainable Weka Segmentation: A machine learning tool for microscopy pixel classification. Bioinformatics 33, 2424–2426.

Bam, L.C., Miller, J.A., Becker, M., Basson, I.J., 2019. X-ray computed tomography: Practical evaluation of beam hardening in iron ore samples. Miner. Eng. 131, 206–215. https://doi.org/10.1016/j.mineng.2018.11.010.

Bay, H., Ess, A., Tuytelaars, T., Van Gool, L., 2008. Speeded-up robust features (SURF). Comput. Vis. image Underst. 110, 346–359.

Bholowalia, P., Kumar, A., 2014. EBK-means: A clustering technique based on elbow method and k-means in WSN. Int. J. Comput. Appl. 105.

Bradley, A.P., 1997. The use of the area under the ROC curve in the evaluation of machine learning algorithms. Pattern Recognit. 30, 1145–1159. https://doi.org/10.1016/S0031-3203(96)00142-2.

Breiman, L., 2001. Random forests. Mach. Learn. 45, 5–32.

Brown, L.G., 1992. A survey of image registration techniques. ACM Comput. Surv. 24, 325–376.

Chauhan, S., Rühaak, W., Khan, F., Enzmann, F., Mielke, P., Kersten, M., Sass, I., 2016a. Processing of rock core microtomography images: Using seven different machine learning algorithms. Comput. Geosci. 86, 120–128. https://doi.org/10.1016/j.cageo.2015.10.013.

Chauhan, S., Rühaak, W., Anbergen, H., Kabdenov, A., Freise, M., Wille, T., Sass, I., 2016b. Phase segmentation of X-ray computer tomography rock images using machine learning techniques: an accuracy and performance study. Solid Earth 7, 1125–1139.

Cnudde, V., Boone, M.N., 2013. High-resolution X-ray computed tomography in geosciences: A review of the current technology and applications. Earth-Sci. Rev. 123, 1–17.

Deng, H., Fitts, J.P., Peters, C.A., 2016. Quantifying fracture geometry with X-ray tomography: Technique of Iterative Local Thresholding (TILT) for 3D image segmentation. Comput. Geosci. 20, 231–244. https://doi.org/10.1007/s10596-016-9560-9.

Duran, B.S., Odell, P.L., 2013. Cluster Analysis: A Survey. Springer Science & Business Media.

Feng, Q., Liu, J., Gong, J., 2015. UAV remote sensing for urban vegetation mapping using random forest and texture analysis. Remote Sens. 7, 1074–1094. https://doi.org/10.3390/rs70101074.

Garcia, D., Lin, C.L., Miller, J.D., 2009. Quantitative analysis of grain boundary fracture in the breakage of single multiphase particles using X-ray microtomography procedures. Miner. Eng. 22, 236–243.

Ghorbani, Y., Becker, M., Petersen, J., Morar, S.H., Mainza, A., Franzidis, J.-P., 2011. Use of X-ray computed tomography to investigate crack distribution and mineral dissemination in sphalerite ore particles. Miner. Eng. 24, 1249–1257. https://doi.org/10.1016/j.mineng.2011.04.008.

Guntoro, P.I., Ghorbani, Y., Koch, P.-H., Rosenkranz, J., 2019. X-ray microcomputed tomography (μCT) for mineral characterization: A review of data analysis methods. Minerals 9, 183. https://doi.org/10.3390/min9030183.

Hall, P., Park, B.U., Samworth, R.J., 2008. Choice of neighbor order in nearest-neighbor classification. Ann. Stat. 36, 2135–2152. https://doi.org/10.1214/07-AOS537.

He, H., Garcia, E.A., 2008. Learning from imbalanced data. IEEE Trans. Knowl. Data Eng. 1263–1284.

Jardine, M.A., Miller, J.A., Becker, M., 2018. Coupled X-ray computed tomography and grey level co-occurrence matrices as a method for quantification of mineralogy and texture in 3D. Comput. Geosci. 111, 105–117. https://doi.org/10.1016/j.cageo.2017.11.005.

Kyle, J.R., Ketcham, R.A., 2015. Application of high resolution X-ray computed tomography to mineral deposit origin, evaluation, and processing. Ore Geol. Rev. 65, 821–839. https://doi.org/10.1016/j.oregeorev.2014.09.034.

Kyle, J.R., Mote, A.S., Ketcham, R.A., 2008. High resolution X-ray computed tomography studies of Grasberg porphyry Cu-Au ores, Papua. Indonesia. Miner. Depos. 43, 519–532. https://doi.org/10.1007/s00126-008-0180-8.

Li, C., 2013. Probability Estimation in Random Forests.

Lin, C.L., Miller, J.D., 2005. 3D characterization and analysis of particle shape using X-ray microtomography (XMT). Powder Technol. https://doi.org/10.1016/j.powtec.2005.04.031.

Lin, C.L., Miller, J.D., 1996. Cone beam X-ray microtomography for three-dimensional liberation analysis in the 21st century. Int. J. Miner. Process. 47, 61–73.

Lin, Q., Barker, D.J., Dobson, K.J., Lee, P.D., Neethling, S.J., 2016a. Modelling particle scale leach kinetics based on X-ray computed micro-tomography images. Hydrometallurgy 162, 25–36.

Lin, Q., Neethling, S.J., Courtois, L., Dobson, K.J., Lee, P.D., 2016b. Multi-scale quantification of leaching performance using X-ray tomography. Hydrometallurgy 164, 265–277. https://doi.org/10.1016/j.hydromet.2016.06.020.

Lin, Q., Neethling, S.J., Dobson, K.J., Courtois, L., Lee, P.D., 2015. Quantifying and minimising systematic and random errors in X-ray micro-tomography based volume measurements. Comput. Geosci. 77, 1–7.

Lindeberg, T., 2015. Image matching using generalized scale-space interest points. J. Math. Imaging Vis. 52, 3–36. https://doi.org/10.1007/s10851-014-0541-0.

Lindeberg, T., 2013. Scale selection properties of generalized scale-space interest point detectors. J. Math. Imaging Vis. 46, 177–210. https://doi.org/10.1007/s10851-012-0378-3.

Lindeberg, T., 2007. Scale-space. Wiley Encycl. Comput. Sci. Eng. 2495–2504.

Maire, E., Withers, P.J., 2014. Quantitative X-ray tomography. Int. Mater. Rev. 59, 1–43. https://doi.org/10.1179/1743280413Y.0000000023.

Majnik, M., Bosnić, Z., 2013. ROC analysis of classifiers in machine learning: A survey. Intell. data Anal. 17, 531–558.

Mees, F., Swennen, R., Van Geet, M., Jacobs, P., 2003. Applications of X-ray computed tomography in the geosciences. Geol. Soc. London Spec. Publ. 215, 1–6.

Miller, J.D., Lin, C.L., Cortes, A.B., 1990. A review of X-ray computed tomography and its applications in mineral processing. Miner. Processing Extr. Metall. Rev. 7, 1–18.

Müter, D., Pedersen, S., Sørensen, H.O., Feidenhans'l, R., Stipp, S.L.S., 2012. Improved segmentation of X-ray tomography data from porous rocks using a dual filtering approach. Comput. Geosci. 49, 131–139. https://doi.org/10.1016/j.cageo.2012.06.024.

Naidoo, L., Cho, M.A., Mathieu, R., Asner, G., 2012. Classification of savanna tree species, in the Greater Kruger National Park region, by integrating hyperspectral and LiDAR data in a Random Forest data mining environment. ISPRS J. Photogramm. Remote Sens. 69, 167–179. https://doi.org/10.1016/J.ISPRSJPRS.2012.03.005.

Oshiro, T.M., Perez, P.S., Baranauskas, J.A., 2012. How many trees in a random forest? In: Perner, P. (Ed.), Machine Learning and Data Mining in Pattern Recognition. Springer, Berlin Heidelberg, Berlin, Heidelberg, pp. 154–168.

Otsu, N., 1979. A threshold selection method from gray-level histograms. IEEE Trans. Syst. Man. Cybern. 9, 62–66.

Reyes, F., Lin, Q., Udoudo, O., Dodds, C., Lee, P.D., Neethling, S.J., 2017. Calibrated X-ray micro-tomography for mineral ore quantification. Miner. Eng. 110, 122–130. https://doi.org/10.1016/j.mineng.2017.04.015.

Russell, S.J., Norvig, P., 2016. Artificial Intelligence: A Modern Approach. Pearson Education Limited, Malaysia.

Schindelin, J., Arganda-Carreras, I., Frise, E., Kaynig, V., Longair, M., Pietzsch, T., Preibisch, S., Rueden, C., Saalfeld, S., Schmid, B., 2012. Fiji: an open-source platform for biological-image analysis. Nat. Methods 9, 676.

Siddique, M., Bakr, A., Arif, R.B., Khan, M.M.R., Ashrafi, Z., 2018. Implementation of Fuzzy C-Means and Possibilistic C-Means Clustering Algorithms, Cluster Tendency Analysis and Cluster Validation. arXiv Prepr. arXiv1809.08417.

Sobel, I., 2014. An Isotropic 3x3 Image Gradient Operator, Presentation at Stanford A.I. Project 1968.

Suthaharan, S., 2016. Machine learning models and algorithms for big data classification. Integr. Ser. Inf. Syst 36, 1–12.

Thanh Noi, P., Kappas, M., 2018. Comparison of random forest, k-nearest neighbor, and support vector machine classifiers for land cover classification using sentinel-2 imagery. Sensors 18. https://doi.org/10.3390/s18010018.

Tiu, G., 2017. Classification of Drill Core Textures for Process Simulation in Geometallurgy : Aitik Mine, Sweden. EMerald Program.

Wang, G., Wang, Y., Li, H., Chen, X., Lu, H., Ma, Y., Peng, C., Wang, Y., Tang, L., 2014. Morphological background detection and illumination normalization of text image

with poor lighting. PLoS ONE 9, e110991.

Wang, Y., Lin, C.L., Miller, J.D., 2015. Improved 3D image segmentation for X-ray to-mographic analysis of packed particle beds. Miner. Eng. 83, 185–191. https://doi.org/10.1016/j.mineng.2015.09.007.

Wanhainen, C., Broman, C., Martinsson, O., 2003. The Aitik Cu-Au-Ag deposit in northern Sweden: A product of high salinity fluids. Miner. Deposita. https://doi.org/10.1007/s00126-003-0363-2.

Wightman, E., Evans, C.L., Wightman, E.M., Yuan, X., 2015. Quantifying mineral grain size distributions for process modelling using X-ray micro-tomography. Miner. Eng.

Xu, H., Mannor, S., 2012. Robustness and generalization. Mach. Learn. 86, 391–423. https://doi.org/10.1007/s10994-011-5268-1.

Yang, B., Wu, A., Narsilio, G.A., Miao, X., Wu, S., 2017. Use of high-resolution X-ray computed tomography and 3D image analysis to quantify mineral dissemination and pore space in oxide copper ore particles. Int. J. Miner. Metall. Mater. 24, 965–973. https://doi.org/10.1007/s12613-017-1484-4.

Zaitoun, N.M., Aqel, M.J., 2015. Survey on image segmentation techniques. Procedia Comput. Sci. 65, 797–806.

Department of Civil, Environmental, and Natural Resources Engineering
Division of Minerals and Metallurgical Engineering

LULEÅ
UNIVERSITY
OF TECHNOLOGY